

## ABSTRACT

SEOK, JAEWOOK. *In Situ* Morphology Control of P3HT:PC<sub>61</sub>BM Bulk Heterojunction (BHJ) Polymer Solar Cells. (Under the direction of Harald W. Ade and C. Maurice Balik.)

Highly regioregular poly(3-hexyl thiophene) (P3HT) and [6,6]-phenyl-C<sub>61</sub>-butyric acid methyl ester (PC<sub>61</sub>BM) are popular materials for use in bulk heterojunction (BHJ) polymer solar cells. For optimized P3HT:PC<sub>61</sub>BM BHJ solar cells, not only should the domain size be similar to the exciton's diffusion length (~10 nm) required, but also the orientation of P3HT crystallites should be optimized. Small domains result in an effective charge separation and also minimize charge recombination at the interface between P3HT and PCBM. Additionally, a 'face-on' crystalline orientation of P3HT, in which the  $\pi$ - $\pi$  stacking direction is parallel to the electric field, enhances hole charge carrier mobility. This paper presents a new strategy to achieve an increased 'face-on' P3HT crystalline orientation and a smaller lateral domain size in P3HT:PC<sub>61</sub>BM BHJ polymer solar cells than what is readily achievable via thermal annealing alone. This improved nanostructure control is achieved by in situ ultraviolet (UV) photo-polymerization of the 2,5-dibromothiophene (DBT) present in the thin films of the BHJ active layer after short-term vapor annealing. The power conversion efficiency (PCE) is improved by approximately 20 percent relative to thermal annealing alone.

*In Situ* Morphology Control of P3HT:PC<sub>61</sub>BM Bulk Heterojunction (BHJ)  
Polymer Solar Cells

by  
Jaewook Seok

A dissertation submitted to the Graduate Faculty of  
North Carolina State University  
in partial fulfillment of the  
requirements for the Degree of  
Doctor of Philosophy

Materials Science and Engineering

Raleigh, North Carolina

2011

APPROVED BY:

---

Daniel Dougherty

---

Yuntian Zhu

---

Harald W. Ade, Committee Chair

---

C. Maurice Balik, Co-Chair

## **DEDICATION**

This work is dedicated with love to  
my parents, my supportive wife and two lovely daughters as well as my whole family.

## **BIOGRAPHY**

Jaewook Seok was born in Daegu, Korea. He attended Kyungpook National University (KNU) in Daegu and earned his B.E. and M.E. in Polymer Science and Engineering from KNU in 1997 and 1999, respectively. After graduation, Jaewook worked in world-wide research and development (R&D) at the Anam Semiconductor Co. and at Amkor Technology, Inc. as a senior research engineer for five years. He researched organic substrates for advanced semiconductor packaging and organic electronics. In 2004, Jaewook was awarded a national scholarship from the Korean Science and Engineering Foundation (KOSEF) to pursue an additional master's degree, completed in 2006, in Materials Science and Engineering at Cornell University, Ithaca, New York, under the direction of Dr. Christopher K. Ober.

In the fall of 2006, Jaewook moved to Raleigh, North Carolina to pursue a doctoral degree at North Carolina State University (NCSU). Under the direction of Dr. Harald W. Ade in Physics and Dr. C. Maurice Balik in Materials Science and Engineering, Jaewook carried out research into P3HT:PC<sub>61</sub>BM BHJ polymer solar cells. While studying at NCSU, he developed a new concept in the morphology control of BHJ polymer solar cells to improve the performance of P3HT:PC<sub>61</sub>BM BHJ polymer solar cells in particular and, as a result, this subject became the topic of his doctoral dissertation.

## ACKNOWLEDGMENTS

I wish to sincerely thank my advisor, Professor Harald W. Ade, for his special mentorship, endless encouragement and support during my graduate studies at North Carolina State University (NCSSU). Dr. Ade has given me new vision as a polymer physicist and a materials scientist. Without him, my research efforts, which began from my own humble ideas, would not have resulted in meaningful output. I am also truly appreciative of my co-advisor, Professor C. Maurice Balik, for our treasured discussions and his advice that guided me in the right direction whenever I met with several critical issues in my work. I have fully enjoyed my time as a graduate student with these two great mentors. I also thank Professor Daniel Dougherty and Professor Yutan Zhu for being my committee members. Furthermore, I would like to thank former Ade group members: Professor Youngwhan Kwon, Dr. Cheng Wang, Dr. Benjamin Watt, Aric Meyer and Shuming Hu for their help and consideration. I would like to give special thanks to my great friends, Dr. Guk-ho Gil, Kyoung Ook Lee, Dr. Bradley Busche of Pacific Northwest National Laboratory (PNNL) and Dr. Marcus Hunt of Oak Ridge National Laboratory (ORNL) for their insightful conversations and helping me to join the Ade group. Also, I wish to thank my current Ade group members: Dr. Brian Collins, Hongping Yan, Eliot Gann, Ziran Gu, Sen Li and Lewis Guignard. In addition, I am grateful to Dr. Benjamin Ocko, Dr. Xinhui Lu of Brookhaven National Laboratory (BNL) for the GIWAXS experiments of my samples, and Dr. Alex Hexamer and Dr. Anthony Young of Lawrence Berkeley National Laboratory (LBL) for their help during my R-SoXS experiments at Advanced Light Source (ALS). In addition, I extend my appreciation to Professor Keith Weninger, who gave me permission to use his spectrophotometers, and to Keith Jones and Dr. Ryan Fuierer of Asylum for their help and permission to access their

advanced AFM facility. I would like also to thank Mark Walter of the Shared Materials Instrumentation Facility (SMIF) at Duke University for his help in performing the XRD and XPS experiments. Finally, I would like to thank Joseph D. DeSousa and Professor Bruce M. Novak in the Department of Chemistry at NCSU for permitting me to use the FT-IR, and Matthew Lyndon of the Mass Spectroscopy Facility (MSF) for his invaluable help in performing the MALDI-TOF measurements.

For my final acknowledgements, I wish to recognize my past mentors and old colleagues. First, I would like to thank Professor Lee-Soon Park at Kyungpook National University (KNU) in Korea who was an excellent mentor and encouraged me to dream of pursuing a Ph.D. in the United States. I would also like to extend my appreciation to Professor In-Kyu Kang and Professor Kwan-Ho Seo at KNU for writing excellent recommendation letters for me. I also thank Professor Christopher K. Ober for his mentorship during the pursuit of my master's degree in Materials Science and Engineering at Cornell University. I especially thank also Ron Huemoeller, Senior Vice President of Amkor Technology, Inc., as well as retired head of R&D, Dr. Byung-Yeol Min of Samsung Electro-Mechanics Co., both of whom gave me endless support and wrote excellent recommendation letters for me. Additionally, I wish to thank my old colleagues, Professor Jin-Kyun Lee at Inha University in Korea, who transferred many words of wisdom in organic chemistry, Dr. Daewon Park at the University of Pittsburgh, Professor Sitaraman Krishnan at Clarkson University, and Dr. Hyun-Soo Lee at the University of Pennsylvania.

## TABLE OF CONTENTS

|  |           |
|--|-----------|
| LIST OF TABLES .....   | x         |
| LIST OF FIGURES .....  | xi        |
| 1. INTRODUCTION .....  | 1         |
| 1.1. Solar Energy.....   | 1         |
| 1.2. Photovoltaic Effect (PVE) and Solar Cells.....  | 2         |
| 1.3. Organic Solar Cells.....  | 5         |
| <i>1.3.1. Small Molecules-Based Organic Solar Cells.....</i>   | <i>5</i>  |
| <i>1.3.2. Polymer Based-Organic Solar Cells.....</i>   | <i>7</i>  |
| 1.4. Conjugated Polymers.....  | 10        |
| 1.5. Device Physics of Organic Solar Cells.....  | 13        |
| <i>1.5.1. General Working Principle.....</i>   | <i>13</i> |
| <i>1.5.2. Electrical Characterization of Solar Cells.....</i>  | <i>14</i> |
| 1.6. Hansen Solubility Parameters.....   | 17        |
| 1.7. Molecular Orientation and Phase Separation-Induced Morphology Control in Bulk Heterojunction (BHJ) Polymer Solar Cells.....         | 19        |
| <i>1.7.1. Molecular Ordering Effects on Device Mobility.....</i>   | <i>19</i> |
| <i>1.7.2. Crystallization and Phase Separation in P3HT:PC<sub>61</sub>BM Bulk Heterojunction(BHJ)Polymer Solar Cells.....</i>            | <i>21</i> |
| <i>1.7.3. Morphology Control: Spin Coating vs. Annealing Processes.....</i>  | <i>26</i> |
| 1.8. Key Factors for Best Bulk Heterojunction (BHJ) Polymer Solar Cells.....   | 28        |
| 1.9. Thesis Motivation and Objectives.....   | 30        |
| 1.10. Thesis Organization.....   | 31        |
| 2. EXPERIMENTAL.....   | 33        |
| 2.1. Materials.....  | 33        |
| 2.2. Chemical Synthesis of Oligothiophenes.....  | 33        |
| <i>2.2.1. Ultraviolet Photo-Polymerization of 2,5-Dibromothiophene (DBT).....</i>  | <i>33</i> |
| <i>2.2.2. Catalytical Synthesis of <math>\alpha,\omega</math>-Dibromo-Oligothiophene using Ferric Tribromide (FeBr<sub>3</sub>).....</i> | <i>37</i> |
| 2.3. Solar Cell Fabrication and Device Performance Characterization.....   | 38        |

|  |    |
|--|----|
| 2.3.1. Fabrication of P3HT:PC <sub>61</sub> BM BHJ Polymer Solar Cells .....   | 38 |
| 2.3.2. Current Density-Voltage (J-V) Curves Characterization of P3HT:PC <sub>61</sub> BM<br>BHJ Polymer Solar Cells .....  | 39 |
| 2.3.3. Charge carrier mobility Characterization of P3HT:PC <sub>61</sub> BM BHJ Polymer<br>Solar Cells.....  | 40 |
| 2.4. Physical and Chemical Structure Analyses.....   | 41 |
| 2.4.1. X-Ray Diffraction (XRD) .....   | 41 |
| 2.4.2. Grazing Incident Wide Angle X-Ray Scattering (GIWAXS) .....   | 42 |
| 2.4.3. Resonant Soft X-Ray Scattering (R-SoXS) .....   | 44 |
| 2.4.4. Fourier Transform Infrared Spectroscopy (FT-IR) .....   | 45 |
| 2.4.5. UVvis Spectrophotometer (UVvis).....  | 45 |
| 2.4.6. Matrix-Assisted Laser Desorption Ionization-Time of Flight Mass<br>Spectroscopy (MALDI-TOF MS) .....  | 46 |
| 2.4.7. X-ray Photoelectron Spectroscopy (XPS).....   | 46 |
| 2.4.8. Photo Fluorescent Experiment .....  | 46 |
| 2.5. Thermal Property Analyses.....  | 47 |
| 2.5.1. Thermal Gravimetric Analysis (TGA).....   | 47 |
| 2.5.2. Differential Scanning Calorimetry (DSC) .....   | 47 |
| 2.6. Surface Property Analysis.....  | 47 |
| 2.6.1. Atomic Force Microscopy.....  | 47 |
| 2.7. Computational Simulation .....  | 48 |
| 2.7.1. Solubility Parameters.....  | 48 |
| 3. UNDERSTANDING CONVENTIONAL THERMAL ANNEALING AND SOLVENT<br>ANNEALING FOR THE ENHANCED PERFORMANCE OF P3HT:PC <sub>61</sub> BM BHJ<br>POLYMER SOLAR CELLS ..... | 49 |
| 3.1. Background .....  | 49 |
| 3.2. Thermal Annealing for Enhanced Crystallization and Morphology Control of<br>P3HT:PC <sub>61</sub> BM BHJ Active Layers .....                                  | 50 |
| 3.2.1. Solvent Effect on Spin Coating of BHJ Active Layers: Hansen Solubility<br>Parameters Calculation .....  | 50 |

|   |    |
|---|----|
| 3.2.2. Morphological Evolution of P3HT:PC <sub>61</sub> BM BHJ Active Layers Due to Thermal Annealing.....  | 53 |
| 3.2.3. Crystalline Phase Growth and Orientation of P3HT:PC <sub>61</sub> BM BHJ Active Layers in Thermal Annealing.....   | 56 |
| 3.2.4. Model for Morphological Evolution of P3HT:PC <sub>61</sub> BM BHJ Polymer Solar Cells in Thermal Annealing .....   | 61 |
| 3.3. Solvent Annealing for Enhanced Crystallization and Morphological Control of P3HT: PC <sub>61</sub> BM BHJ Active Layers .....  | 63 |
| 3.3.1. Solvent Effect on Spin Coating Process and Solvent Annealing for P3HT:PC <sub>61</sub> BM BHJ Active Layers .....  | 63 |
| 3.3.2. Morphological Evolution of P3HT:PC <sub>61</sub> BM BHJ Active Layers in Solvent Annealing .....   | 66 |
| 3.3.3. Morphological Evolution of P3HT:PC <sub>61</sub> BM BHJ Active Layers in DBT Based Solvent Annealing.....  | 70 |
| 3.3.4. Crystalline Phase Growth and Orientation of P3HT:PC <sub>61</sub> BM BHJ Active Layers in DBT Based Solvent Annealing .....  | 73 |
| 3.3.5. DBT Based Solvent Annealing as Pre-Step of In Situ UV Photo-Polymerization Induced Morphological Control for P3HT:PC <sub>61</sub> BM BHJ Active Layers.....         | 76 |
| 3.4. Conclusions.....   | 77 |
| 4. IN SITU UV PHOTO-POLYMERIZATION OF DBT FOR ENHANCED PERFORMANCE OF P3HT:PC <sub>61</sub> BM BHJ POLYMER SOLAR CELLS.....   | 78 |
| 4.1. Background .....   | 78 |
| 4.2. Miscibility Effect of <i>In Situ</i> UV-Photo-Polymerized Oligothiophenes inside P3HT:PC <sub>61</sub> BM BHJ Active Layers.....                                       | 79 |
| 4.2.1. Solubility Prediction of P3HT and PC <sub>61</sub> BM in Various Solvents.....   | 79 |
| 4.2.2. Miscibility Model of <i>In Situ</i> UV Photo-Polymerized Oligothiophenes using Hansen Solubility Parameters .....  | 82 |
| 4.3. <i>In situ</i> UV-Photo-polymerization of DBT: Controls of Nanoscale Morphology and Crystalline Orientations of P3HT: PC <sub>61</sub> BM BHJ Polymer Solar Cells..... | 87 |

|  |     |
|--|-----|
| 4.3.1. Morphological Evolution of P3HT:PC <sub>61</sub> BM BHJ Active Layers in In Situ UV Photo-Polymerization of DBT .....                                     | 88  |
| 4.3.2. Crystalline Phase Growth and Orientation of P3HT:PC <sub>61</sub> BM BHJ Active Layers in In Situ UV Photo-Polymerization of DBT .....                    | 91  |
| 4.3.3. Process Optimization of In Situ UV Photo-Polymerization of DBT for the Best P3HT: PC <sub>61</sub> BM BHJ Polymer Solar Cells .....                       | 94  |
| 4.3.4. Model for Morphological Evolution of P3HT:PC <sub>61</sub> BM BHJ Polymer Solar Cells in In Situ UV Photo-Polymerization of DBT .....                     | 101 |
| 4.4. Conclusions .....   | 103 |
| 5. CHARACTERIZATION OF P3HT: PC <sub>61</sub> BM BHJ POLYMER SOLAR CELLS FABRICATED USING <i>IN SITU</i> UV PHOTO-POLYMERIZATION OF DBT .....                    | 104 |
| 5.1. Background .....  | 104 |
| 5.2. Solar Cell Performance of P3HT: PC <sub>61</sub> BM BHJ Polymer Solar Cells with <i>In Situ</i> UV Photo-Polymerization of DBT .....                        | 105 |
| 5.3. Conclusions .....   | 112 |
| 6. CONCLUSION AND PROPOSED FUTURE WORK .....   | 114 |
| 6.1. Conclusions .....   | 114 |
| 6.2. Future Work .....   | 117 |
| 7. BIBLIOGRAPHY .....  | 121 |
| APPENDICES .....   | 154 |
| APPENDIX A .....   | 155 |
| 8. UV PHOTO-POLYMERIZATION OF 2,5-DIBROMOTHIOPHENE (DBT) AND ITS MATERIAL PROPERTIES .....   | 155 |
| 8.1. Background .....  | 155 |
| 8.2. UV Photo-Polymerization of 2,5-Dibromo-Thiophene (DBT). .....   | 156 |
| 8.3. Catalytical Synthesis of $\alpha,\omega$ -Dibromo-Oligothiophenes using Ferric Tribromide (FeBr <sub>3</sub> ) and Characterization of Its Properties ..... | 161 |
| 8.4. Conclusions .....   | 170 |
| APPENDIX B .....   | 172 |
| 9. PHYSICS OF SOLAR CELLS .....  | 172 |
| 9.1. Equation Derivation for Real Diode that Contains Series and Shunt Resistance ..   | 172 |

## LIST OF TABLES

|  |     |
|--|-----|
| Table 1.1. Table 1.1. Fossil fuel use (in 2004) compared with the reserve. The estimated time left assumes that the annual consumption does not increase (1 TW=1 terawatt = $10^{12}$ W, 1 ZJ = 1 zettajoule = $10^{21}$ J)..... | 2   |
| Table.3.1. P3HT/ PC <sub>61</sub> BM solubility in good solvents (calculated by Hansen Solubility Parameters @25°C).....   | 52  |
| Table.3.2. Calculated degree of crystallinity and crystalline phase sizes of P3HT in an as-cast and thermal annealed (150°C, 20-minutes) P3HT and PCBM BHJ films. ....   | 58  |
| Table.3.3. Calculated P3HT crystalline phase sizes of DBT solvent annealed P3HT :PC <sub>61</sub> BM BHJ active layers.....  | 75  |
| Table 4.1. P3HT/ PC <sub>61</sub> BM miscibility with oligothiophenes (determined by Hansen solubility =parameters @25°C).....   | 84  |
| Table.4.2. Calculated P3HT crystalline phase sizes and the total amount of crystalline phase in P3HT:PC <sub>61</sub> BM BHJ active layers. ....   | 93  |
| Table.5.1. Charge carrier mobility of P3HT: PC <sub>61</sub> BM BHJ Polymer solar cells. ....  | 108 |

## LIST OF FIGURES

|   |    |
|---|----|
| Figure 1.1. Best research solar cell efficiency (NREL) (Figure is reproduced from [25]).  | 4  |
| Figure 1.2. (a) IV curve of first small molecule-based heterojunction solar cells by C. W. Tang, and (b) organic small molecules made of copper phthalocyanine (CuPc) and perylene tetracarboxylic acid derivative (PV) (Figure is reproduced from [67]).   | 5  |
| Figure 1.3. Working principles of polymer solar cells in different structures: (a) single layer, (b) heterojunction polymer solar cell, and (c) bulk heterojunction polymer solar cell (Figure is reproduced from [96]).  | 8  |
| Figure 1.4. (a) Schematic presentation of a bulk heterojunction (BHJ) solar cell, showing the phase separation between donor (red) and acceptor (blue) materials, and (b) schematic energy diagram showing the energy level of the highest occupied and lowest unoccupied molecular orbitals (HOMO and LUMO, respectively) (Figure is reproduced from [1]).   | 9  |
| Figure 1.5. Structures of conjugated polymers and a soluble C <sub>60</sub> derivative (PC <sub>61</sub> BM) for BHJ polymer-based solar cells (Figure is reproduced from [96]).  | 10 |
| Figure 1.6. Chemical structures of the inherent (top) and polaronic (bottom) states of polythiophene (Figure is reproduced from [96]).  | 12 |
| Figure 1.7. Fundamental working principles of organic solar cells (Figure is modified and reproduced from [167]).   | 14 |
| Figure 1.8. Typical J-V curves of solar cells in dark (empty symbols) and illuminated (filled symbols) conditions. Short-circuit density ( $J_{sc}$ ) and open-circuit voltage ( $V_{oc}$ ) are shown. The maximum output power is given as the rectangular area ( $J_{max} \times V_{max}$ ).  | 15 |
| Figure 1.9. ‘Edge on’ and ‘face on’ orientation of P3HT: (a) and (c) are ‘edge on’ orientation, (b) and (d) are ‘face on’ orientation. (a) and (b) are schematic diagrams for charge carrier mobility in P3HT thin films; (c) and (d) are charge carrier mobility results in the OTFT (red squares inside active layers are thiophene rings and adjacent lines are side chains) (Figures are drawn based on the OTFT mobility data of [183]). | 20 |

|  |    |
|--|----|
| Figure 1.10. GISAXS curves of as-cast and annealed (150°C, 15 minutes) P3HT and P3HT:PC <sub>61</sub> BM thin films (Figure is reproduced from [188]).   | 21 |
| Figure 1.11. SANS curves of as-cast and annealed (140°C, 20 minutes) P3HT and P3HT:PC <sub>61</sub> BM thin films (Figure is reproduced from [191]).   | 22 |
| Figure 1.12. Schematic diagram of P3HT:PC <sub>61</sub> BM BHJ films composed of (a) highly crystalline P3HT, and (b) less crystalline P3HT. The black ovals represent PC <sub>61</sub> BM crystals, and the rectangular stacks represent P3HT crystals. (Figures are adopted from [185]).   | 23 |
| Figure 1.13. Light beam-induced current (LBIC) microscopic images of poly(5,7-bis(3-dodecylthiophen-2-yl)thienol[3,4-b]pyrazine-alt-9,9-dioctyl-2,7-fluorene)(BTT-F): PC <sub>61</sub> BM thin films exposed to chlorobenzene (CB) solvent vapors for (a) 30 min and (b) 0 min. The PC <sub>61</sub> BM cluster, labeled A, is surrounded by a region of high current, labeled B. The region furthest from the PC <sub>61</sub> BM cluster has a low photo-current, labeled C. In the unannealed films, photo-current generation is fairly uniform between D and E. (Figures are reproduced from [201]). | 25 |
| Figure 1.14. (a) XRD of regiorandom and regioregular P3HT, and (b) chemical structures of regioregularly controlled different P3HT (Figure (b) is modified based on a Figure in Reference [1]).  | 28 |
| Figure 1.15. <i>In situ</i> UV photo-polymerization-induced phase separation for nano-scale morphology control of P3HT:PC <sub>61</sub> BM BHJ polymer solar cells: (a) DBT vapor deposition on an as-cast P3HT: PC <sub>61</sub> BM BHJ active layer, (b) <i>in situ</i> UV photo-polymerization of DBT for nano-scale morphology control.  | 30 |
| Figure 2.1. UV exposure set-up inside an Ar gas environmental glove box.   | 34 |
| Figure 2.2. Mid-UV band pass filter for UV photo-polymerization of DBT.  | 35 |
| Figure 2.3. Covalent bond dissociation energy that can initiate a radical-based UV photo-polymerization reaction.  | 35 |
| Figure 2.4. Schematic reaction diagram of UV photo-polymerization of DBT (modified based on the UV photo-polymerization reaction scheme of 2,5-diiodothiophene (DIT), from the publications of the S. H. Kim group in PSU). [223-226]  | 36 |

|   |    |
|---|----|
| Figure 2.5. Schematic reaction diagrams of catalytically synthesized Br-terminated $\alpha,\omega$ -dibromo-oligothiophenes.....  | 37 |
| Figure 2.6. Schematic diagram of new process for the fabrication of P3HT:PC <sub>61</sub> BM BHJ polymer solar cells.....   | 39 |
| Figure 2.7. Schematic diagram of Bragg diffraction in the XRD experiment (Figure is reproduced from[230]).....  | 42 |
| Figure 2.8. Schematic diagram of GIWAXS experimental set-up ( $\alpha$ is incident angle, $\delta$ is exit angle, $\nu$ is the in-plane scattering angle, $\phi$ is sample rotation angle, $k_i$ is incident beam and $k_f$ is the exit beam). ....   | 43 |
| Figure 2.9. Schematic diagram of R-SoXS experimental set-up.....  | 44 |
| Figure 3.1. Hansen-solubility parameters ( $\delta_D$ , $\delta_P$ , $\delta_H$ ) sphere models of (a) P3HT and (b) PC <sub>61</sub> BM in good solvents. (The Ra (interaction radius) of solvents is not shown here and different colors indicate different solvents only and no special meaning). ....            | 51 |
| Figure 3.2. AFM images of as-cast and thermally annealed (150°C, 30 min) P3HT:PC <sub>61</sub> BM BHJ thin films. ((e) and (f) are 2D-FFT of phase images).....   | 53 |
| Figure 3.3. (a) 2D-FFT profiles of phase mode images that are shown in Figure 3.2 for lateral domain size analyses, and (b) UVvis spectrophotometer absorption spectra of them. (The samples are as-cast and thermally annealed (150°C, 30 min) P3HT: PC <sub>61</sub> BM BHJ thin films, thickness = 100 nm). .... | 54 |
| Figure 3.4. R-SoXS data of as-cast and thermally annealed (150°C, 30 min) P3HT: PCBM BHJ active layers (thickness = 100 nm). ....   | 55 |
| Figure 3.5. PC <sub>61</sub> BM cluster growth in a P3HT: PC <sub>61</sub> BM BHJ active layer under thermal annealing: (a) 5 minutes annealed and (b) 180 minutes annealed at 180°C (Experiments were performed by Lewis Guignard). ....   | 56 |
| Figure 3.6. GIWAXS data of as-cast and thermally annealed (150°C, 20 min) P3HT:PC <sub>61</sub> BM BHJ active layers (thickness = 100 nm) on Si substrates in out-of- plane scattering (incident angle = 0.1°) (Experiments were performed by Eliot Gann).57  |    |
| Figure 3.7. GIWAXS out-of-plane scan data at various incident angles (sample: a spin cast P3HT: PC <sub>61</sub> BM BHJ thin film with thermal annealing (150°C, 30 min),   |    |

|   |    |
|---|----|
| thickness = 100 nm) (Experiments were done by Xinhui Lu at NSLS). .....   | 60 |
| Figure 3.8. Normalized GIWAXS out-of-plane peaks data at various incident angles based on the experiments shown in Figure 3.7.....  | 61 |
| Figure 3.9. Schematic diagrams of phase separation and crystallization of P3HT:PC <sub>61</sub> BM BHJ polymer solar cells: (a) homogeneous solution, (b) as-cast phase separated film, and (c) growth of crystalline phases after thermal annealing. ....  | 62 |
| Figure 3.10. Calculated Hansen-solubility parameters ( $\delta_D$ , $\delta_P$ , $\delta_H$ ) and sphere models of P3HT and PC <sub>61</sub> BM in different solvents: (a)-(d) for P3HT, (e)-(h) for PC <sub>61</sub> BM (Different colors means different solvents and no special meaning in the used colors). ..... | 64 |
| Figure 3.11. AFM images of vapor annealed P3HT: PC <sub>61</sub> BM BHJ films: first column is height, second column is phase and third column is 2D-FFT of phase images; CB and DBT at 80°C, 1 min; thiophene and 3HT at 50 °C, 1 min; scale bar is 200 nm. ....   | 66 |
| Figure 3.12. R-SoXS data of post solvent annealed P3HT: PC <sub>61</sub> BM films using various annealing solvents (thickness of films = 100 nm). .....   | 68 |
| Figure 3.13. UVvis spectrophotometer absorption spectra of solvent annealed P3HT: PC <sub>61</sub> BM BHJ thin films: (a) full spectra, (b) zoomed-in P3HT spectra and (c) characteristic absorption peaks maximum intensity ratio between P3HT (517 nm) and PCBM (334 nm). ....                                      | 69 |
| Figure 3.14. R-SoXS data of DBT post solvent annealed P3HT:PC <sub>61</sub> BM films with various annealing conditions (thickness = 100 nm). .....  | 71 |
| Figure 3.15. AFM images and 2D-FFT phase mode profiles of DBT vapor annealed P3HT:PC <sub>61</sub> BM BHJ films at various annealing times (DBT vapor annealing at 80°C and thermal annealing at 150°C 20 minutes; $q_m$ means $q_{(max)}$ ). .....   | 72 |
| Figure 3.16. Lateral domain size analysis based on $q_m$ values from 2D-FFT profiles of phase mode images presented in Figure 3.15 (Thermal annealing at 150°C 20 minutes was also applied for all samples, except an as-cast (AC) sample). .....   | 73 |
| Figure 3.17. GIWAXS data of DBT post solvent annealed P3HT:PC <sub>61</sub> BM active layers in various post solvent annealing conditions. (Thermal annealing at 150°C 20   |    |

|  |    |
|--|----|
| minutes was also applied to all samples and all GIWAXS images were rescaled to display). .....   | 74 |
| Figure 4.1. Hansen-solubility parameters ( $\delta_D$ , $\delta_P$ , $\delta_H$ ), sphere models of: (a) P3HT: PC <sub>61</sub> BM and (b) P3HT: C <sub>60</sub> mixtures in several good solvents. (The radius of each solvent is assumed to be the same and different colors indicate different solvents only and no special meaning.) .....   | 79 |
| Figure 4.2. Hansen-solubility parameters ( $\delta_D$ , $\delta_P$ , $\delta_H$ ), sphere models of all good solvents listed in Table 3.1 for P3HT: PCBM BHJ mixtures from various viewpoints. ....  | 82 |
| Figure 4.3. Calculated Flory-Huggins interaction parameters ( $\chi_{12}$ ) and relative energy density (RED) of oligothiophenes with different repeat units in a P3HT: PC <sub>61</sub> BM BHJ mixture. ....  | 83 |
| Figure 4.4. Hansen-solubility parameters ( $\delta_D$ , $\delta_P$ , $\delta_H$ ), sphere models for the miscibility studies of oligothiophenes with P3HT and PC <sub>61</sub> BM: (a) P3HT in DBT, (j) PC <sub>61</sub> BM in DBT, (b) ~ (i) interaction between P3HT and oligothiophenes having different repeating units, (k) ~ (r) interaction between PC <sub>61</sub> BM and oligothiophenes having different repeating units (radii of oligothiophenes are R <sub>a</sub> ) ..... | 85 |
| Figure 4.5. R-SoXS data of (a) the optimized new post casting process steps for P3HT: PC <sub>61</sub> BM BHJ films: DBT vapor deposition at 80°C 1 min and UV exposure 3 min; thermal annealing at 150°C 20 min; thickness = 100 nm, and (b) catalytically synthesized Br-terminated $\alpha,\omega$ -dibromo-oligothiophene (10wt%) introduced P3HT:PC <sub>61</sub> BM BHJ films. ....  | 86 |
| Figure 4.6. <i>In situ</i> UV photo-polymerization-induced phase separation for nano-scale morphology control of P3HT:PC <sub>61</sub> BM BHJ polymer solar cells: (a) DBT vapor deposition on an as-cast P3HT: PC <sub>61</sub> BM BHJ active layer, (b) <i>in situ</i> UV photo-polymerization of DBT for nano-scale morphology control. ....  | 87 |
| Figure 4.7. AFM images and 2D-FFT phase mode profiles of the optimized new post casting process steps for P3HT: PC <sub>61</sub> BM BHJ films: DBT vapor deposition at 80°C 1 min, UV exposure 3 min, and thermal annealing at 150°C 20 min; process steps (b) and (d) are introduced for comparison only; q <sub>m</sub> means q <sub>(max)</sub> . ....  | 88 |

|   |    |
|---|----|
| Figure 4.8. Domain size analysis based on $q_m$ values from 2D-FFT profiles of phase mode images in Figure 4.7. ....  | 89 |
| Figure 4.9. (a) UVvis spectrophotometer spectra of the optimized process steps and (b) zoomed-in P3HT absorption spectra. ....  | 90 |
| Figure 4.10. R-SoXS data of the optimized new post process steps for P3HT: PC <sub>61</sub> BM BHJ films: DBT vapor deposition at 80°C, 1 min, and UV exposure 3 min; post thermal annealing at 150°C 20 min; thickness = 100 nm. Process steps (l) and (n) are introduced for comparison only. ....                        | 90 |
| Figure 4.11. GIWAXS data of <i>in situ</i> UV photo-polymerization of DBT in P3HT: PC <sub>61</sub> BM BHJ active layers: (a) conventional post thermal annealing (150°C 20 min); (b) DBT vapor (80°C 1 min); (c) UV exposure 3 min (Experiment was performed by Dr. Xinhui at NSLS). ....                                  | 92 |
| Figure 4.12. AFM images and 2D-FFT profiles of P3HT: PC <sub>61</sub> BM BHJ films for different UV exposure times: DBT vapor deposition at 80°C 1 min and post thermal annealing at 150°C 20 min; process step (b) is introduced for comparison only; $q_m$ means $q_{(max)}$ . ....                                       | 95 |
| Figure 4.13. Domain size analysis based on $q_m$ values from 2D-FFT profiles of phase mode images in Figure 4.13. ....  | 96 |
| Figure 4.14. Miscibility changes of oligothiophenes during <i>in situ</i> UV photo-polymerization of DBT in a P3HT: PC <sub>61</sub> BM BHJ active layer: (a) RED changes; (b) $\chi_{12}$ changes (Numbers in the x-axis stand for number of repeating units and T means thienyl ). ....                                   | 96 |
| Figure 4.15. AFM images and 2D FFT profiles of phase mode images from P3HT: PC <sub>61</sub> BM BHJ films for different DBT deposition times: DBT vapor deposition at 80°C, UV exposure 3 min, and post thermal annealing at 150°C 20 min; process step (a) is included for comparison only; $q_m$ means $q_{(max)}$ . .... | 98 |
| Figure 4.16. 2D FFT profiles of phase mode images from P3HT: PC <sub>61</sub> BM BHJ films for different DBT deposition times with/without thermal annealing: DBT vapor deposition at 80°C, UV exposure 3 min, and post thermal annealing at 150°C 20 min. ....   | 99 |

|  |     |
|--|-----|
| Figure 4.17 Lateral domain size analysis using AFM: 2D-FFT profiles of phase mode images of P3HT:PC <sub>61</sub> BM BHJ active layers fabricated in various processing conditions of the new post casting process, <i>in situ</i> UV photo-polymerization of DBT (all the samples are analyzed with thermal annealing, 150°C 20-minutes). .....   | 100 |
| Figure 4.18. Schematic diagrams of phase separation and crystallization of P3HT:PC <sub>61</sub> BM BHJ polymer solar cells: (a) homogeneous solution, (b) as-cast phase separated film, (c) growth of crystalline phase after thermal annealing, (d) DBT vapor deposition, (e) <i>in situ</i> UV photo-polymerization of DBT, (f) post thermal annealing. (a) ~ (c) represent the conventional process with post thermal annealing: (a), (b), (d), (e), and (f) are new processes showing the <i>in situ</i> UV photo-polymerization of DBT in P3HT:PC <sub>61</sub> BM BHJ polymer solar cells. .... | 102 |
| Figure 5.1. P3HT: PC <sub>61</sub> BM BHJ polymer solar cells device architecture under the open circuit condition. ....   | 104 |
| Figure 5.2. Comparison of UVvis absorption spectra of P3HT:PC <sub>61</sub> BM BHJ thin films between the conventional post thermal annealing process and new post process (DBT 1 min 80°C, UV 3 minutes), and (b) zoomed-in P3HT main absorption peak area. ....  | 106 |
| Figure 5.3. Charge carrier mobility of P3HT:PC <sub>61</sub> BM polymer solar cells: (a) and (b) are hole mobility from hole-only devices; (c) is electron mobility from electron-only devices, and (d) and (e) are the device architecture of hole-only and electron-only P3HT:PC <sub>61</sub> BM BHJ polymer solar cells, respectively. ....  | 107 |
| Figure 5.4. J-V characteristic curves of P3HT:PC <sub>61</sub> BM BHJ polymer solar cells: (a) with different UV exposure times, and (b) comparison of conventional post thermal annealing only and new post process. ....   | 109 |
| Figure 5.5. Summary of P3HT:PC <sub>61</sub> BM BHJ polymer solar cell parameters with various UV exposure times: (a) PCE vs. lateral domain size, (b) FF vs. lateral domain size, (c) V <sub>oc</sub> vs. lateral domain size, and (d) J <sub>sc</sub> vs. lateral domain size. ....  | 111 |
| Figure 5.6. Summary of resistance values of P3HT:PC <sub>61</sub> BM BHJ polymer solar cells with various UV exposure times: (a) R <sub>s</sub> vs. lateral domain size, and (b) R <sub>sh</sub> vs. lateral domain size. ....   | 112 |

|  |     |
|--|-----|
| Figure 6.1. Comparison of R-SoXS results of: (a) a P3HT:PC <sub>61</sub> BM BHJ active layer, and (b) a P3HT:PC <sub>71</sub> BM active layer in the new post casting process (thermal annealing condition is 150°C, 20-minutes) .....   | 118 |
| Figure 6.2. R-SoXS results of: (a) 10 wt% of dibromobithiophene (DBBT), and (b) 10 wt% dibromofluorene (DBF) in a P3HT:PC <sub>61</sub> BM BHJ active layer with different UV exposure times (post thermal annealing condition: 150°C, 20 minutes). .....  | 119 |
| Figure 6.3. R-SoXS results of: (a) 10 wt% of diBr-biphenylthiophene (BBPT), and (b) 10 wt% of 9,9-diethyl hexyl 2,7-dibromofluorene (DEHDBF) in a P3HT:PC <sub>61</sub> BM BHJ active layer with different UV exposure times (post thermal annealing condition: 150°C, 20-minutes).....  | 120 |
| Figure 8.1. Schematic reaction diagram of UV photo-polymerization of DBT (modified based on the DIT reaction diagram of the Penn State Group).[223-226].....   | 157 |
| Figure 8.2 (a) UVvis Spectrophotometer spectra during the UVphoto polymerization of DBT (Soluble portions only), (b) Abs <sub>max</sub> and (c) optical bandgaps vs. UV exposure times.....  | 158 |
| Figure 8.3. Color photograph of photoluminescence emission of UV photo-polymerized liquid phase oligothiophenes from DBT at 25°C: (a) 5min and (b) 10min UV exposure (excitation @ 365nm) and precipitated UV photo-polymerized insoluble polythiophene for FT-IR analysis: (c) in THF and (d) photoluminescence (excitation @365nm in THF)..... | 159 |
| Figure 8.4. FT-IR spectra during the UV photopolymerization of DBT: (a) Soluble portion only, (b) Insoluble portion only.....  | 160 |
| Figure 8.5. Schematic reaction diagrams of catalytically synthesized Br-terminated $\alpha,\omega$ -dibromo-oligothiophenes.....   | 162 |
| Figure 8.6. MALDI-TOF MS results of $\alpha,\omega$ -dibromo-oligothiophenes for the molecular weight analysis (numbers in (a) graph stand for the # of repeating units). .....  | 163 |
| Figure 8.7. FT-IR spectra of (a) synthesized soluble $\alpha,\omega$ -dibromo-oligothiophenes and (b) commercially available thiophene products. ....  | 164 |
| Figure 8.8. X-ray Photoelectron Spectroscopy (XPS) spectra of $\alpha,\omega$ -dibromo-oligothiophene (HMW). ....  | 165 |

|  |     |
|--|-----|
| Figure 8.9. UVvis spectrophotometer spectra and a photoluminescence color picture of (a) P3HT (Sigma-Aldrich), (b) and (c) $\alpha,\omega$ -dibromo-oligothiophenes (photoluminescence excited at 365nm). .....  | 166 |
| Figure 8.10. X-ray diffraction (XRD) and thermogravimetric analysis (TGA) results of $\alpha,\omega$ -dibromo-oligothiophenes. ....  | 167 |
| Figure 8.11. UVvis spectrophotometer spectra of (a) 20 minutes UV exposed soluble portion of $\alpha,\omega$ -dibromo-oligothiophenes/ DBT mixture, (b) P3HT (Sigma-Aldrich) and (c) pristine $\alpha,\omega$ -dibromo-oligothiophene (HMW) (photoluminescence excited at 365nm). ....   | 168 |
| Figure 8.12. RSoXS analysis of P3HT:PC <sub>61</sub> BM BHJ active films with 10 wt% of $\alpha,\omega$ -dibromo-oligothiophene: (a-b) conventional BHJ films w/wo post thermal annealing, (c-d) 10 wt% $\alpha,\omega$ -dibromo-oligothiophene introduced BHJ films w/wo post thermal annealing and (e-g) <i>in situ</i> UV photo-polymerization of $\alpha,\omega$ -dibromo-oligothiophene (10 wt%) in P3HT:PC <sub>61</sub> BM BHJ active films with various exposure times. .... | 169 |
| Figure 9.1. Equivalent circuit of an ideal solar cell (Figure are reproduced from [21]). ....  | 172 |
| Figure 9.2. Equivalent circuit, including series and shunt resistances (Figure are reproduced from [21]). ....   | 173 |
| Figure 9.3. Effect of (a) increasing series resistance and (b) decreasing shunt resistance on solar cell performance: In each case, the outer curve has $R_s = 0\Omega$ and $R_{sh} = \infty\Omega$ ; the effect of the resistances is to reduce the area of the maximum power compared to $J_{sc} \times V_{oc}$ (Figure are reproduced from [21]). ....  | 174 |

# 1. INTRODUCTION

## 1.1. Solar Energy

In 2004, the total energy consumption of mankind was approximately 15 terawatt (TW), and about 85 % of this energy came from fossil fuel sources.[3, 4] Future energy demands are continuously increasing, and the demand is expected to double by 2050 due to continuous industrialization and the demand for improvements in quality of life due to access to electricity, and associated rapid population growth.[5]

With a simple estimation based on the assumption that the consumption rate will not increase further, it is generally agreed that plenty of fuel is still available, as shown in Table 1.1.[3] However, current energy production that is based on fossil fuel sources cannot meet the increased demand in the near future. Furthermore, energy derived from fossil fuels produces carbon dioxide (CO<sub>2</sub>) and results in global warming and continuous climate change throughout the world.[6-9] The volume of polar ice caps is decreasing 8 % per year due to the direct effect of global warming.[10] Even though it is evident that carbon generated from fossil fuels results in global warming, the demand for fossil energy sources is still high and will probably remain so for decades to come if no new carbon free energy sources are found.[3]

This energy-related issue is an urgent challenge and should be a global primary focus. Several options for carbon free energy sources exist.[4] The most economical and practical option that could replace fossil fuel energy sources and prevent global warming is nuclear energy.[11, 12] However, fears surrounding the proliferation of nuclear weapons, nuclear waste and tragic accidents currently outweigh more widespread usage of nuclear power.[12-21] Unfortunately, most of the other carbon-free renewable energy sources, such as hydroelectric power, wind power, ocean energy and biomass, cannot meet future energy demands completely. However, another viable option is solar energy.

Light energy from the sun to the earth's surface, even taking into account approximately 28% of absorption energy loss in the atmosphere, is approximately  $1.2 \times 10^5$  TW, a huge amount of continuous energy that is more than 1,000 times the world's current energy demand in a year.

Furthermore, readily available solar energy far surpasses the total energy demand of the next than fifty years, even considering the increasing energy consumption rate.[3, 22] Therefore, solar energy is one of the most promising carbon-free renewable energy sources.

**Table 1.1. Fossil fuel use (in 2004) compared with the reserve. The estimated time left assumes that the annual consumption does not increase (1 TW=1 terawatt =  $10^{12}$  W, 1 ZJ = 1 zettajoule =  $10^{21}$  J) (Table is modified and reproduced from [3])**

|                | Form    | Consumption<br>(TW) | Annual<br>consumption<br>(ZJ year <sup>-1</sup> ) | Energy reserve<br>(ZJ <sup>2</sup> ) | Time<br>left<br>(Years) |
|----------------|---------|---------------------|---|--------------------------------------|-------------------------|
| Coal           | Solid   | 3.8                 | 0.12  | 290                                  | 2400                    |
| Oil            | Liquid  | 5.6                 | 0.18  | 57                                   | 316                     |
| Natural<br>gas | Gaseous | 3.5                 | 0.11  | 30                                   | 272                     |

Note: There is an estimated reserve of 2500 ZJ if uranium from the earth's crust is used with currently available extraction techniques. This estimation assumes the use of breeder reactors that generate more fissile material than they consume. Fusion is currently not practical or considered as a serious alternative to energy production.

However, solar energy is not currently popular due to its high energy production costs.[23] Generally, electricity production costs from solar energy sources correspond to the total cost of solar cell fabrication and maintenance, power conversion efficiency (PCE) and costs associated with extending the lifetime of the solar cells. Although no clear standard cost calculation method for solar cells currently exists, improved efficiency and a longer service life are critical to reduce the energy production costs of solar cells. Thus, many scientists are actively working in this field to find a solution to these problems associated with solar energy.

## 1.2. Photovoltaic Effect (PVE) and Solar Cells

The photovoltaic effect (PVE) is a process of converting light (photons) directly into electricity (voltage).[22] The PVE was demonstrated first in 1839 by Edmond Becquerel, a French physicist.[24] The light (photons) absorbed by the materials excites the electrons from the ground state to excited states, leaving holes in the ground state.[22] Those generated electrons are pulled away by the built-in potential before the electrons relax to the ground

state. This built-in potential pushes the electrons and holes to the opposite electrodes, respectively, and photo-electric power is thereby harnessed. The devices that use the PVE to generate electricity are called solar cells.[22]

The first PVE in a solid state was found by William Grylls Adams and his student, Richard Evan Day, during their photoconductivity experiments of selenium in 1876.[25] They placed selenium in between hot platinum (Pt) electrodes to study photoconductivity and found a solid material that generates electric current under light without external electric power. A discovery in 1953 by scientists Gerald Pearson and Calvin Fuller at Bell Laboratories opened the door to the revolution of solar cell technology.[25] They accidentally found that their silicon device could generate five times the electricity as selenium under sunlight. A year later, they improved the efficiency of their silicon-based p-n junction solar cells up to 6 percent power conversion efficiency (PCE). However, commercialization of these solar cells was not successful due to their high production costs. In 1955, the first practical silicon p-n junction solar cells were used as the power source of the first American satellite.[25]

As shown in Figure 1.1.[1], currently the most advanced and efficient solar cells are multi-junction solar cells made of 2~3 layers of different thin inorganic semiconductors (InGaP, GaAs and Ge) that have various absorption spectra. These solar cells have a PCE of over 40 percent.[1] These extremely high-efficient and expensive solar cells, which are normally used for space satellites, are fabricated using molecular beam epitaxy and metalorganic chemical vapor deposition (MOCVD) methods.[26-33] Currently, the most popular solar cell types are mono-crystalline inorganic semiconductor-based p-n junction solar cells[25]. The mono-crystalline silicon (Si) solar cell modules generally show up to 20 percent PCE. Records for small laboratory-scale solar cells from both mono-crystalline silicon (Si) and gallium arsenide (GaAs) show that they approach 25 percent PCE.

However, regardless of material type, mono-crystalline inorganic semiconductor solar cells are very expensive due to the high cost of their materials and complicated fabrication process. As an economical alternative, amorphous silicon (a-Si) is promising [34-38], but it can easily degrade under light.[39-43] Solar cells made of a-Si generally generate 5~12 percent PCE.[1]

Other thin film solar cells that use cadmium telluride (CdTe) [44-48], cadmium sulphide (CdS) [49-51] and copper indium-gallium diselenide (Cu(InGa)Se<sub>2</sub>) [52-56] are reported to have up to 16~20 percent PCE.[1] These thin film-based solar cells are strong candidates to replace expensive mono-crystalline inorganic solar cells. However, each type of thin film solar cell has its own disadvantages. For example, cadmium, which is used in CdS and CdTe solar cells [57-60], is a toxic element, and the supply of indium used in Cu(InGa)Se<sub>2</sub> solar cells is limited.[61]

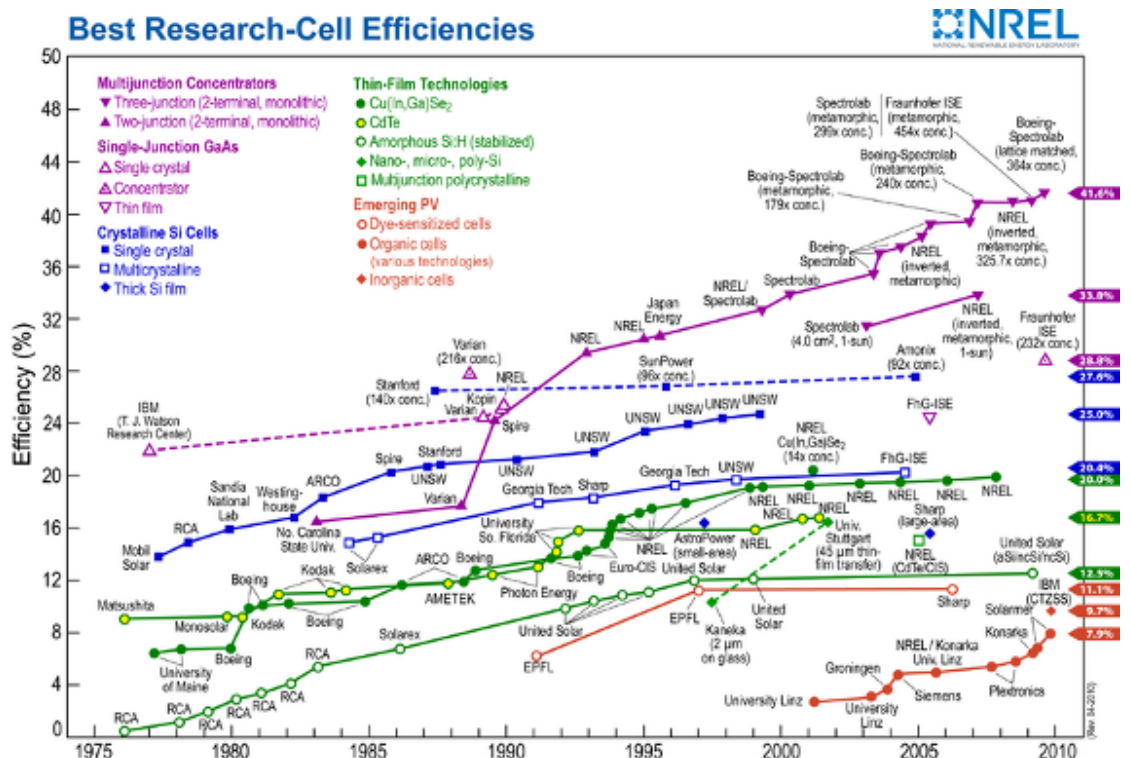


Figure 1.1. Best research solar cell efficiency (NREL) (Figure is reproduced from [1]).

In terms of third generation solar cells, two popular structures are available. The first type are the dye-sensitized solar cells (DSSC), also called the Grätzel cells, and their record efficiency are reported up to 11percent PCE.[1, 62, 63] Another third generation approach is organic solar cells made of small organic molecules or conjugated polymers, with a record efficiency approaching 8 percent PCE.[1, 62, 64, 65] Several unsolved problems remain, such as a short service life and low efficiency. However, due to their easy fabrication and low production costs, organic solar cells are one of most promising types of photovoltaic devices.

## 1.3. Organic Solar Cells

### 1.3.1. Small Molecules-Based Organic Solar Cells

Organic solar cells are made of small organic molecules or conjugated polymers. The earliest small molecule-based organic solar cells are Schottky-type single layer devices that were made of anthracene in 1959 by Kallman and Pope.[66] The organic active layer was sandwiched in between two different metal electrodes. Single-layered devices are inherently inefficient due not only to the limited charges photo-generated in the very thin layer of the organic and metal interface, but also to the high exciton-quenching ratio at that interface.[2]

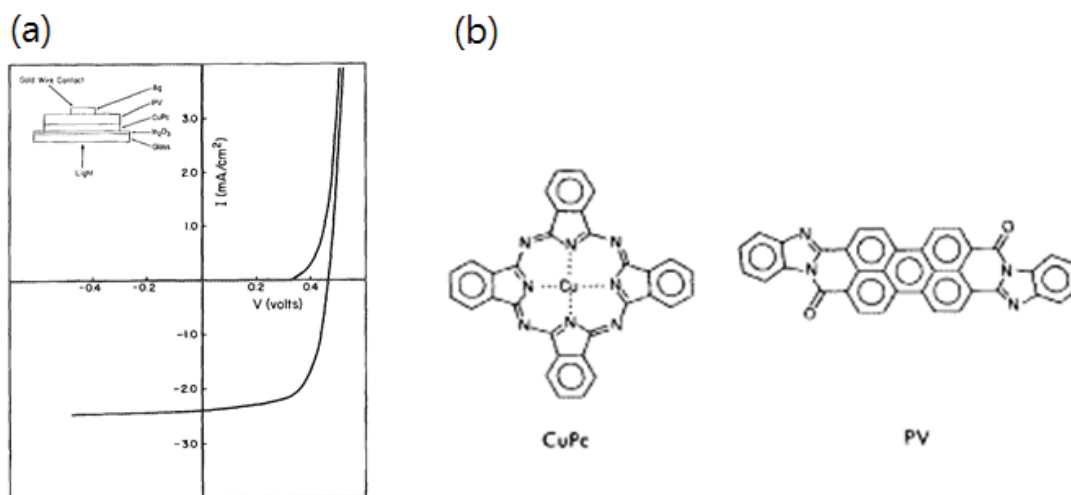


FIG. 1. Configuration and current-voltage characteristics of an ITO/CuPc (250 Å)/PV(450 Å)/Ag cell.

**Figure 1.2. (a) IV curve of first small molecule-based heterojunction solar cells by C. W. Tang, and (b) organic small molecules made of copper phthalocyanine (CuPc) and perylene tetracarboxylic acid derivative (PV) (Figure is reproduced from [67]).**

The most successful small molecule-based organic solar cells have an organic heterojunction (bilayer-structured) architecture based on two separated organic layers. The earliest efficient small molecular organic heterojunction solar cell was demonstrated by Ching W. Tang of Eastman Kodak in 1986 as shown in Figure 1.2.[67] Through thermal evaporation, Tang fabricated a bilayer-structured organic solar cell that consisted of thin layers of small molecules. Sequentially, 25 nm copper phthalocyanine (CuPc) and 45 nm perylene tetracarboxylic acid derivative (PV) evaporated on top of a transparent indium tin oxide (ITO) glass substrate with a silver (Ag) top anode electrode. The PCE was about one percent,

which is roughly one order magnitude better than the previous phthalocyanine-porphyrin-based heterojunction organic solar cells developed by Harima et al. in 1984.[68] CuPc and PV were applied as an electron donor and an electron acceptor, respectively.

In organic semiconductors, the PVE works differently compared with that of inorganic semiconductors.[22] In contrast to the generation of isolated electrons and holes in inorganic semiconductors, excitons, neutral particles that are weakly bound electrons and hole pairs, are generated in organic semiconductors by the absorption of light (photons).[2, 69, 70] The diffusion length of excitons is only around 5~10 nm[2, 25, 29, 69-72], and the primary limitation of heterojunction solar cells is the limited charge generation at the thin interface between the p and n type organic semiconductors.[25]

The co-evaporation concept of p and n type small molecules was introduced to increase the thickness of the inter-mixing zone within the heterojunction as a trilayer structure. This idea is the first bulk heterojunction concept in organic solar cell research. The first trilayer was reported by Hiramoto et al. in 1992.[73] A 40 nm thin co-evaporated bulk heterojunction layer of perylene and phthalocyanine derivatives was made between an electron-transport layer (ETL) and a hole-transport layer (HTL). N,N'-dimethyl-3,4,9,10-perylenetetracarboxylic acid diimide (Me-PTCDI) and phthalocyanine (H<sub>2</sub>PC) were used as the ETL and HTL, respectively. The quantum efficiency of the charge generation was significantly improved, and the PCE was doubled in the PTCDI/H<sub>2</sub>PC device. Gebeyehu et al. also reported 3.37% PCE under 10mW/cm<sup>2</sup> from a similar trilayer device.[74] A morphological effect on the PCE of the bulk heterojunction organic solar cells was studied by Harimoto et al.[73] and Rostalski et al.[75] based on the results of a co-evaporation method for small molecule-based BHJ solar cells. Partially phase-separated organic molecules were proposed as a good option for improved exciton diffusion to the interfaces and improved charge transport.

Despite numerous research efforts into small molecule-based organic solar cells and recent huge improvements by several researchers, such as S. R. Forrest at the University of

Michigan, in applying an exciton blocking layer (EBL) [76-81], practical concerns remain regarding the vacuum process for thermal evaporation, because the thermal evaporation of small molecular active layers under high vacuum condition appears impractical for producing organic solar cells in a high volume production scale.

### **1.3.2. Polymer-Based Organic Solar Cells**

In polymer solar cells, due to the high molecular weight of the polymers and Van Der Waals interaction of polymer chains, it is possible to make a 100 nm thickness active layer very easily on top of a substrate by using conventional coating methods, such as spin coating, screen, ink-jet printing and roll coating, etc.[82-95] These types of printing methods are more practical for the high volume manufacture of large-scale organic solar cells than thermal evaporation under ultra-high vacuum (UHV) for small molecular organic semiconductors.[76-81] The working principles of polymer solar cells in three different architectures are shown in Figure 1.3.[96]

The PVE in conjugated polymers was reported in 1981.[97-103] Due to the ease of fabrication, many scientists have worked with polymer solar cells to improve the PCE. Kanicki and Fedorko first reported single-layer polymer solar cells that use trans-polyacetylene and showed 0.1% PCE under white light illumination of 50 mW/cm<sup>2</sup>. [100] Many different polymer systems were studied over the course of the next ten years, but no further progress was made in terms of PCE. Two big issues needed to be addressed in the case of single-layer polymer solar cells. First, the electric field that originates in the difference between the electrodes' work functions is not sufficient to overcome exciton-binding energy (~ several 10<sup>-1</sup> eV ). [104-106] The quantum yield of the charge generated from the excitons is quite low, and it is only at the cathode metal interface that the excitons can dissociate easily. Second, the charge transport efficiency in a single-layer device is not good. [107, 108] Because most conjugated polymers are electron donors and hole transporters, the hole mobility of conjugated polymers generally is three order magnitude larger than that of electron mobility [25].

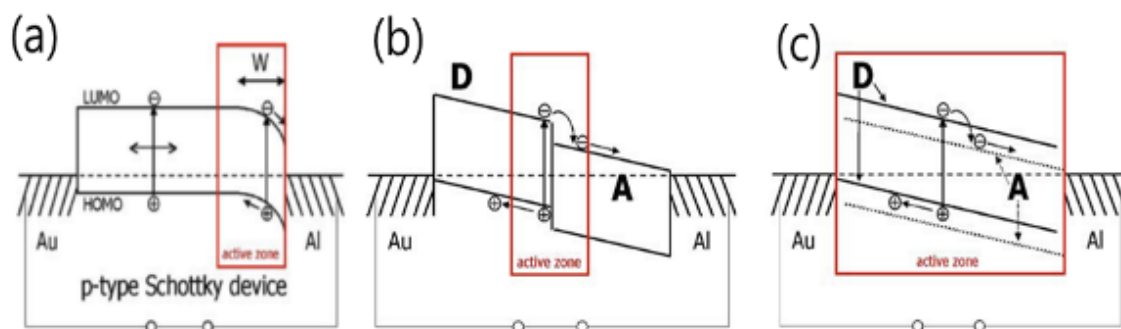


**Figure 1.3. Working principles of polymer solar cells in different structures: (a) single layer, (b) heterojunction polymer solar cell, and (c) bulk heterojunction polymer solar cell (Figure is reproduced from [96]).**

In the case of bilayer-structured (heterojunction) polymer solar cells[109-115], because of the small exciton diffusion length and the limited charge carrier generation that occurs only at the interface of a donor and an acceptor, as well as the poor charge carrier mobility of conjugated polymers, even with an additional electron transport layer, such as fullerene ( $C_{60}$ ), the inherent weakness of conjugated polymers could not be mitigated. The first bilayer-structured polymer solar cells were demonstrated by Sariciftci et al. using poly (2-methoxy-5-(2-ethyl-hexyloxy)-1,4-phenylene vinylene (MEH-PPV) and fullerene ( $C_{60}$ ). The PCE was 0.04% under monochromatic incident light.[116, 117]

Currently, the most popular polymer solar cell system is the bulk heterojunction (BHJ) solar cell, as shown in Figure 1.4. The BHJ concept was adopted from previous work on small molecule-based solar cells and was applied to polymer solar cells first by Alan Heeger and his student, G. Yu, in 1994.[118] The PCE of the first BHJ polymer solar cells was around 2.9% PCE, using poly[2-methoxy-5-(2-ethylhexyloxy)-1,4-phenylene-vinylene] (MEH-PPV) as a donor and fullerene ( $C_{60}$ ) as an acceptor. This advancement came from the improved charge separation efficiency of photo-induced excitons at the MEH-PPV: $C_{60}$  BHJ interface and its efficient charge transport to electrodes.

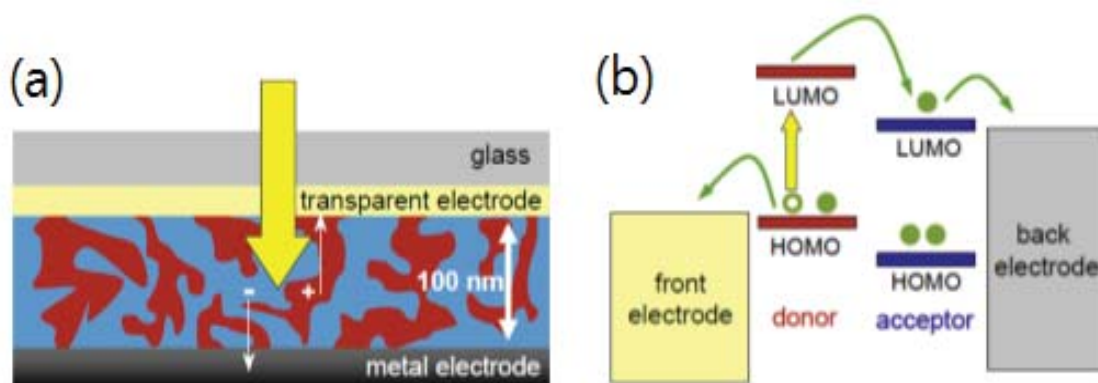


**Figure 1.4. (a) Schematic presentation of a bulk heterojunction (BHJ) solar cell, showing the phase separation between donor (red) and acceptor (blue) materials, and (b) schematic energy diagram showing the energy level of the highest occupied and lowest unoccupied molecular orbitals (HOMO and LUMO, respectively) (Figure is reproduced from [2]).**

Several examples of conjugated polymers and PC<sub>61</sub>BM are shown in Figure 1.3. The most popularly studied material combination for BHJ polymer solar cells is poly(3-hexylthiophene) (P3HT) and [6,6]-phenyl-C<sub>61</sub>-butyric acid methyl ester (PC<sub>61</sub>BM).[119-131]<sup>4,7,8</sup> The first P3HT:PC<sub>61</sub>BM BHJ polymer solar cells were demonstrated by Chirvase et al. in 2003.[132] In this combination, P3HT and PC<sub>61</sub>BM were used as an electron donor and an electron acceptor, respectively. A 1:4 mixture of P3HT and PC<sub>61</sub>BM in chloroform was spun-cast on top of 100 nm poly(3,4-ethylenedioxythiophene):poly(styrenesulfonate) (PEDOT:PSS) coated ITO substrate; the PCE was as low as 0.2 percent. Continuous efforts based on the optimization of the process condition and the further understanding of these promising materials resulted in a record high PCE of 5% reported by Alan Heeger and his student, W. Ma, in 2005.[133]

The PCE of the BHJ polymer solar cells is currently reported as high as 8.13% using a low band gap polymer and fullerene mixture by the Solamer Co., Y. Yang from the University of California, Los Angeles (UCLA) and L. P. Yu from the University of Chicago.[134] Furthermore, it will be possible to have more than 10% PCE in the near future. The strong tunable chemistry of the conjugated polymers has an incredible potential to improve polymer solar cells significantly, even though the issues of a short life time and poor reliability are not yet resolved.

## 1.4. Conjugated Polymers

Synthetic polymers have known as insulators, because of the excellent insulating properties of synthetic polymers; however, some synthetic polymers that have alternating single and double bonds in their chemical structures were discovered to have conducting or semiconducting properties, as shown in Figure 1.5 for polythiophene. The metal-like conductivity of polyacetylene with iodine doping was revealed in the 1970s through the work of Alan Heeger, Alan MacDiarmid, and Hideki Shirakawa. Because of their pioneering research into conducting polymers, these scientists were awarded the Nobel Prize in Chemistry in 2000.[135]

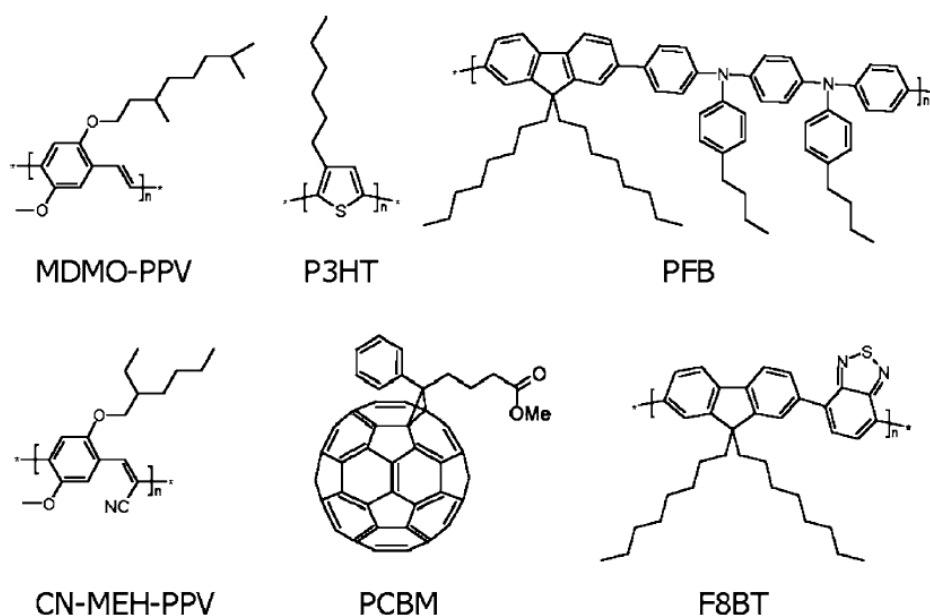


**Figure 1.5. Structures of conjugated polymers and a soluble C<sub>60</sub> derivative (PC<sub>61</sub>BM) for BHJ polymer-based solar cells (Figure is reproduced from [96]).**

The practical applications of these semiconducting conjugated polymers have produced many research topics, such as light-emitting diodes, solar cells, field effect transistors, photodiodes, and so on.[136] Additionally, many other potential applications are likely to emerge, such as corrosion prevention, antistatic coating, optical modulators and switches, and sensor technology.

The strongest merit of these conjugated polymers over conventional inorganic semiconductor technology is their easy and inexpensive processing capability that uses simple spin coating,

ink-jet printing, roll coating and screen printing, even on flexible substrates.[83-85, 87, 95]

The unique electrical and optical properties of conjugated polymers stem from the delocalized  $\pi$  bond electrons along the backbone, which is the reason conjugated polymers are sometimes described as one-dimensional carbon-based semiconductors or metals.[136] Other carbon-based materials, such as graphene and diamond, are considered two-dimensional and three-dimensional carbon-based materials, respectively.[136-141] Therefore, anisotropic physical properties, such as the conductivity of conjugated polymers, come from their unique chain-like structure and optical properties, such as band gap, absorption and emission spectra, depending on the delocalized conjugated chain length. In general, a longer conjugation length provides a smaller band gap and results in the bathochromic (red) shift in the absorption as well as the emission spectrum.[136, 142] Due to these easily tunable optical properties, the absorption spectra of the conjugated polymers could be driven within the visible light spectrum, and the conjugated polymers could serve as strong candidates for solar cell applications.

In addition, these optical properties could be tuned according to temperature and doping levels.[143, 144] These phenomena based on changes in absorption and emission spectra are referred to as the optical chromic effect. The concept of doping in organic semiconductors is different from that of conventional inorganic semiconductors, although the term doping was adopted from it. For conventional inorganic semiconductors, doping refers to the introduction of a tiny amount of III or V column elements, such as boron (B), arsenic (As) and phosphorus (P) into the silicon (Si) semiconductor of column IV (an intrinsic semiconductor) to become a p-type or n-type extrinsic semiconductor. The main charge carriers in conventional semiconductors, i.e., either electrons or holes, are dependent on the types of dopants used. However, the doping process in organic semiconductors, such as conjugated polymers, indicates the chemical reduction-oxidation (Redox) reactions of the molecules.[145, 146] Oxidation is the removal of electrons or the injection of holes with the addition of iodine ( $I_2$ ) or bromine ( $Br_2$ ) oxidants.[147, 148] This process could be regarded as p-type doping for conventional semiconductors. However, reduction here refers to the injection of electrons by alkali metals, such as Li, Na and K.[149] This process could be

compared to n-type doping in conventional inorganic semiconductors. Even though n-type doping in conjugated polymers is far less common than p-type doping because of the abundance of oxygen, oxygen is one of the strongest oxidizing agents in the environment. N-type doped conjugated polymers are easily de-doped (re-oxidized) by their reaction with oxygen in the atmosphere.[150] Generally, p-doped conjugated polymers exhibit improved electrical conductivity seven- or eight-fold in comparison to inherent ones.

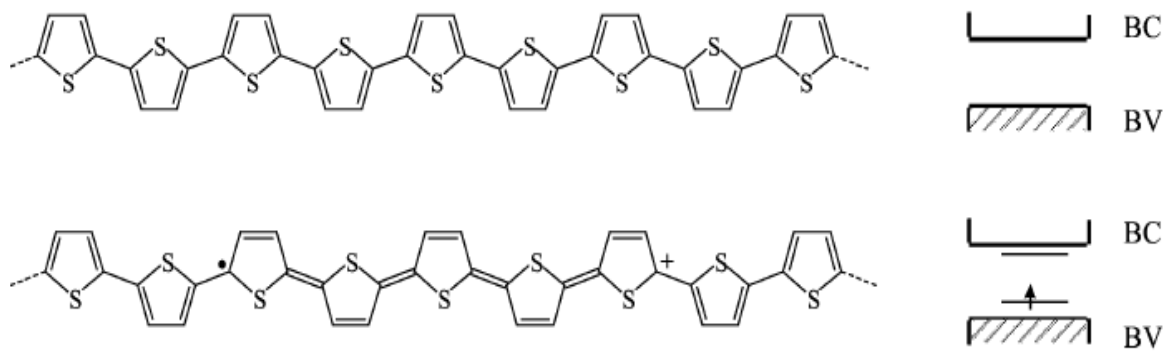


**Figure 1.6. Chemical structures of the inherent (top) and polaronic (bottom) states of polythiophene (Figure is reproduced from [96]).**

For example, the doping of polythiophene by iodine ( $I_2$ ) vapor results in a seven-fold increase of conductivity from  $10^{-10}S/cm$  to  $10^{-3}S/cm$  in one minute.[151, 152] Chemical doping and dynamic doping by either iodine ( $I_2$ ) vapor or light irradiation cause the evolution of the polarons or bipolarons in the conjugated polymers as shown in Figure 1.6.[96, 151, 153, 154]

In general, a polaron has a radical cation in a conjugated polymer chain and a conjugated polymer becomes a p-type semiconductor.[155] Due to the strong coulombic interactions of the polarons in the polymer chain, the conjugated polymer chains are distorted or deformed in the geometric structure of the polymer chains. The existence of polarons in conjugated polymer chains can be described as an additional energy level within the band gap between the valence and conduction band of the inherent conjugated polymers. Due to the physical distortion of the polymer chains and the small band gap from the polaron bands, the optical absorption and emission spectra of the conjugated polymers are changed.[96]

## 1.5. Device Physics of Organic Solar Cells

### 1.5.1. General Working Principles

Four steps are needed to generate electricity from organic solar cells.[131, 156, 157] In most organic materials, a very small portion of the incident photon is absorbed due to the wide band gap. If a band gap approaches 1.1 eV (1100 nm), around 77% solar radiation could be absorbed. However, the band gap of most conjugated polymer is around 2.0 eV (600 nm), and the possible absorption of photons is about 30% of the solar spectrum.[158-160] Due to the low mobility of charge carriers and excitons, the optimal active layer thickness in organic solar cells is around 100 nm.[96, 160] However, the absorption coefficients of organic materials are much larger than those of inorganic semiconductors. With a reflective metal back contact, such as an aluminum cathode found in conventional organic solar cells, the photon absorption could be increased up to 90% even with the 100 nm thickness.[96, 160, 161] As a first step, photons from sunlight are absorbed in an active layer of organic solar cells, and in a second step, electrons are excited from the valence band (VB) to the conduction band (CB) inside the electron donating p-type material such as conjugated polymers. Usually, conjugated polymers, such as P3HT, are electron donors, and dye or fullerenes, such as PC<sub>61</sub>BM, are electron acceptors.[96] This excited state is called as an exciton (third step), which is an unstably bounded electron and hole pair that is a neutral quasi-particle.[72] Due to the extremely short diffusion length of an exciton – as short as 5~10 nm – an electron from the exciton (Frenkel exciton) can easily relax back to its stable ground state of the material, thus resulting in a loss of efficiency.[71, 72, 162-165] As a next step to having the best solar cell performance possible, the exciton diffuses to the interface of the donor and acceptor materials without significant its loss from the electron relaxation (forth steps).

At the interface of organic materials that have sufficiently different electron affinities (EAs) and ionization potential (IP), the exciton finally separates as a discrete electron and a hole, both of which together serve as free carriers thanks to the built-in internal potential from these energy differences. If there is not enough difference in energy levels to overcome the exciton-binding energy (0.4eV)[166], an exciton may not separate into free charge carriers

(fifth step). Those separated free carriers should be transported without recombining and should be collected at the surfaces of the electrodes (sixth step). The final PCE depends on all six steps, and the maximum PCE is achieved under the most optimal conditions. These fundamental steps are shown in Figure 1.7.

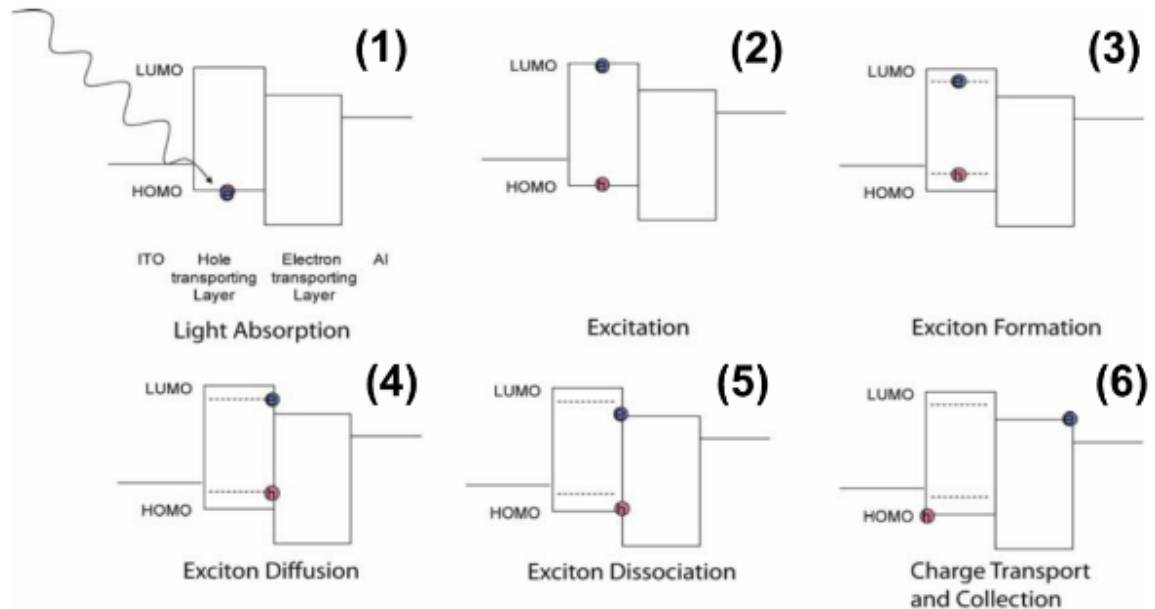


**Figure 1.7. Fundamental working principles of organic solar cells (Figure is modified and reproduced from [167]).**

### 1.5.2. Electrical Characterization of Solar Cells

The PCE of solar cells can be described clearly using conventional J-V curves and several parameters must be considered to understand the working principles of solar cells as shown in Figure 1.8. The equation for the PCE can be derived based on all the parameters discussed heretofore.

$$Power = \frac{P_{out}}{P_{in}} = \frac{J_{max} \cdot V_{max}}{P_{in}} = \frac{FF \cdot J_{sc} \cdot V_{oc}}{P_{in}} \quad (1-1)$$

Short-circuit current ( $J_{sc}$ ) is the maximum current when the voltage is zero, and it is a function of illumination. Open-circuit voltage ( $V_{oc}$ ) is the voltage when no current is in the solar cell.[22] The fill factor (FF) is the ratio of the maximum power to the product of the external short-circuit current ( $J_{sc}$ ) and open-circuit voltage ( $V_{oc}$ ) values.

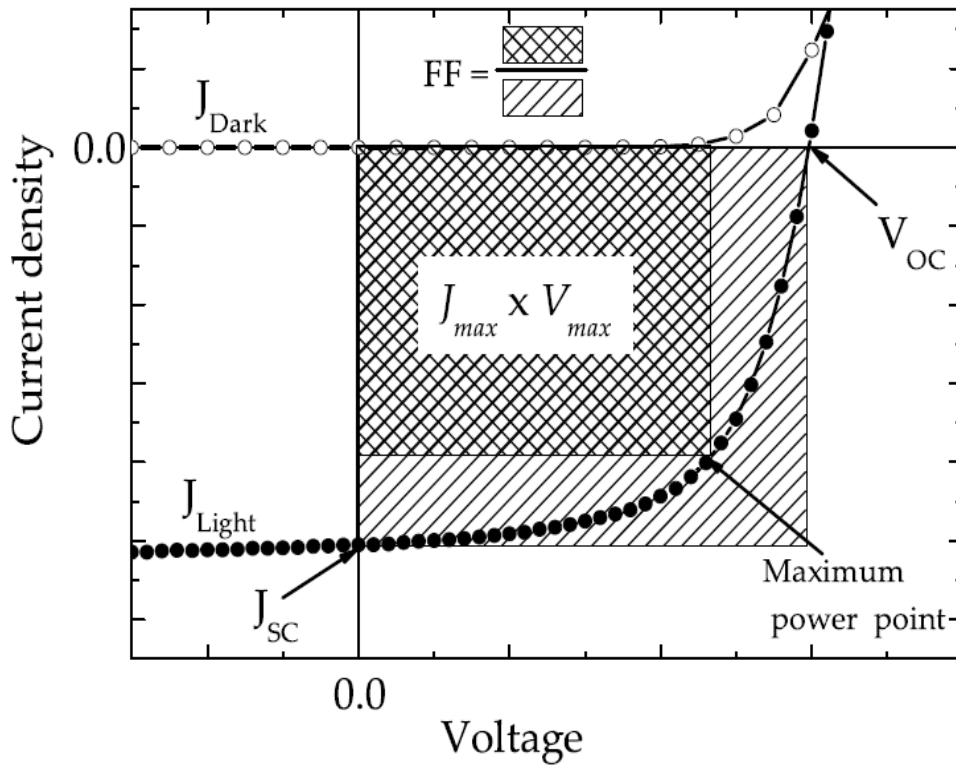


**Figure 1.8. Typical J-V curves of solar cells in dark (empty symbols) and illuminated (filled symbols) conditions. Short-circuit density ( $J_{sc}$ ) and open-circuit voltage ( $V_{oc}$ ) are shown. The maximum output power is given as the rectangular area ( $J_{max} \times V_{max}$ ).**

In addition, the FF can show the degree of rectification of a solar cell. Therefore, the higher the FF, the better the solar cell's performance.[22]

$$FF = \frac{(JV)_{max}}{J_{sc}V_{oc}} \quad (1-2)$$

A high load resistor reduces the current flow, so the generated charges need more time to get out of an active layer. Due to the increased recombination of electrons and holes, an extracted current constantly decreases in the 4th quadrant of J-V coordinates.[22, 70] There are two resistances: series resistance ( $R_s$ ) and shunt resistance ( $R_{sh}$ ). Series resistance depends on the resistivity of the materials, electrodes and metal-organic interfaces. Shunt resistance represents a leak or a short in the diode or charge recombination.[22, 70] For good solar cell performance, those resistances should be optimized. A large shunt resistance and small series resistance result in the good performance of solar cells.

$$R_{sh} \approx \left( \frac{J}{V} \right)^{-1} \quad \text{An inverse slope at } V = 0 \text{ V} \quad (1-3)$$

$$R_s \approx \left( \frac{J}{V} \right)^{-1} \quad \text{An inverse slope at } V > V_{oc} \quad (1-4)$$

Solar cells are conventional diodes in the dark condition, and they allow much more current to flow in the forward bias ( $V > 0$ ) than in the reverse bias ( $V < 0$ ) condition. This kind of rectifying property is a characteristic of ideal diode properties. Using a simple ideal diode equation, called the Shockley equation[22, 70], the  $J_{dark}(V)$  equation is normally formulated as shown in Equation (1-5):

$$J_{dark}(V) = J_o \left( e^{\frac{qV}{nk_B T}} - 1 \right) \quad (1-5)$$

In this equation,  $J_o$  is a constant,  $k_B$  is Boltzmann's constant,  $n$  is the diode ideality factor and  $T$  is temperature in degrees Kelvin. Because  $R_s = 0 \Omega$  and  $R_{sh} = \infty \Omega$  in an ideal diode, current through such an ideal solar cell is determined by current density only, and for an applied positive voltage, the current increases exponentially. Under illuminated conditions, photo-current density from the exposed light photons is generated, and the equation for net current density is modified as Equation (1-6). The overall current-voltage response of solar cells can be approximated as the sum of the short-circuit photo-current and the dark current. This step is known as the superposition approximation.<sup>5,6</sup> Although reverse current, which flows in response to voltage in an illuminated solar cell, is not formally equal to current that flows in dark current, the approximation is reasonable for many materials used in solar cells.

$$J_{dark}(V) = J_o \left( e^{\frac{qV}{nk_B T}} - 1 \right) - J_{sc} \quad (1-6)$$

The  $V_{oc}$  for an ideal diode is shown in Equation (1-7) when the current density = 0.

$$V_{oc} = \frac{nk_B T}{q} \ln \left( \frac{J_{sc}}{J_o} + 1 \right) \quad (1-7)$$

Figure 1.8 shows that the current-voltage product is negative and that a solar cell generates power when voltage is between 0 and  $V_{oc}$ . At  $V < 0$ , an illuminated device acts as a photo-

detector, consuming power to generate a photo-current that is light-dependent but bias-independent. At  $V > V_{oc}$ , that device again consumes power. This region is where light-emitting diodes operate.

The function of solar cells in the real world is slightly different with that of an ideal diode.[22, 70] The two inherent resistances,  $R_{sh}$  and  $R_s$ , are not considered in an ideal diode. Their effect on the final solar cells' performance is critical, and a more realistic model is needed to predict and to explain the real function and performance of solar cells. When parasitic series and shunt resistances are considered, the net current density should be modified as Equation (1-8).

$$J = \frac{J_{sc} - \frac{V}{R_{sh}}}{1 + \frac{R_s}{R_{sh}}} - \frac{J_o}{1 + \frac{R_s}{R_{sh}}} \cdot \left( e^{\frac{V - JR_s}{nk_B T/q}} - 1 \right) \quad (1-8)$$

The open-circuit voltage ( $V_{oc}$ ) also should be modified in consideration of the shunt resistance effect, as shown in Equation (1-9).

$$V_{oc} = \frac{nk_B T}{q} \ln\left(\frac{J_{sc} - V_{oc} / R_{sh}}{J_o} + 1\right) \quad (1-9)$$

## 1.6. Hansen Solubility Parameters

Solubility of solutes in a solvent is critical to have the fine morphology of the blended polymer thin films. Solubility parameters provide the foundation for the understanding of materials' solubility in a solvent and the materials' miscibility. This powerful tool can be applied in the further understanding of the BHJ polymer solar cells. In this sub-chapter, the fundamental principles of solubility parameters calculation are explained.

The term solubility parameter was first used by Hildebrand and Scott, and it is called the Hildebrand solubility parameter.[168] This parameter provides a foundation for the further understanding of solubility, but it is defined by a single number and only considered the

cohesive energy density of the molecules. Therefore, the Hildebrand solubility parameter is also called cohesive energy parameter because they are derived from the energy required to convert a liquid to a gas. The energy of vaporization is the direct measurement of the total energy that holds the liquid's molecules together.[168] The Hildebrand solubility parameter is defined as Equation 1-10.

$$\delta = \sqrt{CED} = \sqrt{\frac{\Delta E}{V}}, \quad (1-10)$$

Where V is the molar volume;  $\Delta E$  is the energy of vaporization; and CED stands for cohesive energy density. This Hildebrand solubility parameter has the same value as total solubility parameter ( $\delta_T$ ) in the Hansen solubility parameters that include dispersion interaction, polar cohesive energy and hydrogen bonding energy, as presented in Equation 1-11.[168]

$$\delta_T = \sqrt{(\delta_D^2 + \delta_P^2 + \delta_H^2)} = \sqrt{\left(\frac{E_D}{V} + \frac{E_P}{V} + \frac{E_H}{V}\right)} \quad (1-11)$$

Therefore, these three interaction parameters ( $\delta_D, \delta_P, \delta_H$ ) can provide more detailed information about fundamental solubility than the Hildebrand solubility parameters that consist of a single number. Similar solubility parameter values of two materials indicate that they have similar affinities. The Hildebrand solubility parameter generally works well only in a non-polar system because it does not consider hydrogen bonding and polar interaction.

The solubility 'distance' ( $R_a$ ) between two materials based on their respective partial Hansen solubility parameters can be calculated using Equation (1-12), and the relative energy density (RED) values are calculated based on the ratio of the  $R_a$  and the inherent solubility 'distance' ( $R_o$ ) values using Equation (1-13). If the RED values are less than 1 ( $RED < 1$ ), the solute dissolves well in a solvent (here, component 1 is a solute, and component 2 is a solvent).

$$R_a = \sqrt{4(\delta_{D_1} - \delta_{D_2})^2 + (\delta_{P_1} - \delta_{P_2})^2 + (\delta_{H_1} - \delta_{H_2})^2} \quad (1-12)$$

$$RED = \frac{R_a}{R_o} \quad (1-13)$$

$$\chi_{12} = 0.5 \times (RED)^2 = 0.5 \times \left(\frac{R_a}{R_o}\right)^2 \quad (1-14)$$

The Flory-Huggins interaction parameter ( $\chi_{12}$ ) can be calculated using Equation (1-14) (assuming a high molecular weight solute, such as a polymer)[168]; if this value is less than 0.5 ( $\chi_{12} < 0.5$ ), then it dissolves well in a solvent. The critical point that expresses the solubility limit of a solute in a solvent has  $RED = 1$  and  $\chi_c = 0.5$ .

In case of the Hansen solubility parameters, the solubility of a solute in many different solvents in a 3D sphere model based on the calculated three interaction parameters ( $\delta_D, \delta_P, \delta_H$ ). If the solubility values of a solvent are close to the borderline of the solubility parameter sphere of the solute, or are greater than the radius of that sphere, then each specific solvent cannot dissolve the particular solute.

## **1.7. Molecular Orientation and Phase Separation-Induced Morphology Control in Bulk Heterojunction (BHJ) Polymer Solar Cells**

### **1.7.1. Molecular Ordering Effects on Device Mobility**

In order to improve the performance of organic solar cells, charge carriers that are separated from excitons should be transported to electrodes through the conjugated  $\pi$ - $\pi$  orbital overlaps in the organic semiconductors. The crystalline orientation and crystallinity of the conjugated polymers or small molecules are thus critical to improve the  $\pi$ - $\pi$  orbital overlaps, which in turn allow an efficient charge transport between the molecules.[165, 169] If defects, such as misalignment of molecules, vacancies and dislocations, are found, the transport efficiency of the charge carriers decreases due to the lowered degree of  $\pi$ - $\pi$  orbital overlaps.[170-172] With improved crystalline orientation and higher crystallinity, enhanced charge carrier mobility can be achieved in a device.[173-182] For example, as-cast amorphous triethylsilylethynyl anthradithiophene (TES ADT) films resulted in increased crystallinity in chlorobenzene (CB) vapor annealing.[173] This increased crystallinity thus the improved charge carrier mobility of an organic thin film transistor (OTFT) up to  $0.1 \text{ cm}^2 \text{ V}^{-1} \text{ s}^{-1}$  compared to  $0.002 \text{ cm}^2 \text{ V}^{-1} \text{ s}^{-1}$  in amorphous TES ADT.[173] The thermal annealing of pentacene thin film also improved molecular orientation and enhanced the charge carrier

mobility of an OTFT from  $0.19 \text{ cm}^2 \text{ V}^{-1} \text{ s}^{-1}$  to  $0.49 \text{ cm}^2 \text{ V}^{-1} \text{ s}^{-1}$ . [177] Additionally, the crystalline orientation is also critical for improved mobility. In an OTFT application, if the ‘edge on’ crystalline orientation (which means that the  $\pi$ - $\pi$  orbital stacking direction is parallel to the substrate) of P3HT dominates, then the charge carrier mobility of the OTFT device is enhanced by two orders of magnitude over a ‘face on’ crystalline orientation (which means that the  $\pi$ - $\pi$  orbital stacking direction is perpendicular to the substrate), as shown in Figure 1.9. [183] In case of P3HT:PC<sub>61</sub>BM BJJ polymer solar cells, the ‘face on’ crystalline orientation (which means that the  $\pi$ - $\pi$  orbital stacking direction is perpendicular to the substrate) of P3HT is preferred and it enhances the charge carrier transport towards both electrodes.

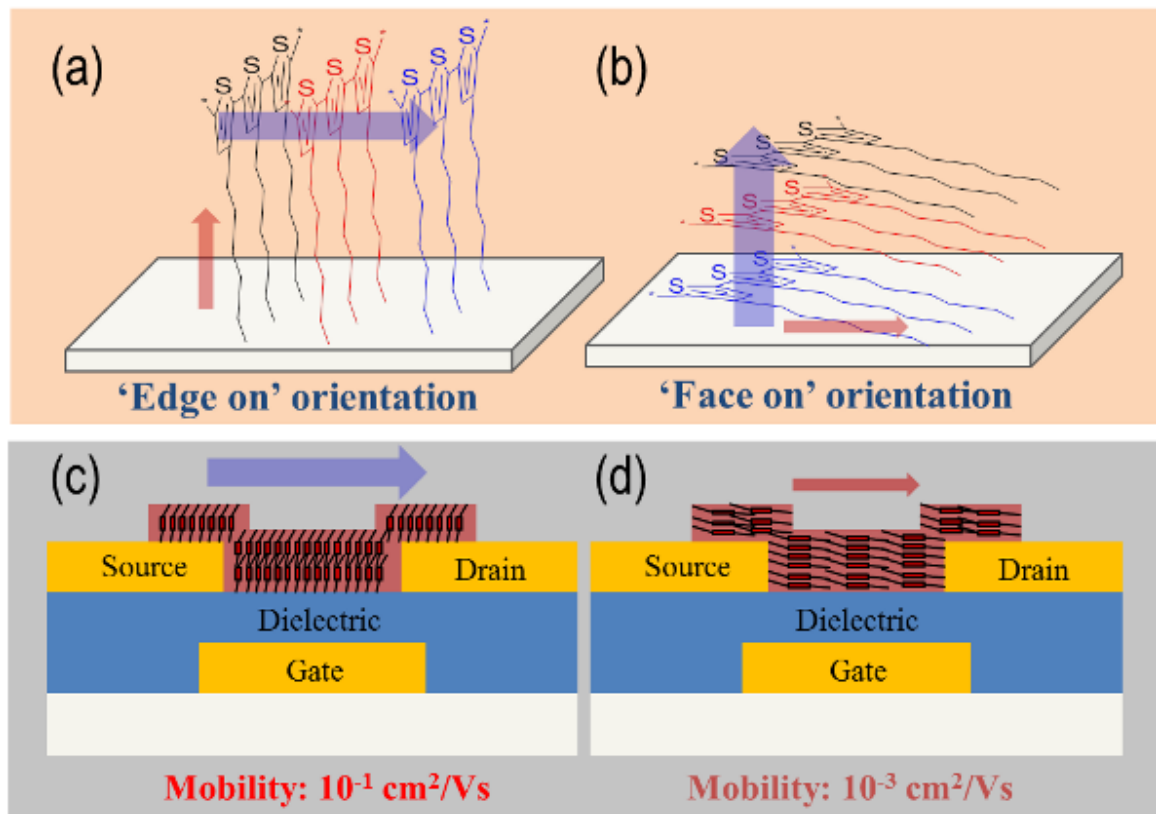
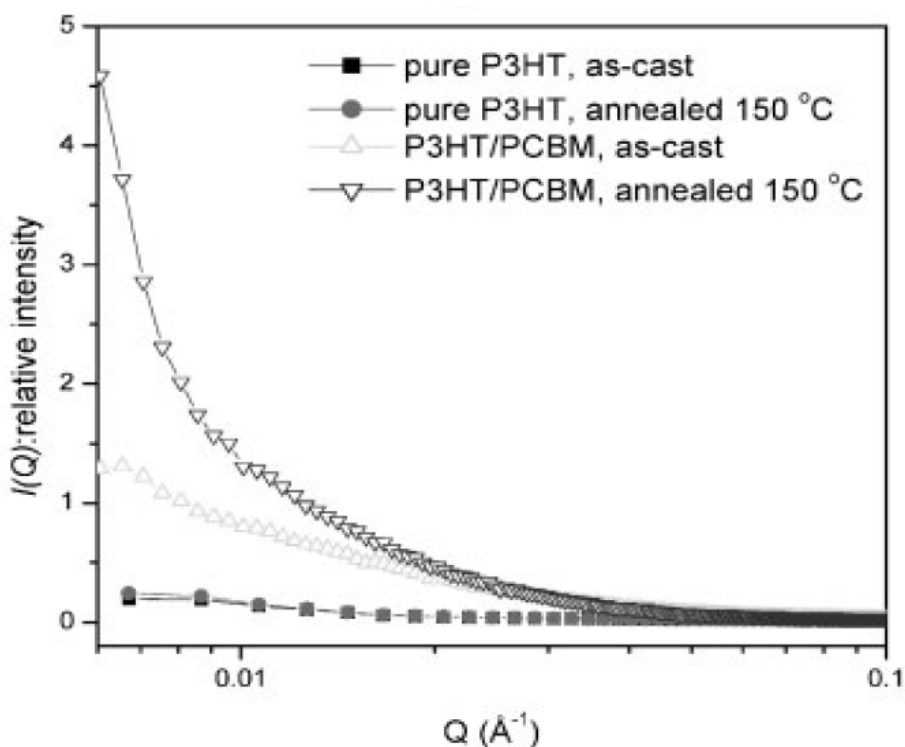


Figure 1.9. ‘Edge on’ and ‘face on’ orientation of P3HT: (a) and (c) are ‘edge on’ orientation, (b) and (d) are ‘face on’ orientation. (a) and (b) are schematic diagrams for charge carrier mobility in P3HT thin films; (c) and (d) are charge carrier mobility results in the OTFT (red squares inside active layers are thiophene rings and adjacent lines are side chains) (Figures are drawn based on the OTFT mobility data of [183]).

### 1.7.2. Crystallization and Phase Separation in P3HT:PC<sub>61</sub>BM Bulk Heterojunction (BHJ) Polymer Solar Cells

In a P3HT:PC<sub>61</sub>BM BHJ polymer solar cells that have two components, the crystallization and crystalline grain growth of one component are known to enhance the phase separation of the other component from the bulk mixture.[184-186] This phenomenon is critical to excellent performance of P3HT:PC<sub>61</sub>BM BHJ polymer solar cells and many researchers have studied the effect of the P3HT crystalline phase in a P3HT: PC<sub>61</sub>BM BHJ mixture. There was a report that PC<sub>61</sub>BM crystalline phase simultaneously grows corresponds to the P3HT crystalline phase growth and the phase separation during the thermal.[185, 186]



**Figure 1.10.** GISAXS curves of as-cast and annealed (150°C, 15 minutes) P3HT and P3HT:PC<sub>61</sub>BM thin films (Figure is reproduced from [188]).

Grazing Incident Wide Angle X-ray Scattering (GIWAXS) studies on a P3HT:PC<sub>61</sub>BM BHJ thin film showed increased intensity of the Bragg reflections of P3HT, which corresponds to increased crystallinity in the P3HT upon post thermal annealing.[185, 187] Additionally, from Grazing Incident Small Angle X-ray Scattering (GISAXS) studies, it is found that

increased X-ray scattering intensity corresponds to an increase in the PC<sub>61</sub>BM cluster size as shown in Figure 1.10.[188] These results are related to the increased phase separation between P3HT and PC<sub>61</sub>BM. It is known that the degree of phase separation between P3HT and PC<sub>61</sub>BM could affect the OPV device performance.[189] For efficient exciton dissociation as well as effective charge carriers transport to the electrodes, a P3HT:PC<sub>61</sub>BM BHJ layer of polymer solar cells should have not only a wide interfacial area between the electron donor and acceptor but also a well-oriented P3HT crystalline phase.[190] Additionally, the coarsening of PC<sub>61</sub>BM crystals under post thermal annealing should be minimized.[185]

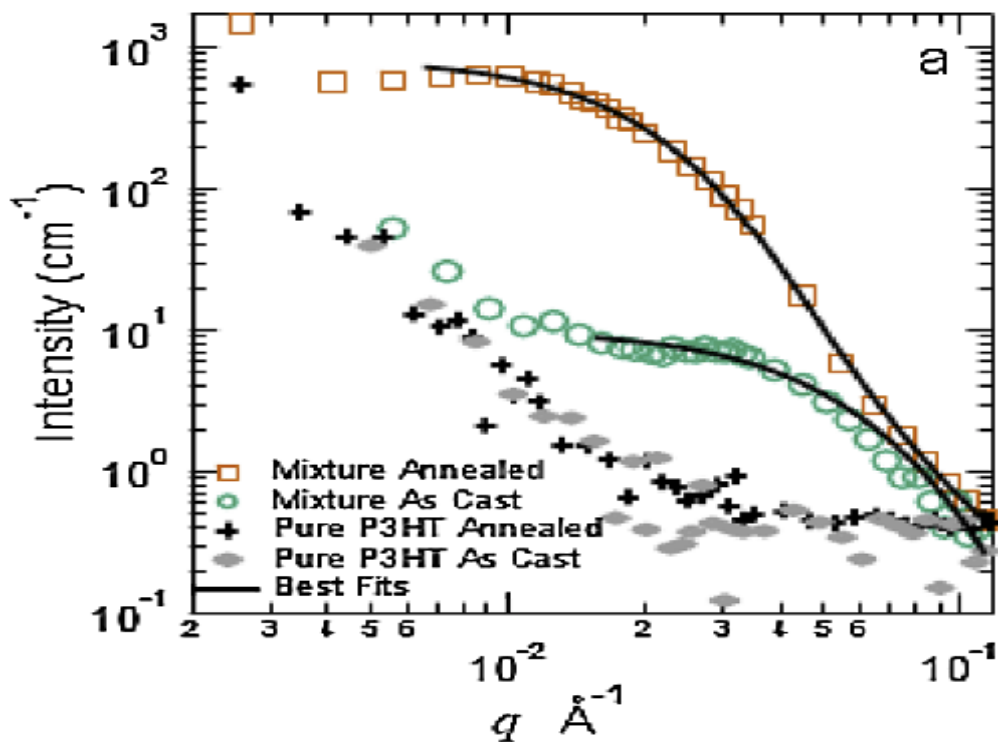


**Figure 1.11. SANS curves of as-cast and annealed (140°C, 20 minutes) P3HT and P3HT:PC<sub>61</sub>BM thin films (Figure is reproduced from[191]).**

Similar results with GISAXS of PC<sub>61</sub>BM coarsening during thermal annealing were reported by using Small Angle Neutron Scattering (SANS) studies as shown in Figure 1.11. Due to the low contrast from the thin thickness, 100 nm of a P3HT:PC<sub>61</sub>BM BHJ active layer, 15 or more stacked films were prepared and used to carry out SANS studies. The increased scattering intensity was explained mainly due to the coarsening of PC<sub>61</sub>BM inside a

P3HT:PC<sub>61</sub>BM BHJ active layer and the pure P3HT thin films did not show any intensity changes regardless of thermal annealing. The domain size of P3HT:PC<sub>61</sub>BM BHJ active layer increased with the post thermal annealing and it was explained that the coarsening of PC<sub>61</sub>BM resulted in the big size of domain that came from the largely phase separated P3HT:PC<sub>61</sub>BM BHJ active layer during thermal annealing than that of an as-cast.

P3HT:PC<sub>61</sub>BM BHJ solar cells that have a high degree of P3HT crystallinity and a large size of PC<sub>61</sub>BM cluster in the active layer showed a decrease in device efficiency with prolonged thermal annealing as shown in Figure 1.12 (a).[185, 192] Furthermore, the large PC<sub>61</sub>BM crystals hindered the P3HT crystalline phase growth in the preferred orientation, whereas the smaller PC<sub>61</sub>BM clusters did not significantly affect the existing orientation of the P3HT crystals, as shown in Figure 1.12 (b).[185]

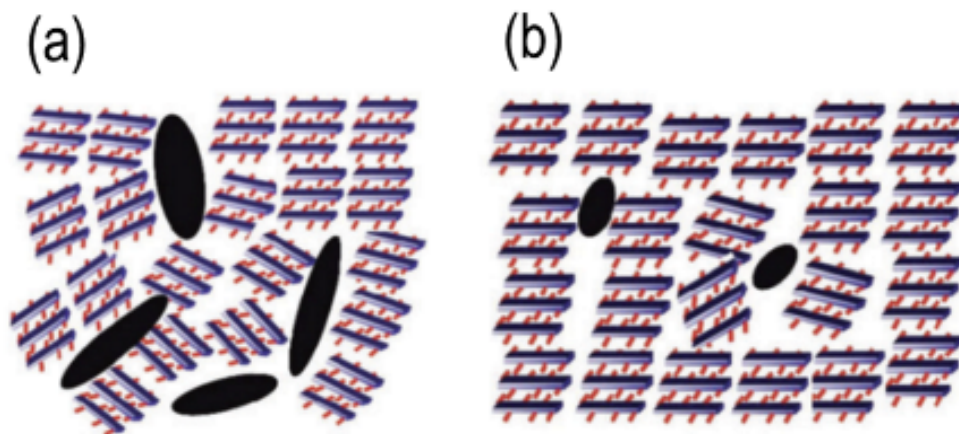


**Figure 1.12. Schematic diagram of P3HT:PC<sub>61</sub>BM BHJ films composed of (a) highly crystalline P3HT, and (b) less crystalline P3HT. The black ovals represent PC<sub>61</sub>BM crystals, and the rectangular stacks represent P3HT crystals. (Figures are adopted from [185])**

The fundamental root causes for the deterioration of solar cell efficiency during the prolonged thermal annealing are not fully understood yet. As a consequence, the efficiency of the solar cells worsened with the extended thermal annealing time of the P3HT:PC<sub>61</sub>BM BHJ layer. Additionally, the big size of PC<sub>61</sub>BM crystals may cause electrical shorts problem. Therefore, special attention during the post annealing process must be given to the BHJ film to control crystallinity of the components. Additionally, the enhanced P3HT crystallinity

resulted in the bathochromic (red) shift of the absorption spectrum into the visible light range and an improvement in photon absorption efficiency.[86, 191, 193]

Phase separation in a P3HT:PC<sub>61</sub>BM BHJ thin film comes from the chemical incompatibility (spinodal decomposition) of the two components[190], in addition to the crystallization.[185, 194]<sup>65-67</sup> Normally, solvent evaporation that occurs during the thin film spin casting limits the large scale of phase separation due to the rapid solidification of the film.[190] Therefore, a post process such as thermal annealing is normally required to drive the film morphology into the enhanced phase-separated state.[185, 194] In the optimal condition, an as-cast active layer exhibits extremely fine structures with wide inter-domain interfacial area.[190] Although the fine structures exist in an as-cast P3HT:PC<sub>61</sub>BM BHJ film, solar cells without thermal annealing exhibit relatively low efficiency because low degree of crystallinity cannot provide charge transport path and the wide interfacial area can promote charge recombination, too.[190]

It is commonly believed that the length scale of phase-separated domains in a BHJ active layer should be in the range of the exciton diffusion length, 10 nm, to maximize its dissociation into free carriers. Many researchers thus have tried to find the best phase separation condition in this range by changing the component ratios[186, 195], introducing additives[196-198], changing post-thermal annealing conditions[188, 189, 199] or solvent vapor annealing conditions[200-202], or by controlling solvent evaporation rates during the spin casting of thin BHJ films using mixed solvents.[198] An interesting study reported that, under prolonged high temperature annealing conditions, PC<sub>61</sub>BM domains grew continuously up to 50 nm, which is much larger than the exciton diffusion length, without further enhancing P3HT crystallinity.[190] In addition, solar cell efficiency continued to increase with an increase in the annealing temperature of this BHJ active layer.[190] One hypothesis was that large PC<sub>61</sub>BM cluster domains improve the 3-D connectivity to the electrodes for improved electron and hole transport.[190, 201] There is much debate regarding the optimal size of the PC<sub>61</sub>BM crystalline cluster and its effect on the P3HT:PC<sub>61</sub>BM BHJ solar cells, and more time is needed for clarification of this issue. However, morphology from the two phase-separated components clearly affects the final solar cell performance.

In another interesting study about the effects of phase separation of a BHJ mixture on device performance, Bull et al. used light beam-induced current (LBIC) microscopy to study the photo-current distribution in poly(5,7-bis(3-dodecylthiophen-2-yl)thieno[3,4-b]pyrazine-*alt*-9,9-dioctyl-2,7-fluorene) (BTTP-F):PC<sub>61</sub>BM BHJ thin films.[201] A BTTP-F/PC<sub>61</sub>BM BHJ thin film was exposed to chlorobenzene (CB) vapors for 30 minutes, and the grown micron-sized PC<sub>61</sub>BM crystalline clusters were studied using LBIC. The LBIC results revealed three distinct regions of photo-current in an annealed film (Figure 1.13. (a)) compared to uniform photo-current in an as-cast film (Figure 1.13. (b)).

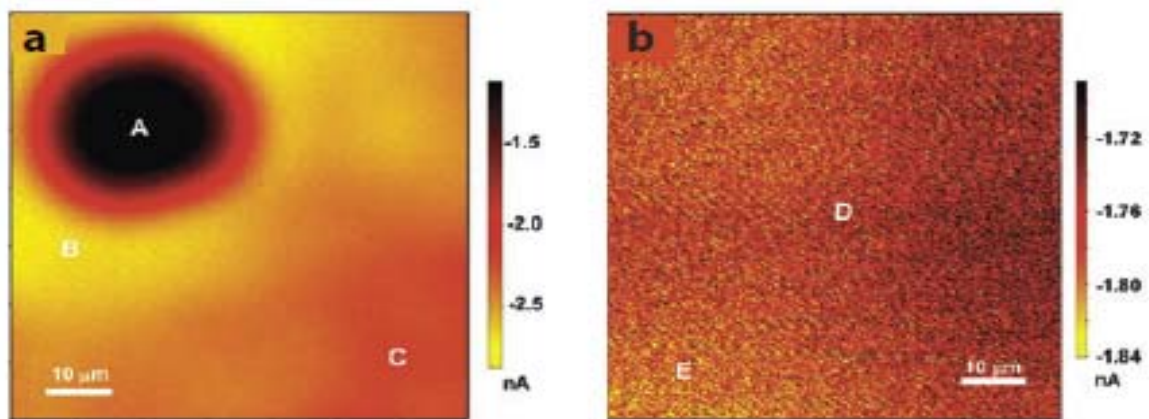


**Figure 1.13. Light beam-induced current (LBIC) microscopic images of poly(5,7-bis(3-dodecylthiophen-2-yl)thieno[3,4-b]pyrazine-*alt*-9,9-dioctyl-2,7-fluorene)(BTTP-F):PC<sub>61</sub>BM thin films exposed to chlorobenzene (CB) solvent vapors for (a) 30 min and (b) 0 min. The PC<sub>61</sub>BM cluster, labeled A, is surrounded by a region of high current, labeled B. The region furthest from the PC<sub>61</sub>BM cluster has a low photo-current, labeled C. In the unannealed films, photo-current generation is fairly uniform between D and E.(Figures are reproduced from [201]).**

When the BHJ film was solvent annealed, no photo-current was evident inside the PC<sub>61</sub>BM cluster in region A. The highest photo-current was in a depletion region, B, between the PC<sub>61</sub>BM cluster region A and the weak photo-current region C. There was no photo-current in PC<sub>61</sub>BM cluster (region A). Although the non-uniform photo-current came from an annealed BHJ film, its PCE of 1.25% exceeds that of the as-cast film of 0.75 percent. This enhancement in the overall photo-current of the solvent annealed BHJ thin film is due mainly to the enhanced photo-current in region B. Region B is a depletion zone that has a strong phase separation between BTTP-F and PC<sub>61</sub>BM, and this strong phase separation in region B

thus led to the improved exciton dissociation toward the free charge carriers. It is surprising that even with big PC<sub>61</sub>BM cluster, the PCE was enhanced more than with the uniform photo-current. Therefore, further understanding of the phase separation length scale is important for future improvements in organic solar cells.

### **1.7.3. Morphology Control: Spin Coating vs. Annealing Processes**

The morphology of BHJ polymer solar cells is heavily dependent on the spin coating condition, and different spin coating solvents result in changes in the degree of phase separation and the crystalline phase growth, or the molecular orientation of polymers and PC<sub>61</sub>BM.[96, 119, 186, 203-206]

The choice of solvent is critical to the control of the morphology in the BHJ polymer solar cell active layer. Finer domain size has been observed in the spun-cast films that use CB solutions compared to films that use toluene solutions.[96, 186] The different effects that are obtained from the different solvents are related closely to both chemical solubility[186, 205] and solvent vapor pressure.[96, 110] When a better solvent, such as ortho-dichlorobenzene (ODCB) is used, a much finer domain size is achieved due to the better solubility and the lower vapor pressure.[119, 202] The vapor pressure of the solvent determines the solvent evaporation rate, which in turn affects the thickness of the film and the drying time during the spinning process. If the spin speed and concentration of the solution are not changed, high vapor pressure solvents, such as chloroform or thiophene, result in an unstable film due to the fast solvent evaporation rate; however, low vapor pressure solvents, such as CB or ODCB drive the morphology into a much finer and stably phase-separated structure.

The spin coating speed is also a critical factor in determining the final film quality. A fast spin coating speed increases the radial flow of the applied solution and also increases the solvent evaporation rate, which results in a thin and uniform film. When spin coating thin films from an initial homogeneous ternary blends that consist of two solid solutes and a common solvent, the rapid solvent evaporation changes the blended system into a metastable or unstable state. Because this kind of solvent quench does not occur instantaneously, the blend system should have time to develop phase separation, which stops when the viscosity

of the film increases with the increased rate of solvent evaporation, and the polymer chains are no longer mobile.

Thermal annealing in a P3HT:PC<sub>61</sub>BM-based BHJ system has been widely used as a post process to improve the performance of solar cells.[111, 121, 130, 188, 207] It applies high temperature (in a range of 120 ~ 150°C), which is above T<sub>g</sub> of P3HT for 5 ~ 30 minutes to the P3HT:PC<sub>61</sub>BM BHJ active layer to enhance the degree of crystallinity of P3HT. The enhanced crystalline phase orientation and crystallinity growth of P3HT found in thermal annealing results in better charge carrier mobility and an enhanced photon absorption spectrum.[207, 208] In the case of PC<sub>61</sub>BM, a micron scale of crystalline phase was reported during the thermal annealing.[192] Because the crystalline phase of PC<sub>61</sub>BM can grow up to several μm under a prolonged thermal annealing condition,[190, 192] it is generally believed to result in a decrease in the interfacial area for charge separation.

The phase separation inside a BHJ active layer is determined primarily by the solvent solubility during spin casting.[96, 186] Good spin-casting solvents, such as CB and ODCB, which have good solubility for both P3HT and PC<sub>61</sub>BM, can lead to much finer domain size than other solvents, such as toluene and xylene.[119, 203] Once the domain size is determined during the spin casting process, as already mentioned, it is difficult to improve the morphology further in terms of a smaller domain size during thermal annealing. However, solvent annealing is regarded as an effective post casting process to control the domain size and to optimize the performance of P3HT:PC<sub>61</sub>BM BHJ polymer solar cells.[201, 202, 209] In solvent annealing, it is possible to adjust the domain size because the annealing solvent can provide physical mobility to the active layer again. The morphology of a solvent annealed P3HT:PC<sub>61</sub>BM BHJ active layer strongly depends on the annealing solvent solubility and vapor pressure, with lower vapor pressure generally indicating a higher boiling point. Further improvement of the P3HT:PC<sub>61</sub>BM BHJ polymer solar cells from this solvent annealing may be achieved under optimal process conditions.[201, 202, 209] However, despite inherent limitations, such as the limited number of optimal solvent options and the lack of a fundamental theory for deeper understanding, the thermal annealing is still the most popular post casting process to enhance the performance of P3HT:PC<sub>61</sub>BM BHJ polymer solar cells.

## 1.8. Key Factors for Best Bulk Heterojunction (BHJ) Polymer Solar Cells

As a summary, several factors are necessary in order for P3HT: PC<sub>61</sub>BM BHJ polymer solar cells to have a good PCE. First, the photon absorption of BHJ polymer solar cells is determined mainly by the band gap of p-type conjugated polymer, and is largely dependent on the 3-D overlap of  $\pi$ - $\pi$  orbitals. This  $\pi$ - $\pi$  orbital overlap can be enhanced by the high order of crystallinity of P3HT and has a close relationship with the regioregularity of P3HT.[210, 211] Regiorandom P3HT has a low degree of crystallinity due to the distorted conformation of a P3HT chain, which results in the loss of the rigid rod shape that can crystallize easily. The head-tail connection of a 3 hexylthiophene ring should be maintained throughout the P3HT chain to attain a high level of regioregularity in P3HT, as shown in Figure 1.14 (b). Most commercially available P3HT has more than 90% regioregularity and the strong (100) peak can be monitored easily from the XRD, as shown in Figure 1.14 (a).[210, 211]

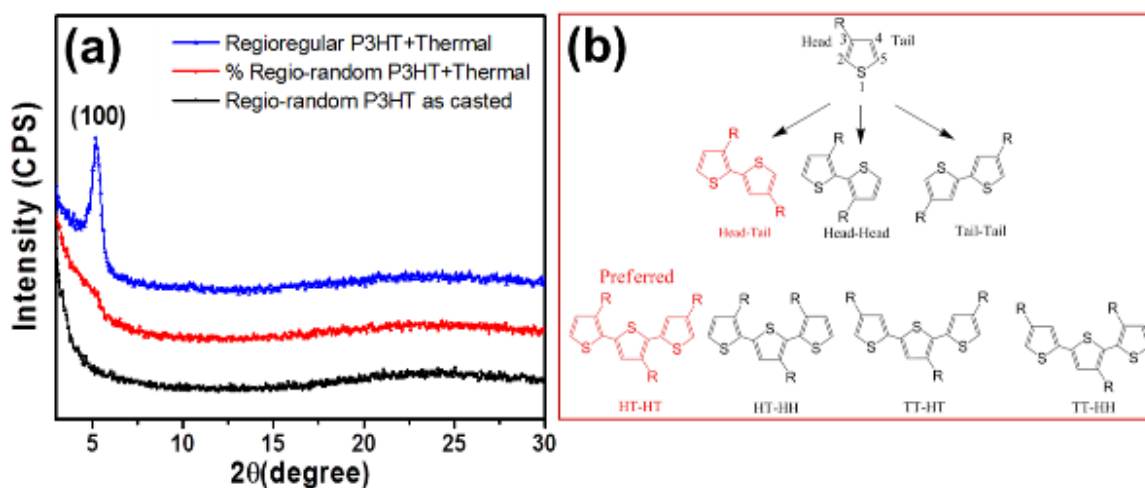


**Figure 1.14. (a) XRD of regiorandom and regioregular P3HT, and (b) chemical structures of regioregularly controlled different P3HT ( Figure (b) is modified based on a Figure in Reference [2]).**

Second, the interfacial area between the P3HT and PC<sub>61</sub>BM BHJ constituents should be large enough to have good charge separation efficiency.[96, 170] A large interfacial area can be achieved by effective phase separation and crystallization during spin coating and subsequent post processes.[129, 130, 173, 185, 186, 194, 202, 206, 207, 209, 210, 212, 213] Thermal annealing significantly enhances the degree of crystallinity. Therefore, the most appropriate co-solvent for both P3HT and PC<sub>61</sub>BM should be a spin casting solvent, such as

ODCB or CB, in order to achieve optimal domain size (phase separation) during the spin coating process.[119, 203] As mentioned before, increased crystallinity of P3HT is achieved mainly during the thermal annealing at the optimal temperature, which is above the  $T_g$  of P3HT. The exciton diffusion length is around 10 nm[72, 104, 156, 157, 161, 163], and to attain effective charge separation and transport to the electrodes, the morphology should be well controlled to produce the best P3HT:PC<sub>61</sub>BM BHJ polymer solar cells.[96] Poorly controlled morphology, even with a highly controlled degree of crystallinity, increases the series resistance and results in a lower FF in the final P3HT:PC<sub>61</sub>BM BHJ polymer solar cells.

Third, an effective active layer thickness[160] and charge blocking layer should be selected. A thick active layer results in more photon absorption but deteriorates the charge transport with increasing series resistance due to the increased numbers of defect sites inside the BHJ active layer, such as disconnection in the charge transport path. The electron block layer (EBL) or hole transport layer (HTL), i.e., PEDOT:PSS, is a well-known water soluble metallic polymer.[214-216] It can effectively block the electron flow to an anode to prevent the recombination of an electron and hole pair and to smooth the roughness of the anode surface by covering the surface. Several metal oxides, such as CrO<sub>x</sub>[217], LiF[193] and Cs<sub>2</sub>CO<sub>3</sub>[218], etc., can serve as a hole blocking layer (HBL).

As a last factor, the cathode and anode electrodes should be selected carefully. Generally, a low work function metal, such as aluminum, is applied as a cathode, and a high work function metal oxide, such as ITO, is selected as the anode. The ITO is transparent to most of the sun spectrum except for a very short wavelength of UV light; thus, photons can effectively penetrate the ITO and reach the active layer. However, ITO is very brittle, and its resistance increases with an increase in the number of mechanical cracks.

Many efforts have been undertaken to improve these critical factors. Chief among them is the optimization of the morphology and crystallinity of a P3HT:PC<sub>61</sub>BM BHJ active layer.

## 1.9. Thesis Motivation and Objectives

In the previous several sections, some critical factors for the improvement of the performance of P3HT:PC<sub>61</sub>BM BHJ polymer solar cells have been reviewed. The most important factor is the optimization of the morphology and crystallinity of the BHJ active layer. An active layer formation during spin coating and annealing process are critical steps to have improved morphology and crystallinity in the P3HT:PC<sub>61</sub>BM BHJ polymer solar cells. Domain size of a BHJ active layer is mainly determined during spin coating process and, the crystalline phase orientation and the crystallinity are defined during the subsequent annealing. Although many efforts have been to optimization of those processes, there are still several issues such as increase of domain size during thermal annealing and the difficulty in the preferred crystalline phase orientation.

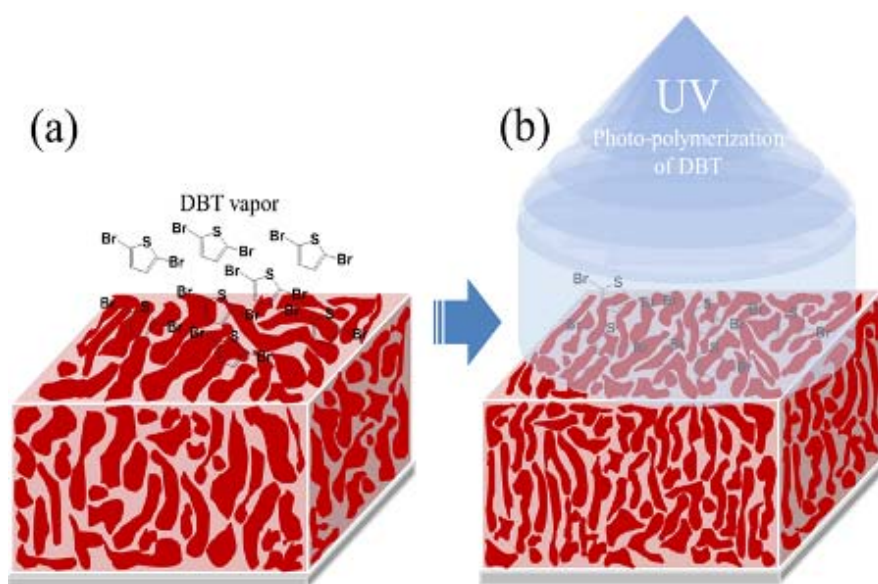


**Figure 1.15.** *In situ* UV photo-polymerization-induced phase separation for nano-scale morphology control of P3HT:PC<sub>61</sub>BM BHJ polymer solar cells: (a) DBT vapor deposition on an as-cast P3HT: PC<sub>61</sub>BM BHJ active layer, (b) *in situ* UV photo-polymerization of DBT for nano-scale morphology control.

Therefore, the motivation for this work to develop a new post process, *in situ* UV-photo-polymerization of 2,5-dibromothiophene (DBT) to have a better control for morphology and crystalline phase orientation. A schematic diagram for the new process is shown in Figure 1.15. This new process is based on polymerization induced phase separation (PIPS) of a

reactive DBT monomer inside a P3HT:PC<sub>61</sub>BM BHJ active layer. DBT has good solubility with P3HT and PC<sub>61</sub>BM and it can diffuse well into the BHJ active layer during the DBT deposition process as a pre-step for the *in situ* UV photo-polymerization of DBT. In the course of UV photo-polymerization, the miscibility of the polymerized oligothiophene inside of the BHJ active layer can rapidly decrease with increase of molecular weight of the polymerized oligothiophene. This miscibility decrease can result in the further phase separation and the formation of the smaller domain than that formed during spin casting process. Due to the similarity in chemical structure between P3HT and DBT, the interdigitated polymerized oligothiophene into P3HT crystalline phase can enhance the photon absorption. In addition, this new post process can hinder the big PC<sub>61</sub>BM formation domain during the thermal annealing because polymerized oligothiophene works as an impurity inside PC<sub>61</sub>BM. It can only maximize the degree of crystallinity of P3HT but also minimize the distortion of P3HT crystalline orientation due to the growth of PC<sub>61</sub>BM crystals during the thermal annealing.

In this thesis, a promising annealing process based on photo-polymerization of DBT, a reactive thiophene based monomer, is newly demonstrated to control the morphology, crystallinity and crystalline orientation. The critical phenomena, such as changes in domain size, crystallinity and crystalline phase orientation in a P3HT:PC<sub>61</sub>BM BHJ active layer during the photo-polymerization of DBT are monitored and analyzed using several analytical techniques, AFM, R-SoXS and GIWAXS and so on.

## **1.10. Thesis Organization**

Chapter 1 serves as background and includes a general introduction to solar cell technology that is focused especially on organic material-based devices, and includes development history, material properties, working principles, various solar cell structures, and so on. Chapter 1 also describes key parameters, such as the degree of crystallinity, crystalline phase orientation and morphological effects. In Chapter 2, the experimental procedures used in this research are summarized and explained. In Chapter 3, conventional post processes, including thermal and solvent annealing, are examined. The fundamental properties of the crystalline phase and morphology obtained from those conventional processes are characterized using

several scientific techniques, such as Grazing incident x-ray scattering (GIWAXS), resonant soft x-ray scattering (R-SoXS)[219-222] and an atomic force microscope (AFM). Discussion of these conventional processes provides a foundation for comparison with the newly proposed post process presented in Chapters 4 and 5. As a pre-step to in situ UV photo-polymerization of DBT, a newly proposed post process, i.e., the DBT vapor annealing effect on the crystalline phase and morphological changes in a P3HT:PC<sub>61</sub>BM BHJ active layer, are investigated in depth. Furthermore, the 3-D Hansen solubility parameters of solutes and various solvents are calculated to provide a deeper understanding of the solubility of the fundamental materials by using official Hansen solubility parameter calculation software, HSPiP. In Chapter 4, analysis of the main outputs of the new post process for improved performance of the P3HT:PC<sub>61</sub>BM BHJ polymer solar cells is undertaken using X-ray techniques, such as GIWAXS, R-SoXS and the AFM. Additionally, the solubility change-driven morphology evolution is explained using the Hansen solubility parameter calculation. In Chapter 5, the solar cell device performance as a result of the optimized fabrication process conditions of the new process is reported. General J-V curve analyses are performed, and charge carrier mobility is characterized by using specially designed contacts. Chapter 6 draws relevant conclusions, discusses the lessons learned, and suggests directions for further research. Chapter 7 includes bibliography and Chapter 8, as an Appendix section, includes the chemical reaction verifications of the UV photo-polymerization of DBT and some fundamental equation derivations for solar cells.

## 2. EXPERIMENTAL

### 2.1. Materials

ACS grade 2,5-dibromothiophene (DBT), 2,5-diiodothiophene (DIT), Poly(3-hexylthiophene) (P3HT), Br-terminated polythiophene,  $\alpha,\omega$ -dihexylthiophene and solvents, such as chlorobenzene (CB), dichlorobenzene (DCB), acetone, chloroform, methanol (MeOH), and tetrahydrofuran (THF), were purchased from the Sigma Aldrich Chemical Company or from Fisher Scientific and were used without further purification, unless otherwise noted. Reagents, ferric trichloride ( $\text{FeCl}_3$ ) and ferric tribromide ( $\text{FeBr}_3$ ), used in the syntheses for  $\alpha,\omega$ -dibromo-oligothiophene and aluminum (Al) targets for metal electrode thermal evaporation, also were purchased from the Sigma Aldrich Chemical Company and used without further purification. [6,6]-phenyl-C<sub>61</sub>-butyric acid methyl ester (PC<sub>61</sub>BM) was purchased from Nano-C, and Poly(3,4-ethylenedioxythiophene) poly(styrenesulfonate) PEDOT:PSS, a water soluble-conducting polymer solution, was purchased from H.C. Starck, Inc. and was used with a diluted solution in D.I. water at a 1:1 ratio. Indium tin oxide (ITO)-coated transparent glass substrates were provided free of charge from ShinAn SNP in Korea.

### 2.2. Chemical Synthesis of Oligothiophenes

#### 2.2.1. Ultraviolet Photo-Polymerization of 2,5-Dibromothiophene (DBT)

A ultraviolet (UV) exposure set-up was purchased from the Newport Company and attached to an argon (Ar) gas environmental glove box using a special aluminum connector, as shown in Figure 2.1. The UV photo-polymerization of DBT was carried out inside the glove box. The UV setup has a 200 W mercury lamp and collimate lens. A mid-UV band path filter that has selective transmittance to the mid-UV band (shown in Figure 2.2) was also purchased from Newport for the UV photo-polymerization of DBT. The uniformity of the UV light intensity from the UV exposure set-up was controlled by an AOI UV power meter with a 365 nm photodiode prior to UV light exposure on the samples. An aluminum container with a wide opening was used for bulk UV photo-polymerization on top of a 40°C pre-heated hot-

plate. UVvis and FT-IR analyses of insoluble  $\alpha,\omega$ -dibromo-oligothiophene from the reaction were carried out after precipitation in n-hexane without further purification. The UV photo-polymerization of DBT vapor, which was deposited on P3HT:PC<sub>61</sub>BM BHJ thin films, was performed on a 40°C pre-heated hot-plate. The covalent bond dissociation energy for the UV photo-polymerization of DBT was calculated based on the fundamental carbon-halide bond-breaking energy, as shown in Figure 2.3. A schematic reaction diagram of the UV photo-polymerization of DBT is shown in Figure 2.4.

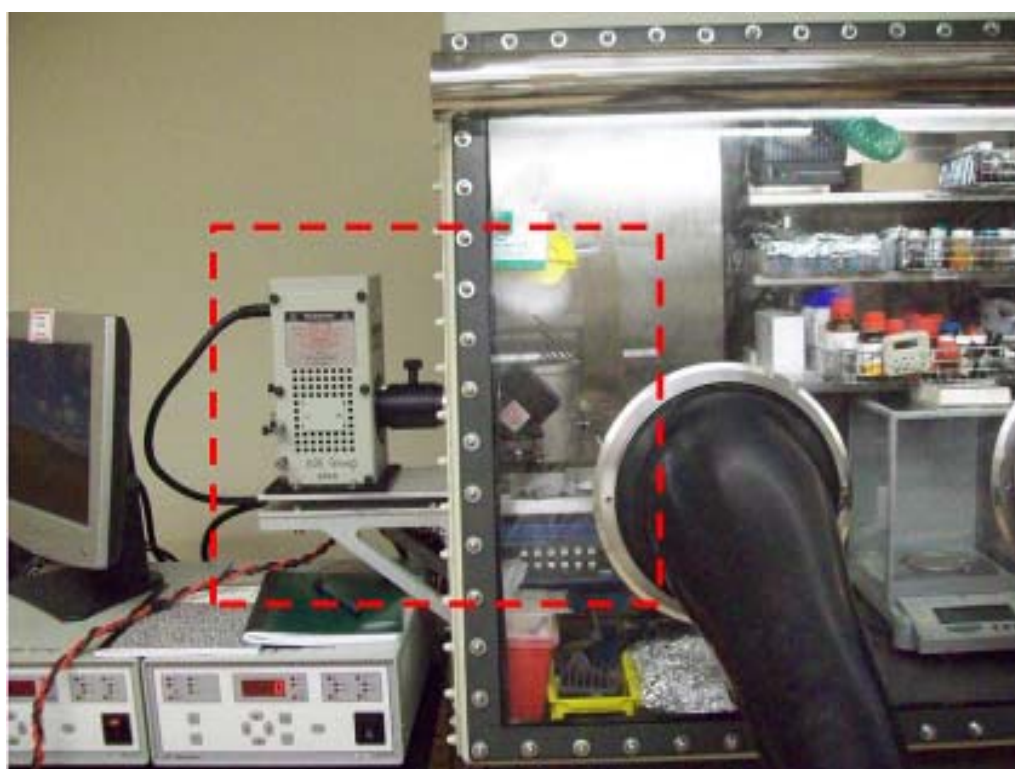


**Figure 2.1.** UV exposure set-up inside an Ar gas environmental glove box.

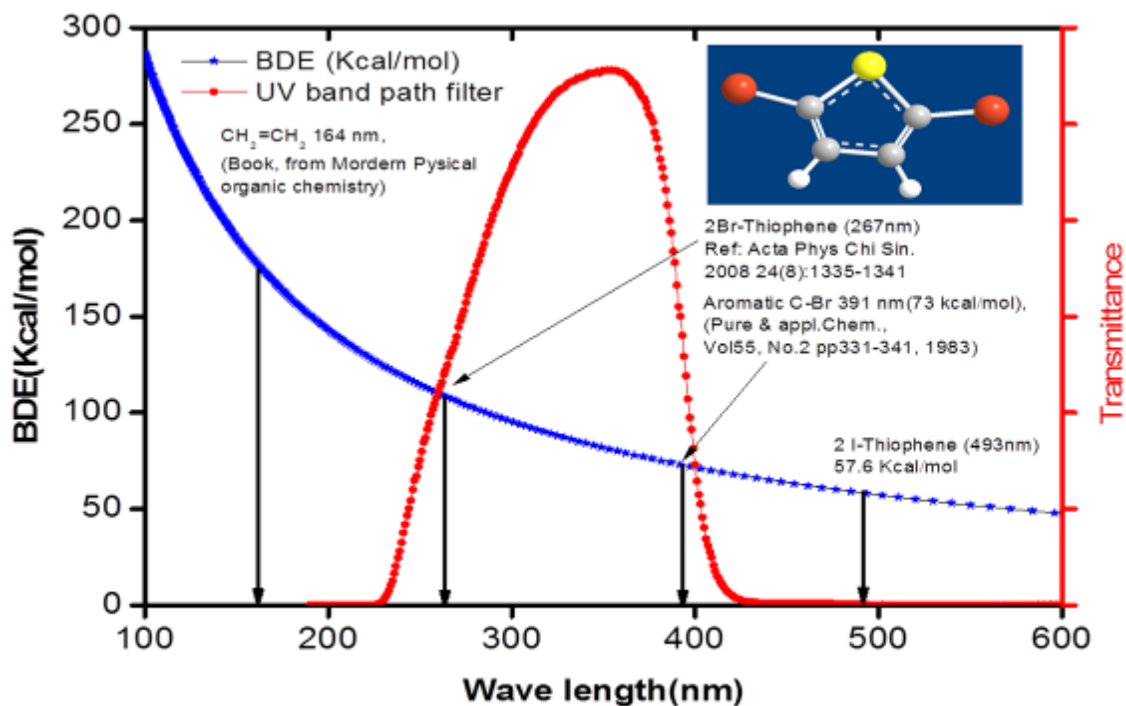


Figure 2.2. Mid-UV band pass filter for UV photo-polymerization of DBT.

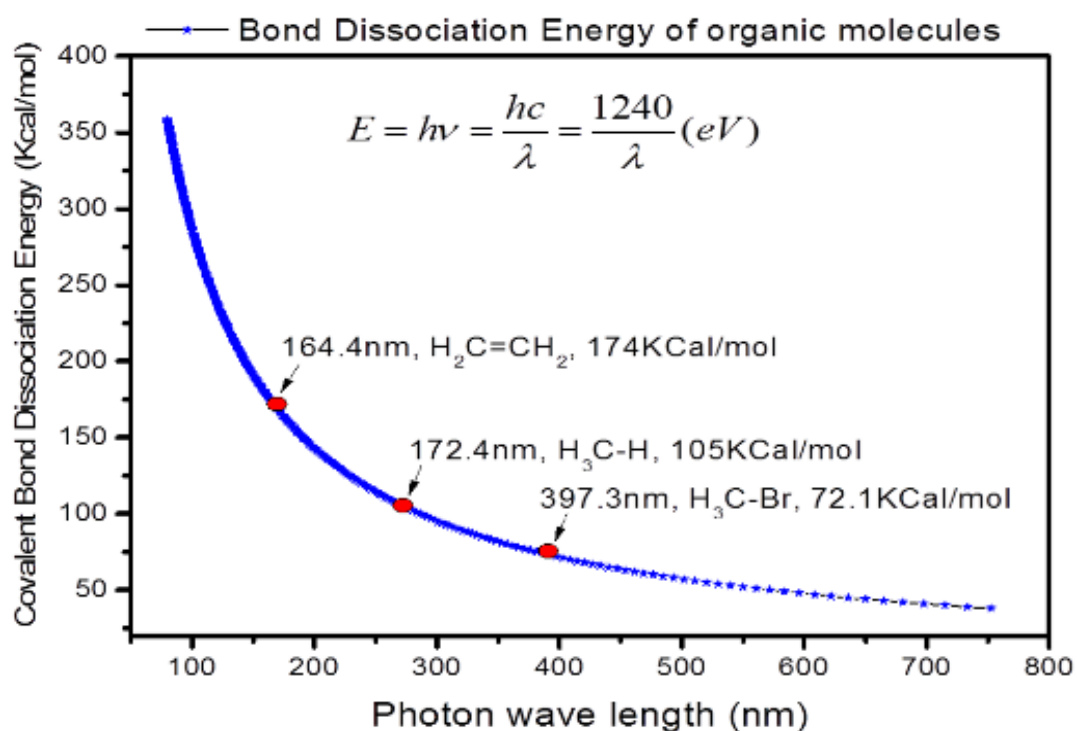
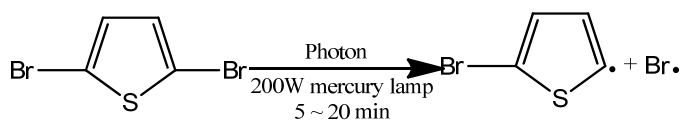
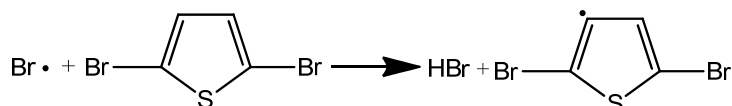
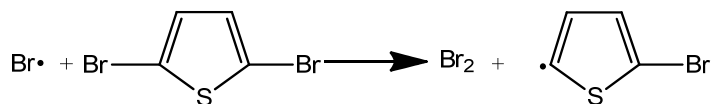
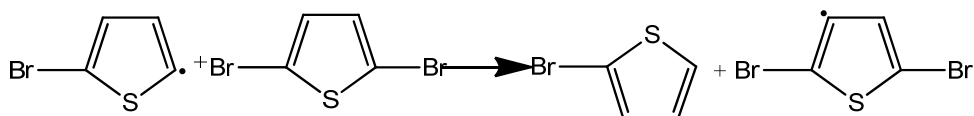
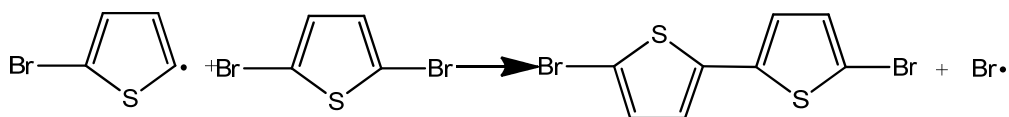


Figure 2.3. Covalent bond dissociation energy that can initiate a radical-based UV photo-polymerization reaction.

1. Photodissociation



2. Reactions of photodissociation fragments with surrounding monomers



3. Reactions between radicals

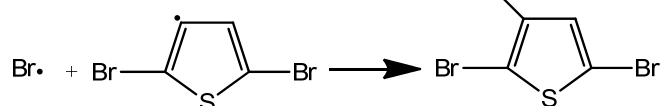
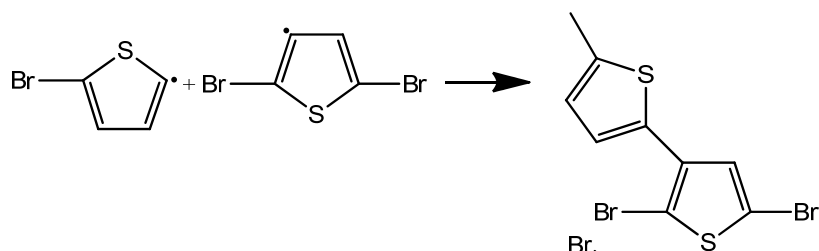
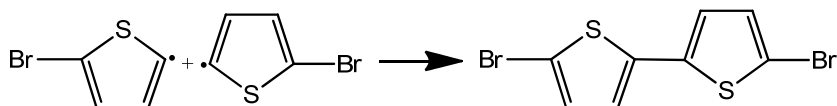
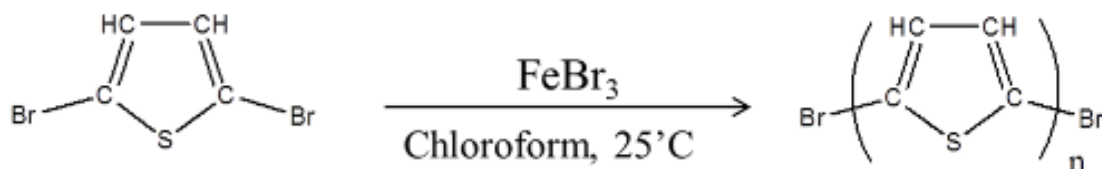


**Figure 2.4. Schematic reaction diagram of UV photo-polymerization of DBT (modified based on the UV photo-polymerization reaction scheme of 2,5-diiodothiophene (DIT), from the publications of the S. H. Kim group in PSU).[223-226]**

### 2.2.2. Catalytical Synthesis of $\alpha,\omega$ -Dibromo-Oligothiophene using Ferric Tribromide ( $\text{FeBr}_3$ ).

0.1 mol (24.1 g) of DBT or 0.1 mol (8.4 g) of thiophene in 100 ml of chloroform was dropped slowly into a reactor containing 35 mg (0.22 mol) of ferric tribromide ( $\text{FeBr}_3$ ) in 400 ml of chloroform, as shown in Figure 2.5. The reaction took place inside a  $\text{N}_2$  glove box for 10 hours, and the chloroform in the reaction was distilled in advance, using  $\text{CaH}_2$  to remove the moisture. After the reaction was complete, polythiophene was precipitated in methanol (MeOH) and dried in a vacuum oven at  $70^\circ\text{C}$  for 24 hours. Further purifications were carried out to extract soluble Br-terminated oligothiophene using a soxhlet set-up in several organic solvents, n-hexane, acetone, THF and chloroform, in sequence. The extracted soluble  $\alpha,\omega$ -dibromo-oligothiophene was precipitated in methanol again and dried in a vacuum oven at  $70^\circ\text{C}$  for 24 hours. UVvis, FT-IR, XPS, MALDI-FOT MS and photo-fluorescent analyses were carried out for chemical structure verification. DSC and TGA experiments were performed for a better understanding of the thermal properties.

#### Reaction 1.



#### Reaction 2.

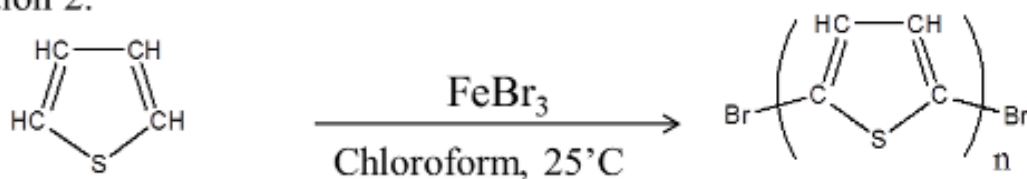


Figure 2.5. Schematic reaction diagrams of catalytically synthesized Br-terminated  $\alpha,\omega$ -dibromo-oligothiophenes.

## 2.3. Solar Cell Fabrication and Device Performance Characterization

### 2.3.1. Fabrication of the P3HT:PC<sub>61</sub>BM BHJ Polymer Solar Cells

For the fabrication of the conventional P3HT:PC<sub>61</sub>BM BHJ polymer solar cells, ITO-coated glass substrates were cleansed in an ultrasonic cleaning bath by dipping them sequentially in acetone, isopropanol and D.I. water for 30 minutes per step. As a last cleaning step, UV-ozone treatment was applied for 30 minutes before spin casting PEDOT:PSS onto them. Half of the surface area of each ITO substrate was etched out using a diluted HCl:H<sub>2</sub>NO<sub>3</sub> (1:1 volume percentage) mixed etchant to define the solar cell working area and to prevent an electrical shorts during current density-voltage (J-V) characterization. PEDOT:PSS (Baytron P) was diluted in D.I water at a 1:1 weight percentage ratio, and the diluted solution was stirred for one day prior to spin casting. The diluted PEDOT:PSS solution was filtered using a 0.4 μm pore size Teflon syringe filter prior to spin casting. Spin casting was carried out in air with a spin speed of 2000~2500 rpm for one minute. The average thickness measured by an ellipsometer was around 40-45 nm. The PEDOT:PSS spun-cast ITO substrates were baked on a 120°C pre-heated hot-plate for 30 minutes in an open-air environment. The baked substrates were transferred to a N<sub>2</sub> glove box, and the P3HT:PC<sub>61</sub>BM active layer was spun-cast on them at a spin speed of 800 rpm for one minute. The average thickness was around 100 nm, as measured by an ellipsometer. An active layer solution was prepared before spin casting at a ratio of P3HT (0.04g):PC<sub>61</sub>BM (0.04g) (1:1 wt%) in 4 ml chlorobenzene and was stirred at room temperature for a minimum of 24 hours. The active layers were spun-cast on the surface of the PEDOT:PSS pre-coated ITO substrates, and those substrates were transferred to a high vacuum chamber. A 100 nm thickness of the aluminum metal layer was thermally evaporated as a cathode under 10<sup>-6</sup> Torr (1 Torr = 1.333 x 10<sup>2</sup> Pa) high vacuum condition. A high vacuum metal thermal evaporator system (Cressington) was used inside N<sub>2</sub> glove box. As a last step, the thermal annealing of the devices was carried out on a 150°C pre-set hot-plate for 20 minutes inside the N<sub>2</sub> glove box.

For the fabrication of P3HT:PC<sub>61</sub>BM BHJ polymer solar cells from the new process, UV photo-polymerization of DBT in the P3HT:PC<sub>61</sub>BM BHJ active films, DBT vapor was exposed to the active layer spun-cast substrates at 80°C for several minutes, and instantly

they were exposed to UV light in an Ar gas environment prior to the last aluminum metal electrode evaporation step. Except DBT deposition and UV exposure steps, other processes were carried out in the same conditions of the conventional devices. All the fabricated solar cells were sealed using a transparent cover glass and UV curable epoxy-acrylate adhesive inside of the N<sub>2</sub> glove box to prevent photo-degradation during the J-V testing in air. The UV adhesive layer used for sealing the device was cured under 3-minute UV exposure using a 365 nm TLC UV lamp.

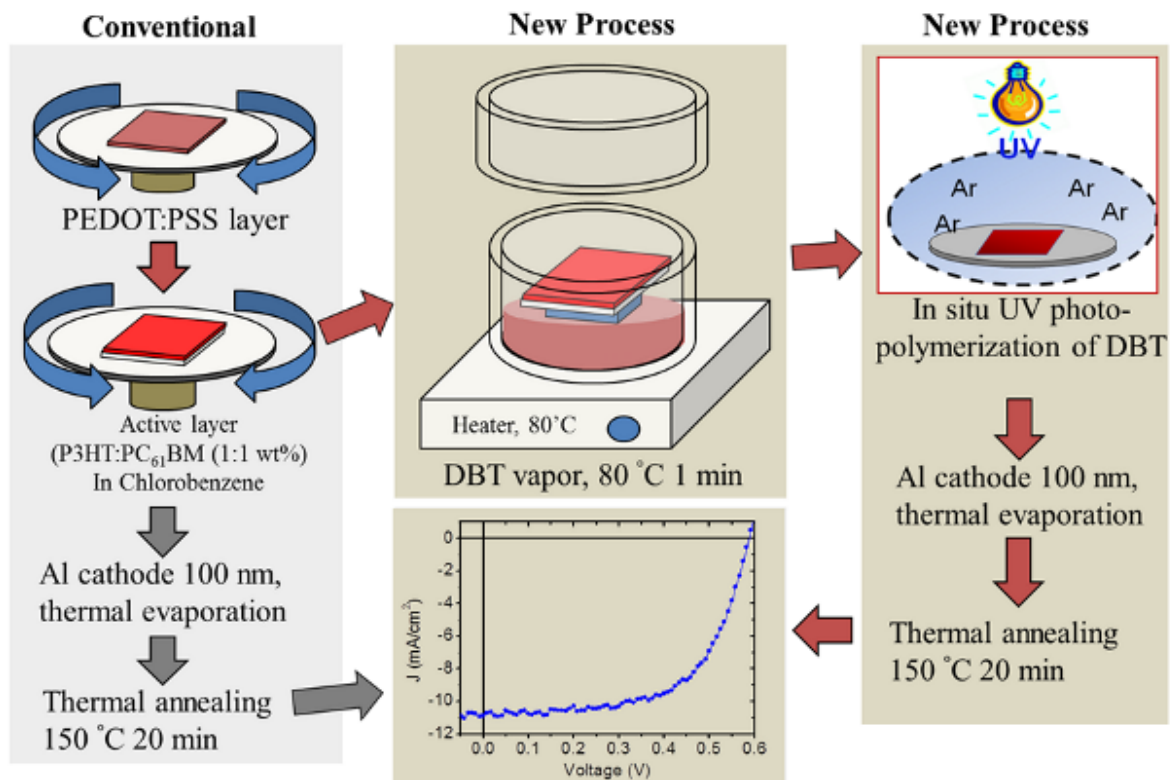


**Figure 2.6. Schematic diagram of new process for the fabrication of P3HT:PC<sub>61</sub>BM BHJ polymer solar cells.**

### 2.3.2. Current Density-Voltage (J-V) Curve Characterization of P3HT:PC<sub>61</sub>BM BHJ Polymer Solar Cells

A 150 W solar simulator was purchased from Newport and includes a 100 mW/cm<sup>2</sup> Xenon (Xe) lamp and collimate lens. An AM 1.5 G glass filter from Newport was installed in front

of simulated sunlight. The light spectrum was calibrated by a NREL-certified Si-photodiode (Hamamatsu, S1133) prior to testing the P3HT:PC<sub>61</sub>BM BHJ polymer solar cells. Characterization of the J-V curves of the solar cells was performed using a Keithley 2400 source meter with four wire connections to minimize the internal resistance from the Keithley source meter. Each solar cell was tested a minimum of six times under dark and light conditions. The active area of the solar cells was 0.095 cm<sup>2</sup>. JV data analysis was performed using Wolfram Mathematica Version 7.

### **2.3.3. Charge Carrier Mobility Characterization of P3HT:PC<sub>61</sub>BM BHJ**

#### **Polymer Solar Cells**

ITO-coated glass substrates were cleansed in an ultrasonic cleaning bath by dipping them sequentially in acetone, isopropanol and D.I. water for 30 minutes per step. As a last cleaning step, UV-ozone treatment was applied for 30 minutes. For the fabrication of hole-only solar cells, and to analyze the hole mobility in the P3HT:PC<sub>61</sub>BM BHJ polymer solar cells, the PEDOT:PSS layer was spun-cast on the ITO substrates. The thickness was around 40 nm. The substrates were baked on a 120°C pre-heated hot-plate for 30 minutes. The P3HT:PC<sub>61</sub>BM active layer was spun-cast on the PEDOT:PSS pre-coated ITO substrates. The DBT deposition and UV exposure for the DBT photo-polymerization were carried out under various conditions, and the active layer thickness was 100 nm. Thickness of active layer was measured by an ellipsometer. A 10 nm MoO<sub>3</sub> electron blocking layer and a 100 nm aluminum metal electrode were evaporated sequentially under the high vacuum condition. The final thermal annealing was carried out on the pre-heated hot-plate (150°C) for 20 minutes inside the N<sub>2</sub> glove box. The devices were sealed with UV curable epoxy-acrylate adhesive and a cover glass under three minutes of UV light exposure using a 365 nm TLC lamp. For the electron-only solar cell fabrication, a 10 nm Cs<sub>2</sub>CO<sub>3</sub> hole blocking layer was thermally evaporated on top of the pre-cleaned ITO substrates under the high vacuum condition instead of spin casting the PEDOT:PSS layer. Following the P3HT:PC<sub>61</sub>BM BHJ active layer spin casting step, DBT UV photo-polymerization, thermal evaporation of the aluminum cathode, post thermal annealing, and sealing of the solar cells were carried out

under the same conditions as were used for the hole-only device fabrication. However, in this case, there was no thermal evaporation step for the MoO<sub>3</sub> electron blocking layer. Dark current density measurements for the charge carrier mobility analyses were taken under the standard JV test condition, as described in Section 2.3.2 regarding characterization of the JV curves. The charge carrier mobility was calculated using Equation 2-1 in the region of space charge limited current (SCLC) in the log-log scale of dark current JV curves.[227-229]

$$J = \frac{8}{9} \epsilon_0 \epsilon_r \mu \frac{V^2}{L^3} \quad (2-1)$$

where  $\mu$  is the charge carrier mobility;  $\epsilon_0$  is the permittivity of free space;  $\epsilon_r$  is the relative permittivity of materials (3 for P3HT and 3.9 for PC<sub>61</sub>BM); L is the thickness of the active layer; and V is the applied voltage.

## 2.4. Physical and Chemical Structural Analysis

### 2.4.1. X-Ray Diffraction (XRD)

For the studies of the crystallinity and crystalline orientation of P3HT only and P3HT:PC<sub>61</sub>BM BHJ active layers, Wide-Angle X-Ray Diffraction (WAXD) measurements were acquired on an X'Pert PRO X-ray diffractometer using a Ni-filtered Cu K $\alpha$  radiation source ( $\lambda = 1.5405 \text{ \AA}$ ) at the Shared Materials Instrumentation Facility (SMIF) at Duke University (Durham, NC). The voltage and current were 30 kV and 20 mA, respectively. X-ray intensities were measured every 0.1° from  $2\theta = 3$  to 40° at a scanning rate of  $2\theta = 3^\circ$  per minute. Samples for the XRD analysis were prepared by spin casting of a P3HT: PC<sub>61</sub>BM BHJ or P3HT only solutions (dissolved in CB) on pre-cleaned Si or glass substrates. The strong diffraction peak that indicates the d-spacing of P3HT 'edge on' crystalline orientation generally showed up at 5° in all P3HT:PC<sub>61</sub>BM BHJ or P3HT only films.

The inter-planar distance of crystalline lattice was calculated using a Bragg equation as shown in Equation (2-2).

$$n\lambda = 2d \sin \theta \quad (2-2)$$

Here, n is an integer,  $\lambda$  is the wavelength of incident, d is the spacing between the planes in the atomic lattice (inter-planar distance), and  $\theta$  is the scattering angle between the incident

X-ray and the scattering planes.

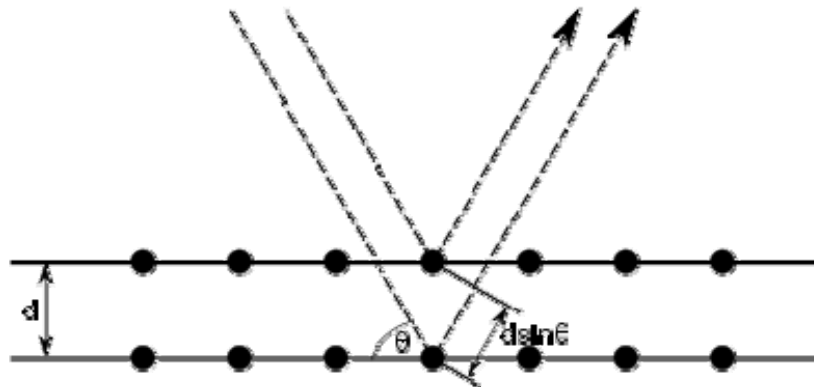


**Figure 2.7. Schematic diagram of Bragg diffraction in the XRD experiment (Figure is reproduced from[230]).**

Bragg diffraction occurs when electromagnetic radiation or subatomic particle waves with wavelength comparable to atomic spacing are incident upon a crystalline sample, scattered in a specular fashion by the atoms in the system, and undergo constructive interference in accordance to Bragg's law.

For a crystalline solid, the waves are scattered from lattice planes separated by the interplanar distance  $d$ . Where the scattered waves interfere constructively, the path difference between two waves undergoing constructive interference is given  $2d\sin\theta$  as shown in Figure 2.7. This explains Bragg's law that describes the condition for constructive interference from the successive crystallographic plane  $(h,k,l)$  of the crystalline lattice. Strong intensities of peaks are acquired in the diffraction pattern when scattered waves satisfy the Bragg condition.

#### **2.4.2. Grazing Incident Wide Angle X-Ray Scattering (GIWAXS).**

Grazing Incident Wide Angle X-Ray Scattering (GIWAXS) measurements were acquired at beam line 7.3.3 in the Advanced Light Source (ALS) at the Lawrence Berkeley National Laboratory (LBNL) (experiments were performed by Eliot Gann), and at beam line X22B of the National Synchrotron Light Source (NSLS), Brookhaven National Laboratory (BNL) (experiments were performed by Dr. Xinhui Lu). The photon energies were 10 keV ( $\lambda = 1.2389 \text{ \AA}$ ) and 8 keV ( $\lambda = 0.873 \text{ \AA}$ ), respectively. An ADSC Quantum 4u CCD detector was equipped at beam line 7.3.3, ALS, and a CCD detector was also used at beam line X22B,

NSLS. Thin films for the GIWAXS analysis were prepared by spin casting solutions on Si wafer substrates. Data analysis was performed using Nika package (freeware software, downloaded from Argonne National Lab Web site) based on Igor Pro Version 6. A simple schematic GIWAXS experimental set-up is shown in Figure 2.8.

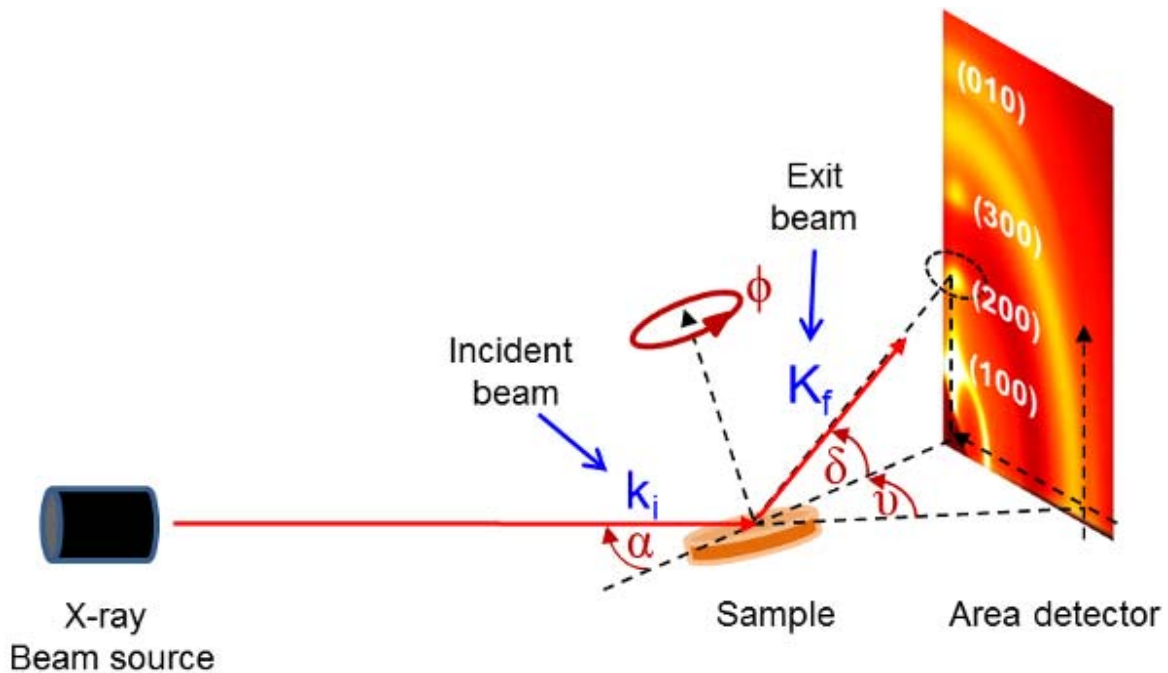


**Figure 2.8. Schematic diagram of GIWAXS experimental set-up ( $\alpha$  is incident angle,  $\delta$  is exit angle,  $\nu$  is the in-plane scattering angle,  $\phi$  is sample rotation angle,  $k_i$  is incident beam and  $k_f$  is the exit beam).**

Wide Angle X-Ray Scattering (WAXS) has a close relation with power diffraction using the conventional XRD. WAXS is generally used in connection with diffuse scatters with only short range order. WAXS regime with scattering angles is larger than  $5^\circ$ , the usual small angles approximation. When the incident angle is large enough, surface scattering features can be ignored for the most part. Some dynamic effects remain when the exit angle approaches the critical angle of the sample studied. In case of GIWAXS, it is more surface effective technique than the conventional WAXS or XRD. The surficial and bulk properties can be separately analyzed changing incident angle and less than critical angle it shows the surficial properties and at the critical angle the bulk property can be studied. In this thesis, the measured critical angle was around  $0.1^\circ$ .

### 2.4.3. Resonant Soft X-Ray Scattering (R-SoXS).

Resonant soft X-ray scattering (R-SoXS) measurements were acquired at beam line 11.0.1.2 of ALS, LBNL. The photon energy was less than 2 keV, and a CCD detector was installed. The size of X-ray beam on the sample was 100 x 100  $\mu\text{m}$ . Free-standing films for the R-SoXS experiments were prepared by spin-casting solutions on top of the water soluble PSS pre-coated glass slides and instantly dipping them into D.I. water. Films floating on the D.I. water surface were picked up using an aluminum frame. This aluminum frame was made by punching a 3 mm diameter hole in the center of thick one-sided sticky aluminum tape. Data analysis was performed using Nika package (free ware software, downloaded from Argonne National Lab Web site) based on Igor Pro Version 6. A simple schematic R-SoXS experimental set-up is shown in Figure 2.9.

Properties of organic materials such as polymers are largely determined by their nano-scale morphologies. Conventional x-ray scatterings, such as Wide Angle X-Ray Scattering (WAXS) and Small Angle X-Ray Scattering (SAXS), are well-established and they have been widely used for the characterization of organic material structures. However, the relatively low scattering cross section and poor contrast of organic materials in the hard x-ray regime allow transmission measurements of thick bulk organic samples only in millimeters scale.

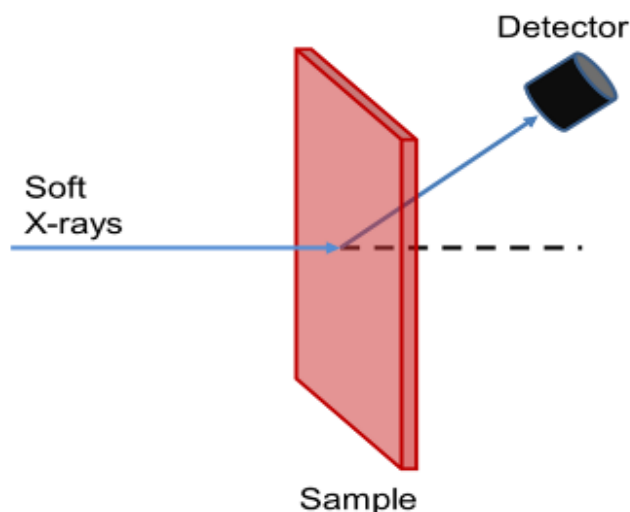


**Figure 2.9. Schematic diagram of R-SoXS experimental set-up.**

In case of soft x-rays, it can effectively characterize organic thin films in nanometer scale by using of photon energies close to core absorption edges of the constituent atoms. Due to the high sensitivity of R-SoXS to specific chemical bonds, the scattering intensity between organic materials gets enhanced with small spectral difference and therefore, the structural information of tested materials can be effectively acquired.

#### **2.4.4. Fourier Transform Infrared Spectroscopy (FT-IR).**

Fourier transform infrared spectroscopy (FT-IR) was performed using a JASCO 610 Fourier transform infrared spectrophotometer in transmittance mode. Powder samples were ground with potassium bromide (KBr) and uniaxially pressed into pellets. Film samples were spun-cast on a double-sided polished Si wafer. The FT-IR chamber was purged with dry air to eliminate water vapor. The spectra were collected over a range of 4000 to 400  $\text{cm}^{-1}$ , with a resolution of 2  $\text{cm}^{-1}$  obtained after 64 scans.

#### **2.4.5. UVvis Spectrophotometer (UVvis).**

UVvis spectrophotometer measurements for absorption spectra analyses were acquired using a Varian Cary 50. The spectra were collected over a range of 300 to 800 nm. Thin films and solution samples were tested as spun-cast films on glass substrates and as diluted solutions in quartz cubes, respectively. The thermochromic effects of P3HT and  $\alpha,\omega$ -dibromo-oligothiophenes were studied using an attached Peltier temperature controller. The UV photo-polymerization of DBT was performed on 10 mL of liquid phase DBT in an aluminum metal can under 200 W strong UV light with a mid-UV band pass filter. A 0.01 mL sample was taken every five minutes using a micropipette, and was diluted in a 2 mL THF vial for the UVvis spectrophotometer analysis. Its  $\lambda_{\text{max}}$  was shown at 500 nm, and the DBT absorption  $\lambda_{\text{max}}$  was 200 nm. The insoluble high molecular weight (HMW) polythiophene was precipitated in methanol.

## **2.4.6. Matrix-Assisted Laser Desorption Ionization-Time of Flight Mass**

### **Spectroscopy (MALDI-TOF MS)**

Matrix-assisted laser desorption ionization-time of flight mass spectroscopy (MALDI TOF MS), used for absolute molecular weight analysis, was performed using a Bruker Ominiflex MALDI-TOF MS with 2,5-Dihydroxybenzoic acid (DHB) as a matrix. Synthesized  $\alpha,\omega$ -dibromo-oligothiophenes were dissolved in HPLC grade tetrahydrofuran (THF) with DHB, and then they were dropped onto a sample stage for absolute molecular weight analysis. A calibration standard sample was tested together for comparison.

### **2.4.7. X-Ray Photoelectron Spectroscopy (XPS).**

X-ray photoelectron spectroscopy (XPS) was performed using a Kratos Analytical Axis Ultra XPS under less than  $3 \times 10^{-8}$  Torr UHV at the SMIF at Duke University. A survey scan was performed in advance of the experiments, and a high resolution scan was performed secondly. Data processing was carried out using Casa XPS software. Thin  $\alpha,\omega$ -dibromo-oligothiophene films for the XPS analysis were prepared by spin casting solutions (5wt% in 4 ml THF) on pre-cleaned Si wafer substrates at 800 rpm for one minute. The thickness of the samples was around 100 nm, which was measured by an ellipsometer. The Si wafer substrates were cleaned using an ultrasonic cleaning bath and dipping them in acetone, isopropanol and D.I. water for 30 minutes per step, and as a last cleaning step, a UV-ozone treatment was applied for 30 minutes.

### **2.4.8 Photo Fluorescent Experiment.**

Fluorescent studies of two different synthesized  $\alpha,\omega$ -dibromo-oligothiophenes and commercial polythiophene derivatives, P3HT and dihexylsexithiophene, were undertaken using a simple TLC lamp. The wave length of the excitation light was 365 nm, and chlorobenzene (CB) and tetrahydrofuran (THF) were used as solvents. Depending on the conjugated length (molecular weight), different colors of fluorescence were monitored. Photographs of the fluorescence of the different materials were taken using a Canon digital camera in a dark room.

## **2.5. Thermal Property Analysis**

### **2.5.1. Thermal Gravimetric Analysis (TGA)**

Sample degradation temperatures and thermal stability were examined using a TA Instruments Q5000 thermal gravimetric analyzer (TGA). The examined temperature range was from 25°C to 600°C at a ramp rate of 5°C/min. Samples were heated in an atmosphere of nitrogen with sample masses of approximately 10 mg. A platinum pan and hang-down wire were used when heating the samples.

### **2.5.2. Differential Scanning Calorimeter (DSC)**

Transition temperatures for the samples were found using a TA Instruments Q1000 differential scanning calorimeter (DSC) with a liquid nitrogen cooling capacity. Calibration of the cell constant was performed using circular sapphire disks ranging in temperature from -140°C to 300°C. Temperature calibration was performed using indium metal that has a melting point of 156.61°C. The temperature accuracy after calibration is stated by the manufacturer to be 0.1°C. The calibrations were performed using standard aluminum sample pans with a heating rate of 10 °C/min under helium gas, and cooling was performed using liquid N<sub>2</sub>. The data were analyzed using TA Universal Analysis software. Thermal examination of the samples was performed while the samples were under a helium purge of 25ml/min. All heating and cooling rates were conducted at 10°C/min. The DSC traces reported in this dissertation were obtained from the second heating cycle. The sample masses for testing were on the order of 10 mg and sealed in a standard aluminum sample pan.

## **2.6. Surface Property Analysis**

### **2.6.1. Atomic Force Microscopy**

Atomic force microscope (AFM) images were collected using an Asylum MFP-3D at the Asylum Company located on NCSU's Centennial Campus. These experiments were conducted in non-contact tapping mode and scanned at 1 Hz with a resolution of 512 x 512

pixels. The scanning probes employed were Vista Probe T300R-25 non-contact mode silicon tips with a nominal resonance frequency of 300 kHz. The minimal digital z-step direction is 15 picometers. Data analyses, including two-dimensional FFT analysis, were performed using WSxM software (freeware software, downloaded from Nanotec web site).

## **2.7. Computational Simulation**

### **2.7.1. Solubility Parameters**

HSPiP Version 3.1 was purchased from Hansen-solubility.com. Hildebrand and Hansen solubility parameters of P3HT, C60, PC<sub>61</sub>BM, oligothiophenes and several commercial solvents, such as CB, DCB, toluene, thiophene, dichloromethane (DCM), chloroform and DBT, etc., were calculated using the official Hansen solubility software, HSPiP. Three-dimensional Hansen-solubility parameter spheres were plotted using Wolfram Mathematica Version 7.

### **3. UNDERSTANDING CONVENTIONAL THERMAL ANNEALING AND SOLVENT ANNEALING FOR THE ENHANCED PERFORMANCE OF P3HT:PC<sub>61</sub>BM BHJ POLYMER SOLAR CELLS**

#### **3.1. Background**

The morphology of P3HT:PC<sub>61</sub>BM BHJ active layer is affected from the processing conditions during spin coating. The incompatibility of two component materials and their interaction with a spin coating solvent result in different morphology in a P3HT:PC<sub>61</sub>BM BHJ active layer. Good spin-coating solvents, such as CB and ODCB, which have good solubility for both P3HT and PC<sub>61</sub>BM, can lead to much finer morphology than other solvents, such as toluene and xylene. The morphology evolved during spin coating is not enough to have the improved performance of BHJ polymer solar cells, due to the low degree of crystallinity. Therefore, a post annealing is required to enhance the degree of crystallinity of P3HT and to have the further phase separation between P3HT and PC<sub>61</sub>BM.

Two commonly used post processes can result in the further morphology and crystallinity change of P3HT:PC<sub>61</sub>BM BHJ polymer solar cells: 1) thermal annealing, also called thermally induced phase separation (TIPS), and 2) solvent annealing, also called solvent induced phase separation (SIPS). Thermal annealing is the most popular post casting. It applies high temperature (in a range of 120 ~ 150°C), which is above T<sub>g</sub> of P3HT for 5 ~ 30 minutes to the P3HT:PC<sub>61</sub>BM BHJ active layer to enhance the degree of crystallinity of P3HT and the phase separation between P3HT and PC<sub>61</sub>BM. Solvent annealing is another effective process to control the morphology and crystallization of a P3HT:PC<sub>61</sub>BM BHJ active layer with exposure to selective or nonselective solvents. Based on experimental results, a solvent that has good affinity with PC<sub>61</sub>BM and relatively poor interaction with P3HT leads to improved morphology during solvent annealing, which leads in an improved PCE. The morphology of a solvent annealed P3HT:PC<sub>61</sub>BM BHJ active layer strongly depends on the annealing solvent solubility and vapor pressure, with lower vapor pressure generally indicating a higher boiling point. Further improvement of the P3HT:PC<sub>61</sub>BM BHJ polymer solar cells from this solvent annealing process may be achieved under optimal process conditions. However, despite inherent limitations, such as the limited number of

optimal solvent options and the lack of a fundamental theory for deeper understanding, the thermal annealing is still the most popular post casting process to enhance the performance of P3HT:PC<sub>61</sub>BM BHJ polymer solar cells.

In this Chapter, using several advanced scientific techniques, GIWAXS, R-SoXS[219-221] and AFM as well as Hansen solubility calculation, the morphology and crystallinity changes during those annealing processes are studied.

## **3.2. Thermal Annealing for Enhanced Crystallization and Morphology**

### **Control of P3HT: PC<sub>61</sub>BM BHJ Active Layers**

#### **3.2.1. Solvent Effect on Spin Coating of BHJ Active Layers: Hansen Solubility Parameters Calculation**

Spin coating a homogeneous solution, which P3HT and PC<sub>61</sub>BM are dissolved in a good solvent such as CB, on the substrates drives the phase separation. In general, under the optimal spin coating condition, the miscibility decrease of P3HT and PC<sub>61</sub>BM is sufficient for fine phase separation around 10 nm. As discussed in the first section of this chapter, two annealing processes are commonly used to control the morphology and crystallization of P3HT: PC<sub>61</sub>BM BHJ polymer solar cells.

The molecular interactions between several good solvents and, P3HT and PC<sub>61</sub>BM are calculated using Hansen solubility parameter sphere models as shown in Figure 3.1. Good solvents such as CB and DCB, which locate inside Hansen solubility parameters spheres of P3HT and PC<sub>61</sub>BM, are closer to the centers of the spheres exhibit excellent solubility that results in a finer morphology in a BHJ active layer during spin coating process than those that are closer to the perimeter, such as toluene and xylene, or outside of the spheres.

The Flory-Huggins interaction parameters ( $\chi_{12}$ ) of CB, which are based on the interactions with P3HT and PC<sub>61</sub>BM, are calculated using Hansen-solubility parameters.[168] These calculated values are 0.24 and 0.16 based on the interactions with P3HT and PC<sub>61</sub>BM

respectively. These numbers indicate that CB is a good solvent that dissolves both P3HT and PC<sub>61</sub>BM well, thus leading to a fine phase separation during the spin coating of the BHJ thin film. All the calculated Hansen solubility parameters and Flory-Huggins interaction parameter[168] values based on the interactions between solvents and, P3HT and PC<sub>61</sub>BM are summarized in Table 3.1.

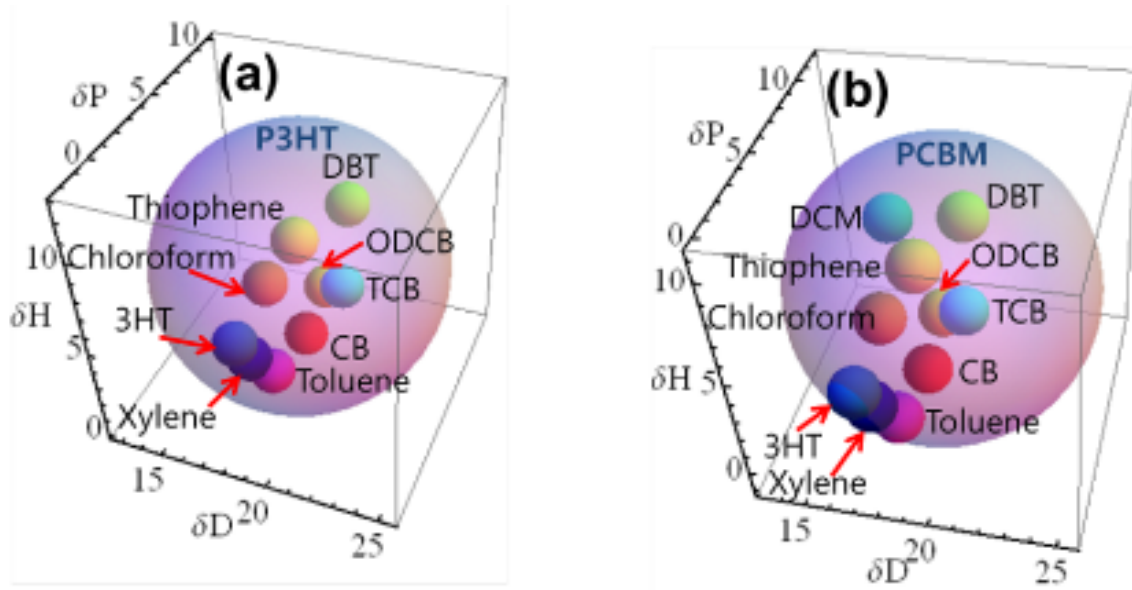


**Figure 3.1. Hansen-solubility parameters ( $\delta_D$ ,  $\delta_P$ ,  $\delta_H$ ) sphere models of (a) P3HT and (b) PC<sub>61</sub>BM in good solvents. (The Ra (interaction radius) of solvents is not shown here and different colors indicate different solvents only and no special meaning).**

Based on above solubility calculations, all the P3HT:PC<sub>61</sub>BM BHJ active layers that are prepared in this paper, are spun cast by using chlorobenzene (CB) at 800 rpm for 1minute, followed by 150 °C 20min post thermal annealing.

In general, fine morphology is created during the spin coating of a P3HT:PC<sub>61</sub>BM BHJ active layer due to the decrease of miscibility between P3HT and PC<sub>61</sub>BM with the relatively slow evaporation rate of CB. The crystallization of P3HT is enhanced via the thermal annealing for better photon absorption and improved charge transport. However, the substantial crystalline growth (micron scale) of PC<sub>61</sub>BM should be minimized during thermal annealing to allow a larger interfacial area that is required to have the better charges separation efficiency, and to have the enhanced charges transport.

**Table 3.1. P3HT/ PC<sub>61</sub>BM solubility in good solvents (calculated by Hansen solubility parameters @ 25°C).**

| <i>Solute &amp; Solvents</i> | $\delta_D$ | $\delta_P$ | $\delta_H$ | $\delta_T (MPa^{1/2})^a$ | $R_o$ or $R_a$         | $RED^b$     | $\chi_{12}^c$ | <i>Solubility</i> |
|------------------------------|------------|------------|------------|--------------------------|------------------------|-------------|---------------|-------------------|
| Poly(3hexylthiophene)P3HT    | 19.1       | 3.9        | 6.4        | 20.52                    | 6.43 (R <sub>o</sub> ) | -           | -             | -                 |
| Thiophene                    | 18.9       | 2.4        | 7.8        | 20.58                    | 2.09                   | 0.33(Best)  | 0.05          | Soluble           |
| Chloroform                   | 17.8       | 3.1        | 5.7        | 18.95                    | 2.81                   | 0.44        | 0.10          | Soluble           |
| 1,3,5-Trichlorobenzene (TCB) | 20.2       | 5.9        | 3.9        | 21.40                    | 3.88                   | 0.60        | 0.18          | Soluble           |
| o-Dichlorobenzene (ODCB)     | 19.2       | 6.3        | 3.3        | 20.47                    | 3.93                   | 0.61        | 0.19          | Soluble           |
| 2,5-dibromothiophene (DBT)   | 20.1       | 7.1        | 7.7        | 22.67                    | 3.99                   | 0.62        | 0.19          | Soluble           |
| Chlorobenzene (CB)           | 19.0       | 4.3        | 2.0        | 19.58                    | 4.42                   | 0.69        | 0.24          | Soluble           |
| Toluene                      | 18.6       | 1.5        | 2.1        | 18.78                    | 5.02                   | 0.78        | 0.31          | Soluble           |
| o-Xylene                     | 17.8       | 1.0        | 3.1        | 18.10                    | 5.10                   | 0.79        | 0.32          | Soluble           |
| 3-Hexylthiophene(3HT)        | 17.4       | 0.6        | 4.2        | 18.30                    | 5.22                   | 0.81(Worst) | 0.33          | Soluble           |

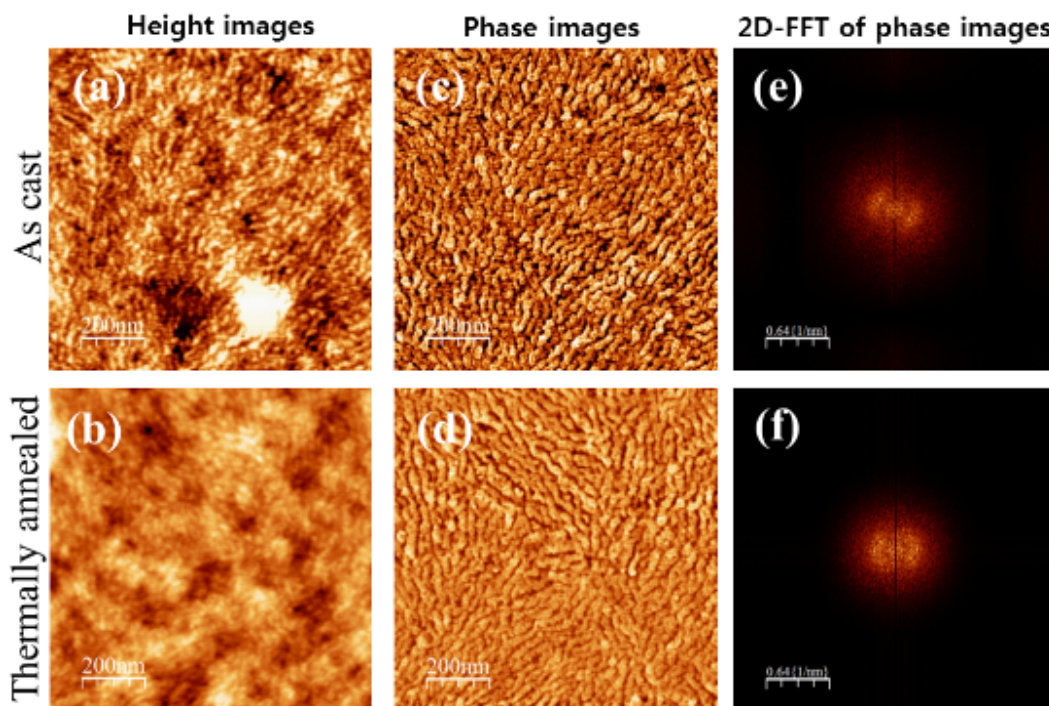
  

| <i>Solute &amp; Solvents</i> | $\delta_D$ | $\delta_P$ | $\delta_H$ | $\delta_T (MPa^{1/2})^a$ | $R_o$ or $R_a$        | $RED^b$     | $\chi_{12}^c$ | <i>Solubility</i>               |
|------------------------------|------------|------------|------------|--------------------------|-----------------------|-------------|---------------|---------------------------------|
| PC <sub>61</sub> BM          | 19.39      | 5.91       | 4.96       | 20.87                    | 6.2 (R <sub>o</sub> ) | -           | -             | -                               |
| o-Dichlorobenzene (ODCB)     | 19.2       | 6.3        | 3.3        | 20.47                    | 1.75                  | 0.28(Best)  | 0.04          | Soluble (47mg/ml) <sup>55</sup> |
| 1,3,5-Trichlorobenzene (TCB) | 20.2       | 5.9        | 3.9        | 21.40                    | 1.94                  | 0.31        | 0.05          | Soluble                         |
| 2,5-dibromothiophene (DBT)   | 20.1       | 7.1        | 7.7        | 22.67                    | 3.31                  | 0.53        | 0.14          | Soluble                         |
| Chlorobenzene (CB)           | 19.0       | 4.3        | 2.0        | 19.58                    | 3.46                  | 0.56        | 0.16          | Soluble (35mg/ml) <sup>55</sup> |
| Chloroform                   | 17.8       | 3.1        | 5.7        | 18.95                    | 4.31                  | 0.69        | 0.24          | Soluble (26mg/ml) <sup>55</sup> |
| Thiophene                    | 18.9       | 2.4        | 7.8        | 20.58                    | 4.62                  | 0.75        | 0.28          | Soluble                         |
| Dichlormethane (DCM)         | 17         | 7.3        | 7.1        | 19.82                    | 5.42                  | 0.87        | 0.38          | Soluble                         |
| Toluene                      | 18.6       | 1.5        | 2.1        | 18.78                    | 5.49                  | 0.89        | 0.39          | Soluble                         |
| o-Xylene                     | 17.8       | 1.0        | 3.1        | 18.10                    | 6.14                  | 0.99        | 0.49          | Soluble (15mg/ml) <sup>55</sup> |
| 3-Hexylthiophene (3HT)       | 17.4       | 0.6        | 4.2        | 18.30                    | 6.24                  | 1.01(Worst) | 0.51          | Partially soluble               |

a: Hildebrand Solubility Parameter ( $\delta_T^2 = \delta_D^2 + \delta_P^2 + \delta_H^2$ ), b: Relative Energy Density (RED) of Hansen Solubility Parameter ( $RED = R_a/R_o$ ), c:  $\chi_{12} = \chi_c(RED)^2$

### 3.2.2. Morphological Evolution of P3HT:PC<sub>61</sub>BM BHJ Active Layers Due to Thermal Annealing

From the AFM analysis of as-cast and thermally annealed P3HT:PC<sub>61</sub>BM BHJ active layers, the surface morphology are compared as shown in Figure 3.2.



**Figure 3.2.** AFM images of as-cast and thermally annealed (150°C, 30 min) P3HT:PC<sub>61</sub>BM BHJ thin films. ((e) and (f) are 2D-FFT of phase images).

From the AFM analysis, it is clearly shown that the main critical step for the phase separation of P3HT and PC<sub>61</sub>BM is the spin coating process. As shown in Figure 3.2, there are no significant differences in the surface morphology between as-cast and thermally annealed BHJ active layers. The surface domain size of an as-cast BHJ active layer is compared with that of a thermally annealed one using the 2D-FFT analysis of the AFM phase mode images as shown in Figure 3.2 (e) and (f) and the 2D profiles of FFT analysis are shown in Figure 3.3 (a). There is a slight increase in the average lateral domain size of a thermally annealed BHJ active layer (12.3 nm) compared with that of an as-cast one (11.2 nm) and this increase is due mainly to the domain size increase that is based on the enhanced crystallization of

P3HT and PC<sub>61</sub>BM. A domain size is half of the d-spacing value in 2D-FFT and the d-spacing value in the real space 2D AFM phase images has a relationship of  $d (\text{\AA}) = 2\pi/q$  with the  $q (\text{\AA}^{-1})$  in the reciprocal space.

The thermal annealing enhances the crystalline phase ordering of P3HT inside the BHJ film also and results in a bathochromic shift (red shift) of the P3HT absorption peak ( $\lambda_{\text{max}}$ ) from 500 to 520 nm and an intensity enhancement of absorption  $\lambda_{\text{max}}$  at around 520 nm, as shown in Figure 3.3 (b). The shoulders around the 550 nm and 600 nm peaks are related to the enhanced intermolecular crystalline phase packing and the intensity increases of those peaks are clearly shown. The intensity of PC<sub>61</sub>BM absorption peak ( $\lambda_{\text{max}}$ ) around 320 nm is generally known not to increase during the thermal annealing regardless of a large PC<sub>61</sub>BM cluster formation.

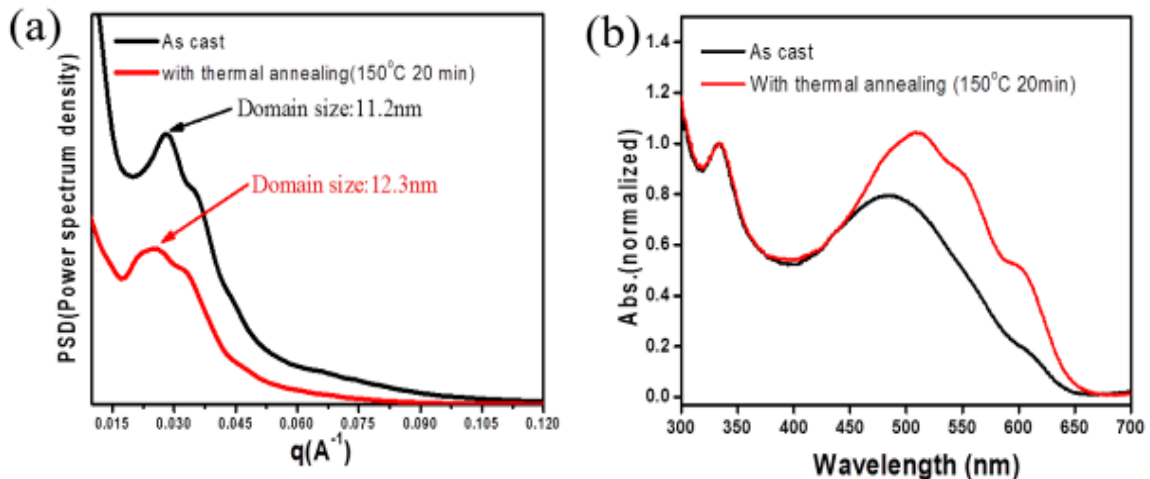


**Figure 3.3. (a) 2D-FFT profiles of phase mode images that are shown in Figure 3.2 for lateral domain size analyses, and (b) UVvis spectrophotometer absorption spectra of them. (The samples are as-cast and thermally annealed (150°C, 30 min) P3HT: PC<sub>61</sub>BM BHJ thin films, thickness = 100 nm).**

The R-SoXS data for P3HT:PC<sub>61</sub>BM BHJ active layers with and without thermal annealing are shown in Figure 3.4. Samples are prepared using free-standing film and the film floating method on the water surface. The R-SoXS experiments are carried out using 284.2 eV X-ray energy, at beam line 11.0.1.2 of ALS, LBNL. R-SoXS data show the bulk morphological information of P3HT:PC<sub>61</sub>BM BHJ Active Layer.

The strong scattering intensity is derived mainly from the strong scattering from the pure crystalline phase of P3HT and PC<sub>61</sub>BM. Therefore, the as-cast film does not show strong

intensity over the entire scan range compared to the thermally annealed film. Because thermal annealing enforces the crystallization of the BHJ active layer and further phase separation between P3HT and PC<sub>61</sub>BM, the scattering intensity of the thermally annealed film was enhanced dramatically due mainly to the increased scattering contrast. The bulk domain size with thermal annealing (150°C, 20 minutes) is seen to be around 12~15 nm (A domain size is half of the d-spacing value and the d-spacing value in the real space has a relationship of  $d \text{ (nm)} = 2\pi/q$  with the  $q \text{ (nm}^{-1}\text{)}$  in the reciprocal space), and matches well with that from the AFM 2D-FFT results of phase mode images in Figure 3.3 (a). In case of the as-cast sample, it has broader domain size distribution than that of thermally annealed one.

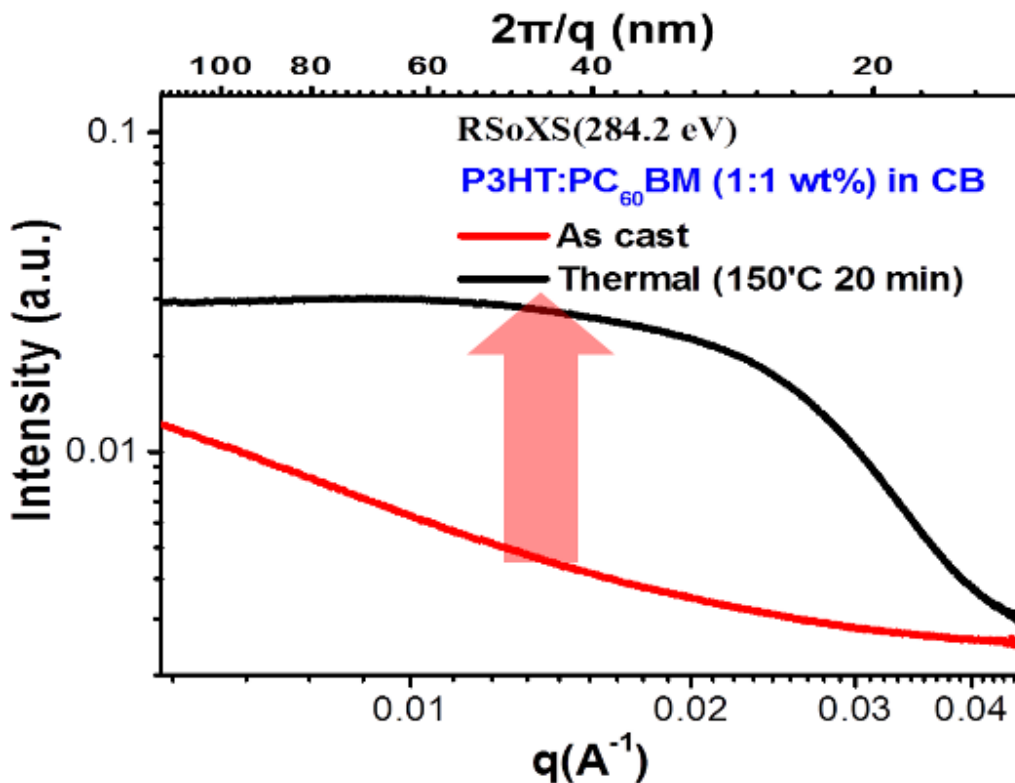


**Figure 3.4. R-SoXS data of as-cast and thermally annealed (150°C, 30 min) P3HT:PCBM BHJ active layers (thickness = 100 nm).**

The PC<sub>61</sub>BM cluster growth, as shown in Figure 3.5, is also a common phenomenon in a thermally annealed BHJ active layer.[185, 192] PC<sub>61</sub>BM cluster growth is a significant issue in the study of P3HT:PC<sub>61</sub>BM BHJ polymer solar cells. PC<sub>61</sub>BM has been used widely in BHJ polymer solar cells as an n-type material, due to its excellent electrical properties as an

excellent electron acceptor that can accept six electrons per molecule. However, PC<sub>61</sub>BM can grow up to several tens of  $\mu\text{m}$  in length under prolonged post thermal annealing, as shown in Figure 3.5. PC<sub>61</sub>BM cluster growth may be a factor not only in the fabrication process but may also affect the life time of the solar cells.

Still, debate remains about the effect of PC<sub>61</sub>BM cluster growth on the performance of the P3HT:PC<sub>61</sub>BM BHJ polymer solar cells, it is generally believed that PC<sub>61</sub>BM cluster growth should be minimized for optimal P3HT: PC<sub>61</sub>BM BHJ polymer solar cells.

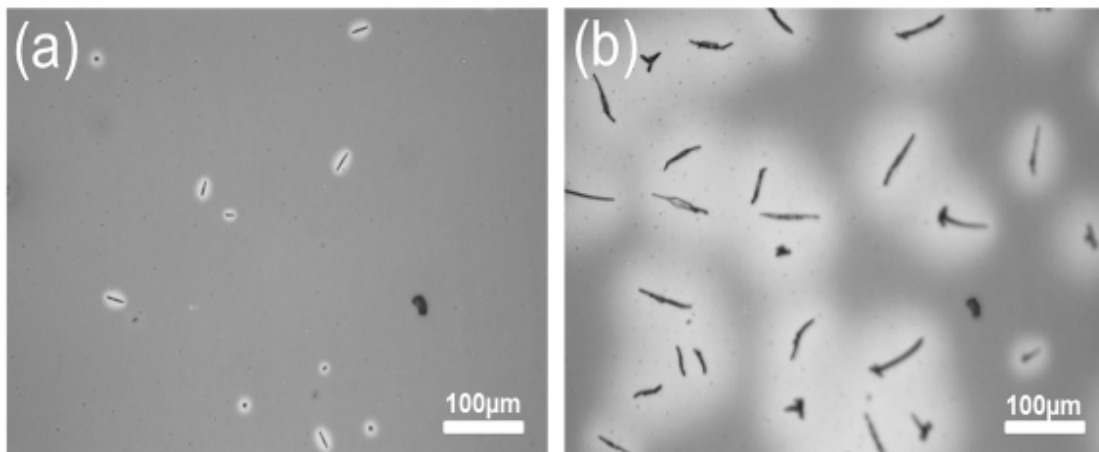


**Figure 3.5. PC<sub>61</sub>BM cluster growth in a P3HT: PC<sub>61</sub>BM BHJ active layer under thermal annealing: (a) 5 minutes annealed and (b) 180 minutes annealed at 180°C (Experiments were performed by Lewis Guignard).**

### **3.2.3. Crystalline Phase Growth and Orientation of P3HT:PC<sub>61</sub>BM BHJ Active Layers in Thermal Annealing**

Wide angle x-ray scattering for the crystallinity analysis is performed using a GIWAXS technique at beam line 7.3.3, ALS, LBNL and the results are shown in Figure 3.6.

As expected based on the analysis of the UVvis absorption spectra in Figure 3.3 (b), the crystallization of P3HT is enhanced with thermal annealing. In out of plane scattering, a (100) peak, which is related to the ‘edge on’ crystalline phase orientation, becomes sharper, and its intensity becomes much stronger than that of as-cast. It means that the crystalline phase size becomes larger and the absolute amount of crystallinity is much more enhanced than that of an as-cast BHJ active layer.

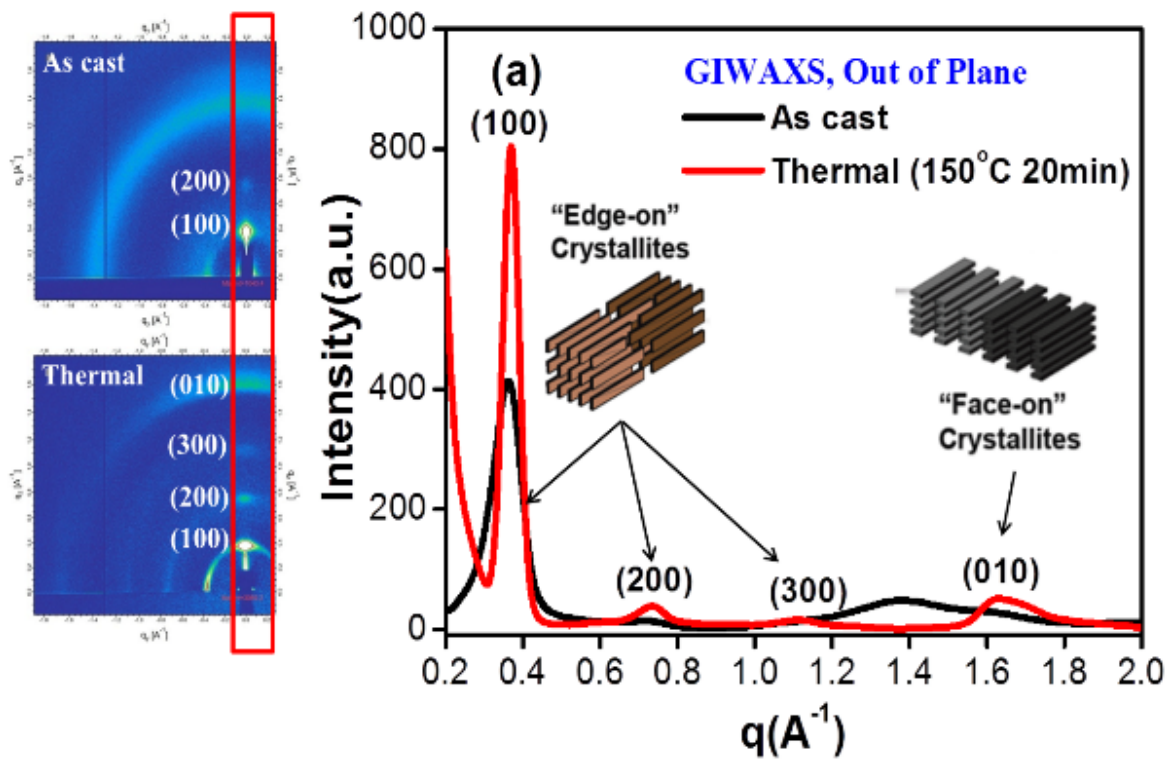


**Figure 3.6.** GIWAXS data of as-cast and thermally annealed (150°C, 20 min) P3HT:PC<sub>61</sub>BM BHJ active layers (thickness = 100 nm) on Si substrates in out-of-plane scattering (incident angle = 0.1°) (Experiments were performed by Eliot Gann at ALS).

For the exact estimations of the changes in the degree of crystallinity and the size of crystalline phase during the thermal annealing, the peak area of crystalline phases were integrated for the comparison of degree of crystallinity and the size of crystalline phases of ‘edge on’ (from (100)) and ‘face on’ (from (010)) crystalline orientations were calculated using a Debye-Scherrer equation[188], which is based on the measured Full Width at Half Maximum (FWHM) values.

$$t = \frac{0.9\lambda}{B \cos \theta_B} \quad (3-1)$$

Where  $\lambda$  is the x-ray beam wave length (1.2389Å at ALS); B is the FWHM value in rad; and  $\theta_B$  is the center position of the B value. The calculated results are summarized in Table 3.2.

**Table. 3.2. Calculated degree of crystallinity and crystalline phase sizes of P3HT in an as-cast and thermally annealed (150°C, 20-minutes) P3HT:PC<sub>61</sub>BM BHJ films**

|                  | $I_{max}$ | Peak Area | $\theta_2(rad)$ | $\theta_1(rad)$ | $B$   | $\Theta_B$ | $t(nm)$ |
|------------------|-----------|-----------|-----------------|-----------------|-------|------------|---------|
| As-cast<br>(100) | 413.64    | 39.54     | 0.031           | 0.04            | 0.009 | 0.035      | 12.53   |
| Thermal<br>(100) | 806.25    | 45.34     | 0.034           | 0.039           | 0.005 | 0.036      | 22.32   |
| (010)            | 51.45     | 9.35      | 0.156           | 0.173           | 0.017 | 0.165      | 6.57    |

In the out of plane scattering, the integrated peak area of (100) peak, a major peak that stands for an ‘edge on’ orientation of P3HT, in a thermal annealed BHJ active layer is increased to 45.34 compared with that of an as-cast as 39.54. It indicates that the total amount of ‘edge on’ oriented crystalline phase increases approximately 14.7% with thermal annealing when it is compared with that of an as-cast.

The sizes of crystalline phases of P3HT that were calculated by equation (3-1) are 12.53 nm and 22.32 nm in the as-cast and thermally annealed films, respectively. As expected, the results indicate not only the degree of crystallinity but also the size of crystalline phase of P3HT increases with thermal annealing. Both the ‘edge on’ and ‘face on’ crystalline orientations of P3HT exist together after post thermal annealing, and the ‘face on’ crystalline orientation is represented by a (010) peak. The crystalline size of the (010) crystalline phase after post thermal annealing, calculated using a Scherrer equation, is 6.73 nm, with no (010) scattering peak in the as-cast film. The ‘edge on’ crystalline phase is the dominant phase of P3HT on the hydrophilic substrate surface[231], which serves to minimize the contact area between hydrophobic long alkyl side chains and the hydrophilic substrate surface; therefore, the stacked  $\pi$ - $\pi$  orbitals direction of the thiophene rings is parallel to the substrate surface. The ‘edge on’ crystalline phase enhances the intermolecular charge carrier mobility in the same direction of the stacked  $\pi$ - $\pi$  orbitals direction of the thiophene rings. The ‘face on’ crystalline phase has stacked  $\pi$ - $\pi$  orbitals of thiophene rings in the perpendicular direction to the substrate surface, and this phase enhances the intermolecular charge carrier percolation in the same direction of the electrical fields between cathode and anode electrodes. The ‘face on’ crystalline orientation is preferred for the P3HT: PC<sub>61</sub>BM BHJ polymer solar cells, but it is not the primary crystalline phase in conventional P3HT: PC<sub>61</sub>BM BHJ polymer solar cells.

The effect of the directional orientation of the P3HT crystalline phase ('edge on' is preferred in OTFT applications) on charge carrier mobility has been reported by many researchers as an improvement of the electrical mobility in OTFT applications.[183, 232, 233] It has also been reported that the charge carrier mobility of the P3HT: PC<sub>61</sub>BM BHJ polymer solar cells are enhanced by 'face on' P3HT crystalline phase orientation.[231]

Because the thermal annealing was carried out on a hot-plate, the variations of the vertical crystalline phase orientations and crystalline sizes are studied at various X-ray incident angles using a 100 nm thick P3HT: PC<sub>61</sub>BM BHJ active layer, as shown in Figure 3.7. The calculated critical incident angle is 0.1°, and values below this angle (0.05°) provide information about the surface only, whereas larger incident angles, such as 0.15° and 0.2°, provide information regarding the bulk properties of the film. The experiments are performed at Brookhaven National Laboratory (BNL).

All the characteristic peaks under the higher incident angles over the critical angle (0.1°) are shifted slightly in the low q direction in the bulk of the film, and peaks width get sharp as compared with that of the surface, as shown in Figure 3.8. That is, the crystalline size inside the bulk film is slightly larger than that on the surface. It is understood that this effect stems from the thermal annealing. Thermal annealing is carried out from the bottom side of the substrate, which is the side that contacted the hot-plate. Thus, the crystalline size of the bottom of the film slightly increased compared to the crystalline size where air contacted the top surface; this phenomenon is due to temperature-induced strain, such as thermal expansion, on the film. This occurrence indirectly explains the vertical morphology formation.[234]

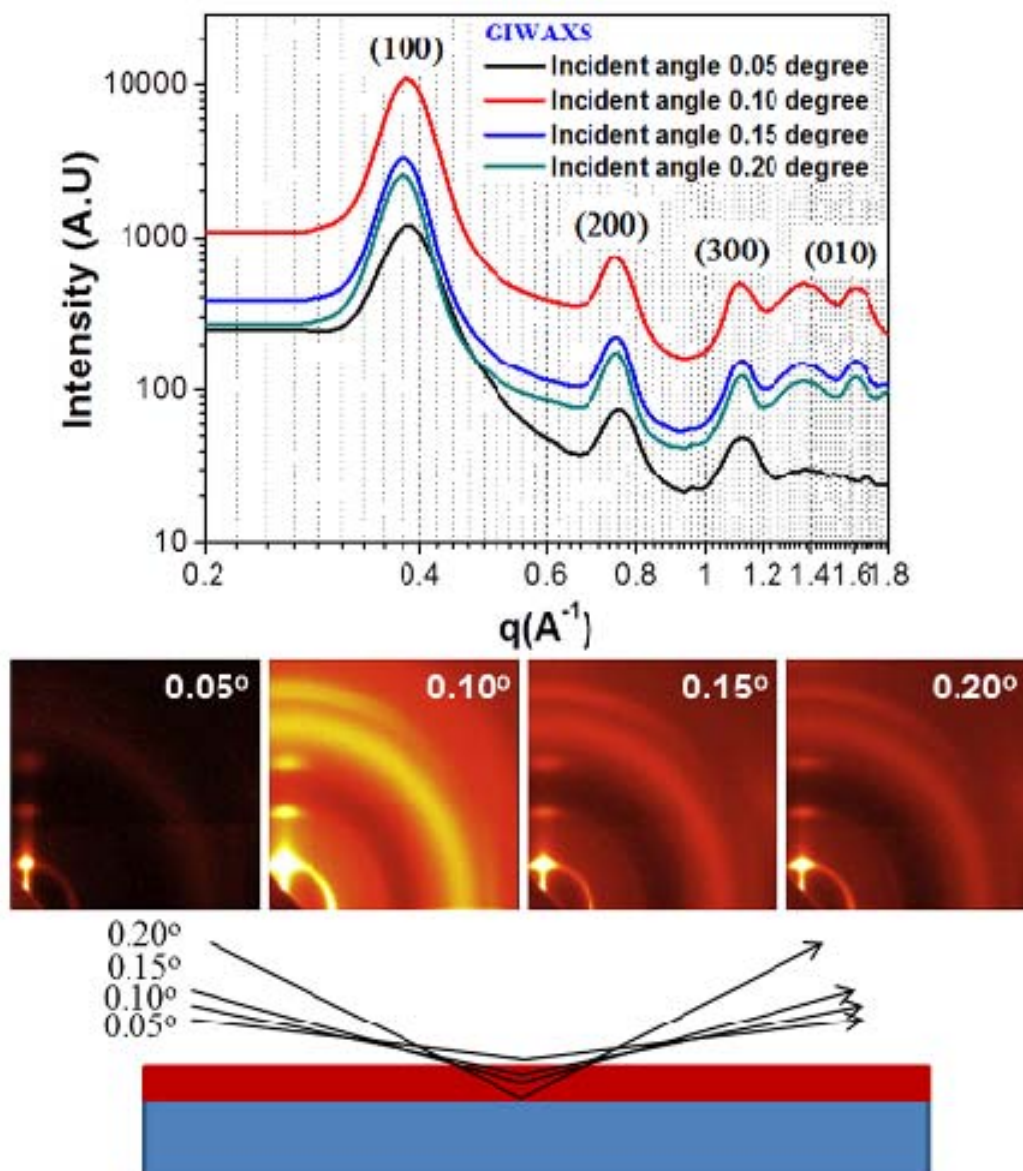


**Figure 3.7.** GIWAXS out-of-plane scan data at various incident angles (sample: a spin cast P3HT: PC<sub>61</sub>BM BHJ thin film with thermal annealing (150°C, 30 min), thickness = 100 nm) (Experiments were done by Xinhui Lu at NSLS).

Vertical segregation of P3HT and PC<sub>61</sub>BM are affected by surface energy interactions with air and substrate interfaces. The reported surface energies of P3HT and PC<sub>61</sub>BM are 26 mN/m and 38.2 mN/m, respectively.[235] It has been reported that P3HT segregates toward a top surface that contacts air due to its hydrophobic property, and that PC<sub>61</sub>BM moves to the opposite, or bottom, side that contacts an anode for a very short time during the post thermal

annealing process.[234] It is the opposite direction that is preferred for optimal P3HT: PC<sub>61</sub>BM BHJ polymer solar cells. Based on this study's GIWAXS results, even though it is not a major factor, the thermal annealing direction and crystalline size variation may also affect the vertical morphological evolution of P3HT:PC<sub>61</sub>BM BHJ polymer solar cells.

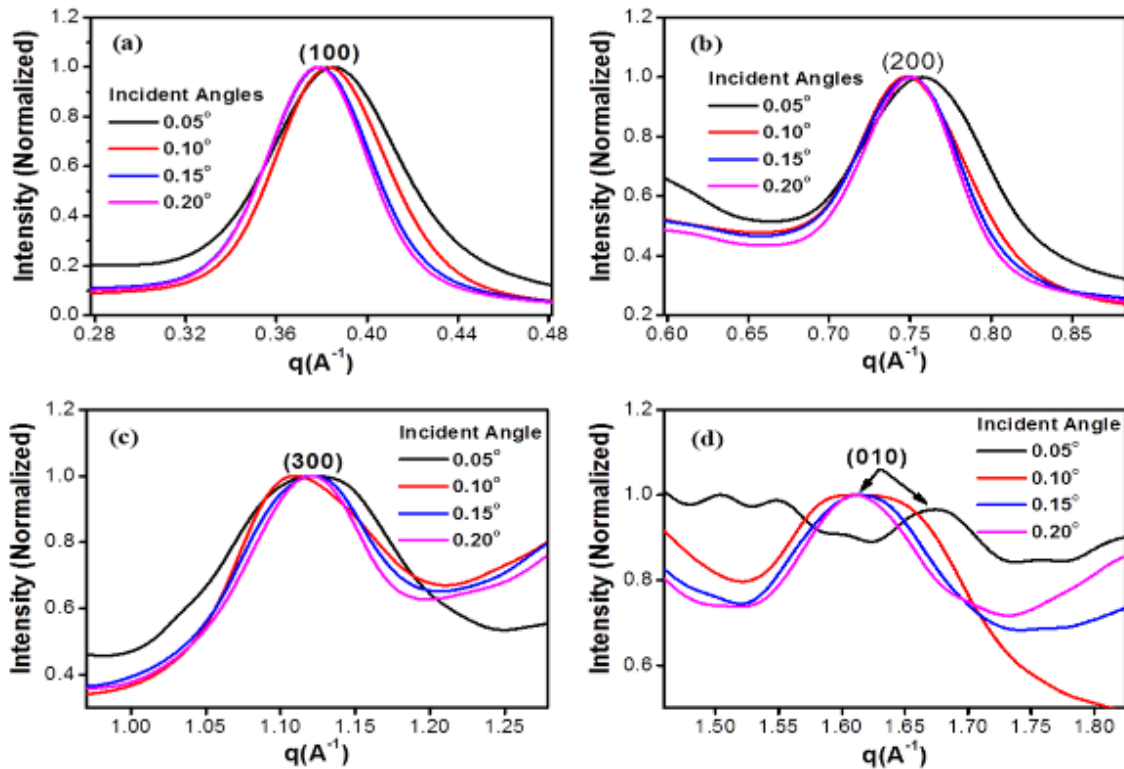


**Figure 3.8. Normalized GIWAXS out-of-plane peaks data at various incident angles based on the experiments shown in Figure 3.7.**

### 3.2.4. Model for Morphological Evolution of P3HT:PC<sub>61</sub>BM BHJ Polymer Solar Cells in Thermal Annealing

In this chapter 3, fundamental phenomena in a P3HT: PC<sub>61</sub>BM BHJ active layer during the thermal annealing process are examined. The thermal annealing process is currently the most effective post casting process that can produce the best P3HT: PC<sub>61</sub>BM BHJ polymer solar cells. However, there are several demerits, such as the wrong P3HT orientation, the wrong vertical segregation of materials and large PC<sub>61</sub>BM crystalline phase growth, should be improved or modified for the improved P3HT: PC<sub>61</sub>BM BHJ polymer solar cells.

In general, there are two popular models that explain the morphological evolution in P3HT:PC<sub>61</sub>BM BHJ polymer solar cells:

A) First is that used in this paper to explain morphological evolution. This model suggests that the morphological evolution in a two-step wise process: 1) fine domain formation comes during the spin coating process based on spinodal decomposition (incompatibility of two component materials in a blend), 2) followed thermal annealing enhances further morphological evolution with the crystalline phase growth.[110, 119, 124, 236]

B) The other explains the whole morphological evolution of the P3HT:PC<sub>61</sub>BM BHJ morphology using the crystalline phase growth only. In this case, it is assumed that there is no phase separation during spin coating process and the morphology evolves during the thermal annealing process.[130, 133, 194]

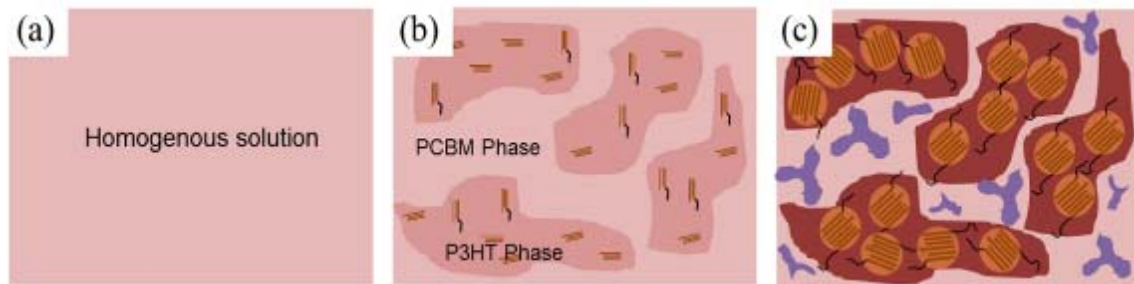


**Figure 3.9. Schematic diagrams of phase separation and crystallization of P3HT:PC<sub>61</sub>BM BHJ polymer solar cells: (a) homogeneous solution, (b) as-cast phase separated film, and (c) growth of crystalline phases after thermal annealing.**

Based on all the experimental results, the morphological evolution developed using a conventional thermal process is suggested as schematic diagrams in Figure 3.9. The main morphology evolves from a homogeneous solution (a); and a good homogeneous solution such as a CB based solution leads to fine morphology during the spin coating process (b). The final post thermal process enhances the crystallization of both P3HT and PC<sub>61</sub>BM (c). Therefore, it is thought that not only spin coating but also post thermal annealing is critical process to have the improved performance of the P3HT:PC<sub>61</sub>BM BHJ polymer solar cells.

### **3.3. Solvent Annealing for Enhanced Crystallization and Morphological Control of P3HT: PC<sub>61</sub>BM BHJ Active Layers**

#### **3.3.1. Solvent Effect on Spin Coating Process and Solvent Annealing for P3HT:PC<sub>61</sub>BM BHJ Active Layers**

The solvent annealing process appears slightly more complicated than the thermal annealing process because the critical factors to be considered are solubility and vapor pressure of solvents. Although the requirements for the annealing solvents appear similar to those for the spin coating solvents, several differences exist. The highest priority for a solvent for the spin coating process is excellent solubility for the target solutes. ODCB is known as the best solvent, and exhibits excellent solubility for P3HT and PC<sub>61</sub>BM. Its Flory-Huggins interaction parameters ( $\chi_{12}$ ), calculated based on its interactions with P3HT and PC<sub>61</sub>BM, are 0.19 and 0.04, respectively, as shown in Table 3.1. These parameters were calculated using Hansen solubility parameter sphere models. Additionally, the boiling point of ODCB is 180°C, which is 50°C higher than that of CB, and therefore, the vapor pressure is low enough to allow an excellent homogeneous solution during the spin casting process. It takes a long time to create a solidified film, so the slow solvent evaporation rate of ODCB during the spin coating process results in a much finer phase separation than that of CB. However, when ODCB is used in the solvent annealing process as a solvent, it can easily dissolve the whole BHJ film, unless special care is taken, rather than enhance the crystallinity and morphology of the film. Solvent annealing is generally preferred to take place within a short time; thus, it is hypothesized that a relatively selective solvent is better than a good solvent for this application.

For example, similarly to ODCB, DBT is a relatively good solvent option for the solvent annealing step, although PC<sub>61</sub>BM has lower solubility in DBT than in ODCB. The Flory-Huggins interaction parameters ( $\chi_{12}$ ), calculated based on the interactions with P3HT and PCBM using the Hansen-solubility parameters, are 0.19 and 0.14, respectively. The interaction level of DBT with P3HT is almost the same as that of ODCB, but the interaction level of DBT and the resultant solubility with PC<sub>61</sub>BM is much smaller than that in ODCB

( $\chi_{\text{DBT/PC}_{61}\text{BM}} = 0.14$  and  $\chi_{\text{ODCB/PC}_{61}\text{BM}} = 0.04$ ). Therefore, DBT does not dissolve the BHJ layer as much as ODCB during the solvent annealing process. Thus, DBT could work as a better solvent option for the solvent annealing than ODCB. Furthermore, it has a much lower vapor pressure due to its higher boiling point ( $b_p$ ) of 211°C than that of ODCB (180°C). The calculated interactions between several solvents and P3HT:PC<sub>61</sub>BM using Hansen solubility parameter sphere models are shown in Figure 3.10.

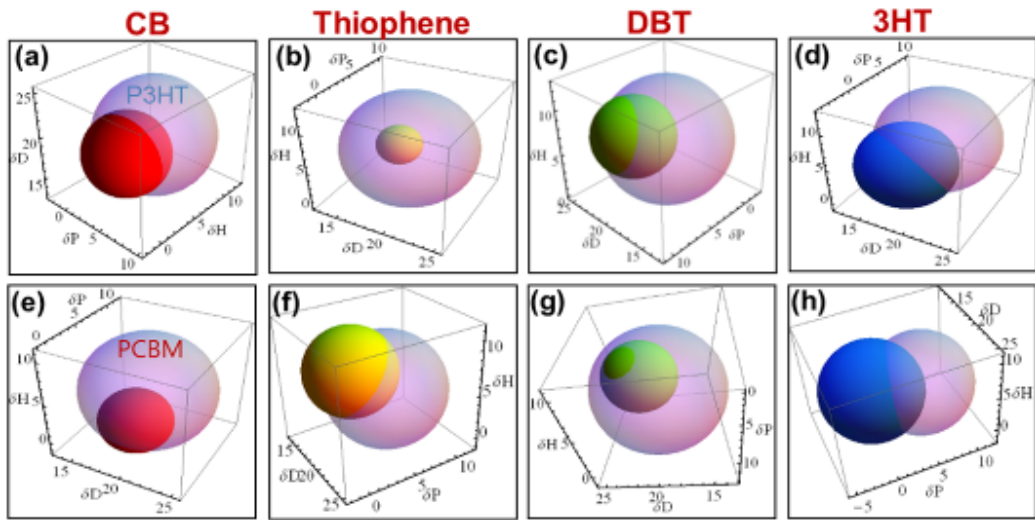


**Figure 3.10.** Calculated Hansen-solubility parameters ( $\delta_D$ ,  $\delta_P$ ,  $\delta_H$ ) and sphere models of P3HT and PC<sub>61</sub>BM in different solvents: (a)-(d) for P3HT, (e)-(h) for PC<sub>61</sub>BM (Different colors means different solvents and no special meaning in the used colors).

The radius of the spheres represents the interactional distance between the BHJ components and each solvent. If a solvent sphere is completely inside a solute sphere, the solvent will have better solubility with the BHJ components than a case where the solvent sphere is outside the solute sphere. Therefore, for the application of a spin coating process to allow a uniform and thin BHJ active layer on the substrate, a solvent should have good interactions and excellent solubility with both the P3HT and PC<sub>61</sub>BM BHJ components. Additionally, a low vapor pressure that comes from the high boiling point ( $b_p$ ) helps to create a uniform thin film. However, if the vapor pressure is too low, it could result in a non-uniform BHJ active layer during the spin coating process, especially at a slow spin coating speed. The thin film thickness is affected by both the spin coating speed (the solvent evaporation rate) and the solid content in the spin casting solution. Due to the increased solvent evaporation rate with

increasing spin coating speed, the film thickness decreases if there is no additional increase of the solid content. Because the solid content in a solution is limited also by the solubility limit of a solute in a solvent, it is not easy to control the film thickness by only one factor, i.e., either the spin coating speed or the solution concentration. Both CB and DBT have relatively good interactions with BHJ solutes, but the boiling point ( $b_p$ ) of DBT is so high, when compared with that of CB, is not a good spin coating solvent option at slow spin casting speeds, as explained heretofore.

In the case of thiophene, it exhibits excellent solubility with P3HT, but poor solubility with PC<sub>61</sub>BM. 3HT exhibits poor solubility for both P3HT and PC<sub>61</sub>BM. Due to these solubility outcomes for P3HT and PC<sub>61</sub>BM, both thiophene and 3HT are not considered as good candidates for the spin coating and the solvent annealing processes. Additionally, they have low boiling points at 84°C and 65°C, respectively, and the associated fast solvent evaporation rates lead to rough morphology, even in the isolated saturated solvent annealing condition. Therefore, as can be seen in Figure 3.10, CB and DBT are selected as good candidates for the post solvent annealing application among the four candidates that have distinctly different interactions with the BHJ components. During my experiments of solvent annealing using different solvents, it was empirically confirmed that a solvent with good solubility for PC<sub>61</sub>BM and slightly poor solubility for P3HT results in a finer morphology and higher current density of P3HT:PC<sub>61</sub>BM BHJ polymer solar cells.

From the 2D-FFT analysis of AFM phase mode images of solvent annealed P3HT:PC<sub>61</sub>BM BHJ active layers, it is proved that the use of DBT leads to finer morphology due to its low vapor pressure and selective interaction with BHJ constituents and it will be discussed in next sub-chapter 3.3.2.

### 3.3.2. Morphological Evolution of P3HT:PC<sub>61</sub>BM BHJ Active Layers in Solvent Annealing

The AFM images of solvent annealed P3HT: PC<sub>61</sub>BM BHJ films are shown in Figure 3.11. Substantial differences are evident in the morphology of the P3HT: PC<sub>61</sub>BM BHJ active layers that are exposed to the four different solvent vapors.

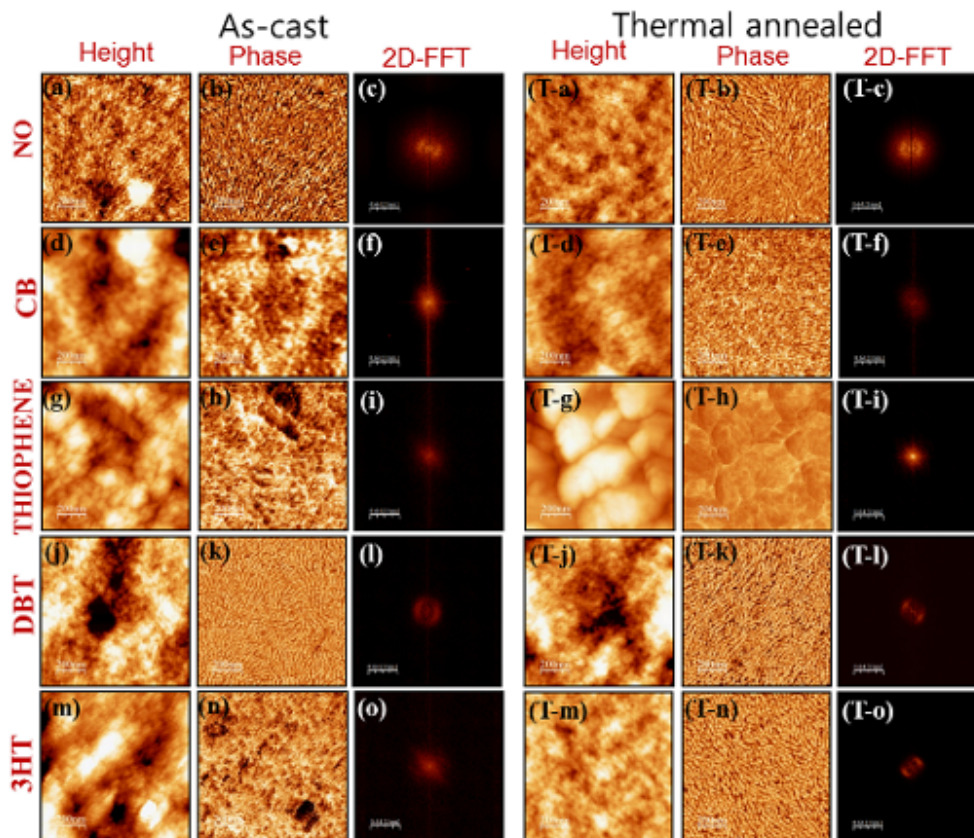


**Figure 3.11. AFM images of vapor annealed P3HT: PC<sub>61</sub>BM BHJ films: first column is height, second column is phase and third column is 2D-FFT of phase images; CB and DBT at 80°C, 1 min; thiophene and 3HT at 50 °C, 1 min; scale bar is 200 nm.**

Although CB produces finer lateral morphology than any of the other solvents and is a good solvent during the spin coating process, it is not the best for solvent annealing. CB exhibits poorer lateral morphology at 80°C for 1 minute, i.e., ((d) and (e)) than those from as-cast ((a) and (b)) or DBT solvent annealed ((j) and (k)) films. These findings support the calculations based on the Hansen solubility parameters sphere model. Thiophene ((g) and (h)) and 3HT

((m) and (n)) are tested at 50°C for 1 minute as the candidate solvents for the solvent annealing; however, as expected from the calculations, they are not successful due to the high vapor pressures from the low boiling points ( $b_p$ ) and the relatively poor solubility with PC<sub>61</sub>BM.

The lateral morphology using DBT at 80 °C for 1 minute ((j) and (k)) is much finer than that of the other films, regardless of thermal annealing, as shown in Figure 3.11. As discussed, the thermal annealing enhances the crystallization of P3HT and PC<sub>61</sub>BM in the P3HT: PC<sub>61</sub>BM BHJ active layers and the thermally induced final morphology of the solvent annealed films generally improved, except a film annealed in a thiophene vapor.

The R-SoXS scattering intensity of the DBT annealed sample is compared with other samples processed with different solvents, such as 3HT and thiophene. Samples are prepared as 100nm thin free-standing films using the film floating method on the water surface. The R-SoXS experiments are carried out using 284.2 eV X-ray energy, at beam line 11.0.1.2 of ALS, LBNL. R-SoXS data show the bulk morphological information of P3HT:PC<sub>61</sub>BM BHJ Active Layers. The strong scattering intensity is derived mainly from the contrast difference of two BHJ constituents. As shown in Figure 3.12, a DBT annealed P3HT:PC<sub>61</sub>BM BHJ active layer is still less intense than the other two samples that are annealed using 3HT and thiophene. It means that a DBT annealed P3HT:PC<sub>61</sub>BM BHJ active layer has much more intermixed region than others annealed using different solvents. This finding strongly supports that DBT is the best annealing solvent among the four different tested solvents, and these results match well with not only surface morphology data from AFM but also the expectation based on the Hansen solubility parameters calculation.

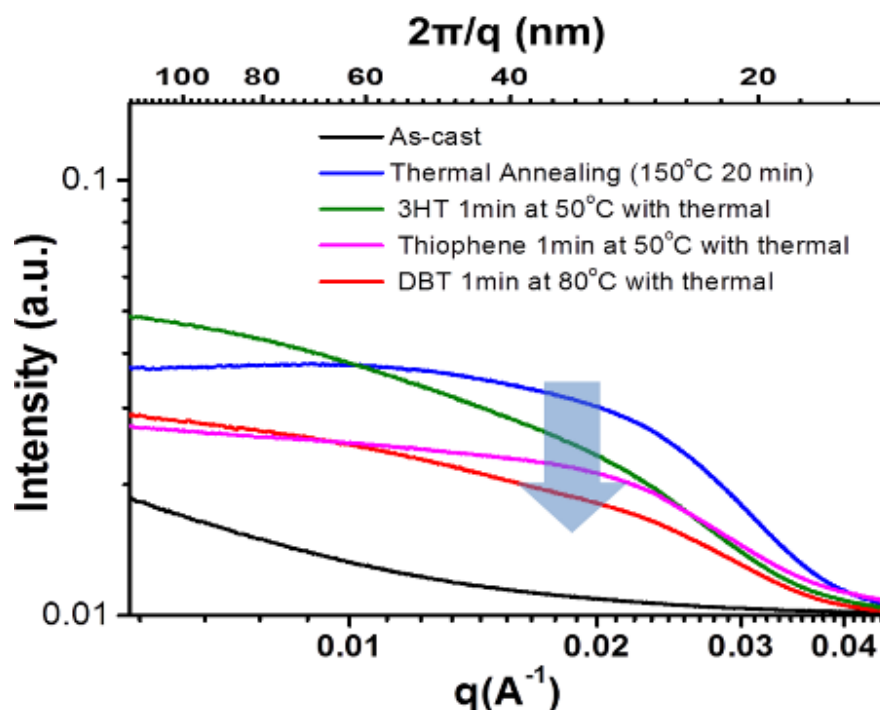


**Figure 3.12. R-SoXS data of post solvent annealed P3HT: PC<sub>61</sub>BM films using various annealing solvents (thickness of films = 100 nm).**

The UVvis absorption spectra of the post solvent annealed P3HT:PC<sub>61</sub>BM BHJ active layers using CB, thiophene, DCB and 3HT are shown in Figure 3.13. Thiophene is the best, and 3HT is the worst selection when only the absorption spectrum is considered. Thiophene is not a good selection for the morphology control of a BHJ film, even though it is good for the growth of the P3HT crystalline phase during solvent annealing (Figure 3.13 (c)). It appears that the best P3HT absorption spectrum is produced using thiophene in the solvent annealing process (Figure 3.13 (a~b)), despite its poor morphology, which may be due to the structural similarity of thiophene with P3HT and the resultant strong interaction between them. The absorption spectra enhancements can be explained by the strong intermolecular interaction between thiophene ring-based solvents that are used and P3HT, and may be due also to the high possibility of its interdigitation into the P3HT crystalline phase during the solvent annealing and the resulted enhancement of the  $\pi$ - $\pi$  orbitals overlap. Strangely, even though 3HT has the same chemical structure of P3HT, it is not as effective, not only in terms of morphology control but also in terms of P3HT crystalline phase growth. This phenomenon appears to be due to the high vapor pressure of 3HT that comes from the low boiling point

(b<sub>p</sub>) – as low as 65°C – and the poor solubility with both P3HT ( $\chi_{3HT/PC_{61}BM} = 0.33$ ) and PC<sub>61</sub>BM ( $\chi_{3HT/PC_{61}BM} = 0.51$ ).

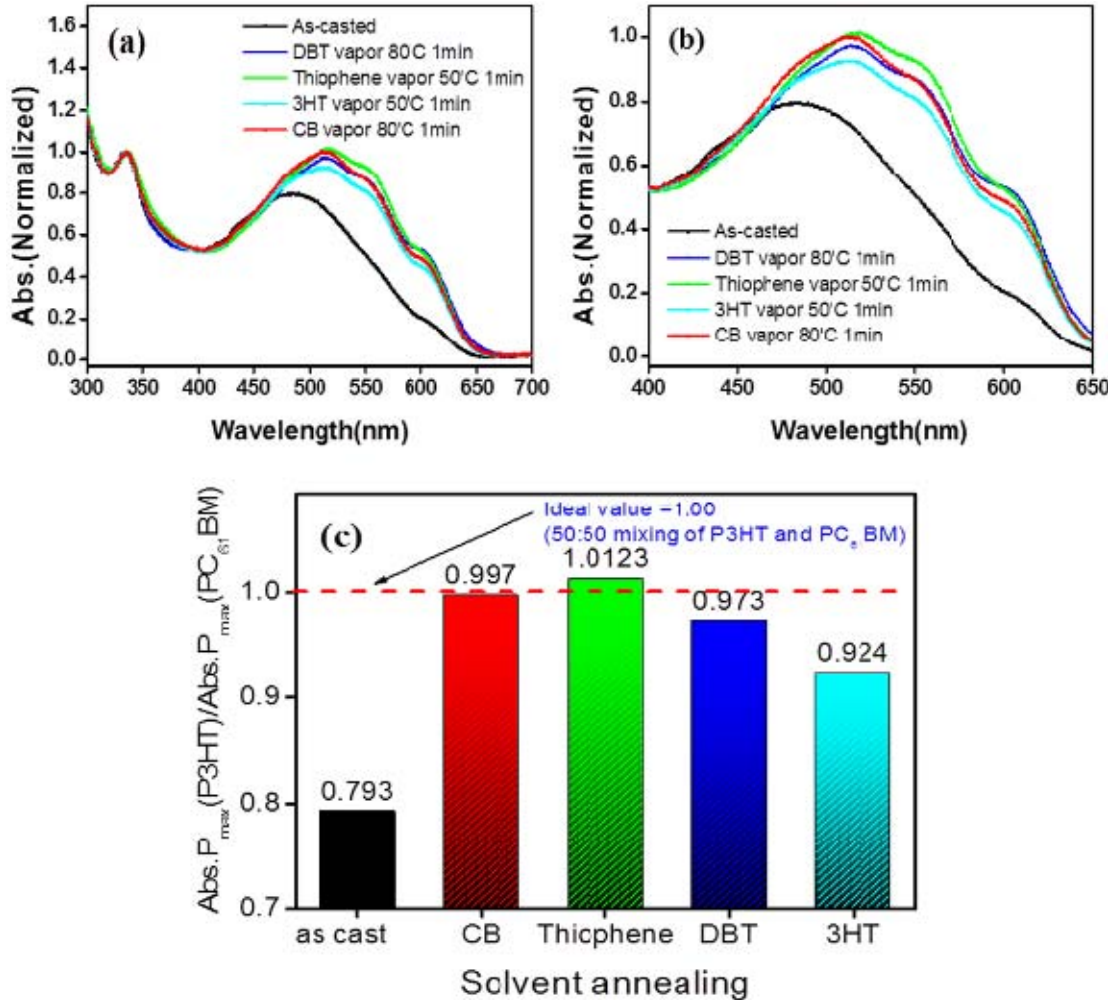


**Figure 3.13.** UVvis spectrophotometer absorption spectra of solvent annealed P3HT:PC<sub>61</sub>BM BHJ thin films: (a) full spectra, (b) zoomed-in P3HT spectra and (c) characteristic absorption peaks maximum intensity ratio between P3HT (517 nm) and PCBM (334 nm).

Considering both the fine morphology and the crystalline phase growth, the best solvent for the solvent annealing among the three thiophene-based solvents (3HT, thiophene and DBT) is DBT. Furthermore, it means that the high degree of the crystallinity does not indicate the good morphology or small domain size in a P3HT:PC<sub>61</sub>BM BHJ active layer.

In addition, from the calculated Hansen solubility parameters ( $\delta_D$ ,  $\delta_P$ ,  $\delta_H$ ) and Flory-Huggins interaction parameters ( $\chi_{12}$ ) of the tested materials, including several candidate solvents and

BHJ components (P3HT and PC<sub>61</sub>BM), the selection of DBT as the best annealing solvent is also strongly supported, as shown in Table 3.1. Thiophene is too good with P3HT and relatively bad solvent with PC<sub>61</sub>BM, and 3HT is bad with both P3HT and PC<sub>61</sub>BM. These two solvents do not follow the empirical statement set forth in this study that a solvent that has relatively poor solubility with P3HT and good solubility with PC<sub>61</sub>BM is the best fit for the solvent annealing process in order to produce finer morphology.

### **3.3.3. Morphological Evolution of P3HT:PC<sub>61</sub>BM BHJ Active Layers in DBT Based Solvent Annealing**

DBT is a starting material, which is a reactive thiophene base monomer, for the new post casting process, *in situ* UV photo-polymerization induced morphology control of the P3HT:PC<sub>61</sub>BM BHJ polymer solar cells. As a pre-step, DBT based solvent annealing (or DBT deposition) is critical to have small domain size and high degree of crystallinity in this new post casting process.

From the AFM, R-SoXS and UVvis spectrophotometer results, it is proved that DBT is a good solvent for solvent annealing. In addition, based on the Hansen solubility parameters calculations of several solvents (as shown in Table 3.1), DBT appears to be a promising option as an annealing solvent too, especially when it is combined with thermal annealing. Thus, DBT could lead to fine morphology and high crystallinity of the P3HT:PC<sub>61</sub>BM BHJ polymer solar cells.

The R-SoXS scattering intensity of the DBT annealed BHJ active layers in various annealing times are compared with that from the conventional thermal annealing only as shown Figure 3.14. Samples are prepared using free-standing film and the film floating method on the water surface. The R-SoXS experiments are carried out using 284.2eV X-ray energy, at beam line 11.0.1.2 of ALS, LBNL. R-SoXS data show the bulk morphological information of P3HT:PC<sub>61</sub>BM BHJ Active Layer.

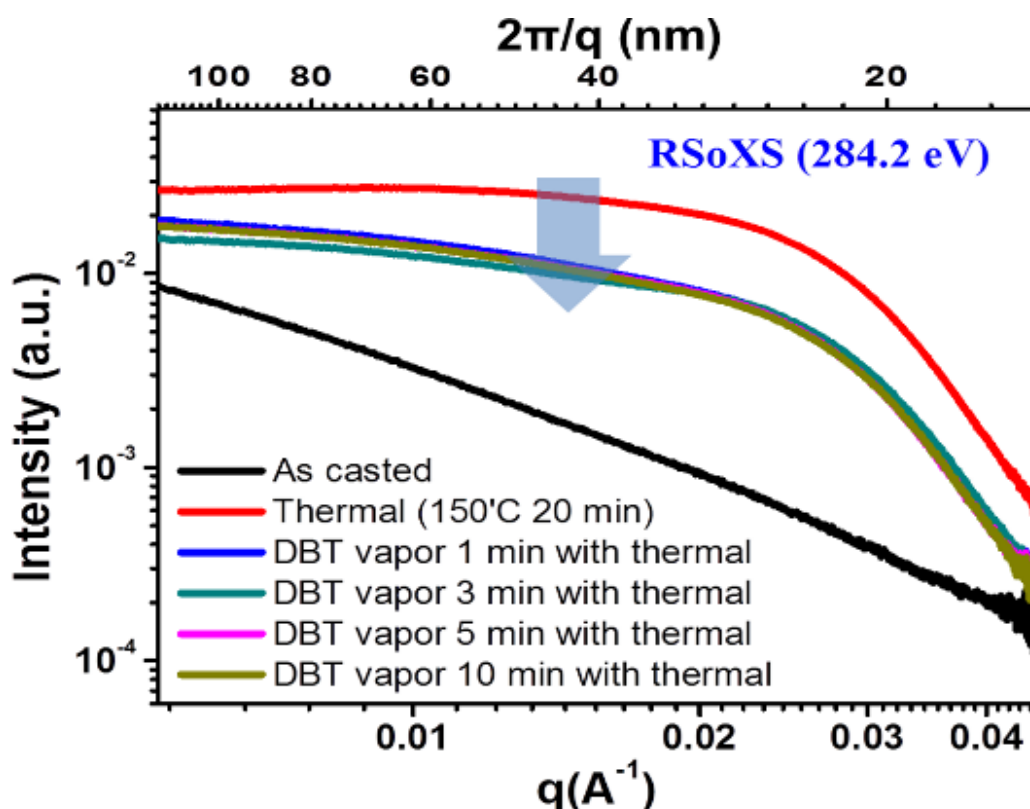


**Figure 3.14. R-SoXS data of DBT post solvent annealed P3HT:PC<sub>61</sub>BM films with various annealing conditions (thickness = 100 nm).**

Regardless of the DBT annealing times, the lower intensity of the R-SoXS data compared with those from conventional thermal annealing only, may be due mainly to the interdigitation of DBT into the P3HT as shown in GIWAXS data in Figure 3.17 and the hindered PC<sub>61</sub>BM crystal growth and thus result in less pure phases of them, as shown in Figure 3.14. In case of bulk domain sizes, there are no distinct differences with increasing DBT annealing times.

The large amount of PC<sub>61</sub>BM crystal growth is generally regarded as not a good sign for charge carrier generation as shown in Figures 1.10 (GISAXS)[188] and Figure 1.11 (SANS)[191] in the chapter 1. A report suggests that a very fine depletion region of P3HT:PC<sub>61</sub>BM exists around a large size of PC<sub>61</sub>BM cluster (in micron-meter scale) and it could lead to better performance for both charge carrier generation and transport.[201] However, this topic is still in debate. In this research, the micron-sized growth of PC<sub>61</sub>BM

cluster after the extended conventional thermal annealing (higher than 150°C, longer than 20 minutes) generally worsened the performance of the P3HT:PC<sub>61</sub>BM BHJ polymer solar cells. AFM analyses of DBT solvent annealed P3HT:PC<sub>61</sub>BM BHJ active layers in various DBT annealing times are conducted, as shown in Figures 3.15. Through analyses of the 2D-FFT profiles of the phase mode images in Figure 3.15, the average lateral domain sizes of the P3HT:PC<sub>61</sub>BM BHJ active layers for various DBT solvent annealing times are also analyzed and the smallest domain size based on the  $q_m$  values are derived from 1-or 10-minute DBT solvent annealing as shown Figure 3.15 and Figure 3.16.

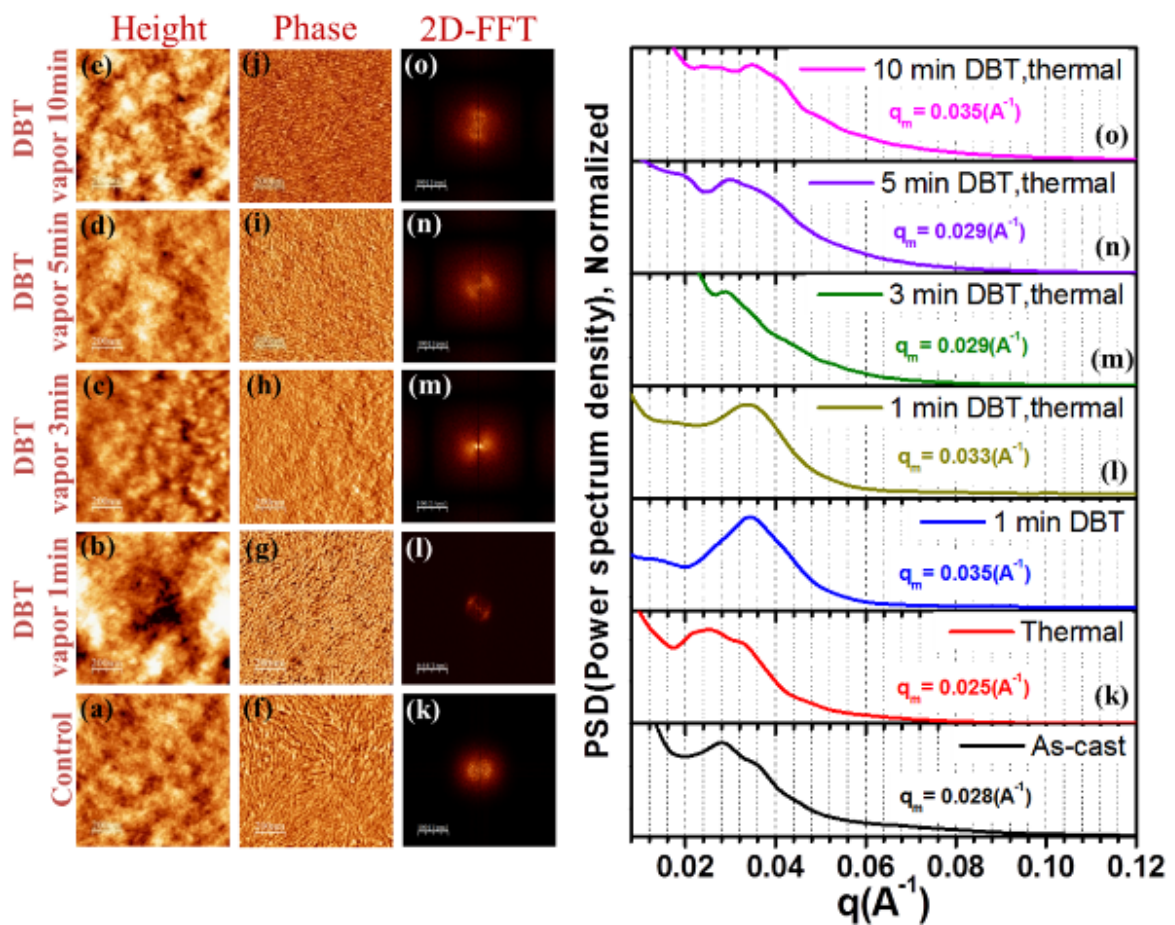


Figure 3.15. AFM images and 2D-FFT phase mode profiles of DBT vapor annealed P3HT:PC<sub>61</sub>BM BHJ films at various annealing times (DBT vapor annealing at 80°C and thermal annealing at 150°C 20 minutes;  $q_m$  means  $q_{(max)}$ ).

Regardless of the DBT annealing times, domain sizes of DBT solvent annealed P3HT:PC<sub>61</sub>BM BHJ active layers are smaller than those from an as-cast or the conventional

post thermal annealing only. The lateral domain size changes with DBT solvent annealing times are summarized in Figure 3.16 and the smallest domain size comes in 1- or 10-minutes DBT annealing within a measuring error range.

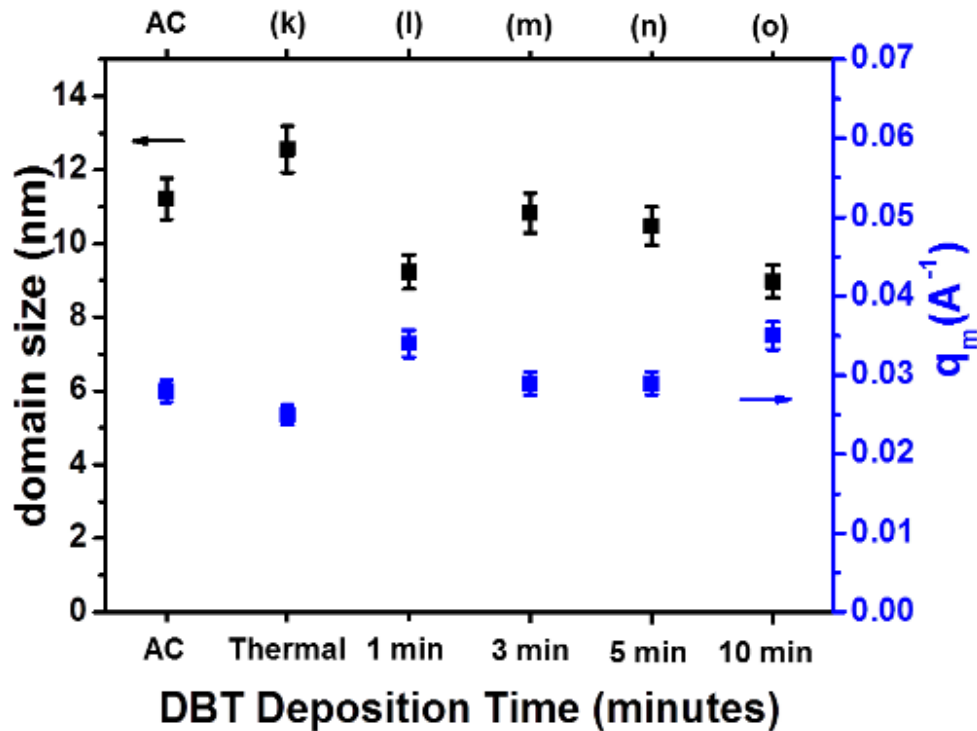
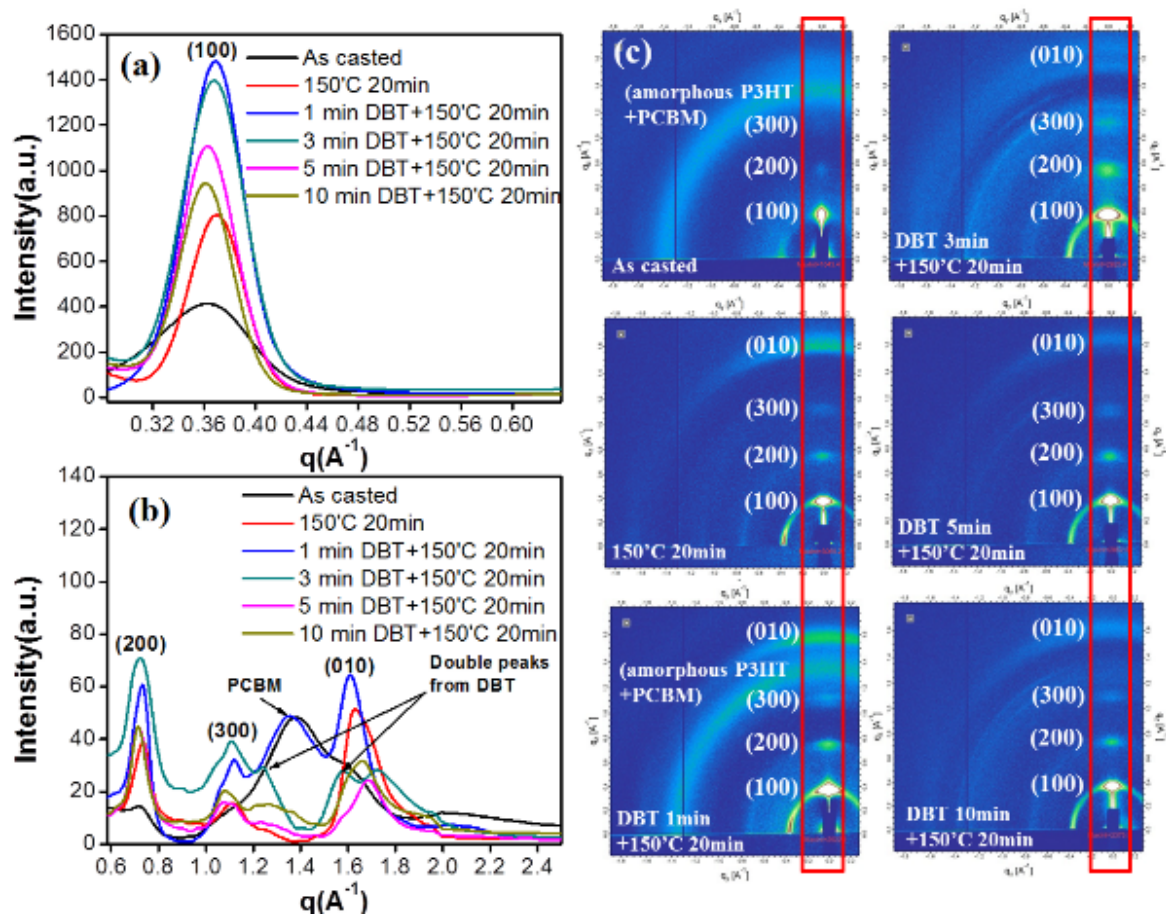


Figure 3.16. Lateral domain size analysis based on  $q_m$  values from 2D-FFT profiles of phase mode images presented in Figure 3.15 (Thermal annealing at 150°C 20 minutes was also applied for all samples, except an as-cast (AC) sample).

### 3.3.4. Crystalline Phase Growth and Orientation of P3HT:PC<sub>61</sub>BM BHJ Active Layers in DBT Based Solvent Annealing

Wide angle x-ray scattering for the crystallinity analysis of the DBT solvent annealed BHJ active layers are performed using a GIWAXS technique at beam line 7.3.3, ALS, LBNL and the results are summarized in Figure 3.17 and Table 3.3. The crystalline sizes of the P3HT crystalline phase are calculated using a Debye-Scherrer equation based on FWHM values. DBT appears to be suitable as an annealing solvent for improvements in photon absorption, charges separation and transport in BHJ polymer solar cells. In a 3-minute DBT solvent annealed sample, shown in Figure 3-17 (b), double peaks are present at both the (300) and

(010) crystalline peak positions. Although this phenomenon is not fully understood, it appears that some interdigitation of DBT into the P3HT crystalline phase during the solvent annealing process occurred. The (100) peaks become sharp in the DBT annealed samples, which strongly supports the crystalline size growth apparent in the prolonged DBT annealing time as compared with that of an as-cast, as shown in Table 3.3.



**Figure 3.17. GIWAXS data of DBT post solvent annealed P3HT:PC<sub>61</sub>BM active layers in various post solvent annealing conditions. (Thermal annealing at 150°C 20 minutes was also applied to all samples and all GIWAXS images were rescaled to display).**

The small crystalline phases come from the short times (1- or 3-minutes) of the DBT solvent annealing indicate a similar trend to the smallest lateral domain size from 2D-FFT analysis of AFM as shown in Figure 3.15 and 3.16. Additionally, from the GIWAXS analysis shown in Figure 3.17 and Table 3.3, the absolute volume of the P3HT crystalline phase in the P3HT:PC<sub>61</sub>BM BHJ active layer, which is calculated based on the integrated area of the

(100) peak, is also the largest volume of the P3HT crystalline phase for 1-minute of DBT solvent annealing out of all the samples prepared with different DBT annealing times and conditions. So, based on the degree of crystallinity and the size of crystalline phases, the optimal DBT solvent annealing time is as short as 1-minute in order to provide both improved crystalline phase growth and a smaller BHJ domain size.

**Table.3.3. Calculated P3HT crystalline phase sizes of DBT solvent annealed P3HT: PC<sub>61</sub>BM BHJ active layers.**

|               | $I_{max}$ | Peak Area | $\theta_2(rad)$ | $\theta_1(rad)$ | $B$   | $\Theta_B$ | $t(nm)$ |
|---------------|-----------|-----------|-----------------|-----------------|-------|------------|---------|
| As-cast (100) | 413.64    | 39.54     | 0.031           | 0.04            | 0.009 | 0.035      | 12.53   |
| Thermal       |           |           |                 |                 |       |            |         |
| (100)         | 806.25    | 45.34     | 0.034           | 0.039           | 0.005 | 0.036      | 22.32   |
| (010)         | 51.45     | 9.35      | 0.156           | 0.173           | 0.017 | 0.165      | 6.57    |
| DBT 1min      |           |           |                 |                 |       |            |         |
| (100)         | 1482.08   | 93.09     | 0.03            | 0.04            | 0.005 | 0.036      | 20.78   |
| (010)         | 64.39     | 10.21     | 0.157           | 0.171           | 0.014 | 0.164      | 7.99    |
| DBT 3min      |           |           |                 |                 |       |            |         |
| (100)         | 1395.95   | 56.0      | 0.033           | 0.039           | 0.006 | 0.036      | 19.40   |
| (010)         | 27.98     | 1.85      | 0.149           | 0.173           | 0.024 | 0.161      | 4.82    |
| §(010)        | 28.21     | 2.34      | 0.153           | 0.189           | 0.035 | 0.171      | 3.19    |
| DBT 5min      |           |           |                 |                 |       |            |         |
| (100)         | 1108.08   | 60.54     | 0.033           | 0.038           | 0.005 | 0.036      | 21.79   |
| (010)         | 24.43     | 3.40      | 0.155           | 0.181           | 0.026 | 0.168      | 4.44    |
| DBT 10min     |           |           |                 |                 |       |            |         |
| (100)         | 945.03    | 54.14     | 0.033           | 0.038           | 0.005 | 0.036      | 22.40   |
| (010)         | 31.60     | 6.23      | 0.154           | 0.174           | 0.020 | 0.164      | 5.68    |

\*All the DBT solvent annealed samples were prepared with the final thermal annealing at 150°C 20 min.

§Double peaks may come from DBT interdigitation into P3HT crystalline phase.

$I_{max}$  values and integrated peak area of the (100) crystallinity peak decrease with the longer DBT annealing time. That is, excess DBT can result in a decrease of the absolute amount of crystallinity, because excess DBT could work as an impurity also, so the order in the crystalline phase of P3HT could decrease. Regardless of DBT annealing time, the absolute amount of crystalline phase based on  $I_{max}$  values and integrated peak area of (100) peak are still much higher than that obtained from conventional thermal annealing only. These increased values that stem from DBT post solvent annealing are shown in all of the characteristic peaks, including (100), (200) and (300) peaks as well as a (010) peak.

Unlike a BHJ active layer for thermal annealing process only, the sizes of the crystalline phase of the DBT annealed BHJ active layers decreases even when combined with the

thermal annealing process. This phenomenon is distinctly visible in both the ‘edge on’ crystalline phase and ‘face on’ phases. Interestingly, the crystalline phase becomes smaller than that of the post thermal annealed crystalline phase, even though the total degree of crystallinity is significantly more enhanced (based on  $I_{max}$  values and integrated peak area) within a short time than that of the conventional thermal annealing only, regardless of DBT solvent annealing times.

### **3.3.5. DBT Based Solvent Annealing as Pre-Step of *In Situ* UV Photo-Polymerization Induced Morphological Control for P3HT:PC<sub>61</sub>BM BHJ Active Layers**

DBT solvent annealing is a pre-step for the new post casting process (i.e., the *in situ* UV photo-polymerization of DBT), which is discussed in Chapters 4 and 5. This new post casting process is designed to further improve performance of the P3HT:PC<sub>61</sub>BM BHJ polymer solar cells. This nicely pre-optimized BHJ active film in the optimized DBT annealing (deposition) condition becomes a concrete foundation for further enhancement in the next step toward a new process based on the *in situ* UV photo-polymerization of DBT in a BHJ film.

The boiling point of DBT is as high as 211°C and it remains inside BHJ after a short time of DBT annealing. Therefore, it is recalled as a DBT deposition not as a DBT annealing in the following chapters about the *in situ* UV photo-polymerization of DBT.

### 3.4. Conclusions

The fundamental functions and principles of thermal and solvent annealing of P3HT:PC<sub>61</sub>BM BHJ polymer solar cells are studied using AFM and x-ray techniques, such as GIWAXS and R-SoXS. Phase separation and crystallization are competing factors and the phase separation is determined primarily by an initial spin casting process, and the crystallinity is improved mostly in the annealing processes. In the thermal annealing process, the crystalline phase exhibits intense ‘edge on’ and ‘face on’ crystalline orientations as compared to that of an as-cast, and their crystalline size also increases slightly. Additionally, the thermal annealed BHJ active layer, when placed on a hot-plate, produces a slightly larger crystalline phase on the side of the film that contacts the hot-plate surface.

Solvent annealing enhances not only the degree of crystallinity but also produces morphological changes. The solvent annealing of a BHJ active layer using DBT results in a better degree of crystallinity, smaller crystalline phases and a smaller domain than those of conventional post thermal annealed P3HT:PC<sub>61</sub>BM BHJ active layers. Additionally, DBT that is interdigitated into the P3HT crystalline results in a more mixed (less pure) domain and finer crystalline phase with the increased degree of crystallinity in the P3HT:PC<sub>61</sub>BM BHJ active layer than that of the thermally annealed conventional one (from GIWAXS data). It may minimize PC<sub>61</sub>BM crystalline phase growth in the BHJ layer also (from the intensity decrease of R-SoXS data), and can result in a better PCE of the final P3HT:PC<sub>61</sub>BM BHJ polymer solar cells than would be the case using a conventional process.

## 4. *IN SITU* UV PHOTO-POLYMERIZATION OF DBT FOR ENHANCED PERFORMANCE OF P3HT:PC<sub>61</sub>BM BHJ POLYMER SOLAR CELLS

### 4.1. Background

Although thermal annealing has been a popular post casting process to improve the performance of P3HT:PC<sub>61</sub>BM BHJ polymer solar cells by enhancing the crystalline phases of P3HT and PC<sub>61</sub>BM, the domain size of the P3HT:PC<sub>61</sub>BM BHJ active layer increases during the post thermal process, as discussed in Chapter 3, due to the increased P3HT chain mobility and PC<sub>61</sub>BM diffusivity. The increased cluster size of PC<sub>61</sub>BM during the prolonged post thermal annealing reduces the interfacial area between P3HT and PC<sub>61</sub>BM and it can cause the electrical shorts also. In addition it hinders the orientation of P3HT crystalline phase inside a P3HT:PC<sub>61</sub>BM BHJ active layer.

In case of solvent annealing, it is regarded as a good post casting process to control the domain size and to optimize the performance of P3HT:PC<sub>61</sub>BM BHJ polymer solar cells; however, solvent options are limited, and no general working principle has been established for solvent annealing compared to thermal annealing.

In this Chapter 4, a new post casting process, *in situ* UV photo-polymerization of DBT, is demonstrated to attain better control over the morphology of P3HT:PC<sub>61</sub>BM BHJ polymer solar cells. This new post casting process is based on photo-polymerization-induced phase separation (PIPS) concept and the UV photo-polymerized oligothiophene derives the phase separation between P3HT and PC<sub>61</sub>BM phases inside the P3HT:PC<sub>61</sub>BM BHJ active layer. The fundamental objective of this new post casting process is to control the morphology and the crystalline phase orientation of a P3HT:PCBM BHJ active layer using *in situ* UV photo-polymerization of the reactive DBT monomer. The resultant miscibility change of the polymerized oligothiophenes during the reaction leads to an additional and finer phase separation between P3HT and PC<sub>61</sub>BM.

In the following subsections, the solubility drop of the *in situ* photo-polymerized oligothiophene, the crystalline phase size and orientation of P3HT as well as the miscibility

of the P3HT and PC<sub>61</sub>BM phases are discussed based on experimental results of the Hansen-solubility parameters, AFM, R-SoXS and GIWAXS.

## 4.2. Miscibility Effect of *In Situ* UV Photo-Polymerized Oligothiophene inside P3HT: PC<sub>61</sub>BM BHJ Active Layers

### 4.2.1. Solubility Prediction of P3HT and PC<sub>61</sub>BM in Various Solvents

P3HT and PC<sub>61</sub>BM are chemically well designed molecules that constitute a homogeneous solution in several common solvents due to their similar solubility in those co-solvents. By chemically attaching a polar side chain to C<sub>60</sub>, the miscibility between P3HT and PC<sub>61</sub>BM increases, and the overlapping volume of spheres that explain the miscibility of those two components in a simulated Hansen solubility spheres model[168] increases also, as shown in Figure 4.1.

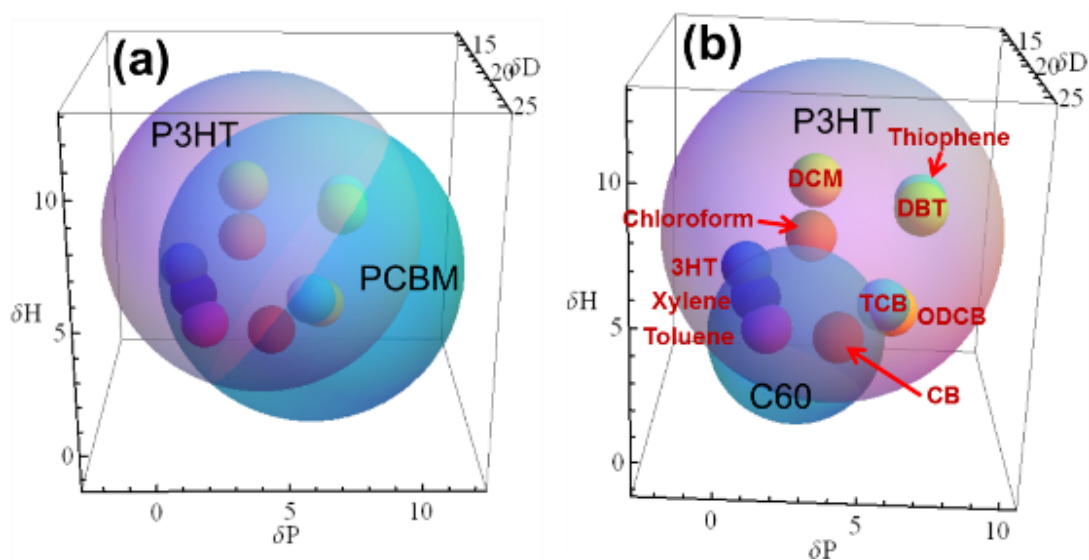


**Figure 4.1. Hansen-solubility parameters ( $\delta_D$ ,  $\delta_P$ ,  $\delta_H$ ), sphere models of: (a) P3HT: PC<sub>61</sub>BM and (b) P3HT: C<sub>60</sub> mixtures in several good solvents. (The radius of each solvent is assumed to be the same and different colors indicate different solvents only and no special meaning.)**

From this improved miscibility, a much finer morphology is produced for the P3HT: PC<sub>61</sub>BM BHJ film than for the P3HT:C<sub>60</sub> BHJ film.

Some ‘bad’ solvents, such as DBT, DCM, thiophene and chloroform for the C<sub>60</sub> could become good solvents for PC<sub>61</sub>BM due to this chemical modification of C<sub>60</sub>, which is one reason that PC<sub>61</sub>BM is widely used and considered to be the best counterpart for P3HT in the P3HT: PC<sub>61</sub>BM BHJ polymer solar cells. The calculated Hansen solubility parameters ( $\delta_D$ ,  $\delta_P$ ,  $\delta_H$ ) of a C<sub>60</sub> are 19.78, 2.67, 2.37, which indicate much lower  $\delta_P$  and  $\delta_H$  values and a slightly higher  $\delta_D$  value compared with the values of 19.39, 5.91, 4.96 of PC<sub>61</sub>BM. The inherent Hansen solubility ‘distance’ values ( $R_o$ ) of PC<sub>61</sub>BM and C<sub>60</sub>, which are calculated by using the official Hansen solubility parameter calculation software HSPiP, also differ significantly, as 6.2 and 3.4, respectively.

The Hildebrand solubility parameters are calculated by using Equation (4-2) for P3HT and P<sub>61</sub>CBM as 20.52 and 20.04 (MPa<sup>1/2</sup>), respectively, and as expected, they have similar affinities. However, the calculated Hildebrand solubility parameter of C<sub>60</sub> is 20.09 (MPa<sup>1/2</sup>), and this old solubility parameter do not effectively show the difference between C<sub>60</sub> and PC<sub>61</sub>BM.

$$\delta_T = \sqrt{(\delta_D^2 + \delta_P^2 + \delta_H^2)} = \sqrt{\left(\frac{E_D}{V} + \frac{E_P}{V} + \frac{E_H}{V}\right)} \quad (4-1)$$

This outcome is a common problem when this old solubility parameter concept is used for any two materials having similar structures. The Hildebrand solubility parameter generally works well in a non-polar system only because it does not consider hydrogen bonding and polar interaction. However, the Hansen solubility parameters are calculated and expressed as three interaction parameters ( $\delta_D, \delta_P, \delta_H$ ) each for P3HT and PC<sub>61</sub>BM as 19.1, 3.9, 6.4 and 19.39, 5.91, 4.96, respectively. Based on these calculated values, both of these parameters have similar dispersion interactions, and PC<sub>61</sub>BM has higher polar interaction from the attached side chain and higher hydrogen bonding than P3HT. The inherent solubility ‘distance’ ( $R_o$ ) values of P3HT and PCBM, using the official Hansen solubility parameter calculation software HSPiP, are 6.43 and 6.2 MPa<sup>1/2</sup>, respectively.

The solubility ‘distance’ ( $R_a$ ) between two materials based on their respective partial Hansen solubility parameters is calculated using Equation (4-2), and the relative energy density (RED) values are calculated based on the  $R_a$  and  $R_o$  values using Equation (4-3).

$$R_a = \sqrt{4(\delta_{D_1} - \delta_{D_2})^2 + (\delta_{P_1} - \delta_{P_2})^2 + (\delta_{H_1} - \delta_{H_2})^2} \quad (4-2)$$

$$RED = \frac{R_a}{R_o} \quad (4-3)$$

If the RED values are less than 1 ( $RED < 1$ ), the solute dissolves well in a solvent (here, component 1 is a solute, and component 2 is a solvent). The Flory-Huggins interaction parameter ( $\chi_{12}$ ) can be calculated using Equation (4-4) (assuming a high molecular weight solute, such as a polymer)[168]; if this value is less than 0.5 ( $\chi_{12} < 0.5$ ), then it dissolves well in a solvent.

$$\chi_{12} = 0.5 \times (RED)^2 = 0.5 \times \left( \frac{R_a}{R_o} \right)^2 \quad (4-4)$$

The critical point that expresses the solubility limit of a solute in a solvent has  $RED = 1$  and  $\chi_c = 0.5$ . In the Hansen solubility parameters sphere model, if the solubility values of a solvent are close to the borderline of the solubility parameter sphere of the solute, or are greater than the radius of that sphere, then each specific solvent cannot dissolve the particular solute.

Based on the calculated Hansen solubility parameters, the interaction between some of the good solvents, such as CB, ODCB, TCB and DBT etc., and solutes, including P3HT and PC<sub>61</sub>BM, are shown in Figure 4.2 and summarized in Table 3.1. The big Hansen solubility parameter spheres of P3HT and PC<sub>61</sub>BM using each calculated inherent solubility ‘distance’ ( $R_o$ ) values as radii contain several co-solvents that could dissolve them. Most of these co-solvents are located at the overlapped portions of the Hansen solubility parameters sphere models of P3HT and PC<sub>61</sub>BM. As the distance between the solute centers and solvent centers increases, the solute’s solubility worsens in those solvents. For example, xylene, toluene and 3HT, which are located near the perimeter of the sphere models, can dissolve both P3HT and PC<sub>61</sub>BM, but they are relatively bad solvents compared with CB and ODCB, which are located near the centers of both the P3HT and PCBM sphere models.

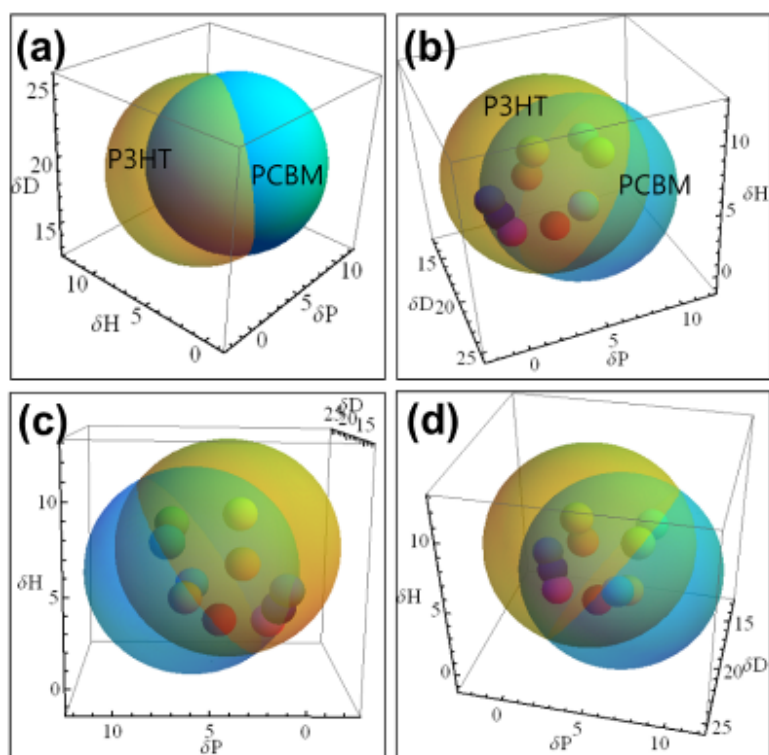


**Figure 4.2. Hansen-solubility parameters ( $\delta_D$ ,  $\delta_P$ ,  $\delta_H$ ), sphere models of all good solvents listed in Table 3.1 for P3HT:PCBM BHJ mixtures from various viewpoints.**

#### **4.2.2. Miscibility Model of *In Situ* UV Photo-polymerized Oligothiophenes using Hansen Solubility Parameters**

The *in situ* UV photo-polymerization of DBT in a P3HT:PC<sub>61</sub>BM BHJ active layer results in changes in the morphology. A DBT monomer is a relatively good solvent for both P3HT and PCBM, and its Flory-Huggins interaction parameters ( $\chi_{12}$ )[168], based on the compatibility with P3HT and PC<sub>61</sub>BM, are calculated as 0.19 and 0.14, respectively. DBT is not a bad solvent for P3HT and PC<sub>61</sub>BM, and has a higher boiling point ( $b_p$ ) and lower vapor pressure than those of chloroform and xylene, etc. Due to the high boiling point ( $b_p$ ) of 211°C, DBT is not a good selection as a spin casting solvent at a low spin casting speed to have 100 nm thickness of P3HT:PC<sub>61</sub>BM BHJ active layers on substrates. However, *in situ* UV photo-polymerization of DBT as a post process worked successfully to control the morphology and crystallinity of P3HT:PC<sub>61</sub>BM BHJ film. As the molecular weight increases, the miscibility

of P3HT and PC<sub>61</sub>BM decreases, as expected from the Hansen solubility parameters calculation. This decrease leads to additional finer morphology in a P3HT:PC<sub>61</sub>BM BHJ active layer.

The calculated RED of the Hansen solubility parameters and  $\chi_{12}$  values of the oligothiophenes gradually increase with an increase in the number of repeating units, and the solubility of *in situ* UV photo-polymerized oligothiophenes decrease, as summarized in Figure 4.3 and Table 4.1.

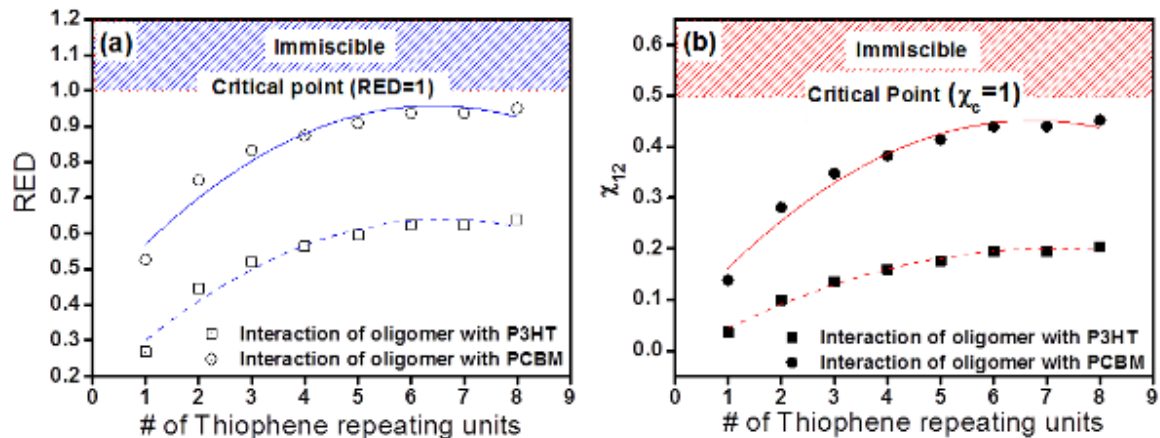


**Figure 4.3. Calculated Flory-Huggins interaction parameters ( $\chi_{12}$ ) and relative energy density (RED) of oligothiophenes with different repeat units in a P3HT: PC<sub>61</sub>BM BHJ mixture.**

The morphology during the DBT deposition (DBT solvent annealing) improves and becomes finer than the morphology of an as-cast BHJ active layer, as discussed in Chapter 3. Further *in situ* UV photo-polymerization of the deposited DBT results in enhanced and finer morphology in a P3HT:PC<sub>61</sub>BM BHJ active layer. Additionally, better crystalline phase orientation of P3HT in BHJ active layer can be achieved in the optimal process condition than those with the conventional thermal annealing.

**Table 4.1. P3HT/ PC<sub>61</sub>BM miscibility with oligothiophenes (determined by Hansen solubility parameters @ 25°C).**

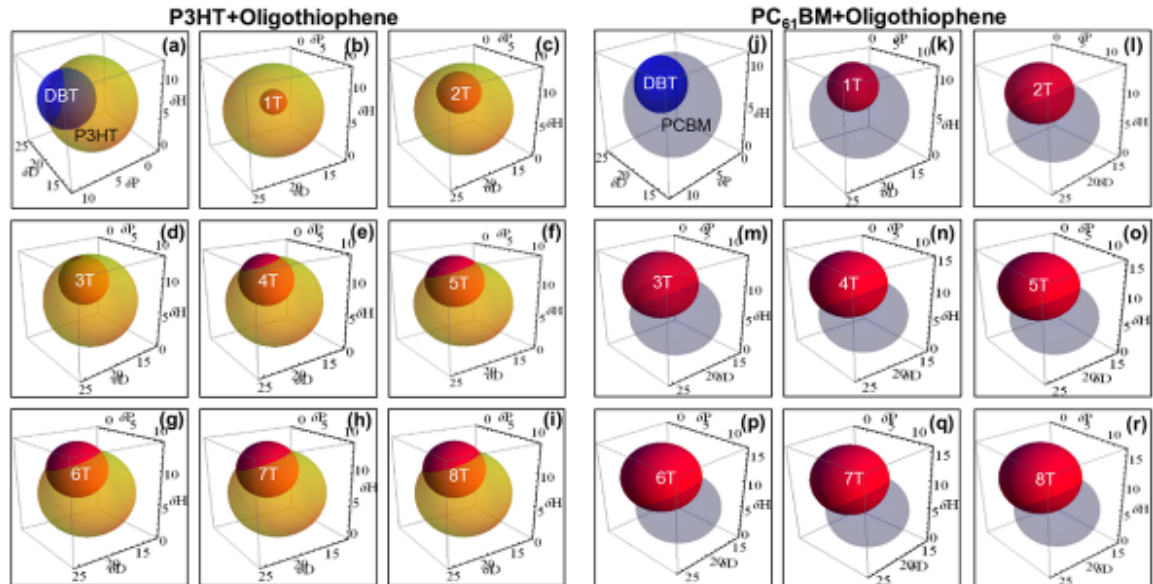
| <i>Solutes</i>             | $\delta_D$ | $\delta_P$ | $\delta_H$ | $\delta_T (MPa^{1/2})^a$ | $R_o$ or $R_a$         | $RED^b$ | $\chi_{12}^c$ | <i>Miscibility</i> | <i>Solubility in CB</i> |
|----------------------------|------------|------------|------------|--------------------------|------------------------|---------|---------------|--------------------|-------------------------|
| Poly(3hexylthiophene) P3HT | 19.1       | 3.9        | 6.4        | 20.52                    | 6.43 (R <sub>o</sub> ) | -       | -             | -                  | Soluble                 |
| 2,5-dibromothiophene (DBT) | 20.1       | 7.1        | 7.7        | 22.67                    | 3.99                   | 0.62    | 0.19          | Soluble (liquid)   | Soluble                 |
| 1T (Thienyl)               | 19.4       | 4.5        | 7.9        | 21.43                    | 1.72                   | 0.27    | 0.04          | Soluble (liquid)   | Soluble                 |
| 2T                         | 19.7       | 3.7        | 9.0        | 21.97                    | 2.87                   | 0.45    | 0.10          | Miscible           | Soluble                 |
| 3T                         | 19.8       | 3.4        | 9.4        | 22.18                    | 3.35                   | 0.52    | 0.14          | Miscible           | Soluble                 |
| 4T                         | 19.9       | 3.3        | 9.6        | 22.34                    | 3.63                   | 0.56    | 0.16          | Miscible           | Soluble                 |
| 5T                         | 19.9       | 3.2        | 9.8        | 22.41                    | 3.82                   | 0.59    | 0.18          | Miscible           | Soluble                 |
| 6T                         | 20.0       | 3.1        | 9.9        | 22.53                    | 4.02                   | 0.53    | 0.195         | Miscible           | Insoluble               |
| 7T                         | 20.0       | 3.1        | 9.9        | 22.53                    | 4.02                   | 0.53    | 0.195         | Miscible           | Insoluble               |
| 8T                         | 20.0       | 3.1        | 10.0       | 22.58                    | 4.10                   | 0.64    | 0.204         | Miscible           | Insoluble               |

| <i>Solutes</i>             | $\delta_D$ | $\delta_P$ | $\delta_H$ | $\delta_T (MPa^{1/2})^a$ | $R_o$ or $R_a$        | $RED^b$ | $\chi_{12}^c$ | <i>Miscibility</i> | <i>Solubility in CB</i> |
|----------------------------|------------|------------|------------|--------------------------|-----------------------|---------|---------------|--------------------|-------------------------|
| PC <sub>61</sub> BM        | 19.39      | 5.91       | 4.96       | 20.04                    | 6.2 (R <sub>o</sub> ) | -       | -             | -                  | Soluble                 |
| 2,5-dibromothiophene (DBT) | 20.1       | 7.1        | 7.7        | 22.67                    | 3.31                  | 0.53    | 0.14          | Soluble (liquid)   | Soluble                 |
| 1T (Thienyl)               | 19.4       | 4.5        | 7.9        | 21.42                    | 3.26                  | 0.526   | 0.14          | Soluble (liquid)   | Soluble                 |
| 2T                         | 19.7       | 3.7        | 9.0        | 21.97                    | 4.65                  | 0.75    | 0.28          | Miscible           | Soluble                 |
| 3T                         | 19.8       | 3.4        | 9.4        | 22.18                    | 5.17                  | 0.83    | 0.35          | Miscible           | Soluble                 |
| 4T                         | 19.9       | 3.3        | 9.6        | 22.34                    | 5.42                  | 0.87    | 0.38          | Miscible           | Soluble                 |
| 5T                         | 19.9       | 3.2        | 9.8        | 22.41                    | 5.64                  | 0.91    | 0.41          | Miscible           | Soluble                 |
| 6T                         | 20.0       | 3.1        | 9.9        | 22.53                    | 5.81                  | 0.94    | 0.44          | Miscible           | Insoluble               |
| 7T                         | 20.0       | 3.1        | 9.9        | 22.53                    | 5.81                  | 0.94    | 0.44          | Miscible           | Insoluble               |
| 8T                         | 20.0       | 3.1        | 10.0       | 22.57                    | 5.90                  | 0.95    | 0.45          | Miscible           | Insoluble               |

a: Hildebrand solubility parameters ( $\delta_T^2 = \delta_D^2 + \delta_P^2 + \delta_H^2$ ), b: relative energy density (RED) of Hansen solubility parameter ( $RED = R_a/R_o$ ), c:  $\chi_{12} = \chi_c (RED)^2$

The simulated Hansen solubility parameter sphere models with an increasing number of repeating units of oligothiophene, are shown in Figure 4.4.



**Figure 4.4. Hansen-solubility parameters ( $\delta_D$ ,  $\delta_P$ ,  $\delta_H$ ), sphere models for the miscibility studies of oligothiophenes with P3HT and PC<sub>61</sub>BM: (a) P3HT in DBT, (j) PC<sub>61</sub>BM in DBT, (b) ~ (i) interaction between P3HT and oligothiophenes having different repeating units, (k) ~ (r) interaction between PC<sub>61</sub>BM and oligothiophenes having different repeating units (radii of oligothiophenes are  $R_a$ ).**

The *in situ* UV photo-polymerized oligothiophenes have molecular weight distributions, but this model, which is calculated based on a single molecular model, does not have molecular weight distribution due to the complexity and difficulty of the calculation.

As the chains grow, the Hansen solubility parameters ‘distances’( $R_0$ ) become longer and the center positions of oligothiophenes are far from the centers of both P3HT and PC<sub>61</sub>BM, which indicates that the solubility of the polymerized oligothiophenes worsenes in the BHJ active mixture. This solubility drop is the fundamental driving force for further phase separation, resulting in a much smaller domain size than is found from the pre-steps, a spin casting and a DBT vapor deposition. The calculated RED and Flory-Huggins interaction parameters ( $\chi_{12}$ ) are still less than the values of the critical points; therefore, severe macro-phase separation is not expected. The solubility drop of the oligothiophenes during the dynamic *in situ* photopolymerization of DBT inside the PC<sub>61</sub>BM domain is more intensified than in the P3HT domain, and as expected, a large PC<sub>61</sub>BM cluster formation is effectively

prohibited during this process. R-SoXS results confirm this results, the weaker scattering intensity of a P3HT:PC<sub>61</sub>BM BHJ active layer in this new process is identified than that using thermal annealing only as shown in Figure 4.5 (a).

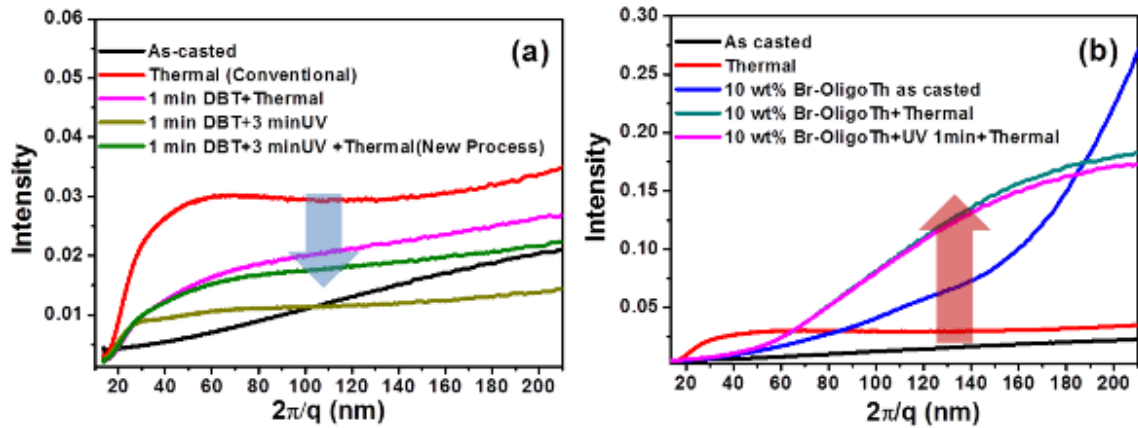


**Figure 4.5.** R-SoXS data of (a) the optimized new post casting process steps for P3HT:PC<sub>61</sub>BM BHJ films: DBT vapor deposition at 80°C 1 min and UV exposure 3 min; thermal annealing at 150°C 20 min; thickness = 100 nm, and (b) catalytically synthesized Br-terminated  $\alpha,\omega$ -dibromo-oligothiophene (10wt%) introduced P3HT:PC<sub>61</sub>BM BHJ films.

This *in situ* UV photo-polymerization of DBT is a dynamic process. The rapid solubility drop that occurs within a short time and within the critical point of solubility ( $\chi_c$ ) limit results in a smaller domain and more homogeneous phase in the P3HT:PCBM BHJ films than those determined in the conventional annealing process. However, a P3HT:PCBM BHJ mixture with synthesized Br-terminated  $\alpha,\omega$ -dibromo-oligothiophenes (10wt%) in a starting solution has a much larger domain and larger PC<sub>61</sub>BM clusters than post thermal annealed P3HT:PCBM BHJ films even using the new process as shown in Figure 4.5 (b) (Detailed chemical information regarding synthesized Br-terminated  $\alpha,\omega$ -dibromo-oligothiophenes is included in the Appendix I) and this huge domain results in poor solar cell performance. The scattering intensity of R-SoXS increases more than five times that of conventional samples processed in the conventional thermal annealing, which means that a purer crystalline phase than that of thermal annealed samples grows via the rapid macro-phase separation between P3HT and PC<sub>61</sub>BM due to the inherent low miscibility of the added Br-terminated  $\alpha,\omega$ -dibromo-oligothiophenes in a P3HT and PC<sub>61</sub>BM BHJ mixture.

In this section, the UV photo-polymerization-induced solubility drop and phase separation of a P3HT:PCBM BHJ mixture are simulated using the Hansen solubility parameters sphere models. These simulations strongly support this study's assumption and explanation of the working principle of the new *in situ* UV photo-polymerization induced phase separation (PIPS) process in a P3HT:PC<sub>61</sub>BM BHJ active layer as an new effective post casting process to enhance the performance of P3HT:PC<sub>61</sub>BM BHJ polymer solar cells.

### 4.3. *In Situ* UV-Photo-Polymerization of DBT: Control of Nano-Scale Morphology and Crystalline Orientations of P3HT:PC<sub>61</sub>BM BHJ Polymer Solar Cells

In this section, the *in situ* UV photo-polymerization of DBT in a P3HT:PC<sub>61</sub>BM BHJ active layer is demonstrated as a new idea for the post casting process for P3HT:PC<sub>61</sub>BM BHJ polymer solar cells, as shown in Figure 4.6.

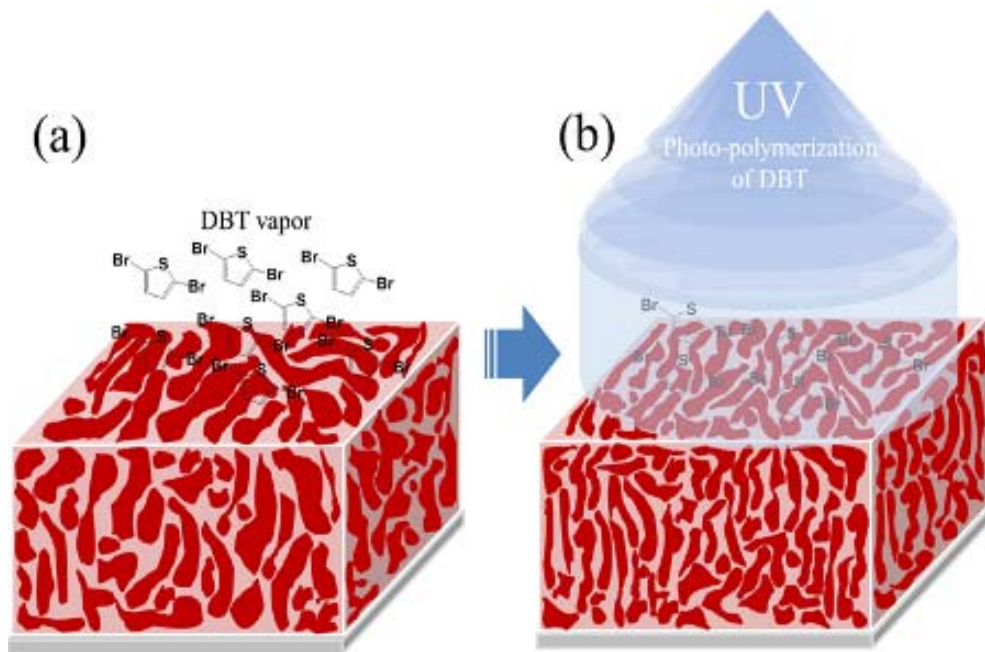


Figure 4.6. *In situ* UV photo-polymerization-induced phase separation for nano-scale morphology control of P3HT:PC<sub>61</sub>BM BHJ polymer solar cells: (a) DBT vapor deposition on an as-cast P3HT: PC<sub>61</sub>BM BHJ active layer, (b) *in situ* UV photo-polymerization of DBT for nano-scale morphology control.

### 4.3.1. Morphological Evolution of P3HT:PC<sub>61</sub>BM BHJ Active Layers in *In Situ* UV Photo-polymerization of DBT

The surface morphology of the *in situ* UV photo-polymerization of DBT in a P3HT: PC<sub>61</sub>BM BHJ active layer is examined using AFM images, as shown in Figure 4.7. The domain size of an as-cast P3HT:PC<sub>61</sub>BM BHJ active layer, calculated from the 2D-FFT phase mode images, increases slightly with conventional thermal annealing at 150°C for 20 minutes due to the growth of the crystallinity of P3HT and PC<sub>61</sub>BM inside the phase separated domains as studied in Chapter 3.

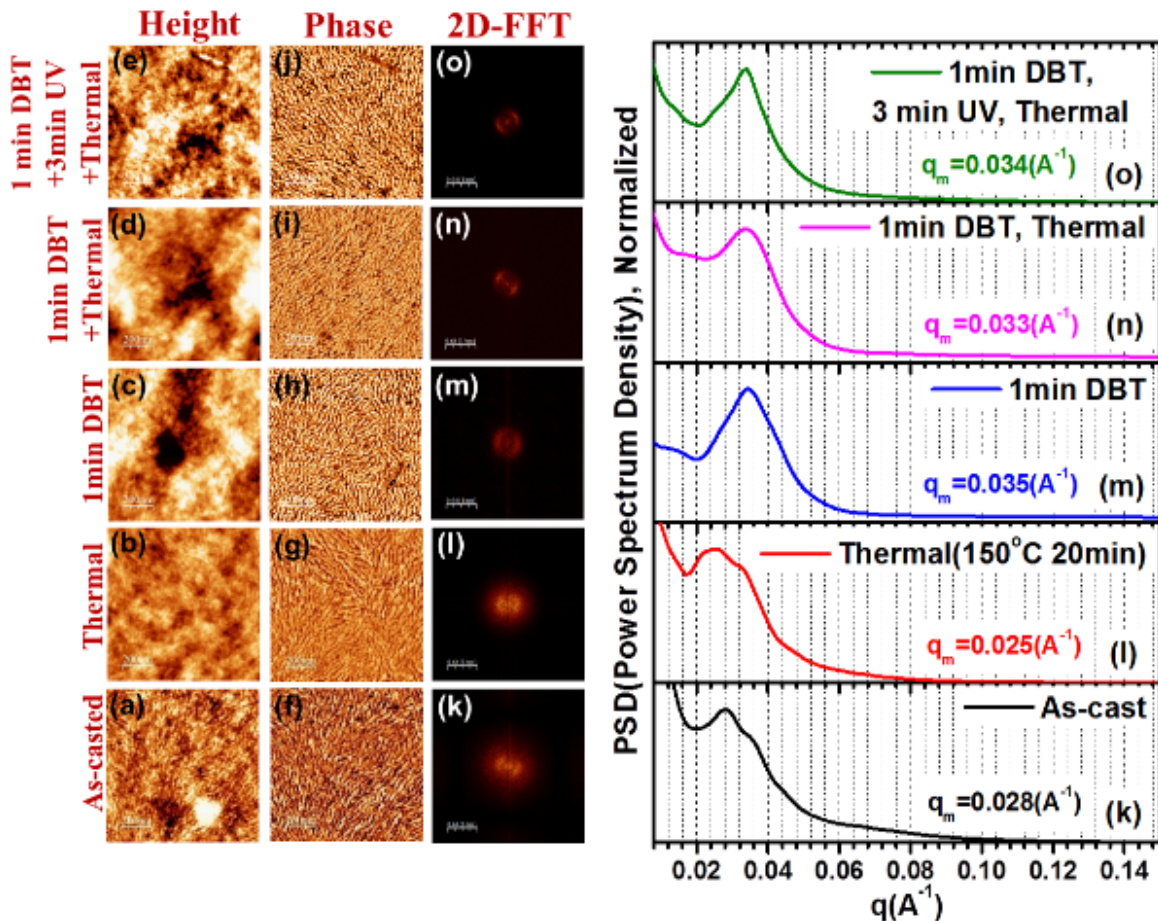
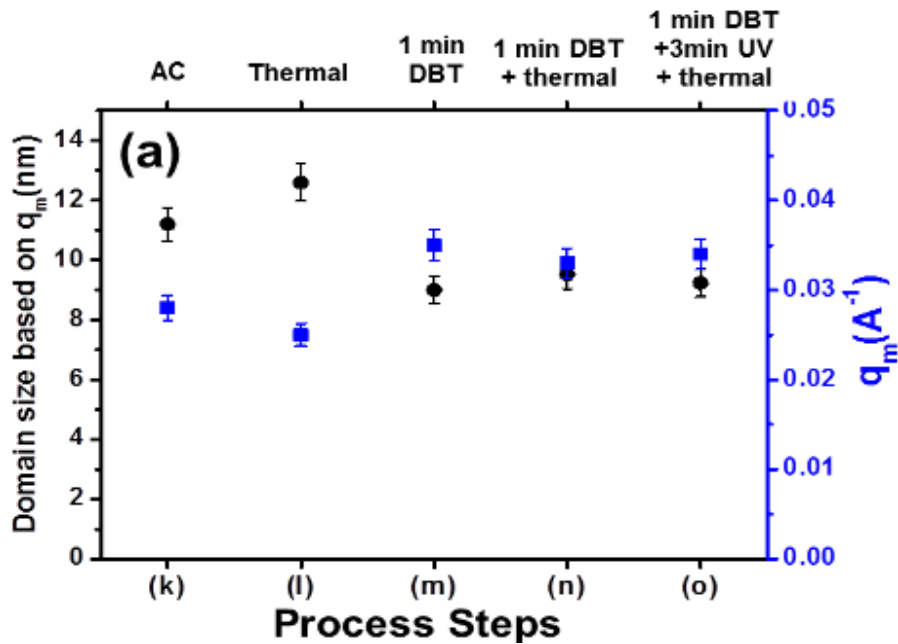


Figure 4.7. AFM images and 2D-FFT phase mode profiles of the optimized new post casting process steps for P3HT: PC<sub>61</sub>BM BHJ films: DBT vapor deposition at 80°C 1 min, UV exposure 3 min, and thermal annealing at 150°C 20 min; process steps (b) and (d) are introduced for comparison only;  $q_m$  means  $q_{(max)}$ .

When DBT vapor deposition occurs on a P3HT:PC<sub>61</sub>BM BHJ active layer for 1 minute and broadens the domain size distribution with 3 minutes of UV exposure, the 2D FFT peak from the phase image of the AFM becomes sharper than it does for 1 minute DBT vapor only, even with final post thermal annealing, as shown in Figure 4.8 (b). The final domain size shown in Figure 4.7 (o) and Figure 4.8 (a), as determined through the new post casting process, is less than 10 nm.



**Figure 4.8. Domain size analysis based on  $q_m$  values from 2D-FFT profiles of phase mode images in Figure 4.7.**

This domain size is close to the exciton diffusion length in the final thermal annealing, and the resultant improvement of the PCE is around 20% higher than that with conventional thermal annealing only. (Details regarding solar cell performance are discussed in Chapter 5.) The photon absorption spectrum is also enhanced by the new post casting process, as shown in Figure 4.9. However, enhancement of the photon absorption is not large enough to explain of 20% PCE improvement in the final P3HT:PC<sub>61</sub>BM BHJ polymer solar cells. Therefore, this improvement is due not to thickness or photon absorption, but mainly due to improvement of the charge separation and transport from the optimized morphology and crystalline phase orientation.

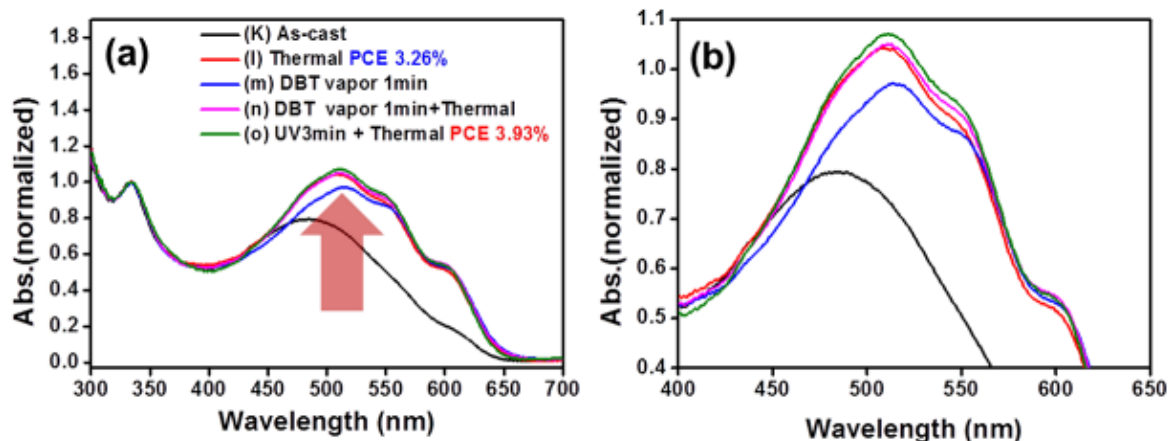


Figure 4.9. (a) UVvis spectrophotometer spectra of the optimized process steps and (b) zoomed-in P3HT absorption spectra.

The R-SoXS intensity of the BHJ active layers from the new post process are compared with that from the conventional post thermal annealing only as shown in Figure 4.10.

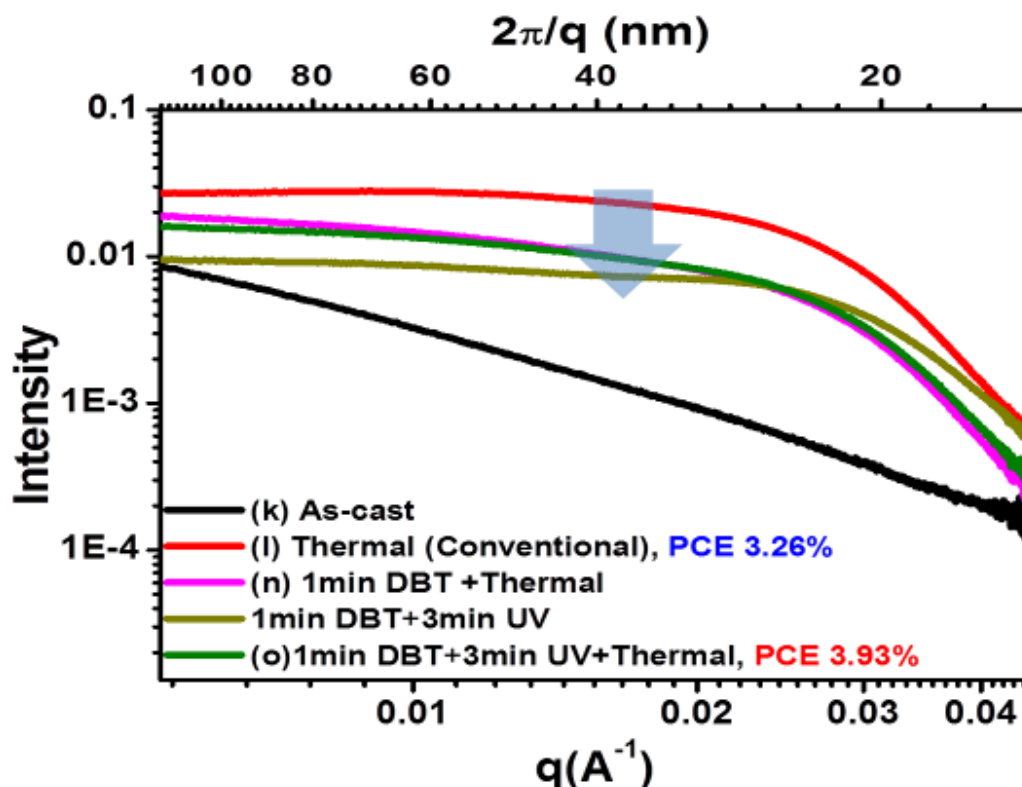


Figure 4.10. R-SoXS data of the optimized new post process steps for P3HT: PC<sub>61</sub>BM BHJ films: DBT vapor deposition at 80°C, 1 min, and UV exposure 3 min; post thermal annealing at 150°C 20 min; thickness = 100 nm. Process steps (l) and (n) are introduced for comparison only.

The spin coated P3HT:PC<sub>61</sub>BM BHJ films on the PSS pre-coated Si wafer are floated on the water surface and free-standing films are prepared. The R-SoXS experiments are carried out using 284.2eV X-ray energy, at beam line 11.0.1.2 of ALS, LBNL. R-SoXS data show the bulk morphological information of P3HT:PC<sub>61</sub>BM BHJ Active Layer.

The lower scattering intensity of the new post casting process is shown in comparison with that of the conventional thermal annealing only. The scattering intensity originates in the contrast difference between P3HT and PC<sub>61</sub>BM inside a BHJ active layer and the lower scattering intensity means that there is less pure domain inside a BHJ active layer due to the existence of the intermixed zone between P3HT and PC<sub>61</sub>BM.

Less pure domain leads to better performance in terms of charge carrier generation in the P3HT:PC<sub>61</sub>BM BHJ polymer solar cells. The 3-minute UV exposure on a 1-minute DBT deposited P3HT:PC<sub>61</sub>BM BHJ active layer results in a much smaller nano-scale domain size than occurs with conventional thermal annealing only, as already determined from the AFM results. This is due to the rapid solubility drop of the UV photo-polymerized oligothiophenes inside P3HT:PC<sub>61</sub>BM BHJ active layer and it results in additional finer nano-scale phase separation inside BHJ active layer than that of the conventional thermal annealing only.

The domain size of a P3HT:PC<sub>61</sub>BM BHJ active layer with 3-minute UV exposure increases again with thermal annealing due to the enhanced crystallization of P3HT and PC<sub>61</sub>BM. The scattering intensity of R-SoXS also increases slightly with thermal annealing, but its intensity is still much less than that from conventional thermal annealing only, which it means that the new post casting process can enhance the performance of P3HT:PC<sub>61</sub>BM BHJ polymer solar cells.

#### **4.3.2. Crystalline Phase Growth and Orientation of P3HT:PC<sub>61</sub>BM BHJ Active Layers in *In Situ* UV Photo-polymerization of DBT**

Wide angle x-ray scattering study of the P3HT:PC<sub>61</sub>BM BHJ active layers processed in the new post casting process were performed using a GIWAXS technique at Brookhaven National Laboratory (BNL). Experiment was performed by Dr. Xinhui Lu and the critical

angle is  $0.1^\circ$  and the back group subtraction including Si and PEDOT:PSS is done by using a Nika package. It is the study of the bulk property P3HT:PC<sub>61</sub>BM BHJ active layers.

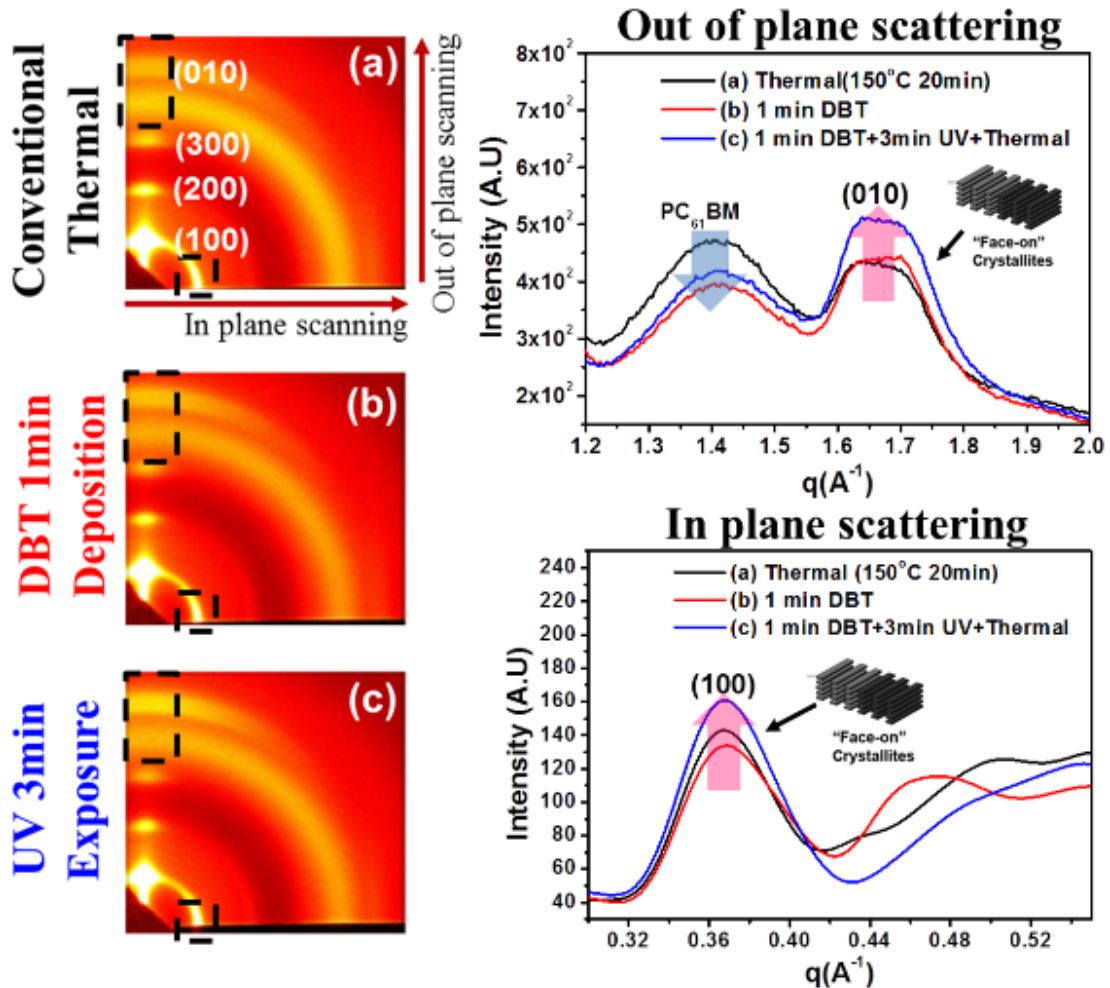


Figure 4.11. GIWAXS data of *in situ* UV photo-polymerization of DBT in P3HT:PC<sub>61</sub>BM BHJ active layers: (a) conventional post thermal annealing (150°C 20 min); (b) DBT vapor (80°C 1 min); (c) UV exposure 3 min (Experiment was performed by Dr. Xinhui at NSLS).

There are two phases of crystalline orientation of P3HT in a thin film on a hydrophilic surface, such as thin PEDOT:PSS film coated ITO. The major orientation is the ‘edge on’ orientation, and its  $\pi$ - $\pi$  orbital orientation direction is perpendicular to the electric field between a cathode and an anode. It is not effective to have enhanced charge transport in P3HT:PC<sub>61</sub>BM BHJ polymer solar cells. However, the ‘face on’ orientation has the  $\pi$ - $\pi$  orbital orientation of the aromatic thiophene ring parallel to the electric field, and this slight

enhancement results in a large improvement in the charge carrier transport because the inter molecular charge percolation comes from the right direction. The P3HT:PC<sub>61</sub>BM BHJ polymer solar cells that are processed using the new post casting process, *in situ* UV photo-polymerization of DBT, exhibit a larger volume fraction of the ‘face on’ orientation in the P3HT:PC<sub>61</sub>BM BHJ active layer than it does from conventional post thermal annealing only, as shown in Figure 4.11 and Table 4.2.

**Table.4.2. Calculated P3HT crystalline phase sizes and the total amount of crystalline phase in P3HT: PC<sub>61</sub>BM BHJ active layers.**

|                           |       | $Peak_{Area}$ | $Area\ Ratio\ (010)/(100)$ | $I_{max}$ | $Size, t(nm)$ |
|---------------------------|-------|---------------|----------------------------|-----------|---------------|
| (a) Thermal (150°C 20min) | (100) | 623.5         | 0.043                      | 10409.3   | 13.11         |
|                           | (010) | 27.0          |                            | 178.42    | 5.65          |
| (b) DBT 1min              | (100) | 539.8         | 0.059                      | 7504.15   | 11.9          |
|                           | (010) | 32.1          |                            | 208.32    | 4.94          |
| (c) UV 3min + Thermal     | (100) | 534.9         | 0.073                      | 7415.23   | 11.73         |
|                           | (010) | 39.3          |                            | 259.64    | 4.85          |

As shown in Figure 4.11, the in-plane and out-of-plane GIWAXS scanning analysis of the P3HT crystalline phase orientation in a P3HT:PC<sub>61</sub>BM BHJ active layer confirms the increased weight fraction of the ‘face on’ orientation. That is, the integrated area ratio of the (100) and (010) peaks shows that ‘face on’ orientation of the P3HT crystalline phases (from the out-of-plane scan) inside a P3HT:PC<sub>61</sub>BM BHJ active layer from the new post casting process contains approximately 70% more ‘edge on’ orientation than the ratio of ‘edge on’ and ‘face on’ orientations obtained from conventional post thermal annealing only. This finding could be one of explanations to the better performance in terms of the PCE of the P3HT:PC<sub>61</sub>BM BHJ polymer solar cells fabricated using a new post casting process (detail solar cell performance will be reviewed in Chapter 5). Although a 14% decrease of volume fraction is evident in the ‘edge on’ P3HT orientation from the new post casting process compared with that of the conventional thermal annealing, this decrease may not critically affect the final solar cell performance, because the ‘edge on’ P3HT orientation is not the preferred P3HT crystalline phase orientation for P3HT:PC<sub>61</sub>BM BHJ polymer solar cells.

Using a Debye-Scherrer equation the P3HT crystalline sizes can also be calculated for the new post casting process based on the GIWAXS results, which are compared with results from the conventional thermal annealing in Table 4.2. In the case of the new post casting

process, *in situ* UV photo-polymerization of DBT, the crystalline phase in the P3HT:PC<sub>61</sub>BM BHJ active layer is smaller than that of the conventional P3HT:PC<sub>61</sub>BM BHJ active layer with thermal annealing only. The crystalline phase sizes in the ‘edge on’ orientation of P3HT in a BHJ active layer from the new post casting process and the conventional thermal annealing are around 11.73 and 13.11 nm, respectively. This finding supports the goal of this research that this new post casting process provides critical changes in the morphology and crystalline phase to improve the performance of P3HT: PC<sub>61</sub>BM BHJ polymer solar cells.

### **4.3.3. Process Optimization of *In situ* UV Photo-polymerization of DBT for the Best P3HT:PC<sub>61</sub>BM BHJ Polymer Solar Cells**

It is critical to find the optimal process conditions for the new post casting process, *in situ* UV photo-polymerization of DBT, in order to obtain optimal performance from the P3HT:PC<sub>61</sub>BM BHJ polymer solar cells. UV exposure time (Figure 4.12) and DBT deposition time (Figure 4.15) are the most critical factors in achieving the highest level of efficiency in P3HT:PC<sub>61</sub>BM BHJ polymer solar cells.

The lateral domain size changes in various UV exposure times are shown in Figure 4.12 and 4.13. The lateral domain size of a DBT-deposited P3HT:PC<sub>61</sub>BM BHJ active layer for 1-minute is around 9 nm, based on the Peak<sub>max</sub> positions of 2D-FFT profiles of AFM phase mode images. The lateral domain size then increases slightly to 10.5 nm under 1-minute UV exposure followed by post thermal annealing. Under 3-minutes of UV exposure, the lateral domain size of the P3HT:PC<sub>61</sub>BM BHJ active layer again becomes smaller than any of the other devices as around 9 nm even followed by post thermal annealing. This processing condition, which includes 1-minute of DBT deposition and 3-minutes of UV exposure followed by a 150°C 20-minutes of post thermal annealing, reflects 20% more improved PCE of a P3HT:PC<sub>61</sub>BM BHJ polymer solar cell than is from the conventional post thermal annealing only (Detail solar cell performance will be discussed in Chapter 5). However, longer UV exposure, such as 5-or 10-minutes followed by post thermal annealing, shows a further increase in domain size due to the larger miscibility drop of *in situ* UV photo-

polymerized oligothiophenes from the longer time of the *in situ* UV photo-polymerization of DBT with a decrease in solar cell performance.

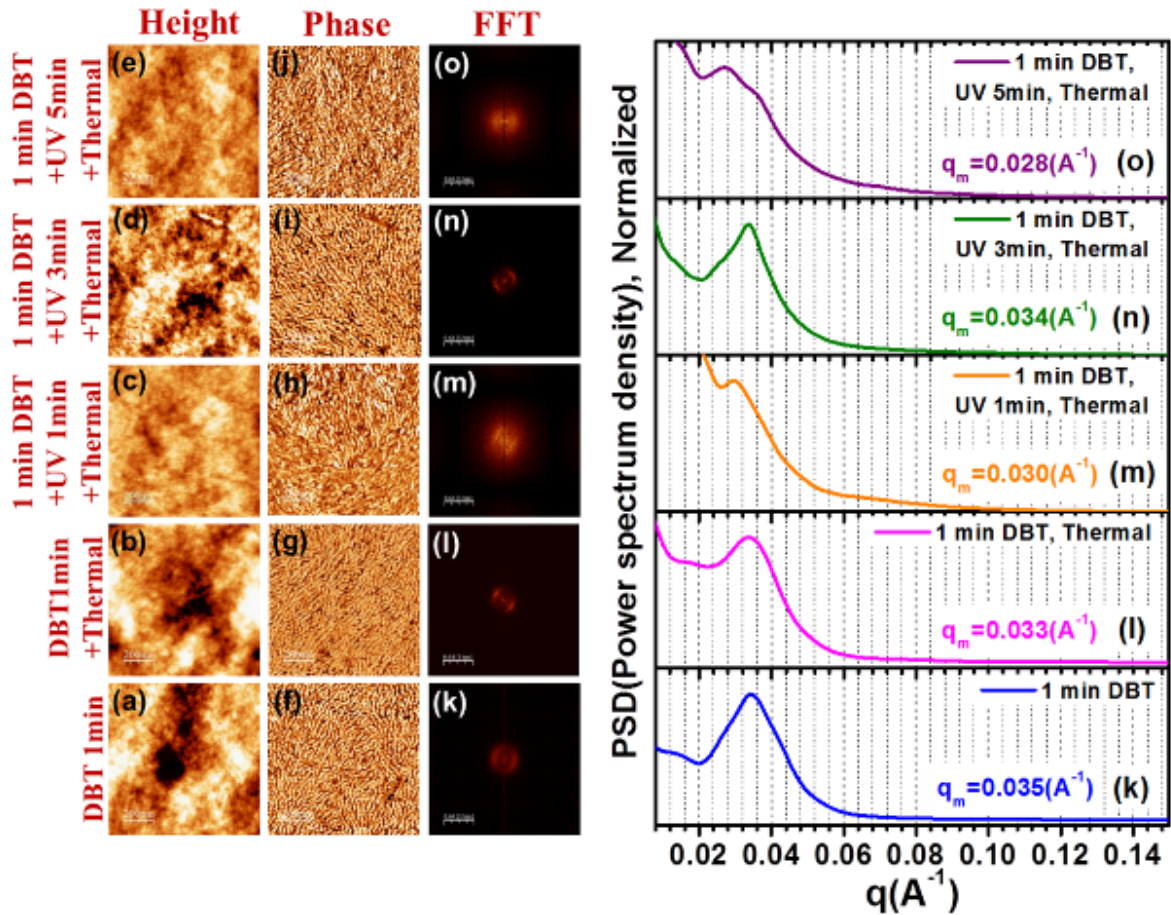


Figure 4.12. AFM images and 2D-FFT profiles of P3HT: PC<sub>61</sub>BM BHJ films for different UV exposure times: DBT vapor deposition at 80°C 1 min and post thermal annealing at 150°C 20 min; process step (b) is introduced for comparison only;  $q_m$  means  $q_{(\text{max})}$ .

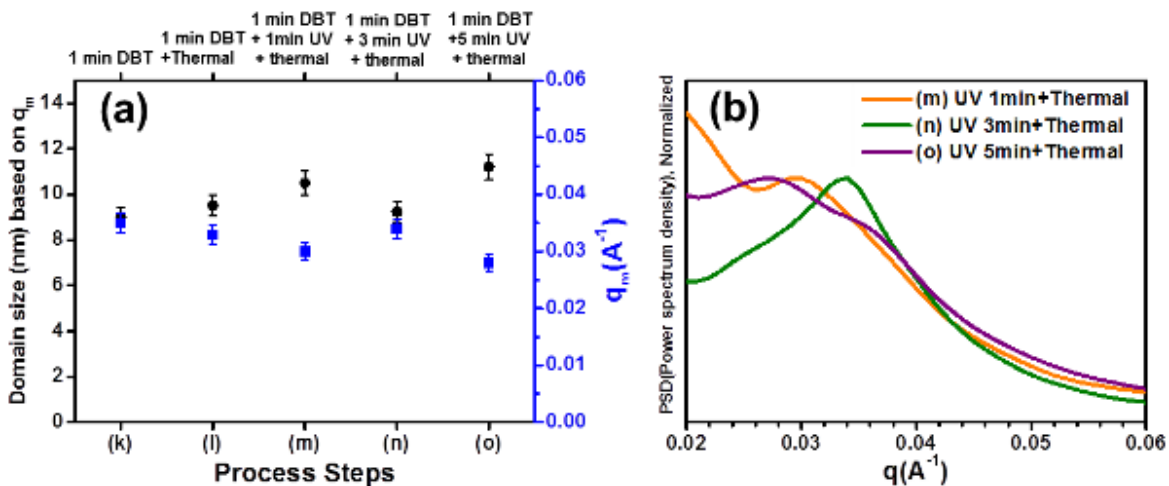


Figure 4.13. Domain size analysis based on  $q_m$  values from 2D-FFT profiles of phase mode images in Figure 4.13.

It appears that the rapid increase in lateral domain size in the early stage of 1-minute UV exposure is due mainly to the sudden increase in miscibility of DBT with P3HT caused by the transformation to thienyl radicals (1T), as shown in Figure 4.14.

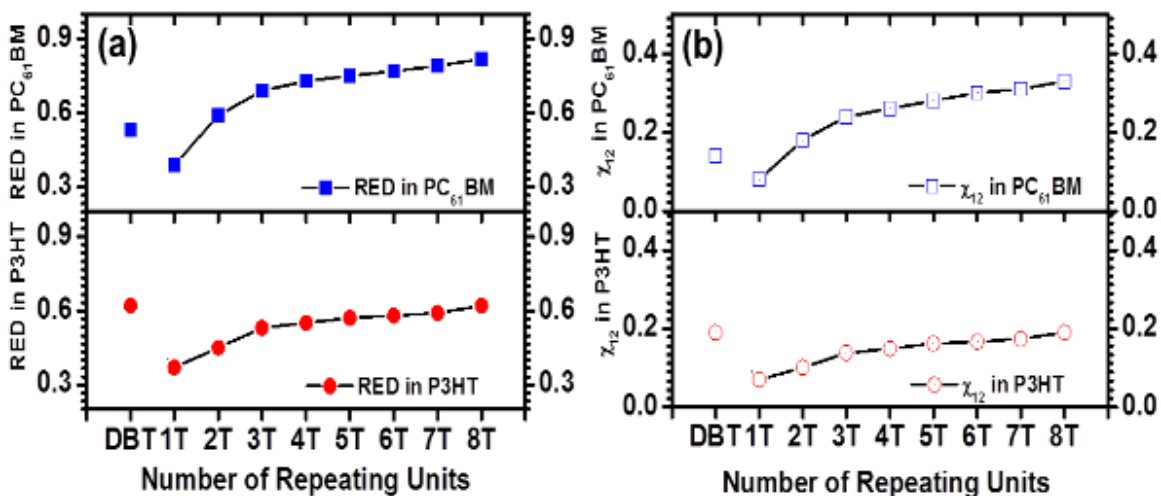


Figure 4.14. Miscibility changes of oligothiophenes during *in situ* UV photo-polymerization of DBT in a P3HT: PC<sub>61</sub>BM BHJ active layer: (a) RED changes; (b)  $\chi_{12}$  changes (Numbers in the x-axis stand for number of repeating units and T means thienyl).

Thienyl radicals form under controlled strong UV light by breaking the weak carbon-bromine bond during the *in situ* UV photo-polymerization of DBT. Polymer chain growth is carried out in a step-wise fashion with the bromine radical by-products inside a controlled O<sub>2</sub> free

environment. The critical points of RED and the Flory-Huggins interaction parameter ( $\chi_{12}$ ) are 1 and 0.5, respectively, and both values (RED and  $\chi_{12}$ ) gradually reach these critical points with an increasing number of repeating units during the *in situ* UV polymerization of DBT. The miscibility drop of *in situ* UV photo-polymerized oligothiophenes during the reaction with PC<sub>61</sub>BM is much stronger than for P3HT. The miscibility of DBT and thienyl radicals (1T) with PC<sub>61</sub>BM is similar and decreases gradually with an increase in the number of repeating units in an *in situ* UV photo-polymerized oligothiophene chain. Above the repeating unit number 6, the values of RED and  $\chi_{12}$  for PC<sub>61</sub>BM become saturated and almost reach the critical points as 0.95 and 0.45, respectively. In the case of P3HT, due to the similar chemical structure between thienyl and P3HT, the miscibility drop is not as severe as for PC<sub>61</sub>BM, but it does show a similar trend in that begins to become saturated at repeating number 6, and RED and  $\chi_{12}$  values for P3HT are 0.53 and 0.2, respectively.

In general, an annealing solvent that has not only good interaction with PC<sub>61</sub>BM, but also relatively poor solubility with P3HT, results in good morphology as shown in Chapter 3. However, *in situ* UV photo-polymerization of DBT is a dynamic process such that the rapid solubility change of the photo-polymerized oligothiophenes drives the change its miscibility with both P3HT and PC<sub>61</sub>BM in the BHJ active layer at the optimized process condition. Therefore, if the initial reactive monomer such as DBT is good enough to dissolve BHJ constituents, P3HT and PC<sub>61</sub>BM well, a special requirement as likely as that mentioned in solvent annealing does not required in this new post casting process. The miscibility of BHJ constituents can be finely tuned in this new post casting process and it easily results in finer lateral morphology than those from the conventional annealing processes.

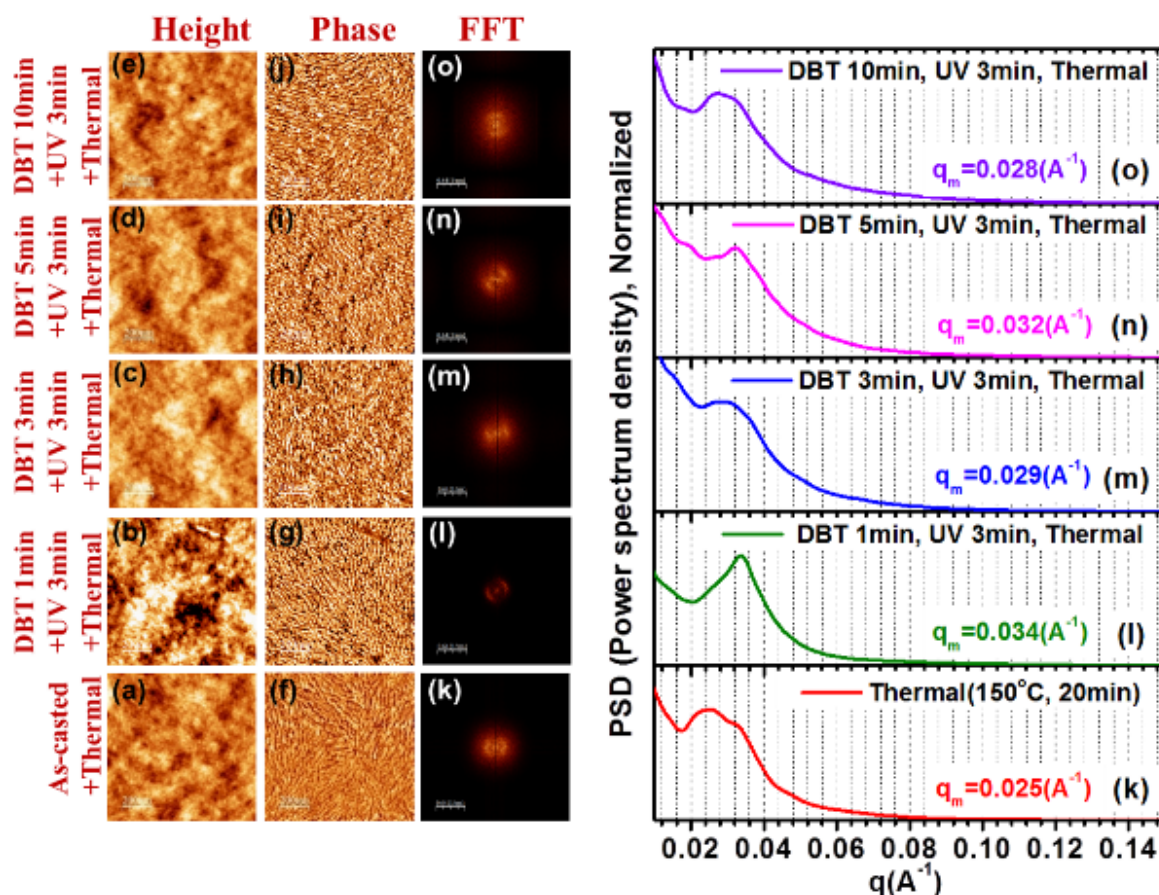


Figure 4.15. AFM images and 2D FFT profiles of phase mode images from P3HT:PC<sub>61</sub>BM BHJ films for different DBT deposition times: DBT vapor deposition at 80°C, UV exposure 3 min, and post thermal annealing at 150°C 20 min; process step (a) is included for comparison only;  $q_m$  means  $q_{(max)}$ .

As shown in Figure 4.15, a second critical factor for optimization is the DBT deposition time. This process itself does not differ from that of conventional solvent annealing. Normally, for the best performance, the solvent annealing time should be long enough to produce the best morphology with the best annealing solvent; however, DBT deposition as a pre-step for *in situ* UV photo-polymerization does not require a long time for the process.

As seen in Figures 4.15 and 4.16, a longer time for DBT deposition, such as 3-, 5-, and 10-minutes, results in larger lateral domain size than that in 1-minute, even when including UV exposure. The optimal DBT deposition time is 1-minute followed by 3-minutes of UV exposure.

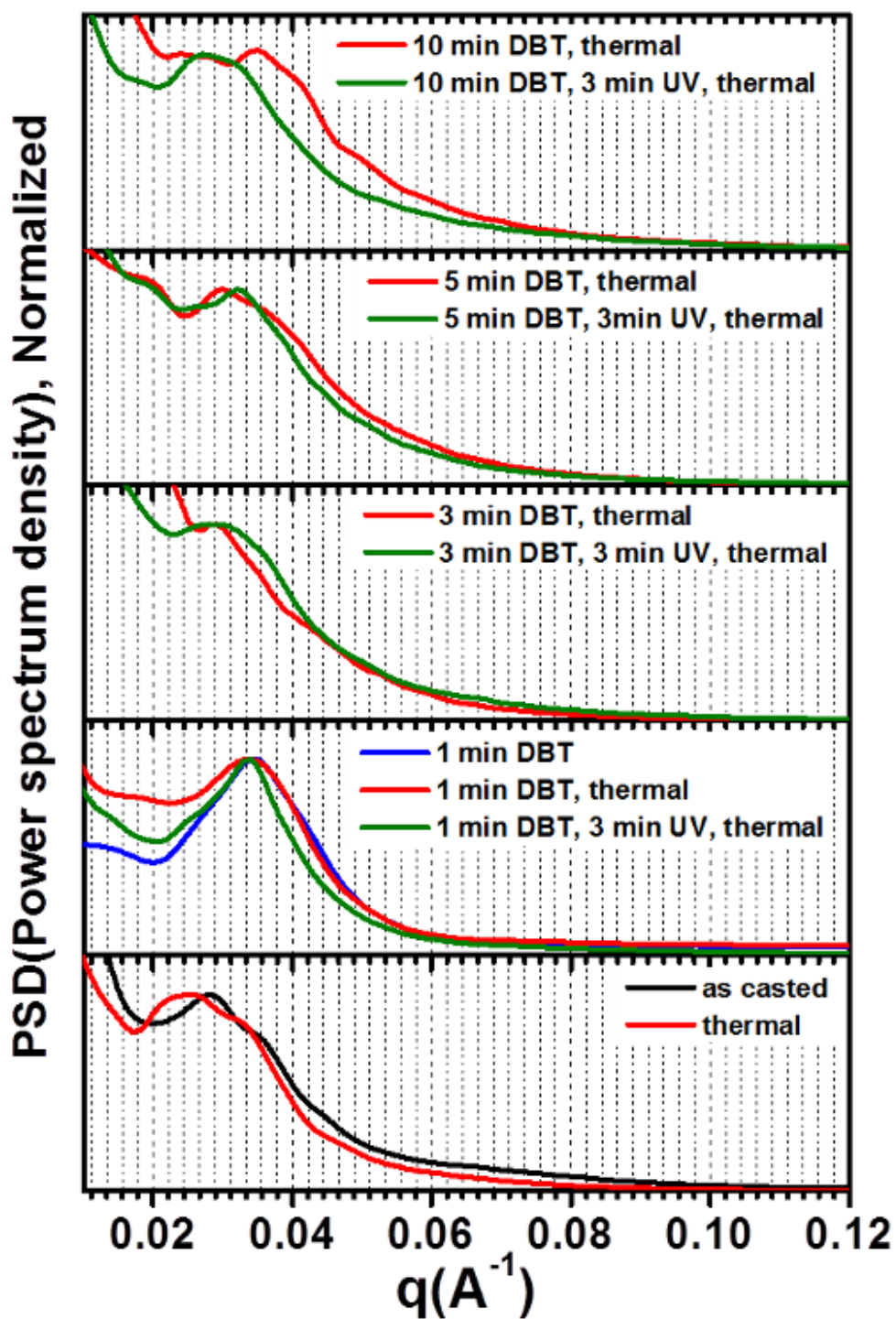
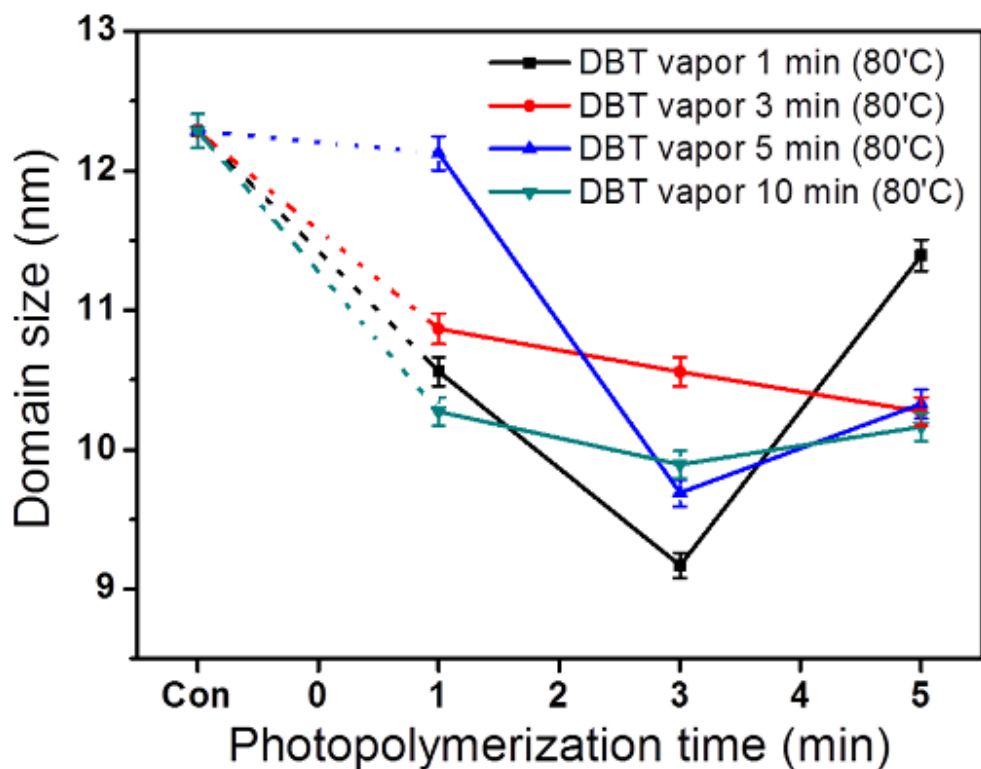


Figure 4.16. 2D FFT profiles of phase mode images from P3HT: PC<sub>61</sub>BM BHJ films for different DBT deposition times with/without thermal annealing: DBT vapor deposition at 80°C, UV exposure 3 min, and post thermal annealing at 150°C 20 min.



**Figure 4.17 Lateral domain size analysis using AFM: 2D-FFT profiles of phase mode images of P3HT:PC<sub>61</sub>BM BHJ active layers fabricated in various processing conditions of the new post casting process, *in situ* UV photo-polymerization of DBT (all the samples are analyzed with thermal annealing, 150°C 20-minutes).**

Figure 4.17 shows a summary for the process optimization of *in situ* UV photo-polymerization of DBT in various processing conditions based on the lateral domain sizes analyzed by AFM. In general, with an increase in DBT pre-deposition time, the domain size decreases, which is explained by the solubility effect during the solvent annealing process using DBT and the 3-minutes UV exposure is optimum, regardless of the DBT pre-deposition times. Longer UV exposure time results in the increase of their domain size again.

#### **4.3.4. Model for Morphological Evolution of P3HT:PC<sub>61</sub>BM BHJ Polymer Solar Cells in *In Situ* UV Photo-Polymerization of DBT**

In this Chapter 4, fundamental phenomena in a P3HT: PC<sub>61</sub>BM BHJ active layer during the new post casting process, *in situ* UV photo-polymerization of DBT, are examined. The thermal annealing process is currently the most effective post casting process that can produce the best P3HT: PC<sub>61</sub>BM BHJ polymer solar cells, but improvements can be made. Factors mentioned in this paper, such as the wrong P3HT orientation, the wrong vertical segregation of materials, and large PC<sub>61</sub>BM crystalline phase growth, should be improved or modified for optimal P3HT: PC<sub>61</sub>BM BHJ polymer solar cells. As a new answer to above listed problems, a new post casting process, *in situ* UV photo-polymerization of DBT, is demonstrated in this paper.

In general, there are two popular models that explain the morphological evolution in P3HT:PC<sub>61</sub>BM BHJ polymer solar cells. As mentioned in Chapter 3, in this paper, the first model that is based on the incompatibility of two component materials in a blend is adopted as a fundamental morphological evolution. And secondary, in the new process, *in situ* UV photo-polymerization of DBT, the solubility drop of the UV photo-polymerized oligothiophenes inside a BHJ active layer during the UV photo-polymerization of DBT, derives the further phase separation in P3HT: PC<sub>61</sub>BM BHJ active layer to have finer domain size, enhanced P3HT crystalline orientation, minimized the growth of PC<sub>61</sub>BM cluster.

Based on all the experimental results, the morphological evolution developed using the new post casting process, *in situ* UV photo-polymerization of DBT, is suggested as schematic diagrams in Figure 4.18. (a) ~ (c) represent the conventional thermal annealing steps. The morphology of the BHJ active layer is pre-conditioned during the spin casting step (b), and the post thermal annealing step (c) at the high temperature enhances the degree of crystallinity of P3HT and PC<sub>61</sub>BM inside phase separated domains. After spin casting (b), the new process follows the steps illustrated in Figure 4.18 (d) ~ (f).

The reactive monomer, DBT is vapor deposited on the P3HT:PC<sub>61</sub>BM BHJ active layer as a pre-step to UV exposure under the saturated vapor condition (at 80°C for 1 minute) as shown in step (d). During this step the morphology changes, depending on the deposition time and temperature, because the DBT is a low vapor pressure liquid that has a high boiling point, and fundamentally, this step is a solvent annealing step that uses the reactive monomer DBT. The next step (e) is UV exposure for a short time to initiate the condensation photo-polymerization of DBT by breaking the carbon-bromine bond.[237] The thienyl radicals that have reacted with other thienyl radicals result in the relatively small molecular weight of oligothiophene with bromine (Br<sub>2</sub>) gas as a by-product. The lowered solubility of the *in situ* UV photo-polymerized oligothiophene in a P3HT:PC<sub>61</sub>BM BHJ active layer leads to more phase separation of the BHJ active layer during the reaction than is the case with an as-cast BHJ active layer. Additionally, this lowered solubility of the photo-polymerized oligothiophene inside a BHJ active layer hinders the growth of the PC<sub>61</sub>BM crystalline cluster.

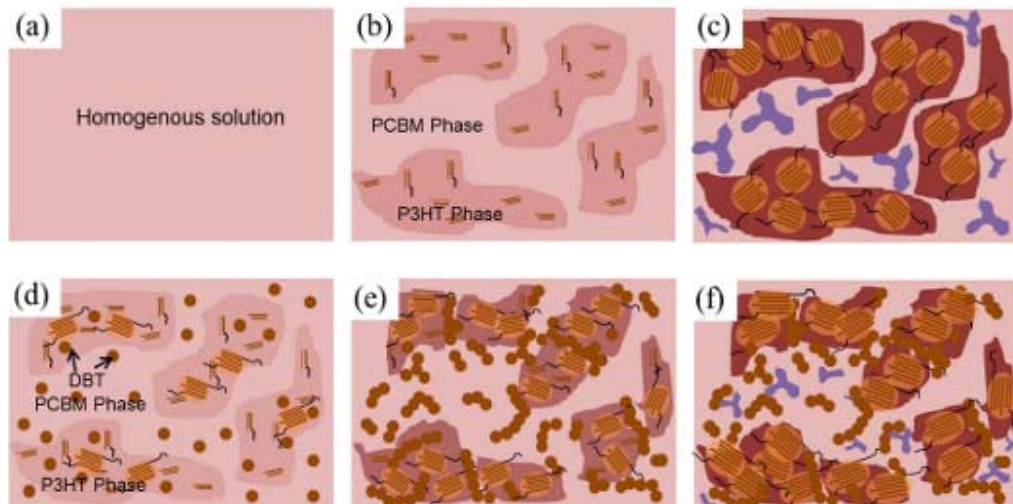


**Figure 4.18. Schematic diagrams of phase separation and crystallization of P3HT:PC<sub>61</sub>BM BHJ polymer solar cells: (a) homogeneous solution, (b) as-cast phase separated film, (c) growth of crystalline phase after thermal annealing, (d) DBT vapor deposition, (e) *in situ* UV photo-polymerization of DBT, (f) post thermal annealing. (a) ~ (c) represent the conventional process with post thermal annealing: (a), (b), (d), (e), and (f) are new processes showing the *in situ* UV photo-polymerization of DBT in P3HT:PC<sub>61</sub>BM BHJ polymer solar cells.**

#### 4.4 Conclusions.

In Chapter 4, a new post process based on the *in situ* UV photo-polymerization of DBT is presented and discussed. Under optimal process conditions, i.e., 1-minute of DBT deposition and 3-minutes of UV exposure, the smallest domain size can be achieved, and the volume fraction of ‘face on’ orientation of P3HT inside BHJ active layer is largely improved than that from conventional thermal annealing. The R-SoXS results for a P3HT:PC<sub>61</sub>BM BHJ active layer processed under optimal conditions of the new post casting process indicate that finer depletion zone between P3HT and PC<sub>61</sub>BM within the phase separated domains without loss of photon absorption and crystallinity. The solubility drop of UV photo-polymerized polythiophene is simulated using Hansen solubility parameters, and the RED and Flory-Huggins interaction parameters also are calculated. The miscibility drop of the *in situ* photo-polymerized oligothiophenes with PC<sub>61</sub>BM during the new post process is much larger than with P3HT. Regardless of whether P3HT or PC<sub>61</sub>BM is used, the miscibility of UV photo-polymerized oligothiophenes decreases with an increase in the number of repeating units for both. This new *in situ* UV photo-polymerization of DBT is a dynamic post process, and the initial DBT exhibits good miscibility with BHJ constituents; however, this miscibility decreases under UV exposure and leads to the nano-scale phase separation inside a P3HT:PC<sub>61</sub>BM BHJ active layer.

## 5. CHARACTERIZATION OF P3HT:PC<sub>61</sub>BM BHJ POLYMER SOLAR CELLS FABRICATED USING *IN SITU* UV PHOTO-POLYMERIZATION OF DBT

### 5.1. Background

The working principles of the optimized P3HT:PC<sub>61</sub>BM BHJ polymer solar cells are summarized as a schematic diagram in Figure 5.1. The optimal active layer thickness is around 100~200 nm, and PEDOT:PSS and aluminum are commonly used as the standard materials for a HTL and a cathode respectively. The aluminum thickness is around 100 nm, and the PEDOT:PSS thickness on an ITO anode substrate is around 40 nm.

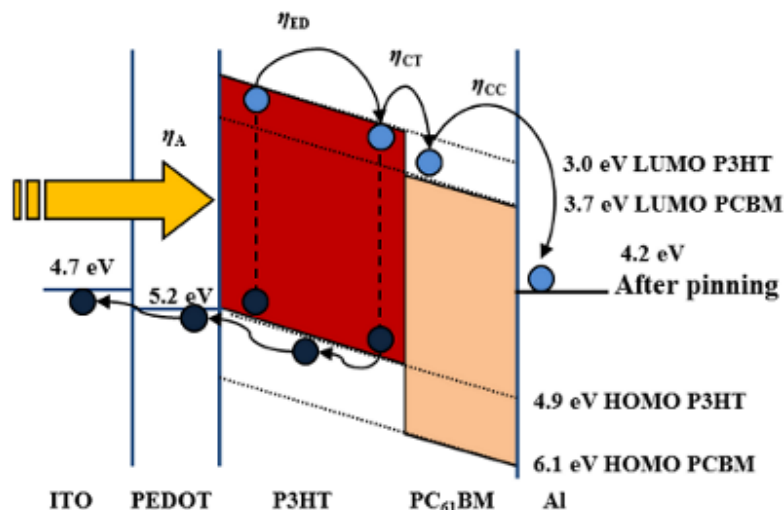


**Figure 5.1. P3HT: PC<sub>61</sub>BM BHJ polymer solar cells device architecture under the open circuit condition.**

The absorbed photon in the P3HT portion of a P3HT:PCBM BHJ active layer generates an exciton, and the exciton diffuses to the P3HT and PCBM interface. A small domain size that is similar to the exciton diffusion length leads to higher efficiency in the exciton separation into the discrete charge pair. The built-in potential of the active layer provides the driving force of the charge carrier separation. The separated electron and hole pair is transported toward the electrodes that are located on the opposite surface of the active layer. The charge carrier transport is related to the degree of crystallinity in the P3HT and PCBM domains.

Higher crystallinity and proper orientation of the crystalline phase lead to improved charge carrier mobility. As reviewed in the previous chapters, the new post casting process, *in situ* UV photo-polymerization of DBT in a P3HT:PC<sub>61</sub>BM BHJ active film, results in small domains of about 8~9 nm, which are close to the exciton diffusion length. Furthermore, it derives the crystalline phase orientation toward a much preferred ‘face on’ that improves charge carrier transport better than conventional thermal annealing can achieve.

In this chapter, the improved performance of P3HT:PC<sub>61</sub>BM BHJ polymer solar cells through the optimization of active layer morphology in the new post casting process is compared with performance from conventional annealing processes. For accurate verification of the morphology effects in *in situ* UV photopolymerization of DBT, other critical factors such as an aluminum cathode, PEDOT:PSS electron blocking layer and ITO anode, are incorporated into well-known standard device architecture, as shown in Figure 5.1.

## **5.2. Solar Cell Performance of P3HT:PC<sub>61</sub>BM BHJ Polymer Solar Cells with *In Situ* UV Photo-Polymerization of DBT**

DBT deposition time and UV exposure time lead to changes in the degree of crystallinity, the crystalline phase orientation and morphology changes, as discussed in the previous chapters. These kinds of property changes result in varied P3HT:PC<sub>61</sub>BM BHJ polymer solar cell performance. The more intensified ‘face on’ crystalline phase orientation and decrease in the PC<sub>61</sub>BM crystalline phase peak in GIWAXS, as shown in Figure 4.11, result in a better charge transport property than would be the case using conventional post thermal annealing only due to the increase volume of the ‘face on’ crystalline phase orientation. The smaller P3HT crystalline phase inside the BHJ active layer, as shown in Table 4.2, results in better charge separation at the P3HT and PC<sub>61</sub>BM interface than from conventional thermal annealing only, due to the increase in the interfacial area. The domain size from the *in situ* UV photo polymerization of DBT is smaller than that obtained from conventional post thermal annealing, which improves both charge carrier separation and transport properties. R-SoXS data clearly show that more homogeneous and finer P3HT and PC<sub>61</sub>BM inter-mixed zone exists inside the BHJ active layer from the new post casting process, which also

strongly supports this study's assumptions and expectations regarding improvements in P3HT:PC<sub>61</sub>BM BHJ polymer solar cell performance. Additionally, even though it does not show a huge improvement, some improvement to photon absorption is evident with this new process, as shown in the UVvis absorption spectra in Figure 5.2.

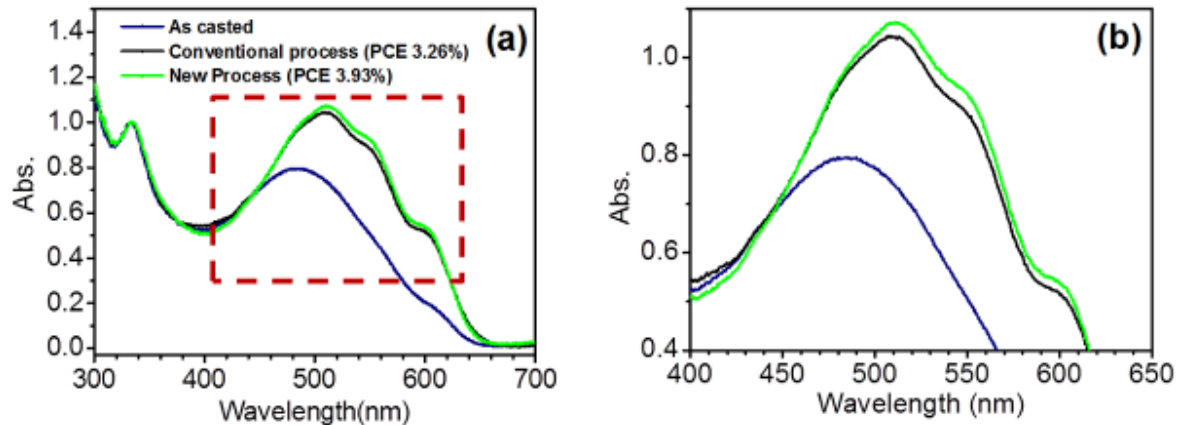


**Figure 5.2. Comparison of UVvis absorption spectra of P3HT:PC<sub>61</sub>BM BHJ thin films between the conventional post thermal annealing process and new post process (DBT 1 min 80°C, UV 3 minutes), and (b) zoomed-in P3HT main absorption peak area.**

In this section, devices performance of the P3HT:PC<sub>61</sub>BM BHJ polymer solar cells in the new post casting process, *in situ* UV photo-polymerization of DBT, is compared with that achieved through conventional thermal processes.

Solar cells are the devices that generate electric power from incident sunlight. Thus, analysis of charge carrier mobility inside such devices can provide deeper understanding of solar cell performance. In this research, charge carrier mobility studies using hole-only and electron-only P3HT:PC<sub>61</sub>BM BHJ polymer solar cells were performed to measure the charge carrier mobility of P3HT:PC<sub>61</sub>BM BHJ polymer solar cells based on the space charge limited current (SCLC) theory.[122, 132, 227-229] A thin layer of MoO<sub>3</sub> was thermally evaporated prior to Al thermal evaporation of the electron blocking layer, and a hole only worked as a charge carrier inside the P3HT:PC<sub>61</sub>BM BHJ polymer solar cells.[238] From this device, the hole mobility was calculated. Cs<sub>2</sub>CO<sub>3</sub> was thermally evaporated as a hole blocking layer on top of ITO instead of PEDOT:PSS in the conventional P3HT:PC<sub>61</sub>BM BHJ polymer solar cells to measure the electron charge carrier mobility inside the devices.[238] The architecture of these special P3HT:PC<sub>61</sub>BM BHJ polymer solar cells is shown in Figure 5.3 (d) and (e).

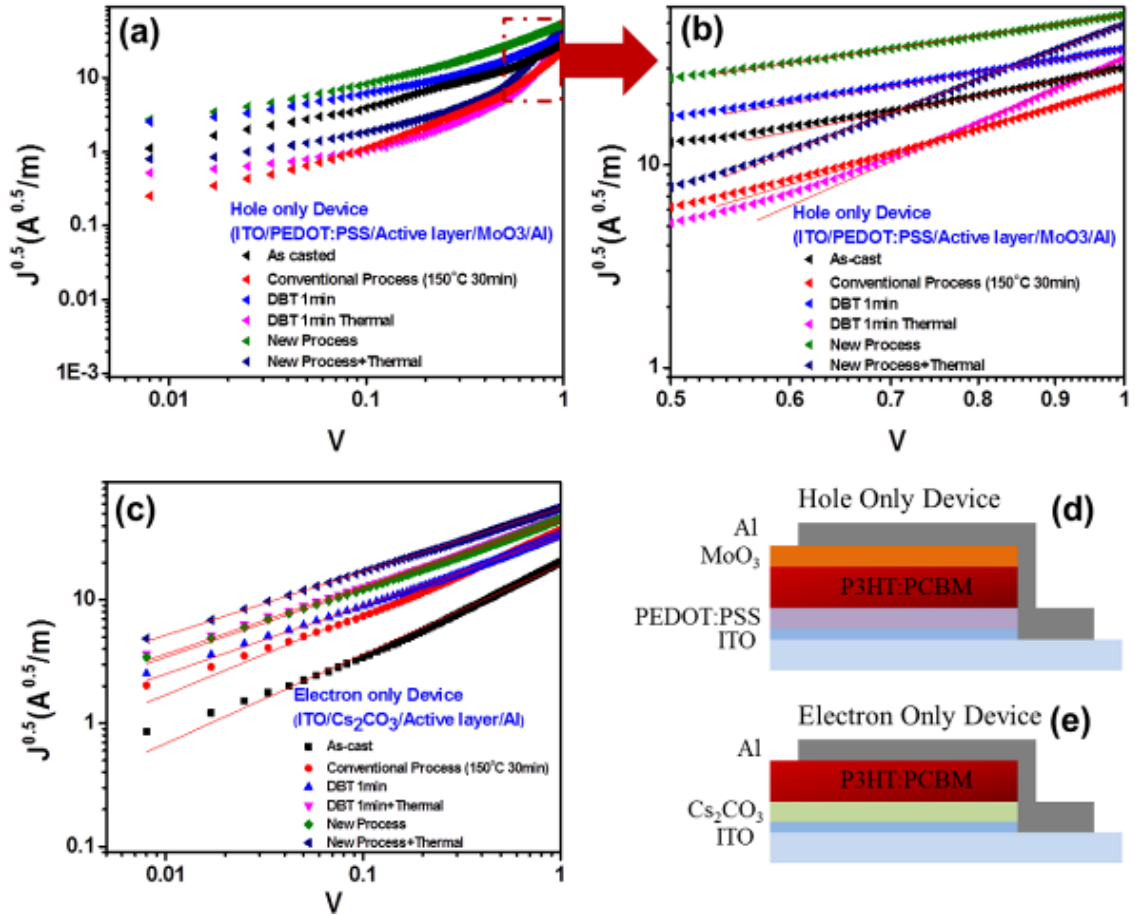


**Figure 5.3.** Charge carrier mobility of P3HT:PC<sub>61</sub>BM polymer solar cells: (a) and (b) are hole mobility from hole-only devices; (c) is electron mobility from electron-only devices, and (d) and (e) are the device architecture of hole-only and electron-only P3HT:PC<sub>61</sub>BM BHJ polymer solar cells, respectively.

The developed dark current-voltage curves from these special devices are shown, and J-V curves are plotted in log-log scale. Using the SCLC equation shown in Equation 5-1, hole-only and electron-only mobility were calculated. Here,  $\epsilon_0$  is the permittivity of free space, and  $\epsilon_r$  is the dielectric constant of materials. In the case of P3HT,  $\epsilon_r$  is assumed as 3.0, and for PC<sub>61</sub>BM,  $\epsilon_r$  is 3.9, based on the references.[122, 132, 227-229] V is the applied voltage; L is the thickness of an active layer; and  $\mu$  is the charge carrier mobility.

$$J = \frac{8}{9} \epsilon_0 \epsilon_r \mu \frac{V^2}{L^3} \quad (5-1)$$

The analyzed charge carrier mobility is shown in Figure 5.3 as log-log scale plots, and the calculated mobility data are summarized in Table. 5.1. Detailed experimental procedures and

related information can be found in Chapter 2. The charge carrier mobility of an as-cast P3HT:PC<sub>61</sub>BM BHJ active layer is as low as  $7.804 \times 10^{-6} \text{ cm}^2 \text{ s}^{-1} \text{ V}^{-1}$  for the electron mobility and  $5.807 \times 10^{-5} \text{ cm}^2 \text{ s}^{-1} \text{ V}^{-1}$  for the hole mobility. Regardless of the type of post process, charge carrier mobility improved. In the conventional thermal annealing process, electron mobility improved significantly more than that of hole mobility. It appears that enhanced electron mobility is related to PC<sub>61</sub>BM cluster growth and the depletion region formation.

**Table.5.1. Charge carrier mobility of P3HT: PC<sub>61</sub>BM BHJ polymer solar cells**

| <i>Carrier Mobility</i><br>( $\text{cm}^2 \text{ S}^{-1} \text{ V}^{-1}$ ) | <i>Electron-only Mobility</i><br>( $\text{Cs}_2\text{CO}_3$ ) | <i>Hole-only Mobility</i><br>( $\text{MoO}_3$ ) | <i>Ratio</i><br>( $\mu_e/\mu_h$ ) |
|--|---|---|-----------------------------------|
| As-cast  | $7.804 \times 10^{-6}$  | $5.807 \times 10^{-5}$                          | 0.134                             |
| Thermal (150°C, 20 min)<br>(Conventional)                                  | $2.168 \times 10^{-5}$  | $7.064 \times 10^{-5}$                          | 0.307                             |
| DBT 1 min (80°C)   | $1.238 \times 10^{-5}$  | $6.595 \times 10^{-5}$                          | 0.195                             |
| DBT 1 min + Thermal  | $2.318 \times 10^{-5}$  | $3.011 \times 10^{-4}$                          | 0.077                             |
| DBT 1 min + UV 3 min   | $2.378 \times 10^{-5}$  | $1.158 \times 10^{-4}$                          | 0.205                             |
| New Process<br>(UV 3 min) + Thermal  | $3.425 \times 10^{-5}$  | $4.887 \times 10^{-4}$                          | 0.070                             |

One minute of DBT solvent annealing at 80°C generally enhances charge carrier mobility for both an electron and a hole together, but enhances the hole mobility slightly more than the electron mobility. Combined with thermal annealing at 150°C for 20 minutes, both the electron and hole mobility were further enhanced as  $2.318 \times 10^{-5} \text{ cm}^2 \text{ s}^{-1} \text{ V}^{-1}$  for the electron mobility and  $3.011 \times 10^{-4} \text{ cm}^2 \text{ s}^{-1} \text{ V}^{-1}$  for the hole mobility.

The charge carrier mobility values in the new post casting process are  $2.378 \times 10^{-5} \text{ cm}^2 \text{ s}^{-1} \text{ V}^{-1}$  for electron mobility and  $1.158 \times 10^{-4} \text{ cm}^2 \text{ s}^{-1} \text{ V}^{-1}$  for hole mobility after 3 minutes of UV exposure. Combined with thermal annealing, the mobility values were further improved, as indicated by  $3.425 \times 10^{-5} \text{ cm}^2 \text{ s}^{-1} \text{ V}^{-1}$  for electron mobility and  $4.887 \times 10^{-4} \text{ cm}^2 \text{ s}^{-1} \text{ V}^{-1}$  for hole mobility. The new post casting process based on the *in situ* UV photo-polymerization of DBT is much more effective in enhancing hole mobility than the conventional thermal annealing.

It looks that these improvements are due mainly to the enhanced  $\pi$ - $\pi$  orbital overlap and the ‘face on’ crystalline phase orientation from the new post casting process, *in situ* UV photo-polymerization of DBT in the P3HT:PC<sub>61</sub>BM BHJ polymer solar cells.

For the characterization of current density and voltage (J-V) curves of the P3HT:PC<sub>61</sub>BM BHJ polymer solar cells, devices were prepared using the following established fabrication procedure. The active layer thickness is 100 nm, and PEDOT:PSS is used as an electron blocking layer. ITO and Al are used as anode and cathode electrodes, respectively. The post thermal annealing was performed at 150°C for 20-minutes. The J-V characterization was performed under a solar simulator that was calibrated using a NREL-certified photo diode. Electrical signals were gathered using a source meter with four wire connections to minimize the resistance effects from the measuring facilities. A detailed explanation of the experimental set-up can be found in Chapter 2.

The J-V characteristic curves of P3HT:PC<sub>61</sub>BM BHJ polymer solar cells, developed using the new post casting process, are shown in Figure 5.4. The recorded PCE is 3.93%, which is approximately 20% higher than that of the device developed using the conventional thermal annealing only. The best P3HT:PC<sub>61</sub>BM BHJ polymer solar cell performance, as shown in Figure 5.4, comes from conditions of 1-minute DBT deposition at 80°C and 3-minutes of UV exposure followed by 150°C 20-minutes thermal annealing.

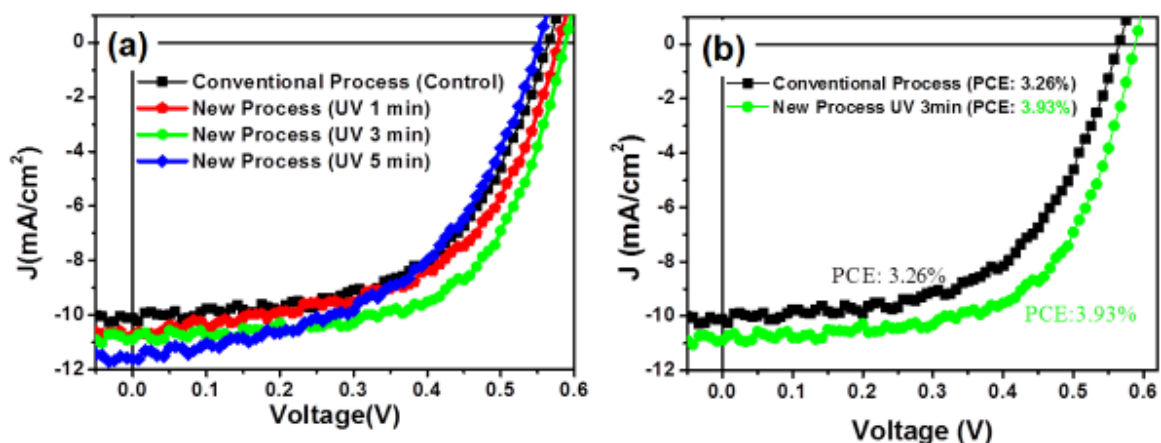


**Figure 5.4. J-V characteristic curves of P3HT:PC<sub>61</sub>BM BHJ polymer solar cells: (a) with different UV exposure times, and (b) comparison of conventional post thermal annealing only and new post process.**

Morphology is the output from a combination of complicated factors, such as the degree of crystallinity, miscibility of components and interaction with solvents during the spin coating process, etc., which makes it difficult to explain everything about morphology with a simple theory. So, domain size helps simplify the verification and comparison of the morphological changes between the new and conventional processes. Therefore, P3HT:PC<sub>61</sub>BM BHJ polymer solar cells are fabricated in various processing conditions and their solar cells performance are compared based on the difference lateral domain sizes analyzed by AFM.

As shown in Figure 5.5, the PCE is best when the lateral domain sizes, analyzed using the AFM, are around 9 nm with 3-minutes of UV exposure. The lateral domain size from conventional thermal annealing is around 12 nm with a PCE of 3.26%. The FF of the solar cells fabricated using the new process is best when processed with 3-minutes of UV exposure, and provides values as large as 62%. The open circuit voltage ( $V_{oc}$ ) reaches 0.59 V with 3-minutes of UV exposure. The short circuit current ( $J_{sc}$ ) with 3-minutes of UV exposure is 10.9 mA, which is higher than that from conventional thermal annealing (10.1 mA). However, the short circuit current continues to increase with longer UV exposure times. This phenomenon is not fully understood, but it appears that the short circuit current is related to enhanced photon absorption with longer UV exposure times.

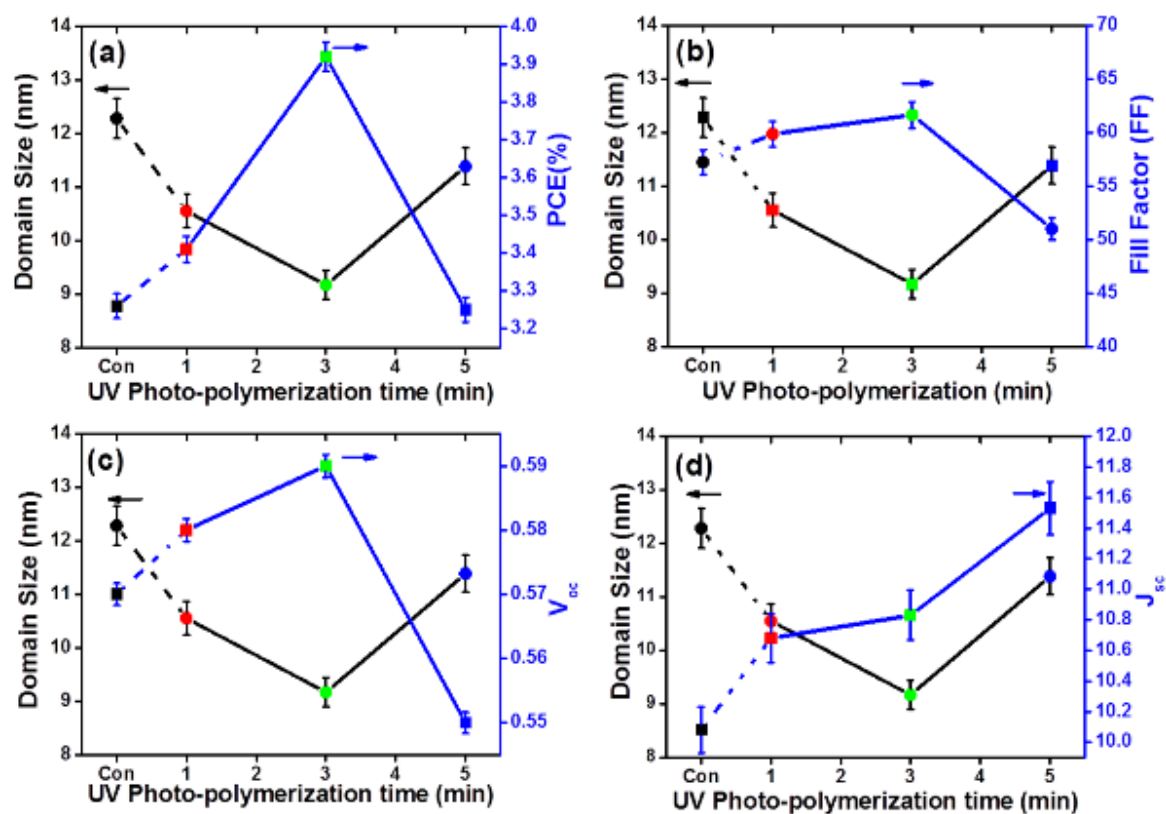


Figure 5.5. Summary of P3HT:PC<sub>61</sub>BM BHJ polymer solar cell parameters with various UV exposure times: (a) PCE vs. lateral domain size, (b) FF vs. lateral domain size, (c)  $V_{oc}$  vs. lateral domain size, and (d)  $J_{sc}$  vs. lateral domain size.

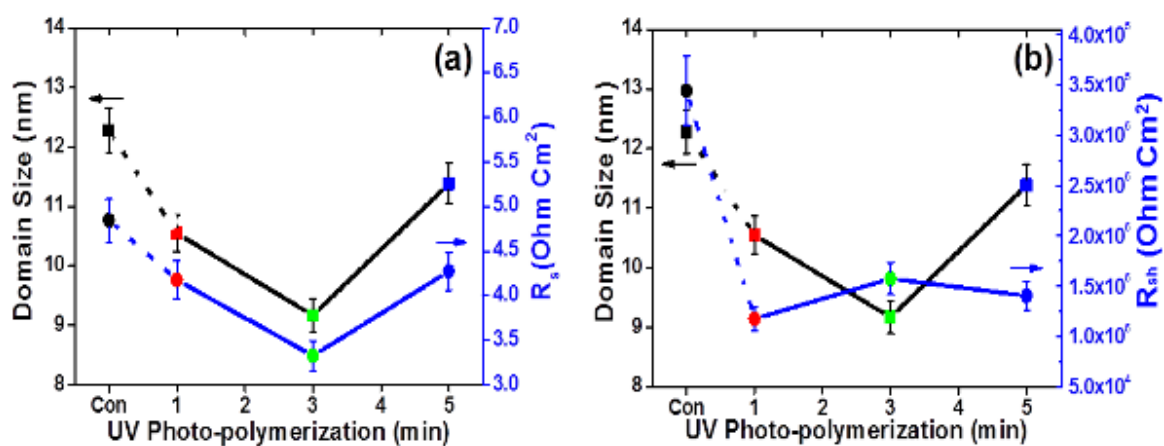


Figure 5.6. Summary of resistance values of P3HT:PC<sub>61</sub>BM BHJ polymer solar cells with various UV exposure times: (a)  $R_s$  vs. lateral domain size, and (b)  $R_{sh}$  vs. lateral domain size.

The series resistance ( $R_s$ ) is small ( $3.4 \text{ Ohm cm}^2$ ) with 3 minutes of UV exposure compared to around  $6 \text{ Ohm cm}^2$  for the conventional solar cells as shown in Figure 5.6 (a). This finding follows the trend in lateral domain size change seen in the AFM phase mode analyses. That is, series resistance has a close relationship with the interfacial area, and the smaller lateral domain size indicates a larger interfacial area. These factors provide better charge carriers separation performance than is found from the conventional thermal annealing, which includes a domain size of around 12 nm. The shunt resistance ( $R_{sh}$ ) values from the new process show lower values, regardless of the UV exposure times, than those of the conventional devices as shown in Figure 5.6 (b). That is, the new post casting process produces low rectification performance of the solar cells. However, the overall values are within an acceptable range, as high as  $\sim 10^5 \text{ Ohm cm}^2$ , so it is clear that shunt resistance does not affect solar cell performance, even though the shunt resistance values are lower than those obtained from the conventional thermal annealing only. Further study is required to gain deeper understanding of device resistance in the new post casting process.

### 5.3. Conclusions

In this chapter, the P3HT:PC<sub>61</sub>BM BHJ polymer solar cell performance is characterized based on current-voltage (J-V) curve analysis of the P3HT:PC<sub>61</sub>BM BHJ polymer solar cells fabricated in new post casting process, and charge carrier mobility analysis using specially fabricated electron-only and hole-only P3HT:PC<sub>61</sub>BM BHJ polymer solar cells.

The charge carrier mobility values of the electron-only and hole-only devices clearly show that charge carrier mobility, regardless of electron and hole mobility, are improved using the new post casting process.

The PCE of P3HT:PC<sub>61</sub>BM BHJ polymer solar cells fabricated using the new *in situ* UV photo-polymerization of DBT shows the best performance as 3.93% under the optimal process condition of 1-minute DBT deposition and 3-minute UV exposure followed by 150 °C, 20-minutes thermal annealing. This PCE value is 20% greater than that obtained from conventional thermal annealing only. Other characteristic values of the J-V curves, such as fill factor (FF), open circuit voltage ( $V_{oc}$ ), and short circuit current ( $J_{sc}$ ), are shown as 62 %, 0.59 V and 10.9 mA respectively for the optimal conditions of the new process. The slightly

lower values of shunt resistance ( $R_{sh}$ ) compared to those obtained from the conventional post thermal process are still within a reasonably good value range and appear not to hinder the performance of the final P3HT:PC<sub>61</sub>BM BHJ polymer solar cell. Further study is required to have a clear understanding of this phenomenon.

## 6. CONCLUSIONS AND PROPOSED FUTURE WORK

### 6.1 Conclusions

Two fundamental post processes have been commonly used to improve the performance of P3HT:PC<sub>61</sub>BM BHJ polymer solar cells. In the chapter 3, the fundamental functions and principles of two representative conventional post processes, post thermal and post solvent annealing, are studied using AFM and X-ray techniques, such as GIWAXS and R-SoXS. The phase separation is determined mainly by an initial spin casting process, and crystallinity is improved mostly through the post thermal annealing process. In the thermal annealing process, the crystalline phase has intense ‘edge-on’ and ‘face on’ crystalline phase orientations compared to an as-cast and their crystalline sizes also increase slightly. In the solvent annealing, both the degree of crystallinity and the morphology improve.

DBT solvent annealing results in a better degree of crystallinity, a smaller crystalline phase and a smaller domain than in conventional thermal annealed P3HT:PC<sub>61</sub>BM BHJ active layers. It is hypothesized that the interdigitated DBT into the P3HT crystalline phase (based on GIWAXS results) results in a better inter-mixed BHJ active layer and finer crystalline phase than that of a thermal annealed crystalline phase of a P3HT:PC<sub>61</sub>BM BHJ active layer. Specifically, DBT shows good performance as an annealing solvent and is an excellent reactive monomer for the *in situ* UV photo-polymerization inside the P3HT:PC<sub>61</sub>BM BHJ active layer.

In the chapter 4, a new post casting process based on *in situ* UV photo-polymerization of DBT is demonstrated herein. Under optimal process conditions, i.e., 1-minute of DBT deposition and 3-minutes of UV exposure followed by 150°C, 20-minutes thermal annealing, the ratio of ‘face on’ and ‘edge on’ orientations of P3HT improves approximately 70% compared with that from the conventional thermal annealing, and the overall crystalline size decreases. The R-SoXS data clearly indicate that a P3HT:PC<sub>61</sub>BM BHJ active layer processed under these optimal conditions of the new post casting process has a homogenous and finer inter-mixed zone compared with that from conventional thermal annealing only. This phenomenon minimizes the PC<sub>61</sub>BM crystalline phase growth in the BHJ layer and

results in a better PCE of the final P3HT:PC<sub>61</sub>BM BHJ polymer solar cells than occurs using the conventional thermal annealing.

The solubility drop of UV photo-polymerized oligothiophene is explained using Hansen solubility parameters. Based on these parameters, relative energy density (RED) and Flory-Huggins interaction parameters are calculated to predict the miscibility drop of the *in situ* UV photo-polymerized oligothiophenes in a P3HT: PC<sub>61</sub>BM BHJ active layer. The miscibility drop of the *in situ* UV photo-polymerized oligothiophenes with PC<sub>61</sub>BM during the new post casting process is much larger than that with P3HT. Regardless of P3HT and PC<sub>61</sub>BM, within the critical limits, the miscibility of UV photo-polymerized oligothiophenes decreases with an increase in the number of repeating units under UV exposure. The *in situ* UV photo-polymerization of DBT is a dynamic process. Initially, DBT exhibits good miscibility with the BHJ constituents; however, the decreased miscibility of the polymerized oligothiophenes under UV exposure drives the nano-scale phase separation inside a P3HT: PC<sub>61</sub>BM BHJ active layer.

Based on the analysis results of lateral morphology of the P3HT: PC<sub>61</sub>BM BHJ active layers by using AFM, a P3HT:PC<sub>61</sub>BM BHJ active layer from the new post casting process, *in situ* UV photo-polymerization of DBT, shows the smallest domain and P3HT crystalline sizes, which together improves the charge carrier separation at the P3HT and PC<sub>61</sub>BM interface.

In the chapter 5, the P3HT:PC<sub>61</sub>BM BHJ polymer solar cell performance is characterized based on current-voltage (J-V) curve analysis of the P3HT:PC<sub>61</sub>BM BHJ polymer solar cells fabricated in new post casting process, and charge carrier mobility analysis using specially fabricated electron-only and hole-only P3HT:PC<sub>61</sub>BM BHJ polymer solar cells.

The charge carrier mobility values of the electron-only and hole-only devices clearly show that charge carrier mobility, regardless of electron and hole mobility, are improved using this new post casting process. The charge carrier mobility of an as-cast P3HT:PC<sub>61</sub>BM BHJ active layer is as low as  $7.804 \times 10^{-6} \text{ cm}^2 \text{ s}^{-1} \text{ V}^{-1}$  for the electron mobility and  $5.807 \times 10^{-5} \text{ cm}^2 \text{ s}^{-1} \text{ V}^{-1}$  for the hole mobility. Regardless of the type of post process, charge carrier mobility improved. In the conventional thermal annealing process, electron mobility improved

significantly more than that of hole mobility. It appears that enhanced electron mobility is related to PC<sub>61</sub>BM crystalline phase growth and the depletion region formation.

One minute of DBT solvent annealing at 80°C, a pre-step for the *in situ* UV photo-polymerization of DBT, generally enhances charge carrier mobility for both an electron and a hole together, but enhances the hole mobility slightly more than the electron mobility. Combined with thermal annealing at 150°C for 20 minutes, both the electron and hole mobility were further enhanced as  $2.318 \times 10^{-5} \text{ cm}^2\text{s}^{-1}\text{V}^{-1}$  for the electron mobility and  $3.011 \times 10^{-4} \text{ cm}^2\text{s}^{-1}\text{V}^{-1}$  for the hole mobility.

The charge carrier mobility values after 3-minutes of UV exposure are  $2.378 \times 10^{-5} \text{ cm}^2\text{s}^{-1}\text{V}^{-1}$  for electron mobility and  $1.158 \times 10^{-4} \text{ cm}^2\text{s}^{-1}\text{V}^{-1}$  for hole mobility. Combined with thermal annealing, the mobility values are further improved, as indicated by  $3.425 \times 10^{-5} \text{ cm}^2\text{s}^{-1}\text{V}^{-1}$  for electron mobility and  $4.887 \times 10^{-4} \text{ cm}^2\text{s}^{-1}\text{V}^{-1}$  for hole mobility. The new post casting process based on the combination of *in situ* UV photo-polymerization of DBT and thermal annealing at 150°C, 20-minutes is much more effective in enhancing hole mobility than the conventional thermal annealing only. It looks that these improvements are due mainly to the enhanced  $\pi$ - $\pi$  orbital overlap and the 'face on' crystalline phase orientation from the new post casting process, *in situ* UV photo-polymerization of DBT, in the P3HT:PC<sub>61</sub>BM BHJ polymer solar cells.

The PCE of P3HT:PC<sub>61</sub>BM BHJ polymer solar cells fabricated using the new *in situ* UV photo-polymerization of DBT shows the best performance at 3.93% under the optimal process condition of 1-minute DBT deposition and 3-minute UV exposure. This PCE value is 20% greater than that obtained from conventional post thermal annealing only.

Other characteristics values of the J-V curves, such as fill factor (FF), open circuit voltage ( $V_{oc}$ ), and short circuit current ( $J_{sc}$ ), are shown to be excellent outputs for the optimal conditions of the new post casting process. The slightly lower values of shunt resistance ( $R_{sh}$ ) compared to that from the conventional post thermal annealing is still within a reasonably good value range and appears not to hinder the performance of the final P3HT:PC<sub>61</sub>BM BHJ polymer. Further study is required to have a clear understanding of this phenomenon.

In summary, the demonstrated new post casting process for the P3HT:PC<sub>61</sub>BM BHJ polymer solar cells enhances the critical factors that are needed in order to produce the good P3HT:PC<sub>61</sub>BM BHJ polymer solar cell performance. These factors include high crystallinity, a small crystalline phase, 'face-on' crystalline phase orientation, a small domain and finer inter-mixed zone in BHJ active layer.

In this research, it is shown that the P3HT:PC<sub>61</sub>BM BHJ polymer solar cells fabricated from the new post casting process, *in situ* UV photo-polymerization of DBT, perform better than those from conventional thermal annealing only.

## 6.2 Future Work

Morphology control of BHJ polymer solar cells based on the *in situ* UV photo-polymerization of a reactive monomer is a new concept; no similar ideas have been reported, to the best of the researcher's knowledge. Therefore, the fundamental studies presented in this research could serve as a foundation for future experiments and improvements. DBT monomer is selected as a candidate for the *in situ* UV photopolymerization because it has a similar chemical structure to that of P3HT (i.e., p-type, and electron donor) and has relatively good solubility with both P3HT and PC<sub>61</sub>BM.

There is an expectation that the maximum PCE from P3HT:PCBM BHJ polymer solar cells can achieve 8~10% PCE based on the calculations, which are considering of the maximum photon absorption and energy bands alignments. However, It looks that PCE of this materials system can not be over 5% PCE. Practically speaking, There are debates regarding the record PCE values over 5% PCE of P3HT:PC<sub>61</sub>BM BHJ polymer solar cells.[239-242] Therefore, many chemists are trying to synthesize different materials based on low band gap polymers[228, 243-252] instead of P3HT and a new-found record efficiency of BHJ polymer solar cells is around 8% PCE[134], which has already been reported, as described in Chapter 1. In order for it to be a common and universal method, the *in situ* morphology control of BHJ polymer solar cells using the *in situ* UV photo-polymerization of a reactive monomer

that is proposed in this thesis should be tested using other promising materials, except the P3HT:PC<sub>61</sub>BM BHJ system. This kind of trial should be the first priority in any future work. As a preliminary study, bulk morphologies of several new material combinations are studied using R-SoXS. The first example is *in situ* UV photopolymerization of DBT in a P3HT:PC<sub>71</sub>BM BHJ active layer.

As shown in Figure 6.1 (b), the P3HT:PC<sub>71</sub>BM BHJ system shows less intensity from the *in situ* UV photo-polymerization of DBT than that from conventional thermal annealing only. Additionally, the bulk domain from the new process are smaller than those derived from conventional thermal annealing only. It is regarded that DBT also has good solubility with PC<sub>71</sub>BM due to this well-controlled small domain. Several reports indicate that PC<sub>71</sub>BM shows improved PCE performance with a combination of low band gap polymers or even with P3HT in a BHJ active layer.[238, 253-255] It is already proven that the energy bands alignment between P3HT and PC<sub>71</sub>BM work greatly for the BHJ polymer solar cells without any problem, so it is expected that an enhanced PCE for P3HT:PC<sub>71</sub>BM BHJ polymer solar cells will emerge from this new post casting process.

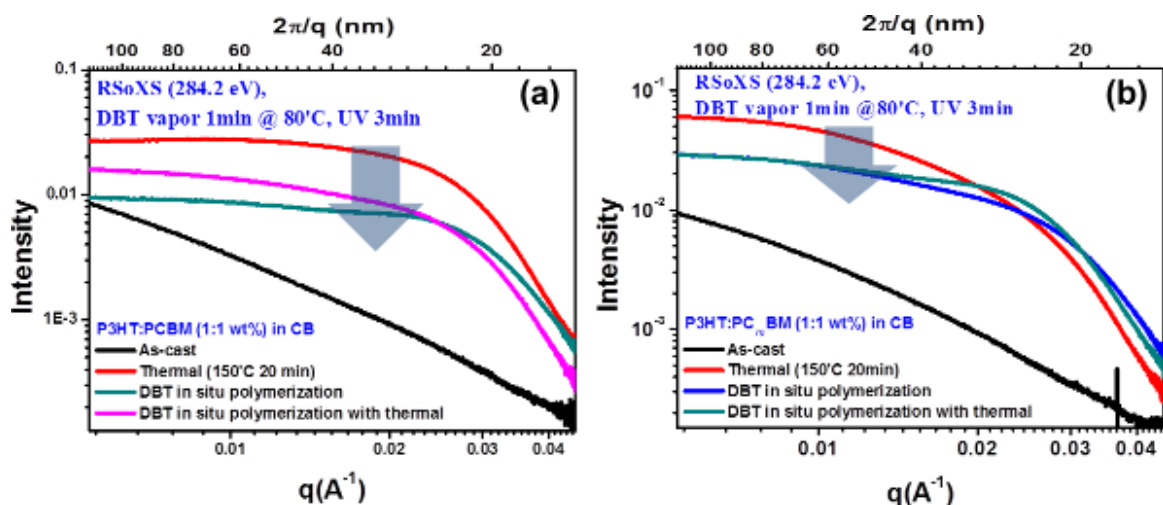


**Figure 6.1. Comparison of R-SoXS results of: (a) a P3HT:PC<sub>61</sub>BM BHJ active layer, and (b) a P3HT:PC<sub>71</sub>BM active layer in the new post casting process (thermal annealing condition is 150°C, 20-minutes) .**

For a second idea, different types of reactive monomers were tested. Fluorene is a commonly used monomer that is widely employed in the synthesis of low band gap conjugated polymer with the combination of thiophene monomers that have various lengths of alkyl side chain.

Because fluorene-based low band gap conjugated polymers have become popular for applications in BHJ polymer solar cells, fluorene-based monomer is tested and compared, using R-SoXS, to the morphological changes that occur with bithiophene-based reactive monomers. Both types of monomers are solid phases at room temperature and have a relatively high melting temperature of over 100°C. 10 wt% of these solid phase reactive monomers are introduced and both types dissolved well in CB solvent.

R-SoXS data of P3HT:PC<sub>61</sub>BM BHJ active layers having 10 wt% of two different solid phase reactive monomers are shown in Figure 6.2. It appears that they are not as effective in producing the homogeneous inter-mixed phase in a BHJ active layer, as DBT which starts from a liquid phase monomer, because no big decrease in scattering intensity with increasing UV exposure is evident. However, it appears that no macro-phase separation occurs.

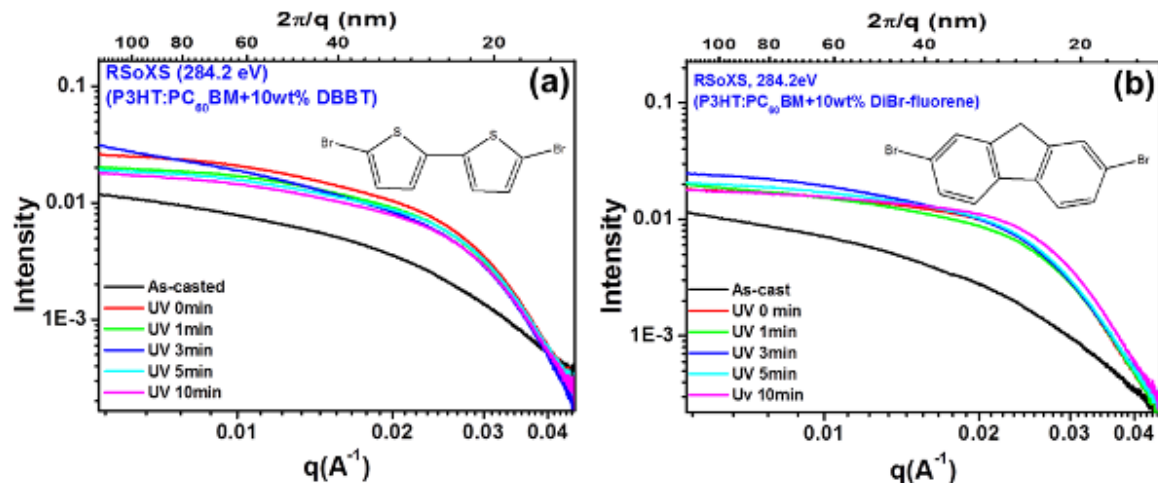


**Figure 6.2. R-SoXS results of: (a) 10 wt% of dibromobithiophene (DBBT), and (b) 10 wt% dibromofluorene (DBF) in a P3HT:PC<sub>61</sub>BM BHJ active layer with different UV exposure times (post thermal annealing condition: 150°C, 20 minutes).**

Figure 6.3 shows interesting R-SoXS results from two other reactive monomers. R-SoXS intensity increases with increasing UV exposure in the case of a P3HT:PC<sub>61</sub>BM BHJ active layer that has 10 wt% of diBr-biphenylthiophene (BBPT), as indicated in Figure 6.3 (a); however, in the case of 10 wt% 9,9-diethyl hexyl 2,7-dibromofluorene (DEHDBF) in a P3HT:PC<sub>61</sub>BM BHJ active layer, the R-SoXS intensity decreases with increasing UV exposure time. These results may come from the different miscibility of these reactive monomers in a P3HT:PC<sub>61</sub>BM BHJ active layer. The increased scattering intensity of R-

SoXS means that the crystalline phases inside the P3HT:PC<sub>61</sub>BM BHJ active layer are purified and no homogeneous inter-mixed zone exists due to the big difference in miscibility.

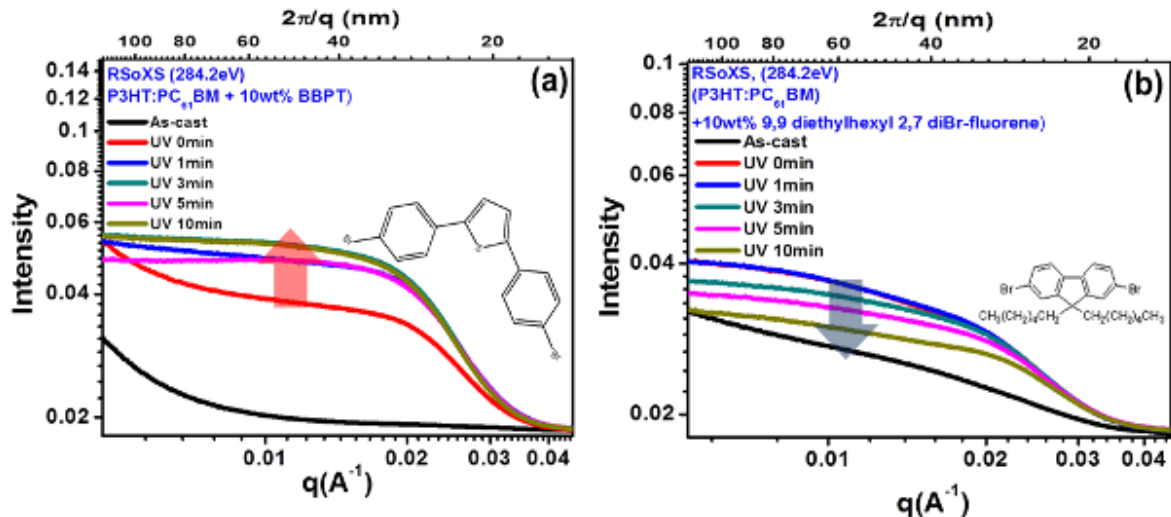


Figure 6.3. R-SoXS results of: (a) 10 wt% of diBr-biphenylthiophene (BBPT), and (b) 10 wt% of 9,9-diethyl hexyl 2,7-dibromofluorene (DEHDBF) in a P3HT:PC<sub>61</sub>BM BHJ active layer with different UV exposure times (post thermal annealing condition: 150°C, 20-minutes).

Due to limited materials, there are no data for other BHJ materials, such as low band gap polymers. These kinds of different material combinations for *in situ* UV photo-polymerization-induced morphology control would provide an interesting topic of future study.

## 7. BIBLIOGRAPHY

1. NREL. *Research Solar Cell Record Efficiency*. 2011; Available from: [http://en.wikipedia.org/wiki/File:PVeff\(rev100414\).png](http://en.wikipedia.org/wiki/File:PVeff(rev100414).png).
2. Brabec, C., V. Dyakonov, and U. Scherf, eds. *Organic Photovoltaics: Materials, Device Physics and Manufacturing Technologies*. 2008, Wiley-VCH
3. Krebs, F.C., ed. *Polymer Photovoltaics-A Practical Approach*. 2007, SPIE.
4. Landon, S.M., *Energy: Yesterday, today, and the opportunities and challenges of tomorrow*. *International Geology Review*, 2002. **44**(12): p. 1105-1114.
5. Shafiee, S. and E. Topal, *When will fossil fuel reserves be diminished?* *Energy Policy*, 2009. **37**(1): p. 181-189.
6. Penner, S.S., J. Haraden, and S. Mates, *LONG-TERM GLOBAL ENERGY SUPPLIES WITH ACCEPTABLE ENVIRONMENTAL IMPACTS*. *Energy*, 1992. **17**(10): p. 883-899.
7. Houghton, R.A., J.D. Unruh, and P.A. Lefebvre, *CURRENT LAND-COVER IN THE TROPICS AND ITS POTENTIAL FOR SEQUESTERING CARBON*. *Global Biogeochemical Cycles*, 1993. **7**(2): p. 305-320.
8. Jijaescu, L., *ENVIRONMENTAL POLLUTION AND GLOBAL CLIMATE CHANGE THE IMPACT OF INDUSTRIAL ACTIVITY ON THE ENVIRONMENT*. *Metalurgia International*, 2009. **14**: p. 84-86.
9. Hileman, B., *Stark effects from global warming*. *Chemical & Engineering News*, 2005. **83**(12): p. 47-48.
10. Polyakov, I.V., et al., *Arctic Ocean Warming Contributes to Reduced Polar Ice Cap*. *Journal of Physical Oceanography*, 2010. **40**(12): p. 2743-2756.

11. Duffey, R.B., *Sustainable futures using nuclear energy*. Progress in Nuclear Energy, 2005. **47**(1-4): p. 535-543.
12. Culley, M.R. and H. Angelique, *Nuclear Power: Renaissance or Relapse? Global Climate Change and Long-Term Three Mile Island Activists' Narratives*. American Journal of Community Psychology, 2010. **45**(3-4): p. 231-246.
13. Bluth, C., *Civilian Nuclear Cooperation and the Proliferation of Nuclear Weapons*. International Security, 2010. **35**(1): p. 184-188.
14. *It is 5 minutes to midnight: Confronting nuclear energy's proliferation problem*. Bulletin of the Atomic Scientists, 2009. **65**(2): p. 1-3.
15. Haggard, S. and M. Noland, *Sanctioning North Korea The Political Economy of Denuclearization and Proliferation*. Asian Survey, 2010. **50**(3): p. 539-568.
16. Strupczewski, A., *Accident risks in nuclear-power plants*. Applied Energy, 2003. **75**(1-2): p. 81-88.
17. Rashad, S.M. and F.H. Hammad, *Nuclear power and the environment: comparative assessment of environmental and health impacts of electricity-generating systems*. Applied Energy, 2000. **65**(1-4): p. 211-229.
18. Babenko, V.A., L.L. Jenkovszky, and V.N. Pavlovych, *Nuclear power industry: Tendencies in the world and Ukraine*. Physics of Particles and Nuclei, 2007. **38**(6): p. 795-826.
19. O'Connor, M. and S. van den Hove, *Prospects for public participation on nuclear risks and policy options: innovations in governance practices for sustainable development in the European Union*. Journal of Hazardous Materials, 2001. **86**(1-3): p. 77-99.

20. Aleksakhin, R.M., *Radioactive contamination as a type of soil degradation*. Eurasian Soil Science, 2009. **42**(12): p. 1386-1396.
21. Napier, B.A., E.A. Schmieman, and O. Voitsekovitch, *Radioactive waste management and environmental contamination issues at the Chernobyl site*. Health Physics, 2007. **93**(5): p. 441-451.
22. Nelson, J., ed. *The Physics of Solar Cells*. 2003, Imperial College Press.
23. Lee, A.H.I., H.H. Chen, and H.Y. Kang, *A model to analyze strategic products for photovoltaic silicon thin-film solar cell power industry*. Renewable & Sustainable Energy Reviews, 2011. **15**(2): p. 1271-1283.
24. Galdabini, S., G. Giuliani, and N. Robotti, *PHOTOELECTRICITY WITHIN CLASSICAL PHYSICS - FROM THE PHOTOCURRENTS OF BECQUEREL, EDMOND TO THE 1ST MEASURE OF THE ELECTRON CHARGE*, in *1st Eps Conference on History of Physics in Europe in the 19th and 20th Centuries*, F. Bevilacqua, Editor 1993. p. 149-156.
25. Sun, S.S. and N.S. Sariciftci, eds. *Organic Photovoltaics: Mechanisms, Materials and Devices* 2005, CRC.
26. Yang, M.J., et al., *ALXGA1-XAS/SI (X=0-0.22) TANDEM SOLAR-CELLS GROWN BY METALORGANIC CHEMICAL-VAPOR-DEPOSITION*. Japanese Journal of Applied Physics Part 1-Regular Papers Short Notes & Review Papers, 1994. **33**(12A): p. 6605-6610.
27. Allerman, A.A., et al., *The growth of InGaAsN for high efficiency solar cells by metalorganic chemical vapor deposition*, in *Photovoltaics for the 21st Century*, V.K. Kapur, et al., Editors. 1999. p. 178-184.

28. Soga, T., et al., *HIGH-EFFICIENCY ALGAS/SI MONOLITHIC TANDEM SOLAR-CELL GROWN BY METALORGANIC CHEMICAL-VAPOR-DEPOSITION*. Journal of Applied Physics, 1995. **78**(6): p. 4196-4199.
29. Soga, T., et al., *High-efficiency monolithic three-terminal GaAs/Si tandem solar cells fabricated by metalorganic chemical vapor deposition*. Japanese Journal of Applied Physics Part 1-Regular Papers Short Notes & Review Papers, 1996. **35**(2B): p. 1401-1404.
30. Yamamoto, A., et al., *THE METALORGANIC CHEMICAL VAPOR DEPOSITION GROWTH OF INN FOR INN/SI TANDEM SOLAR CELL*. 7th International Photovoltaic Science and Engineering Conference, Technical Digest 1993. 581-582.
31. Yamamoto, A., et al., *METALORGANIC CHEMICAL-VAPOR-DEPOSITION GROWTH OF INN FOR INN/SI TANDEM SOLAR-CELL*. Solar Energy Materials and Solar Cells, 1994. **35**(1-4): p. 53-60.
32. Soga, T., et al., *Photovoltaic properties of an Al<sub>x</sub>Ga<sub>1-x</sub>As solar cell (x=0-0.22) grown on Si substrate by metalorganic chemical vapor deposition and thermal cycle annealing*. Journal of Applied Physics, 1996. **79**(12): p. 9375-9378.
33. Yamaguchi, M., T. Warabisako, and H. Sugiura, *CHEMICAL BEAM EPITAXY AS A BREAKTHROUGH TECHNOLOGY FOR PHOTOVOLTAIC SOLAR-ENERGY APPLICATIONS*. Journal of Crystal Growth, 1994. **136**(1-4): p. 29-36.
34. Ghosh, K., et al., *EXPLANATION OF THE DEVICE OPERATION PRINCIPLE OF AMORPHOUS SILICON/CRYSTALLINE SILICON HETEROJUNCTION SOLAR CELL AND ROLE OF THE INVERSION OF CRYSTALLINE SILICON SURFACE*, in *35th Ieee Photovoltaic Specialists Conference* 2010.

35. Stuckelberger, M., et al., *INTERNAL ELECTRIC FIELD AND FILL FACTOR OF AMORPHOUS SILICON SOLAR CELLS*, in *35th Ieee Photovoltaic Specialists Conference 2010*.
36. Fathi, E., A. Sazonov, and Ieee, *OPTIMIZATION OF SEMI-TRANSPARENT AMORPHOUS SILICON SOLAR CELLS FOR BUILDING INTEGRATED APPLICATIONS*, in *35th Ieee Photovoltaic Specialists Conference 2010*.
37. Ho, C.I., et al., *PHOTOCURRENT ENHANCEMENTS IN AMORPHOUS SILICON SOLAR CELLS BY EMBEDDED METALLIC NANOPARTICLES*, in *35th Ieee Photovoltaic Specialists Conference 2010*.
38. Tseng, F.M., et al., *Using patent data to analyze trends and the technological strategies of the amorphous silicon thin-film solar cell industry*. *Technological Forecasting and Social Change*, 2011. **78**(2): p. 332-345.
39. Radue, C. and E.E. van Dyk, *A comparison of degradation in three amorphous silicon PV module technologies*. *Solar Energy Materials and Solar Cells*, 2010. **94**(3): p. 617-622.
40. Hugger, P.G., et al., *Electronic characterization and light-induced degradation in nc-Si : H solar cells*, in *Amorphous and Polycrystalline Thin-Film Silicon Science and Technology 2006*, S. Wagner, et al., Editors. 2007. p. 21-26.
41. Chowdhury, A., S. Mukhopadhyay, and S. Ray, *Fabrication of thin film nanocrystalline silicon solar cell with low light-induced degradation*. *Solar Energy Materials and Solar Cells*, 2009. **93**(5): p. 597-603.

42. Lu, P., et al., *Influence of n-type layer structure on performance and light-induced degradation of n-i-p microcrystalline silicon solar cells*. Acta Physica Sinica, 2010. **59**(6): p. 4330-4336.
43. Hugger, P.G., et al., *Properties of light-induced degradation and the electronic properties of nanocrystalline silicon solar cells grown under functionally graded hydrogen dilutions*. Journal of Non-Crystalline Solids, 2008. **354**(19-25): p. 2460-2463.
44. Bagnall, D.M. and M. Boreland, *Photovoltaic technologies*. Energy Policy, 2008. **36**(12): p. 4390-4396.
45. Hadrich, M., et al., *Modelling the quantum efficiency of cadmium telluride solar cells*. Solar Energy Materials and Solar Cells, 2011. **95**(3): p. 887-893.
46. Luschnitz, J., et al., *CdTe thin film solar cells: Interrelation of nucleation, structure, and performance*. Thin Solid Films, 2009. **517**(7): p. 2125-2131.
47. Miles, R.W., K.M. Hynes, and I. Forbes, *Photovoltaic solar cells: An overview of state-of-the-art cell development and environmental issues*. Progress in Crystal Growth and Characterization of Materials, 2005. **51**(1-3): p. 1-42.
48. Palekis, V., et al., *Structural Properties of CdTe Thin Films for Solar Cell Applications Deposited on Flexible Foil Substrates*, in *Thin-Film Compound Semiconductor Voltaics-2009*, A. Yamada, et al., Editors. 2010. p. 349-354.
49. Chaure, N.B., et al., *Investigation of electronic quality of chemical bath deposited cadmium sulphide layers used in thin film photovoltaic solar cells*. Thin Solid Films, 2003. **437**(1-2): p. 10-17.

50. Nikumbh, M., V. Gore, and R.B. Gore, *Structural, optical and photoelectrochemical studies of the cadmium sulphide films grown by chemical bath deposition*. Renewable Energy, 1997. **11**(4): p. 459-467.
51. Soliman, M.M., M.M. Shabana, and F. Abulfotuh, *CdS/CdTe solar cell using sputtering technique*. Renewable Energy, 1996. **8**(1-4): p. 386-389.
52. Bhattacharya, R.N., M.A. Contreras, and G. Teeter, *18.5% copper indium gallium diselenide (CIGS) device using single-layer, chemical-bath-deposited ZnS(O,OH)*. Japanese Journal of Applied Physics Part 2-Letters & Express Letters, 2004. **43**(11B): p. L1475-L1476.
53. Bohnke, T. and M. Edoff, *Copper indium gallium diselenide thin films for sun angle detectors in space applications*. Thin Solid Films, 2009. **517**(6): p. 2063-2068.
54. Chaure, N.B., et al., *Electrodeposition of p(+), p, i, n and n(+)-type copper indium gallium diselenide for development of multilayer thin film solar cells*. Thin Solid Films, 2005. **472**(1-2): p. 212-216.
55. Hegedus, S., *Thin film solar modules: The low cost, high throughput and versatile alternative to Si wafers*. Progress in Photovoltaics, 2006. **14**(5): p. 393-411.
56. Naghavi, N., et al., *High-efficiency copper indium gallium diselenide (CIGS) solar cells with indium sulfide buffer layers deposited by atomic layer chemical vapor deposition (ALCVD)*. Progress in Photovoltaics, 2003. **11**(7): p. 437-443.
57. Baumann, A.E., K.M. Hynes, and R. Hill, *AN INVESTIGATION OF CADMIUM TELLURIDE THIN-FILM PV MODULES BY IMPACT PATHWAY ANALYSIS*. Renewable Energy, 1995. **6**(5-6): p. 593-599.

58. Morgan, D.L., et al., *Acute pulmonary toxicity of copper gallium diselenide, copper indium diselenide, and cadmium telluride intratracheally instilled into rats.* Environmental Research, 1995. **71**(1): p. 16-24.
59. Sengul, H. and T.L. Theis, *An environmental impact assessment of quantum dot photovoltaics (QDPV) from raw material acquisition through use.* Journal of Cleaner Production, 2011. **19**(1): p. 21-31.
60. Zayed, J. and S. Philippe, *Acute Oral and Inhalation Toxicities in Rats With Cadmium Telluride.* International Journal of Toxicology, 2009. **28**(4): p. 259-265.
61. Maness, L.V. and Ieee, *Predicting Indium and Tellurium Availability,* in *35th Ieee Photovoltaic Specialists Conference* 2010.
62. Gratzel, M., *Photovoltaic and photoelectrochemical conversion of solar energy.* Philosophical Transactions of the Royal Society a-Mathematical Physical and Engineering Sciences, 2007. **365**(1853): p. 993-1005.
63. Sirimanne, P.M. and V.P.S. Perera, *Progress in dye-sensitized solid state solar cells.* Physica Status Solidi B-Basic Solid State Physics, 2008. **245**(9): p. 1828-1833.
64. Green, M.A. and Ieee, *Recent developments and future prospects for third generation and other advanced cells.* Conference Record of the 2006 IEEE 4th World Conference on Photovoltaic Energy Conversion, Vols 1 and 2 2006. 15-19.
65. Symko-Davies, M., et al., *Future generation technology status within the High-Performance PV Project.* Conference Record of the 2006 IEEE 4th World Conference on Photovoltaic Energy Conversion, Vols 1 and 2 2006. 175-178.
66. Kallmann, H. and M. Pope, *PREPARATION OF THIN ANTHRACENE SINGLE CRYSTALS.* Review of Scientific Instruments, 1958. **29**(11): p. 993-994.

67. Tang, C.W., *Two-layer organic photovoltaic cell*. Applied Physics Letters, 1986. **48**(2): p. 184.
68. Matsumura, Y., et al., *n-TYPE SEMICONDUCTING BEHAVIOR OF 5,10,15,20-TETRA(3-PYRIDYL)PORPHYRIN*. Chemistry Letters, 1984. **4**: p. 489.
69. Difley, S. and T. Van Voorhis, *Exciton/Charge-Transfer Electronic Couplings in Organic Semiconductors*. Journal of Chemical Theory and Computation, 2011. **7**(3): p. 594-601.
70. Würfel, P., ed. *Physics of Solar Cells: From Principles to New Concepts*. 2005, Wiley-VCH.
71. Savenije, T.J., J.M. Warman, and A. Goossens, *Visible light sensitisation of titanium dioxide using a phenylene vinylene polymer*. Chemical Physics Letters, 1998. **287**(1-2): p. 148-153.
72. Halls, J.J.M., et al., *Exciton diffusion and dissociation in a poly(p-phenylenevinylene)/C-60 heterojunction photovoltaic cell*. Applied Physics Letters, 1996. **68**(22): p. 3120-3122.
73. Hiramoto, M., H. Fujiwara, and M. Yokoyama, *P-I-N LIKE BEHAVIOR IN 3-LAYERED ORGANIC SOLAR-CELLS HAVING A CO-DEPOSITED INTERLAYER OF PIGMENTS*. Journal of Applied Physics, 1992. **72**(8): p. 3781-3787.
74. Gebeyehu, D., et al., *Bulk-heterojunction photovoltaic devices based on donor-acceptor organic small molecule blends*. Solar Energy Materials and Solar Cells, 2003. **79**(1): p. 81-92.
75. Rostalski, J. and D. Meissner, *Monochromatic versus solar efficiencies of organic solar cells*. Solar Energy Materials and Solar Cells, 2000. **61**(1): p. 87-95.

76. Peumans, P. and S.R. Forrest, *Very-high-efficiency double-heterostructure copper phthalocyanine/C-60 photovoltaic cells*. Applied Physics Letters, 2001. **79**(1): p. 126-128.
77. Peumans, P., V. Bulovic, and S.R. Forrest, *Efficient photon harvesting at high optical intensities in ultrathin organic double-heterostructure photovoltaic diodes*. Applied Physics Letters, 2000. **76**(19): p. 2650-2652.
78. Peumans, P., A. Yakimov, and S.R. Forrest, *Small molecular weight organic thin-film photodetectors and solar cells (vol 93, pg 3693, 2003)*. Journal of Applied Physics, 2004. **95**(5): p. 2938-2938.
79. Peumans, P., A. Yakimov, and S.R. Forrest, *Small molecular weight organic thin-film photodetectors and solar cells*. Journal of Applied Physics, 2003. **93**(7): p. 3693-3723.
80. Peumans, P., S. Uchida, and S.R. Forrest, *Efficient bulk heterojunction photovoltaic cells using small-molecular-weight organic thin films*. Nature, 2003. **425**(6954): p. 158-162.
81. Peumans, P. and S.R. Forrest, *Very-high-efficiency double-heterostructure copper phthalocyanine/C-60 photovoltaic cells (vol 79, pg 126, 2001)*. Applied Physics Letters, 2002. **80**(2): p. 338-338.
82. Voigt, M.M., et al., *Gravure printing for three subsequent solar cell layers of inverted structures on flexible substrates*. Solar Energy Materials and Solar Cells, 2011. **95**(2): p. 731-734.
83. Maattanen, A., et al., *Wetting and print quality study of an inkjet-printed poly(3-hexylthiophene) on pigment coated papers*. Colloids and Surfaces a-Physicochemical and Engineering Aspects, 2010. **367**(1-3): p. 76-84.

84. Lange, A., et al., *A new approach to the solvent system for inkjet-printed P3HT:PCBM solar cells and its use in devices with printed passive and active layers*. Solar Energy Materials and Solar Cells, 2010. **94**(10): p. 1816-1821.
85. Manceau, M., et al., *ITO-free flexible polymer solar cells: From small model devices to roll-to-roll processed large modules*. Organic Electronics, 2011. **12**(4): p. 566-574.
86. Lilliedal, M.R., et al., *The effect of post-processing treatments on inflection points in current-voltage curves of roll-to-roll processed polymer photovoltaics*. Solar Energy Materials and Solar Cells, 2010. **94**(12): p. 2018-2031.
87. Krebs, F.C., V. Senkovskyy, and A. Kiriya, *Preorganization of Nanostructured Inks for Roll-to-Roll-Coated Polymer Solar Cells*. Ieee Journal of Selected Topics in Quantum Electronics, 2010. **16**(6): p. 1821-1826.
88. Krebs, F.C., T. Tromholt, and M. Jorgensen, *Upscaling of polymer solar cell fabrication using full roll-to-roll processing*. Nanoscale, 2010. **2**(6): p. 873-886.
89. Krebs, F.C., J. Fyenbo, and M. Jorgensen, *Product integration of compact roll-to-roll processed polymer solar cell modules: methods and manufacture using flexographic printing, slot-die coating and rotary screen printing*. Journal of Materials Chemistry, 2010. **20**(41): p. 8994-9001.
90. Krebs, F.C., *All solution roll-to-roll processed polymer solar cells free from indium-tin-oxide and vacuum coating steps*. Organic Electronics, 2009. **10**(5): p. 761-768.
91. Sakai, J., et al., *High efficiency organic solar cells by screen printing method*, in *Conference Record of the Thirty-First IEEE Photovoltaic Specialists Conference - 2005* 2005. p. 125-128.

92. Krebs, F.C., et al., *Large area plastic solar cell modules*. Materials Science and Engineering B-Solid State Materials for Advanced Technology, 2007. **138**(2): p. 106-111.
93. Krebs, F.C., et al., *A complete process for production of flexible large area polymer solar cells entirely using screen printing-First public demonstration*. Solar Energy Materials and Solar Cells, 2009. **93**(4): p. 422-441.
94. Krebs, F.C., *Polymer solar cell modules prepared using roll-to-roll methods: Knife-over-edge coating, slot-die coating and screen printing*. Solar Energy Materials and Solar Cells, 2009. **93**(4): p. 465-475.
95. Krebs, F.C., *Fabrication and processing of polymer solar cells: A review of printing and coating techniques*. Solar Energy Materials and Solar Cells, 2009. **93**(4): p. 394-412.
96. Hoppe, H. and N.S. Sariciftci, *Polymer Solar Cells*, in *Photoresponsive Polymers* *I*2008. p. 1-86.
97. Tsukamoto, J. and H. Ohigashi, *CHARACTERISTICS OF SCHOTTKY-BARRIER SOLAR-CELLS USING POLYACETYLENE, (CH)<sub>3</sub>X*. Synthetic Metals, 1982. **4**(3): p. 177-186.
98. Tsukamoto, J., et al., *A SCHOTTKY-BARRIER TYPE SOLAR-CELL USING POLYACETYLENE*. Japanese Journal of Applied Physics, 1981. **20**(2): p. L127-L129.
99. Fedorko, P. and J. Kanicki, *ELECTRICAL AND PHOTOVOLTAIC PROPERTIES OF METAL CONTACTS TO TRANS-POLYACETYLENE*. Thin Solid Films, 1984. **113**(1): p. 1-14.

100. Kanicki, J. and P. Fedorko, *ELECTRICAL AND PHOTOVOLTAIC PROPERTIES OF TRANS-POLYACETYLENE*. Journal of Physics D-Applied Physics, 1984. **17**(4): p. 805-817.
101. Vanderdonckt, E., J. Kanicki, and P. Fedorko, *ELECTRICAL AND PHOTOVOLTAIC PROPERTIES OF PB/TRANS-(CH)<sub>x</sub> AND PB/CH(ASF<sub>5</sub>)<sub>y</sub> X SCHOTTKY BARRIERS*. Journal of Applied Polymer Science, 1984. **29**(2): p. 619-627.
102. Glenis, S., et al., *ELECTROCHEMICALLY GROWN POLYTHIOPHENE AND POLY(3-METHYLTHIOPHENE) ORGANIC PHOTOVOLTAIC CELLS*. Thin Solid Films, 1984. **111**(2): p. 93-103.
103. Koezuka, H., K. Hyodo, and A.G. Macdiarmid, *ORGANIC HETEROJUNCTIONS UTILIZING 2 CONDUCTING POLYMERS - POLY(ACETYLENE) POLY(N-METHYLPYRROLE) JUNCTIONS*. Journal of Applied Physics, 1985. **58**(3): p. 1279-1284.
104. Campbell, I.H., et al., *Direct measurement of conjugated polymer electronic excitation energies using metal/polymer/metal structures*. Physical Review Letters, 1996. **76**(11): p. 1900-1903.
105. Alvarado, S.F., et al., *Direct determination of the exciton binding energy of conjugated polymers using a scanning tunneling microscope*. Physical Review Letters, 1998. **81**(5): p. 1082-1085.
106. Rossi, L., et al., *Influence of alkoxy substituents on the exciton binding energy of conjugated polymers*. Synthetic Metals, 2000. **111**: p. 527-530.

107. Blom, P.W.M., M.J.M. deJong, and J.J.M. Vlegaar, *Electron and hole transport in poly(p-phenylene vinylene) devices*. Applied Physics Letters, 1996. **68**(23): p. 3308-3310.
108. Antoniadis, H., M.A. Abkowitz, and B.R. Hsieh, *CARRIER DEEP-TRAPPING MOBILITY-LIFETIME PRODUCTS IN POLY(P-PHENYLENE VINYLENE)*. Applied Physics Letters, 1994. **65**(16): p. 2030-2032.
109. Lee, K.H., et al., *Morphology of All-Solution-Processed "Bilayer" Organic Solar Cells*. Advanced Materials, 2011. **23**(6): p. 766-+.
110. Kekuda, D., et al., *The effect of solvent induced crystallinity of polymer layer on poly(3-hexylthiophene)/C-70 bilayer solar cells*. Solar Energy Materials and Solar Cells, 2011. **95**(2): p. 419-422.
111. Huang, J.H., et al., *Efficient bilayer polymer solar cells possessing planar mixed-heterojunction structures*. Journal of Materials Chemistry, 2010. **20**(16): p. 3295-3300.
112. Stevens, D.M., et al., *Enhancement of the Morphology and Open Circuit Voltage in Bilayer Polymer/Fullerene Solar Cells*. Journal of Physical Chemistry C, 2009. **113**(26): p. 11408-11415.
113. Gadisa, A., et al., *Bipolar Charge Transport in Fullerene Molecules in a Bilayer and Blend of Polyfluorene Copolymer and Fullerene*. Advanced Materials, 2010. **22**(9): p. 1008-+.
114. Erten, S. and S. Icli, *Bilayer heterojunction solar cell based on naphthalene bis-benzimidazole*. Inorganica Chimica Acta, 2008. **361**(3): p. 595-600.

115. Daoud, W.A. and M.L. Turner, *Effect of interfacial properties and film thickness on device performance of bilayer TiO<sub>2</sub>-poly(1,4-phenylenevinylene) solar cells prepared by spin coating*. Reactive & Functional Polymers, 2006. **66**(1): p. 13-20.
116. Sariciftci, N.S., et al., *PHOTOINDUCED ELECTRON-TRANSFER FROM A CONDUCTING POLYMER TO BUCKMINSTERFULLERENE*. Science, 1992. **258**(5087): p. 1474-1476.
117. Sariciftci, N.S., et al., *SEMICONDUCTING POLYMER-BUCKMINSTERFULLERENE HETEROJUNCTIONS - DIODES, PHOTODIODES, AND PHOTOVOLTAIC CELLS*. Applied Physics Letters, 1993. **62**(6): p. 585-587.
118. Yu, G., K. Pakbaz, and A.J. Heeger, *SEMICONDUCTING POLYMER DIODES - LARGE-SIZE, LOW-COST PHOTODETECTORS WITH EXCELLENT VISIBLE-ULTRAVIOLET SENSITIVITY*. Applied Physics Letters, 1994. **64**(25): p. 3422-3424.
119. Yu, H.Z., *Different solvents effect on the performance of the solar cells based on poly(3-hexylthiophene):methanofullerenes*. Synthetic Metals, 2010. **160**(23-24): p. 2505-2509.
120. Moon, J.S., et al., *Spontaneous Formation of Bulk Heterojunction Nanostructures: Multiple Routes to Equivalent Morphologies*. Nano Letters, 2011. **11**(3): p. 1036-1039.
121. Bagienski, W. and M.C. Gupta, *Temperature dependence of polymer/fullerene organic solar cells*. Solar Energy Materials and Solar Cells, 2011. **95**(3): p. 933-941.
122. Yu, P.Q., et al., *Investigation of electric charge transport in conjugated polymer P3HT: PCBM solar cell with temperature dependent current and capacitance*

- measurements, in *Physica Status Solidi C - Current Topics in Solid State Physics*, Vol 7 No 3-4, R.E.I. Schropp, Editor 2010. p. 1000-1004.
123. Tsai, Y.T., et al., *Charge Transporting Properties and Output Characteristics in Polythiophene: Fullerene Derivative Solar Cells*. Japanese Journal of Applied Physics, 2011. **50**(1).
124. Li, W.M., et al., *Effect of solvents on the performance of P3HT: PCBM solar cells*, in *Optoelectronic Devices and Integration Iii*, X. Zhang, H. Ming, and A.X. Wang, Editors. 2010.
125. Arora, S., et al., *Role of donor-acceptor domain formation and interface states in initial degradation of P3HT:PCBM-based solar cells*. Physica Scripta, 2011. **83**(3).
126. Xiao, T., et al., *Simple routes for improving polythiophene: fullerene-based organic solar cells*. Organic Electronics, 2011. **12**(2): p. 257-262.
127. Yamanaka, D., et al., *Nano-structure Control in the Bulk Heterojunction Layer for Organic Solar Cells*, in *Organic Photonics Iv*, P.L. Heremans, R. Coehoorn, and C. Adachi, Editors. 2010.
128. Sakai, K., et al., *Organic solar cell performance and nano-morphology of poly(3-hexylthiophene-2,5-diyl) (P3HT)/PCBM thin film using poly(3-ocylthiophene)*, in *Organic Photonics Iv*, P.L. Heremans, R. Coehoorn, and C. Adachi, Editors. 2010.
129. Khan, M.T., et al., *Effect of cadmium sulphide quantum dot processing and post thermal annealing on P3HT/PCBM photovoltaic device*. Thin Solid Films, 2010. **519**(3): p. 1007-1011.

130. Verploegen, E., et al., *Effects of Thermal Annealing Upon the Morphology of Polymer-Fullerene Blends*. *Advanced Functional Materials*, 2010. **20**(20): p. 3519-3529.
131. Howard, I.A., et al., *Effect of Morphology on Ultrafast Free Carrier Generation in Polythiophene:Fullerene Organic Solar Cells*. *Journal of the American Chemical Society*, 2010. **132**(42): p. 14866-14876.
132. Chirvase, D., et al., *Electrical and optical design and characterisation of regioregular poly(3-hexylthiophene-2,5diyl)/fullerene-based heterojunction polymer solar cells*. *Synthetic Metals*, 2003. **138**(1-2): p. 299-304.
133. Ma, W.L., et al., *Thermally stable, efficient polymer solar cells with nanoscale control of the interpenetrating network morphology*. *Advanced Functional Materials*, 2005. **15**(10): p. 1617-1622.
134. Solamer. Available from: <http://www.solarmer.com>.
135. <http://nobelprize.org>.
136. Skotheim, T.A. and J.R. Reynolds, eds. *Conjugated Polymers, Theory, Synthesis, Properties, and Characterization*. 2007, CRC.
137. Pribat, D. and C.S. Cojocaru, *Carbon Nanotubes, Semiconductor Nanowires and Graphene for Thin Film Transistor and Circuit Applications*. *Japanese Journal of Applied Physics*, 2011. **50**(3).
138. Otsuji, T. and Ieee, *Emission of Terahertz Radiation from Two-Dimensional Electron Systems in Semiconductor Nano-Heterostructures*. 35th International Conference on Infrared, Millimeter, and Terahertz Waves2010.

139. Safron, N.S., A.S. Brewer, and M.S. Arnold, *Semiconducting Two-Dimensional Graphene Nanoconstriction Arrays*. *Small*, 2011. **7**(4): p. 492-498.
140. Tongay, S., et al., *Tuning Schottky diodes at the many-layer-graphene/semiconductor interface by doping*. *Carbon*, 2011. **49**(6): p. 2033-2038.
141. Achard, J., et al., *Thick boron doped diamond single crystals for high power electronics*. *Diamond and Related Materials*, 2011. **20**(2): p. 145-152.
142. Pilzak, G.S., et al., *Hybrid Conjugated Organic Oligomers Consisting of Oligodiacetylene and Thiophene Units: Synthesis and Optical Properties*. *Chemistry-a European Journal*, 2009. **15**(36): p. 9085-9096.
143. Gregg, B.A., S.G. Chen, and R.A. Cormier, *Coulomb forces and doping in organic semiconductors*. *Chemistry of Materials*, 2004. **16**(23): p. 4586-4599.
144. Califano, V., et al., *Substrate temperature dependence of the structure of polythiophene thin films obtained by Matrix Assisted Pulsed Laser Evaporation (MAPLE)*. *European Physical Journal-Applied Physics*, 2009. **48**(1).
145. Gunbas, G.E., et al., *A fast switching, low band gap, p- and n-dopable, donor-acceptor type polymer*. *Journal of Electroanalytical Chemistry*, 2008. **615**(1): p. 75-83.
146. Levi, M.D. and D. Aurbach, *A short review on the strategy towards development of pi-conjugated polymers with highly reversible p- and n-doping*. *Journal of Power Sources*, 2008. **180**(2): p. 902-908.
147. Koyuncu, S., et al., *Electrochemical and optical properties of novel donor-acceptor thiophene-perylene-thiophene polymers*. *Journal of Polymer Science Part a-Polymer Chemistry*, 2008. **46**(6): p. 1974-1989.

148. Zhang, F.X. and M.P. Srinivasan, *Structure-related lower surface resistivity and faster doping of poly(thiophene-3-acetic acid-co-3-hexylthiophene) compared with poly(thiophene-3-acetic acid)*. *Materials Chemistry and Physics*, 2008. **112**(1): p. 223-225.
149. Ling, Q.D., et al., *In situ interfacial analysis of evaporated potassium on the electroluminescent fluorene-thiophene copolymer*. *Surface and Interface Analysis*, 2002. **33**(7): p. 552-558.
150. Liao, H.H., et al., *Dynamics and reversibility of oxygen doping and de-doping for conjugated polymer*. *Journal of Applied Physics*, 2008. **103**(10).
151. Vaterlein, C., et al., *Electrical conductivity and oxygen doping of vapour-deposited oligothiophene films*. *Synthetic Metals*, 1996. **76**(1-3): p. 133-136.
152. Sinigersky, V., et al., *Doped non-conjugated polymers with enhanced electrical conductivity* .2. *Macromolecular Chemistry and Physics*, 1996. **197**(5): p. 1713-1720.
153. Shoute, L.C.T., et al., *Redox driven conductance changes for resistive memory*. *Applied Physics a-Materials Science & Processing*, 2011. **102**(4): p. 841-850.
154. Zhang, F., et al., *Molecular and electronic structure of cyclo 10 thiophene in various oxidation states: polaron pair vs. bipolaron*. *Chemical Science*, 2011. **2**(4): p. 781-784.
155. Jiang, X.Q., et al., *Mobilities of charge carriers hopping between pi-conjugated polymer chains*. *Journal of Materials Chemistry*, 2001. **11**(12): p. 3043-3048.
156. Coffey, D.C., et al., *Photovoltaic Charge Generation in Organic Semiconductors Based on Long-Range Energy Transfer*. *Acs Nano*, 2010. **4**(9): p. 5437-5445.

157. Drori, T., J. Holt, and Z.V. Vardeny, *Optical studies of the charge transfer complex in polythiophene/fullerene blends for organic photovoltaic applications*. Physical Review B, 2010. **82**(7).
158. Facchetti, A., *pi-Conjugated Polymers for Organic Electronics and Photovoltaic Cell Applications*. Chemistry of Materials, 2011. **23**(3): p. 733-758.
159. Nelson, T.L., et al., *Transistor Paint: High Mobilities in Small Bandgap Polymer Semiconductor Based on the Strong Acceptor, Diketopyrrolopyrrole and Strong Donor, Dithienopyrrole*. Advanced Materials, 2010. **22**(41): p. 4617-4621.
160. Hoppe, H., et al., *Modeling the optical absorption within conjugated polymer/fullerene-based bulk-heterojunction organic solar cells*. Solar Energy Materials and Solar Cells, 2003. **80**(1): p. 105-113.
161. van Bavel, S., et al., *Relation between Photoactive Layer Thickness, 3D Morphology, and Device Performance in P3HT/PCBM Bulk-Heterojunction Solar Cells*. Macromolecules, 2009. **42**(19): p. 7396-7403.
162. Pettersson, L.A.A., L.S. Roman, and O. Inganäs, *Modeling photocurrent action spectra of photovoltaic devices based on organic thin films*. Journal of Applied Physics, 1999. **86**(1): p. 487-496.
163. Haugeneder, A., et al., *Exciton diffusion and dissociation in conjugated polymer fullerene blends and heterostructures*. Physical Review B, 1999. **59**(23): p. 15346-15351.
164. Stoessel, M., et al., *Cathode-induced luminescence quenching in polyfluorenes*. Journal of Applied Physics, 2000. **87**(9): p. 4467-4475.

165. Chandross, M., et al., *EXCITONS IN POLY(PARA-PHENYLENEVINYLENE)*. Physical Review B, 1994. **50**(19): p. 14702-14705.
166. Nolasco, J.C., et al., *Relation between the barrier interface and the built-in potential in pentacene/C-60 solar cell*. Applied Physics Letters, 2010. **97**(1).
167. Km, S., M., in *Materials Science and Engineering* 2009, The University of Michigan.
168. Hanse, C.M., *Hansen Solubility Parameter, A user's Handbook*. Vol. 2. 2007: CRC.
169. Park, J.H., et al., *Enhanced device performance of organic solar cells via reduction of the crystallinity in the donor polymer*. Journal of Materials Chemistry, 2010. **20**(28): p. 5860-5865.
170. Parisi, J., et al., *Charge transfer and transport in polymer-fullerene solar cells*. Zeitschrift Fur Naturforschung Section a-a Journal of Physical Sciences, 2002. **57**(12): p. 995-1000.
171. Nguyen, T.P., *Defects in organic electronic devices*. Physica Status Solidi a-Applications and Materials Science, 2008. **205**(1): p. 162-166.
172. Konezny, S.J., M.N. Bussac, and L. Zuppiroli, *Trap-limited transport in rubrene transistors*. Applied Physics Letters, 2009. **95**(26).
173. Dickey, K.C., J.E. Anthony, and Y.L. Loo, *Improving organic thin-film transistor performance through solvent-vapor annealing of solution-processable triethylsilylethynyl anthradithiophene*. Advanced Materials, 2006. **18**(13): p. 1721-+.
174. Era, M., T. Tsutsui, and S. Saito, *POLARIZED ELECTROLUMINESCENCE FROM ORIENTED P-SEXIPHENYL VACUUM-DEPOSITED FILM*. Applied Physics Letters, 1995. **67**(17): p. 2436-2438.

175. Chen, X.L., et al., *Morphological and transistor studies of organic molecular semiconductors with anisotropic electrical characteristics*. Chemistry of Materials, 2001. **13**(4): p. 1341-1348.
176. Kang, S.J., et al., *Effect of rubbed polyimide layer on the field-effect mobility in pentacene thin-film transistors*. Applied Physics Letters, 2008. **92**(5).
177. Chou, W.Y. and H.L. Cheng, *An orientation-controlled pentacene film aligned by photoaligned polyimide for organic thin-film transistor applications*. Advanced Functional Materials, 2004. **14**(8): p. 811-815.
178. Jin, S.H., et al., *Surface-induced alignment of pentacene by photo-alignment technology for organic thin film transistors*. Journal of Materials Chemistry, 2005. **15**(47): p. 5029-5036.
179. Dyreklev, P., et al., *POLYMERIC FIELD-EFFECT TRANSISTORS USING ORIENTED POLYMERS*. Synthetic Metals, 1993. **57**(1): p. 4093-4098.
180. Cimrova, V., et al., *Polarized light emission from LEDs prepared by the Langmuir-Blodgett technique*. Advanced Materials, 1996. **8**(2): p. 146-&.
181. Jo, S.J., et al., *Inducement of Azimuthal molecular orientation of pentacene by imprinted periodic groove patterns for organic thin-film transistors*. Advanced Materials, 2008. **20**(6): p. 1146-+.
182. Yang, H.C., et al., *Structural transitions of nanocrystalline domains in regioregular poly(3-hexyl thiophene) thin films*. Journal of Polymer Science Part B-Polymer Physics, 2007. **45**(11): p. 1303-1312.
183. Sirringhaus, H., et al., *Two-dimensional charge transport in self-organized, high-mobility conjugated polymers*. Nature, 1999. **401**(6754): p. 685-688.

184. van Duren, J.K.J., et al., *Relating the morphology of poly(p-phenylene vinylene)/methanofullerene blends to solar-cell performance*. *Advanced Functional Materials*, 2004. **14**(5): p. 425-434.
185. Woo, C.H., et al., *The Influence of Poly(3-hexylthiophene) Regioregularity on Fullerene-Composite Solar Cell Performance*. *Journal of the American Chemical Society*, 2008. **130**(48): p. 16324-16329.
186. Hoppe, H., et al., *Nanoscale morphology of conjugated polymer/fullerene-based bulk-heterojunction solar cells*. *Advanced Functional Materials*, 2004. **14**(10): p. 1005-1011.
187. Erb, T., et al., *Correlation between structural and optical properties of composite polymer/fullerene films for organic solar cells*. *Advanced Functional Materials*, 2005. **15**(7): p. 1193-1196.
188. Chiu, M.Y., et al., *Simultaneous use of small- and wide-angle X-ray techniques to analyze nanometerscale phase separation in polymer heterojunction solar cells*. *Advanced Materials*, 2008. **20**(13): p. 2573-+.
189. Yang, X.N., et al., *Nanoscale morphology of high-performance polymer solar cells*. *Nano Letters*, 2005. **5**(4): p. 579-583.
190. Lee, S.S. and Y.L. Loo, *Structural Complexities in the Active Layers of Organic Electronics*, in *Annual Review of Chemical and Biomolecular Engineering, Vol 12* 2010. p. 59-78.
191. Kiel, J.W., A.P.R. Eberle, and M.E. Mackay, *Nanoparticle Agglomeration in Polymer-Based Solar Cells*. *Physical Review Letters*, 2010. **105**(16).

192. Collins, B.A., et al., *Molecular Miscibility of Polymer-Fullerene Blends*. Journal of Physical Chemistry Letters, 2010. **1**(21): p. 3160-3166.
193. Padinger, F., R.S. Rittberger, and N.S. Sariciftci, *Effects of postproduction treatment on plastic solar cells*. Advanced Functional Materials, 2003. **13**(1): p. 85-88.
194. Motaung, D.E., et al., *The influence of thermal annealing on the morphology and structural properties of a conjugated polymer in blends with an organic acceptor material*. Journal of Materials Science, 2009. **44**(12): p. 3192-3197.
195. Kim, J.S., et al., *Phase separation in polyfluorene-based conjugated polymer blends: Lateral and vertical analysis of blend spin-cast thin films*. Macromolecules, 2004. **37**(8): p. 2861-2871.
196. Kim, C.S., et al., *Altering the Thermodynamics of Phase Separation in Inverted Bulk-Heterojunction Organic Solar Cells*. Advanced Materials, 2009. **21**(30): p. 3110-+.
197. Peet, J., et al., *Method for increasing the photoconductive response in conjugated polymer/fullerene composites*. Applied Physics Letters, 2006. **89**(25).
198. Yao, Y., et al., *Effect of solvent mixture on the nanoscale phase separation in polymer solar cells*. Advanced Functional Materials, 2008. **18**(12): p. 1783-1789.
199. Reyes-Reyes, M., et al., *Meso-structure formation for enhanced organic photovoltaic cells*. Organic Letters, 2005. **7**(26): p. 5749-5752.
200. Nilsson, S., et al., *Morphology and phase segregation of spin-casted films of Polyfluorene/PCBM blends*. Macromolecules, 2007. **40**(23): p. 8291-8301.
201. Bull, T.A., et al., *The Role of Mesoscopic PCBM Crystallites in Solvent Vapor Annealed Copolymer Solar Cells*. ACS Nano, 2009. **3**(3): p. 627-636.

202. Chen, F.C., et al., *Morphological study of P3HT:PCBM blend films prepared through solvent annealing for solar cell applications*. *Solar Energy Materials and Solar Cells*, 2010. **94**(12): p. 2426-2430.
203. Shaheen, S.E., et al., *2.5% efficient organic plastic solar cells*. *Applied Physics Letters*, 2001. **78**(6): p. 841-843.
204. Liu, J., Y.J. Shi, and Y. Yang, *Solvation-induced morphology effects on the performance of polymer-based photovoltaic devices*. *Advanced Functional Materials*, 2001. **11**(6): p. 420-424.
205. Rispens, M.T., et al., *Influence of the solvent on the crystal structure of PCBM and the efficiency of MDMO-PPV : PCBM 'plastic' solar cells*. *Chemical Communications*, 2003(17): p. 2116-2118.
206. Chirvase, D., et al., *Influence of nanomorphology on the photovoltaic action of polymer-fullerene composites*. *Nanotechnology*, 2004. **15**(9): p. 1317-1323.
207. Savenije, T.J., et al., *The effect of thermal treatment on the morphology and charge carrier dynamics in a polythiophene-fullerene bulk heterojunction*. *Advanced Functional Materials*, 2005. **15**(8): p. 1260-1266.
208. Quist, P.A.C., et al., *The effect of annealing on the charge-carrier dynamics in a polymer/polymer bulk heterojunction for photovoltaic applications*. *Advanced Functional Materials*, 2005. **15**(3): p. 469-474.
209. Wei, G.D., et al., *Efficient, Ordered Bulk Heterojunction Nanocrystalline Solar Cells by Annealing of Ultrathin Squaraine Thin Films*. *Nano Letters*, 2010. **10**(9): p. 3555-3559.

210. Li, G., et al., *Manipulating regioregular poly(3-hexylthiophene): 6,6 -phenyl-C-61-butyric acid methyl ester blends - route towards high efficiency polymer solar cells.* Journal of Materials Chemistry, 2007. **17**(30): p. 3126-3140.
211. Kim, Y., et al., *A strong regioregularity effect in self-organizing conjugated polymer films and high-efficiency polythiophene: fullerene solar cells.* Nature Materials, 2006. **5**(3): p. 197-203.
212. Helgesen, M., et al., *Influence of the Annealing Temperature on the Photovoltaic Performance and Film Morphology Applying Novel Thermocleavable Materials.* Chemistry of Materials, 2010. **22**(19): p. 5617-5624.
213. Yang, M.D., et al., *Improvement of material quality of multijunction solar cells by rapid thermal annealing.* Japanese Journal of Applied Physics, 2008. **47**(6): p. 4499-4501.
214. Lee, J.H., et al., *Wiper coating method for PEDOT:PSS film on fabricating organic photovoltaic modules.* Current Applied Physics, 2010. **10**(4): p. E185-E188.
215. Weickert, J., et al., *Spray-deposited PEDOT:PSS for inverted organic solar cells.* Solar Energy Materials and Solar Cells, 2010. **94**(12): p. 2371-2374.
216. Eom, S.H., et al., *High efficiency polymer solar cells via sequential inkjet-printing of PEDOT:PSS and P3HT:PCBM inks with additives.* Organic Electronics, 2010. **11**(9): p. 1516-1522.
217. Wang, M.D., et al., *Performance and Stability Improvement of P3HT:PCBM-Based Solar Cells by Thermally Evaporated Chromium Oxide (CrOx) Interfacial Layer.* Acs Applied Materials & Interfaces, 2010. **2**(10): p. 2699-2702.

218. Chen, F.C. and C.H. Lin, *Construction and characteristics of tandem organic solar cells featuring small molecule-based films on polymer-based subcells*. Journal of Physics D-Applied Physics, 2010. **43**(2).
219. Swaraj, S., et al., *The utility of resonant soft x-ray scattering and reflectivity for the nanoscale characterization of polymers*. European Physical Journal-Special Topics, 2009. **167**: p. 121-126.
220. Swaraj, S., et al., *Nanomorphology of Bulk Heterojunction Photovoltaic Thin Films Probed with Resonant Soft X-ray Scattering*. Nano Letters, 2010. **10**(8): p. 2863-2869.
221. McNeill, C.R., et al., *Evolution of the nanomorphology of photovoltaic polyfluorene blends: sub-100 nm resolution with x-ray spectromicroscopy*. Nanotechnology, 2008. **19**(42).
222. Ade, H., et al., *Characterization of Multicomponent Polymer Trilayers with Resonant Soft X-Ray Reflectivity*. Journal of Polymer Science Part B-Polymer Physics, 2009. **47**(13): p. 1291-1299.
223. Kim, S.H., S. Natarajan, and G.M. Liu, *Photochemical synthesis of oligothiophene thin films and nano-patterns in condensed multilayer films of 2,5-diiodothiophene - Effects of surface chemistry of substrates*. Catalysis Today, 2007. **123**(1-4): p. 104-112.
224. Liu, G.M., S. Natarajan, and S.H. Kim, *Photochemical production of oligothiophene and polythiophene micropatterns from 2,5-diiodothiophene on Au in UHV*. Surface Science, 2005. **592**(1-3): p. L305-L309.

225. Natarajan, S. and S.H. Kim, *Photochemical oligomerization pathways in 2,5-diiodothiophene film*. Journal of Photochemistry and Photobiology a-Chemistry, 2007. **188**(2-3): p. 342-345.
226. Natarajan, S. and S.H. Kim, *Photochemical conversion of 2,5-diiodothiophene condensed on substrates to oligothiophene and polythiophene thin films and micro-patterns*. Thin Solid Films, 2006. **496**(2): p. 606-611.
227. Mihailetchi, V.D., et al., *Charge transport and photocurrent generation in poly (3-hexylthiophene): Methanofullerene bulk-heterojunction solar cells*. Advanced Functional Materials, 2006. **16**(5): p. 699-708.
228. Zhou, H.X., et al., *A Weak Donor-Strong Acceptor Strategy to Design Ideal Polymers for Organic Solar Cells*. Acs Applied Materials & Interfaces, 2010. **2**(5): p. 1377-1383.
229. Dante, M., et al., *Self-Assembly and Charge-Transport Properties of a Polythiophene-Fullerene Triblock Copolymer*. Advanced Materials, 2010. **22**(16): p. 1835-+.
230. ; Available from: [http://en.wikipedia.org/wiki/Bragg's\\_law](http://en.wikipedia.org/wiki/Bragg's_law).
231. Kim, J.S., et al., *Poly(3-hexylthiophene) Nanorods with Aligned Chain Orientation for Organic Photovoltaics*. Advanced Functional Materials, 2010. **20**(4): p. 540-545.
232. Meredig, B., A. Salleo, and R. Gee, *Ordering of Poly(3-hexylthiophene) Nanocrystallites on the Basis of Substrate Surface Energy*. Acs Nano, 2009. **3**(10): p. 2881-2886.
233. Kazarinoff, P.D., et al., *OTFT performance of air-stable ester-functionalized polythiophenes*. Journal of Materials Chemistry, 2010. **20**(15): p. 3040-3045.

234. Chen, D.A., et al., *P3HT/PCBM Bulk Heterojunction Organic Photovoltaics: Correlating Efficiency and Morphology*. Nano Letters, 2011. **11**(2): p. 561-567.
235. Watts, B., et al., *A Quantitative Study of PCBM Diffusion during Annealing of P3HT:PCBM Blend Films*. Macromolecules, 2009. **42**(21): p. 8392-8397.
236. Baek, W.H., et al., *Effect of P3HT:PCBM concentration in solvent on performances of organic solar cells*. Solar Energy Materials and Solar Cells, 2009. **93**(8): p. 1263-1267.
237. Anslyn, E.A. and D.A. Dougherty, eds. *Modern Physical Organic Chemistry*. 2006, University Science Book.
238. Lee, Y.I., et al., *Highly efficient inverted poly(3-hexylthiophene): Methano-fullerene 6,6 -phenyl C71-butyrac acid methyl ester bulk heterojunction solar cell with Cs<sub>2</sub>CO<sub>3</sub> and MoO<sub>3</sub>*. Organic Electronics, 2011. **12**(2): p. 353-357.
239. Kim, K., et al., *Roles of donor and acceptor nanodomains in 6% efficient thermally annealed polymer photovoltaics*. Applied Physics Letters, 2007. **90**(16).
240. Emery, K.A., *Comment on "Roles of donor and acceptor nanodomains in 6% efficient thermally annealed polymer photovoltaics" Appl. Phys. Lett. 90, 163511 (2007)*. Applied Physics Letters, 2007. **91**(26).
241. Carroll, D.L., et al., *Response to "Comment on 'Roles of donor and acceptor nanodomains in 6% efficient thermally annealed polymer photovoltaics' Appl. Phys. Lett. 91, 266101 (2007) "*. Applied Physics Letters, 2007. **91**(26).
242. Carroll, D.L., et al., *Response to "Comment on 'Roles of donor and acceptor nanodomains in 6% efficient thermally annealed polymer photovoltaics'" Appl. Phys. Lett. 90, 163511 (2007)*. Applied Physics Letters, 2008. **92**(7).

243. Scharber, M.C., et al., *Influence of the Bridging Atom on the Performance of a Low-Bandgap Bulk Heterojunction Solar Cell*. *Advanced Materials*, 2010. **22**(3): p. 367-+.
244. Sensfuss, S., et al., *Thienopyrazine-based low-bandgap polymers for flexible polymer solar cells*. *European Physical Journal-Applied Physics*, 2010. **51**(3).
245. Guo, J.C., et al., *Structure, Dynamics, and Power Conversion Efficiency Correlations in a New Low Bandgap Polymer: PCBM Solar Cell*. *Journal of Physical Chemistry B*, 2010. **114**(2): p. 742-748.
246. Sahu, D., et al., *Synthesis and Characterization of Novel Low-Bandgap Triphenylamine-Based Conjugated Polymers with Main-Chain Donors and Pendent Acceptors for Organic Photovoltaics*. *Journal of Polymer Science Part a-Polymer Chemistry*, 2010. **48**(24): p. 5812-5823.
247. Renz, J.A., et al., *Correlation Between Crystallinity and Solar-Cell Efficiency of the Low-Bandgap Polymer PDDTP*. *Macromolecular Chemistry and Physics*, 2010. **211**(15): p. 1689-1694.
248. Zhang, G.B., et al., *Synthesis and Photovoltaic Properties of New Low Bandgap Isoindigo-Based Conjugated Polymers*. *Macromolecules*, 2011. **44**(6): p. 1414-1420.
249. Noone, K.M., et al., *Broadband Absorbing Bulk Heterojunction Photovoltaics Using Low-Bandgap Solution-Processed Quantum Dots*. *Nano Letters*, 2010. **10**(7): p. 2635-2639.
250. Zhang, G.B., et al., *Low bandgap polymers with benzo 1,2-b:4,5-b ' dithiophene and bithiophene-dioxopyrrolothiophene units for photovoltaic applications*. *Polymer*, 2011. **52**(2): p. 415-421.

251. Wang, Q.W. and W.Y. Wong, *New low-bandgap polymetallaynes of platinum functionalized with a triphenylamine-benzothiadiazole donor-acceptor unit for solar cell applications*. *Polymer Chemistry*, 2011. **2**(2): p. 432-440.
252. Zhang, G.B., et al., *Synthesis of low bandgap polymer based on 3,6-dithien-2-yl-2, 5-dialkylpyrrolo 3,4-c pyrrole-1,4-dione for photovoltaic applications*. *Solar Energy Materials and Solar Cells*, 2011. **95**(4): p. 1168-1173.
253. Liang, Y.Y., et al., *For the Bright Future-Bulk Heterojunction Polymer Solar Cells with Power Conversion Efficiency of 7.4%*. *Advanced Materials*, 2010. **22**(20): p. E135-+.
254. Lee, Y.I., et al., *Degradation of Poly(3-hexylthiophene):Methano-Fullerene 6,6 - Phenyl-C71 Butyric Acid Methyl Ester Bulk Heterojunction Solar Cells and Annealing Effect on the Degraded Devices*. *Japanese Journal of Applied Physics*, 2011. **50**(1).
255. Namkoong, G., et al., *Design of organic tandem solar cells using PCPDTBT: PC61BM and P3HT: PC71BM*. *Journal of Applied Physics*, 2010. **107**(12).
256. Fichou, D., ed. *Oligo- and Polythiophenes*. 1999, Wiley-VCH.
257. Roncali, J., *CONJUGATED POLY(THIOPHENES) - SYNTHESIS, FUNCTIONALIZATION, AND APPLICATIONS*. *Chemical Reviews*, 1992. **92**(4): p. 711-738.
258. Tanaka, K., et al., *PLASMA POLYMERIZATION OF THIOPHENE AND 3-METHYLTHIOPHENE*. *Synthetic Metals*, 1990. **38**(1): p. 107-116.
259. Ryan, M.E., et al., *Plasma polymerization of 2-iodothiophene*. *Chemistry of Materials*, 1996. **8**(4): p. 916-921.

260. Groenewoud, L.M.H., et al., *Pulsed plasma polymerization of thiophene*. Langmuir, 2000. **16**(15): p. 6278-6286.
261. Nishio, S., et al., *Preparation of polythiophene thin films by UV laser-assisted deposition of 2,5-dichlorothiophene with a 248 nm excimer laser beam*. Journal of Photochemistry and Photobiology a-Chemistry, 1998. **116**(3): p. 245-249.
262. Wochnowski, C. and S. Metev, *UV-laser-assisted synthesis of iodine-doped electrical conductive polythiophene*. Applied Surface Science, 2002. **186**(1-4): p. 34-39.
263. Salaneck, W.R., et al., *UHV-COMPATIBLE PROCESSING OF CONDUCTING POLYMERS - POLYTHIOPHENE*. Synthetic Metals, 1987. **21**(1): p. 57-61.
264. Land, T.A. and J.C. Hemminger, *PHOTOEMISSION AND THERMAL-DESORPTION STUDIES OF ELECTRON-BEAM POLYMERIZED THIOPHENE FILMS ON PT(111)*. Surface Science, 1992. **268**(1-3): p. 179-188.
265. Tepavcevic, S., Y. Choi, and L. Hanley, *Surface polymerization by ion-assisted deposition for polythiophene film growth*. Journal of the American Chemical Society, 2003. **125**(9): p. 2396-2397.
266. Raza, H., et al., *X-ray and electron beam modification of thiophene overlayers on TiO<sub>2</sub>(100)1 x 1 and 1 x 3*. Surface Science, 1997. **390**(1-3): p. 256-260.
267. Nambu, A., et al., *Film growth and X-ray induced chemical reactions of thiophene adsorbed on Au(111)*. Surface Science, 2003. **530**(1-2): p. 101-110.
268. Hernandez, J.E., H. Ahn, and J.E. Whitten, *X-ray and electron induced oligomerization of condensed 3-hexylthiophene*. Journal of Physical Chemistry B, 2001. **105**(35): p. 8339-8344.

269. Liu, G.M., et al., *Dendritic aggregation of oligothiophene during desorption of 2,5-diiodothiophene multilayer and topography-induced alignment of oligothiophene nanofibers*. Journal of Physical Chemistry B, 2006. **110**(41): p. 20197-20201.
270. Liu, G., K. Ryoo, and S.H. Kim, *Thermal reaction and desorption behavior of 2,5-diiodothiophene on clean and passivated Au surfaces*. Surface Science, 2007. **601**: p. 2967-2972.
271. Tepavcevic, S., et al., *Improved Hybrid Solar Cells via in situ UV Polymerization*. Small, 2009. **5**(15): p. 1776-1783.
272. Perepichka, I.F. and D.F. Perepichka, eds. *Handbook of Thiophene-based Materials: Applications in Organic Electronics and Photonics-Properties and Applications*. Vol. 2. 2009, Wiley.
273. Perepichka, I.F. and D.F. Perepichka, eds. *Handbook of Thiophene-based Materials: Applications in Organic Electronics and Photonics*. Vol. 1. 2009, Wiley.
274. Biemann, I., *Tables of Spectral Data for Structure Determination of Organic Compounds*. 2 ed1989: Springer-Verlag.

## APPENDICES

## APPENDIX A

### 8. UV PHOTO-POLYMERIZATION OF 2,5-DIBROMOTHIOPHENE (DBT) AND ITS MATERIAL PROPERTIES

#### 8.1. Background

Poly(thiophene) (PT) is one of the most popular semiconductor polymers because it has excellent electrical properties and thermal stability. Furthermore, it is relatively stable in oxidation.[256] The inherent problem of PT is the low solubility like most other inherent semiconducting polymers such as poly(phenylenevinylene) (PPV), poly(paraphenylene) (PPP), poly(phenylene sulfide) (PPS) and poly(acetylene) (PA). This is the result of the high intermolecular  $\pi$ - $\pi$  orbital overlapping and the enhanced crystallinity. Solubility of PT dramatically decreases with the increase of molecular weight and it is transformed into an insoluble PT even with 6 repeating units (sexithiophene). Sexithiophene has superior electrical properties and is typically employed in OTFT (organic thin film transistor) using a thermal evaporation process.[256]

There are two popular in situ polymerization methods of conjugated polymers such as polythiophene. The first is electrochemical polymerization[257] and the other is plasma polymerization. In the case of electrochemical polymerization, it is accomplished by applying a voltage into a monomer solution with diluted electrolyte, the oxidative coupling of thiophene ring on the surface of anode. This electrochemical polymerization can only be applied with a solvent and substrate having the higher oxidizing potential than that of thiophene monomer. In case of plasma polymerization of polythiophene[258-260], it is not yet well understood, the detail mechanisms of the initiation and propagation reactions are not clear. Additionally, there is an expected degradation from the high energy of species during the reaction. Random coupling of monomer and monomer fragmentation are usually produced and they resulted in a highly cross-linked polymer with many structural defects. This process is normally recommended for an antistatic coating process on non-conducting substrates without the critical concern for the quality of the coated film. Some other methods such as laser induced chemical vapor deposition[261, 262] and x-ray[263, 264], ion[265] and

electron induced polymerization[266-268]<sup>12-16</sup> were also reported and similar defragmentation related defects resulted due to the high energy species included.

In situ UV photo-polymerization of 2,5-diiodothiophene (DIT) was recently carried out by S. Natarajan et al. to make negative tone polythiophene patterns based on the solubility drop of polythiophene with the increase of molecular weight.[223-226, 269, 270] They thermally deposited a thin layer of solid DIT on Si wafer or Cu metal surfaces and made insoluble PT patterns under the various UV exposure conditions. S. Tepavcevic et al recently used this idea for their inorganic-organic hybrid polymer solar cells.[271] The UV photo-polymerization of DIT was carried out inside the vertically aligned TiO<sub>2</sub> nanotube arrays and P3HT was spin-coated as a p type semiconductor material on top of that array. The performance of solar cells was poor, perhaps the unreacted DIT monomers work as impurities.

In this thesis, a new concept of promising post process for the further improvement of the P3HT: PC<sub>61</sub>BM polymer solar cells is demonstrated. The key idea is that the solubility drop from an in situ UV photo-polymerization of DBT can result in a much finer morphology and the better crystalline orientation in P3HT: PC<sub>61</sub>BM polymer solar cells than that of the conventional post thermal annealing. In this chapter, a fundamental idea of the UV photo-polymerization of 2,5-dibromothiophene (DBT) was reviewed and verified. Additionally, the solubility decrease, the molecular weight increase, the crystallinity, and the thermal stability were studied using direct or indirect experimental methods.

## **8.2. UV Photo-Polymerization of 2,5-Dibromo-Thiophene (DBT).**

The covalent bond dissociation energy of carbon-bromine (C-Br) is 72.1Kcal/mol[237] and the UV photo-polymerization, regardless of DIT or DBT, is a radical based condensation reaction caused by breaking the carbon-halide bonding and the halogen gas is given off as a by-product. It has a slow polymerization rate, a low molecular weight and a broad molecular weight distribution in the final products. Furthermore, the unreacted monomers should be washed out using an organic solvent to be used for an application which requires the high purity of polythiophene. In the *in situ* UV photo-polymerization of DBT for P3HT: PC<sub>61</sub>BM BHJ polymer solar cells in this thesis, the introduced DBT amount for the reaction is

minimized using a vapor deposition and no further step is required to remove the unreacted DBT monomers. The fundamental reaction is shown as a schematic diagram in Figure 8.1.

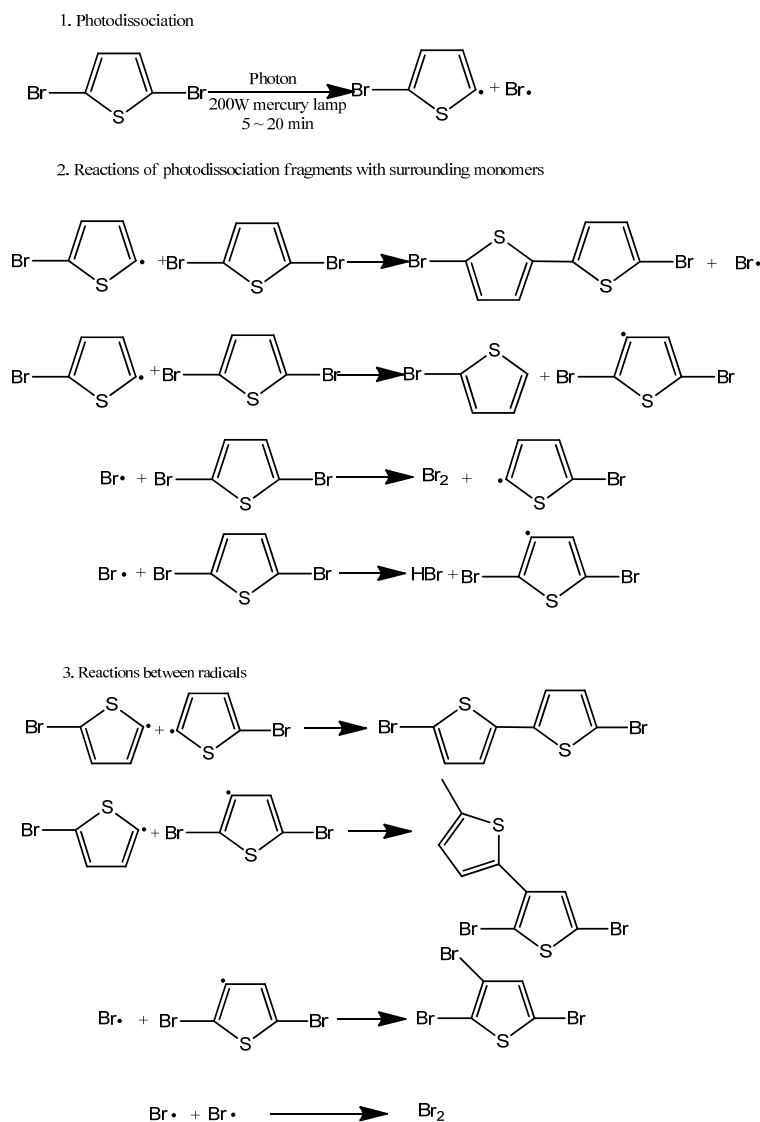


**Figure 8.1. Schematic reaction diagram of UV photo-polymerization of DBT (modified based on the DIT reaction diagram of the Penn State Group).[223-226]**

The reaction verifications of the UV photo-polymerization of DBT were performed by using a UV vis spectrophotometer and an FT-IR. The absorption peak maximum( $Abs_{max}$ ) at 500nm is increased and the optical bandgap decreases from the bathochromic shift of absorption

spectra as time goes by and there was a precipitation of relative high molecular weight of insoluble polythiophene.

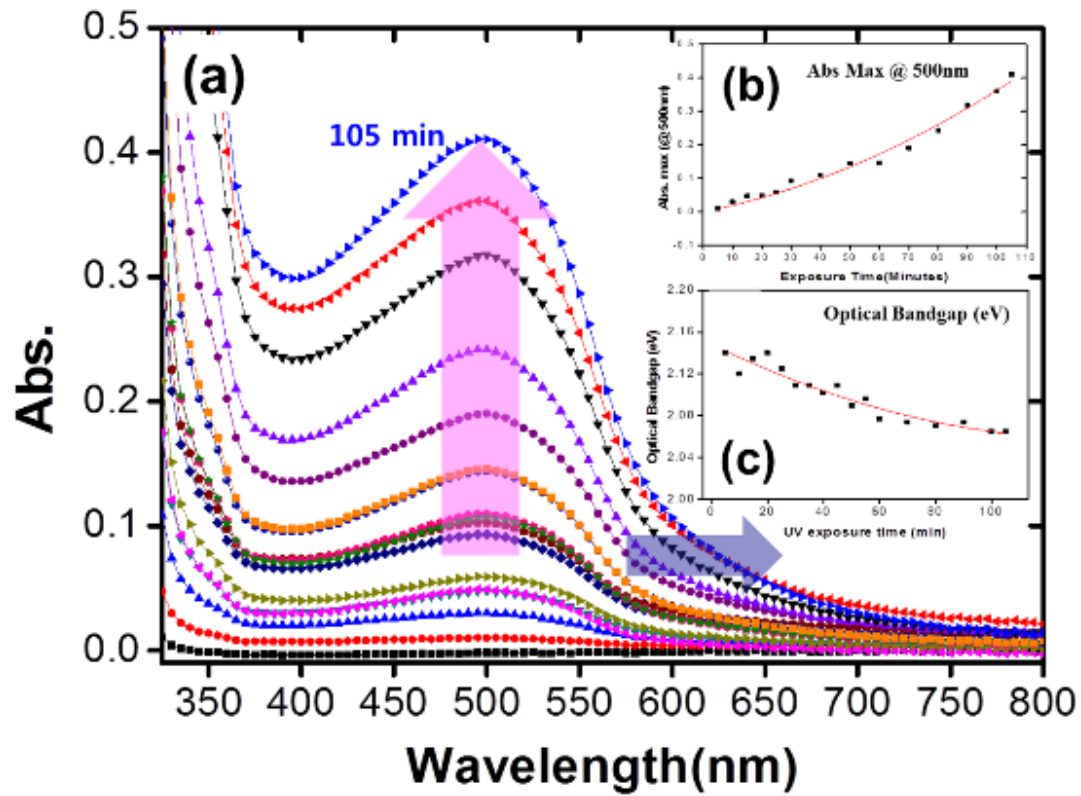
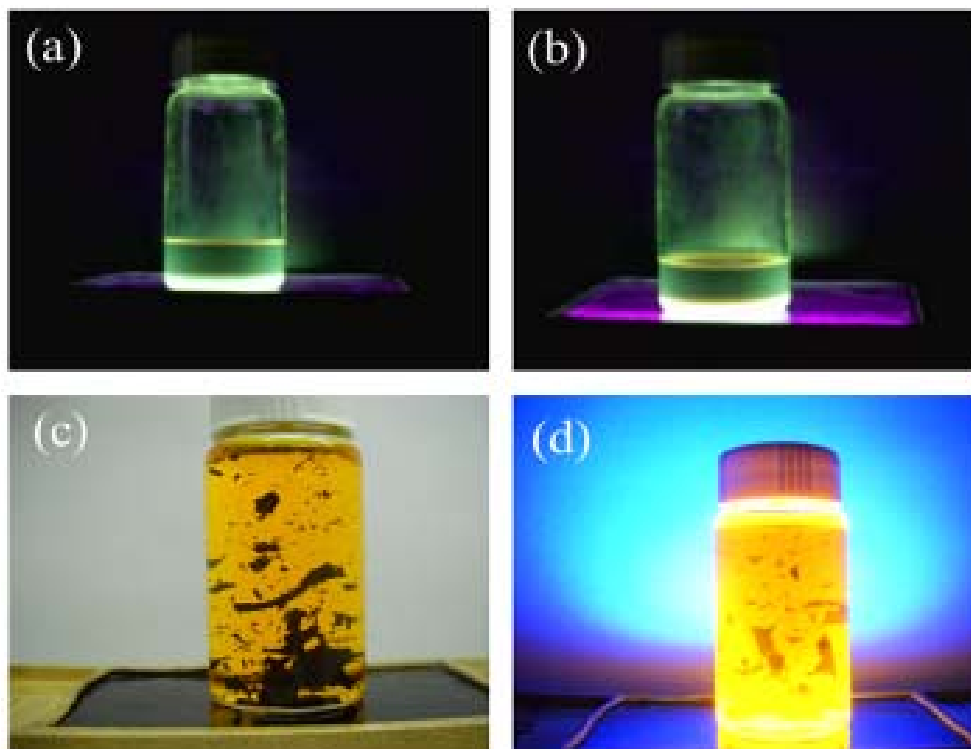


Figure 8.2 (a) UVvis Spectrophotometer spectra during the UVphoto polymerization of DBT (Soluble portions only), (b)  $Abs_{max}$  and (c) optical bandgaps vs. UV exposure times.



**Figure 8.3. Color photograph of photoluminescence emission of UV photo-polymerized liquid phase oligothiophenes from DBT at 25°C: (a) 5min and (b) 10min UV exposure (excitation @ 365nm) and precipitated UV photo-polymerized insoluble polythiophene for FT-IR analysis: (c) in THF and (d) photoluminescence (excitation @365nm in THF).**

The UVvis spectrophotometer results are shown in Figure 8.2 and the color photographs of the photoluminescence of the UV exposed DBT after 5min and 10min UV exposure are shown in Figure 8.3 (a) and (b). The color photoluminescence photographs of the UV photopolymerized insoluble PT are also shown in Figure 8.3 (c) and (d).

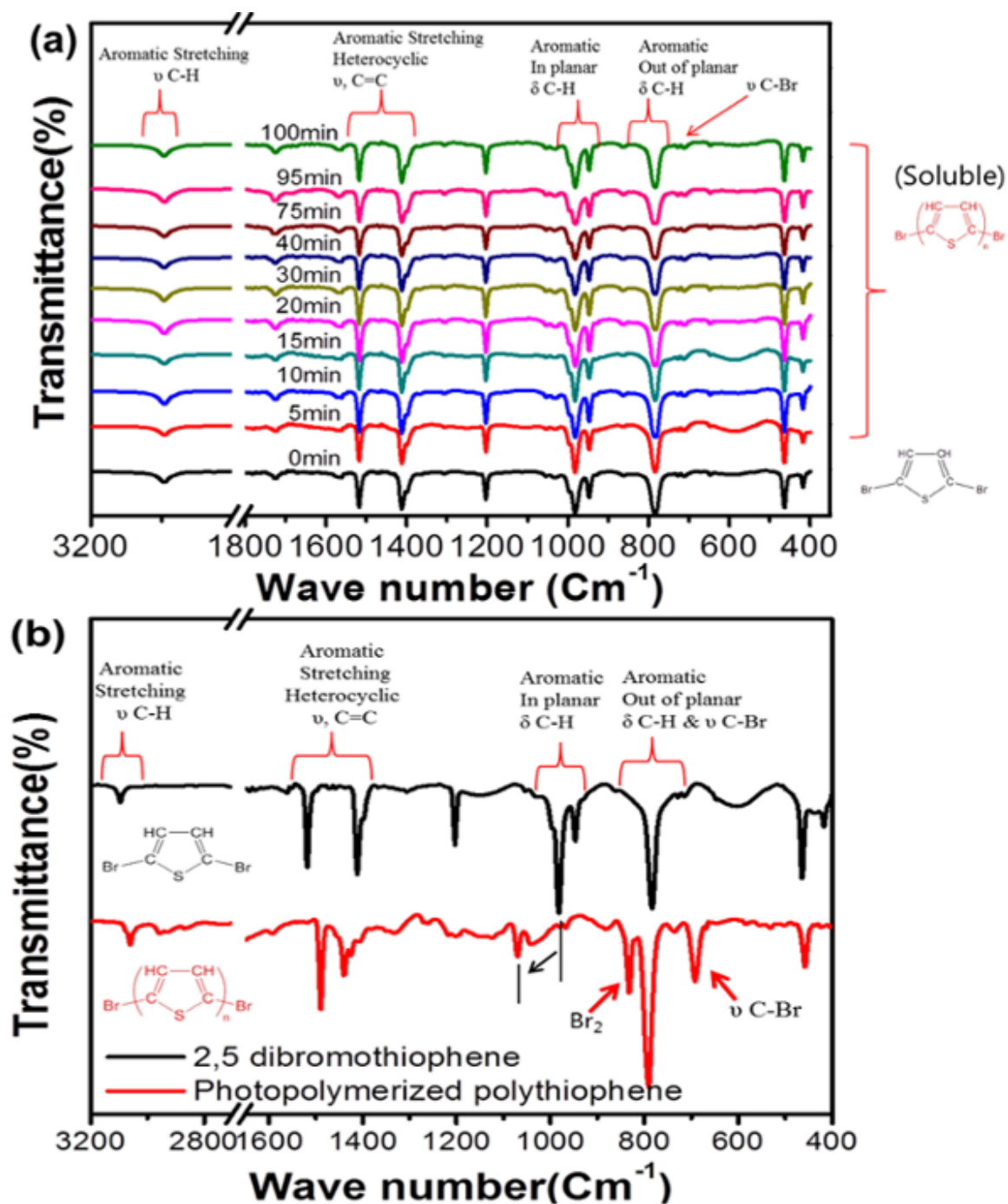


Figure 8.4. FT-IR spectra during the UV photopolymerization of DBT: (a) Soluble portion only, (b) Insoluble portion only.

Both precipitated insoluble and soluble portions during the UV photopolymerization were analyzed by using a FT-IR spectrophotometer (Figure 8.4) and all characteristic polythiophene peaks [272-274] are preserved without any photodegradation under our

optimum exposure conditions. In the soluble portion, aromatic stretching vibrational C-H and C=C peaks are shown at 3080~3030  $\text{cm}^{-1}$  and 1570 ~1475 $\text{cm}^{-1}$  (as a doublet) respectively and an aromatic in planar and out of planar C-H bending peaks are also shown at 1000 and 750 $\text{cm}^{-1}$  respectively. The strong C-Br vibration peak looks overlap with a C-H out of planar peak. Due to the similarity in the chemical structures of a DBT monomer and a soluble low molecular weight polythiophene, there is no distinct difference in their FT-IR spectra. In the insoluble portion, aromatic stretching vibrational C-H and C=C peaks are shown at the similar peaks positions with those of the soluble portion. An aromatic in planar peak is slightly shifted to 1100~1050  $\text{cm}^{-1}$  and an out of planar C-H bending peak is also shown at 800  $\text{cm}^{-1}$  at the same position of soluble portion. An isolated bromine peak and a strong C-Br vibration peak are shown at 850  $\text{cm}^{-1}$  and 700  $\text{cm}^{-1}$  respectively. It is clearly verified that all the characteristic peaks are preserved without any chemical degradation e.g., a thiophene ring breakage during our optimized strong UV exposure. When it is further compared with that of a commercially available high molecular insoluble polythiophene, the shape of their FT-IR spectra match exactly. When it is exposed to the deep UV light which has a wavelength less than 200nm, without a band pass filter, thiophene ring breakage of the insoluble precipitated product is easily recognized using a FT-IR and those characteristic thiophene peaks which are mentioned earlier have disappeared. Characteristic FT-IR peaks of the soluble UV photopolymerized portions which were dissolved in the unreacted DBT monomers during the reaction are also verified to have no photo-degradation.

### **8.3. Catalytical Synthesis of $\alpha,\omega$ -Dibromo-Oligothiophene using Ferric Tribromide ( $\text{FeBr}_3$ ) and Characterization of Its Properties.**

*In situ* UV photo-polymerization of DBT is used to enforce the phase separation of P3HT:PC<sub>61</sub>BM BHJ active layer with the rapid solubility drop during UV exposure. The reaction was carried out with a liquid phase of DBT inside a solid P3HT:PC<sub>61</sub>BM BHJ thin film. Therefore, the high molecular weight of polythiophene is not expected due to the difficulty of solid state polymerization.

For the further understanding of reaction, it is necessary to characterize the fundamental properties of UV photo-polymerized polythiophenes. UV photo-polymerization of DBT is a radical based condensation reaction and requires a long reaction time and soluble oligothiophenes were still dissolved in DBT during reaction. Furthermore, it is difficult to isolate the soluble oligothiophenes only from the final product that mixes with unreacted liquid phase DBT monomers and the high molecular weight polythiophenes during the UV photo-polymerization were insoluble in conventional organic solvents and precipitated. Due to these reaction characteristics, there were many difficulties to carry out the critical chemical analyses. Except for FT-IR and Uvvis analyses, it was difficult to perform other chemical analysis techniques such as GPC and MALDI-TOF MS etc. With the above mentioned analytical difficulties, soluble  $\alpha,\omega$ -dibromo-oligothiophenes, which have molecular weight that is low enough to be soluble in organic solvents, are catalytically synthesized as shown in Figure 8.5.

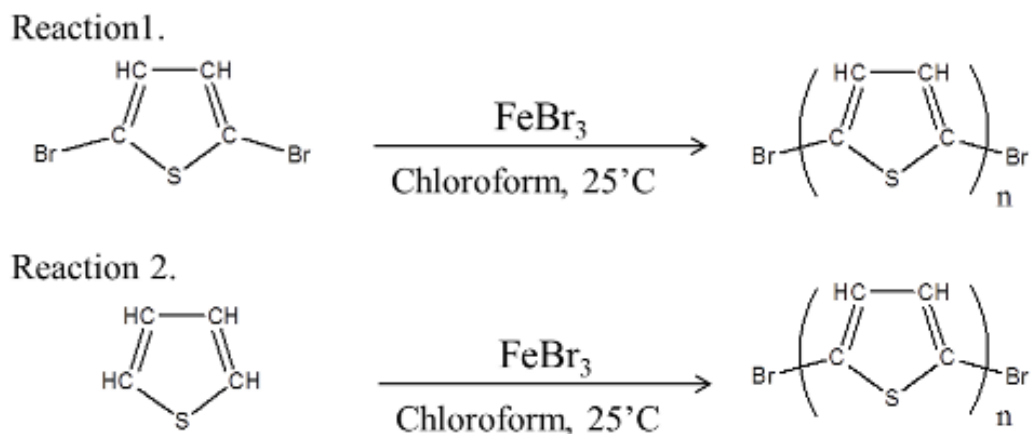


**Figure 8.5. Schematic reaction diagrams of catalytically synthesized Br-terminated  $\alpha,\omega$ -dibromo-oligothiophenes.**

Catalytically synthesized  $\alpha,\omega$ -dibromo-oligothiophenes presumably have same chemical structures that are compared with those from the UV photo-polymerized oligothiophenes and are used as a model system to understand the fundamental material properties of UV photo-polymerized oligothiophenes. Soluble  $\alpha,\omega$ -dibromo-oligothiophenes were synthesized by using Ferric tetrabromide ( $\text{FeBr}_3$ ) as an oxidizing agent in a solution polymerization and the

resulted soluble  $\alpha,\omega$ -dibromo-oligothiophenes were purified using a soxhlet extractor in several differential solvents. The detailed experimental procedures are described in Chapter 2.

Two  $\alpha,\omega$ -dibromo-oligothiophenes that have slight different molecular weight distribution were synthesized and both of them are soluble in many organic solvents such as CB, THF and even in DBT monomer. Furthermore, it is possible to do a spin coating of them on a substrate due to the good solubility in conventional solvents. This good solubility comes from the molecular weight that is low enough to be soluble in organic solvents.

The molecular weight analysis using a MALDI-TOF-MS was performed as shown in Figure 8.6. The polydispersity index (PDI) is around 1.03 and  $M_n$  and  $M_w$  are around 891.3 and 924.1 Da respectively in a high molecular weight (HMW) type that was extracted by using THF. A low molecular weight (LMW) type that was extracted by using acetone has 686.9 Da ( $M_n$ ) and 891.3 Da ( $M_w$ ).

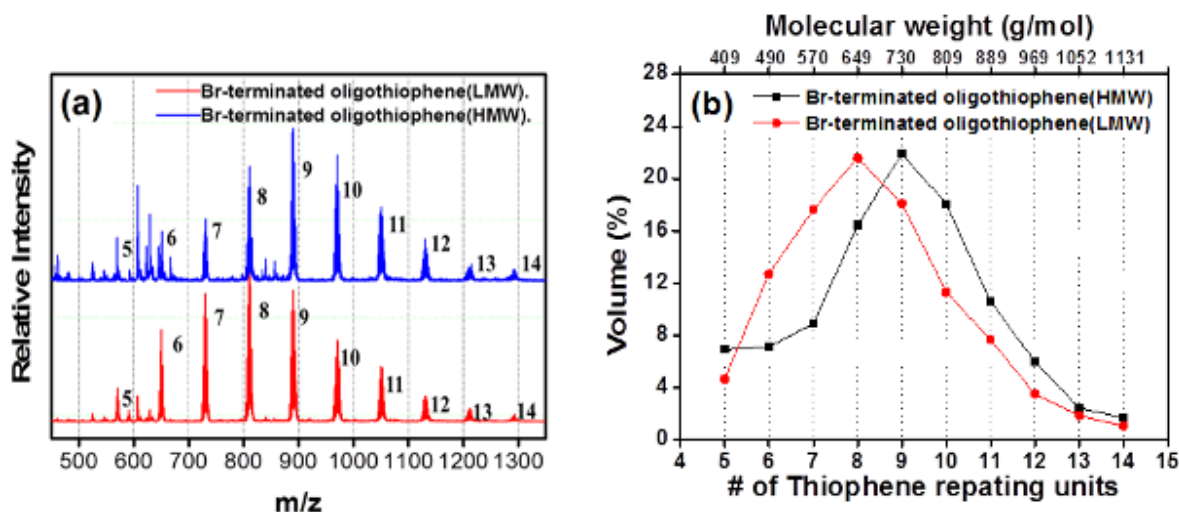


**Figure 8.6.** MALDI-TOF MS results of  $\alpha,\omega$ -dibromo-oligothiophenes for the molecular weight analysis (numbers in (a) graph stand for the # of repeating units).

Reaction verifications was performed using a FT-IR, a X-ray photoelectron spectroscopy (XPS) and a Uv-vis spectrophotometer. All the thiophene characteristic peaks in the FT-IR results are clearly preserved and those peaks are also compared with several commercial thiophene products such as Br-terminated high molecular weight polythiophene,  $\alpha$ -sexithiophene and 2hexylthiophene as shown in Figure 8.7.

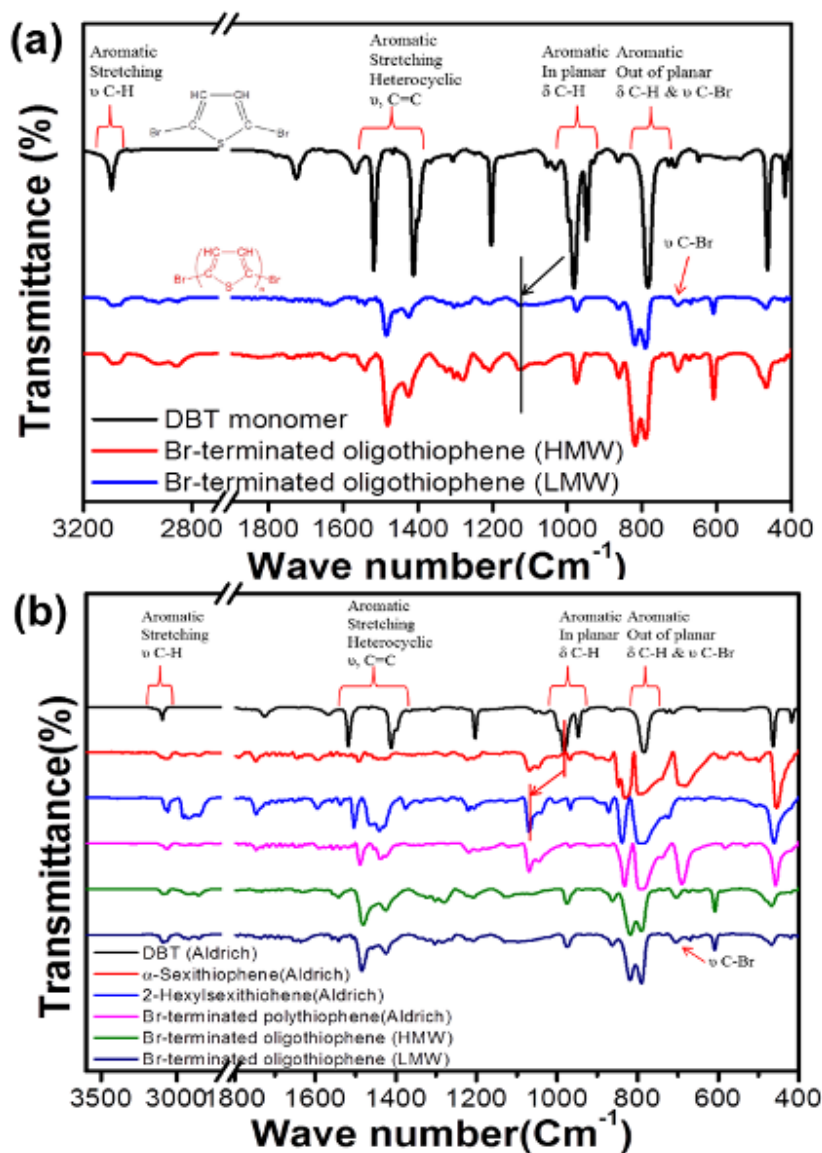


**Figure 8.7. FT-IR spectra of (a) synthesized soluble  $\alpha,\omega$ -dibromo-oligothiophenes and (b) commercially available thiophene products.**

Aromatic stretching vibrational C-H and C=C peaks are shown at  $3080\sim 3030\text{ cm}^{-1}$  and  $1570\sim 1475\text{ cm}^{-1}$  (as a doublet) respectively. In case of an aromatic in planar bending, peaks are slightly shifted from  $1000\text{ cm}^{-1}$  to  $1100\text{ cm}^{-1}$  but an aromatic out of planar C-H bending peaks are shown at  $800\text{ cm}^{-1}$  without any shift. These kinds of trends are also shown in the compared commercial thiophene products.

The calculated XPS results of  $\alpha,\omega$ -dibromo-oligothiophene film which was spun cast on Si wafer is shown in Figure 8.8.

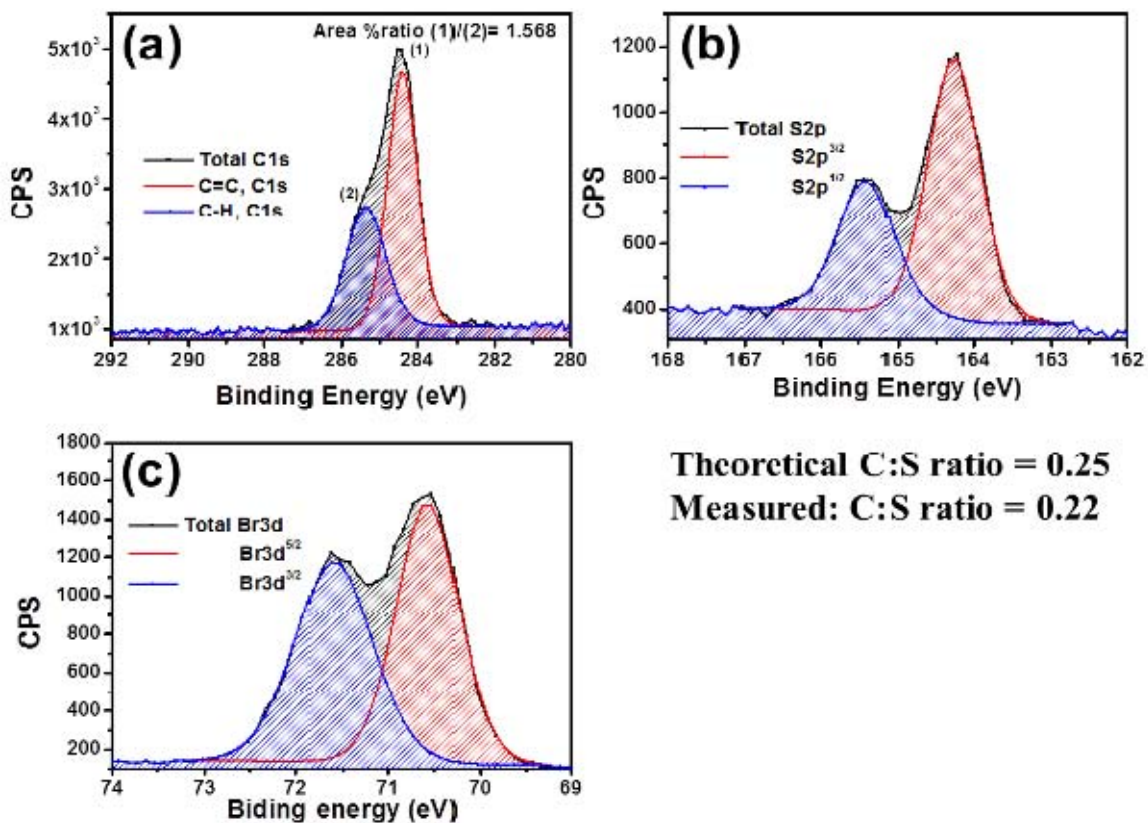


**Figure 8.8. X-ray Photoelectron Spectroscopy (XPS) spectra of  $\alpha,\omega$ -dibromo-oligothiophene (HMW).**

Carbon region in XPS results has two different carbon peaks, C<sub>1s</sub> peak from a C=C bond at 284 eV and the C<sub>1s</sub> peak from C-H at 285.5 eV [270], as shown in Figure 8.8 (a). Absence of other carbonaceous species suggests the homogeneity of the carbon in a synthesized  $\alpha,\omega$ -dibromo-oligothiophene. In the high-resolution of S<sub>2p</sub> XPS region, there is a well-resolved spin-orbit doublet peak at 164.1 and 165.5 eV, as shown in Figure 8.8 (b). These peaks are attributed to 2p<sup>3/2</sup> and 2p<sup>1/2</sup>. Their positions are consistent with the reported XPS values for polythiophene that indicate the intactness of the thiophene monomeric unit in the synthesized polymer film.<sup>27</sup> The ratio of the doublet peak areas is found to be 2:1, which is consistent with theoretical value. The average S/C atomic ratio is found to be around 0.22. It looks like there was some damage to the samples during the XPS survey scan of samples but this is in

agreement with the theoretical value of 0.25 within experimental error ranges. Br  $3d^{5/2}$  and  $3d^{3/2}$  peaks are at 70.5eV and 71.5eV respectively shown in Figure 8.8 (c).

Abs<sub>max</sub> spectra of  $\alpha,\omega$ -dibromo-oligothiophenes from the UVvis spectrophotometer are around 410nm in THF as shown in Figure 8.9.

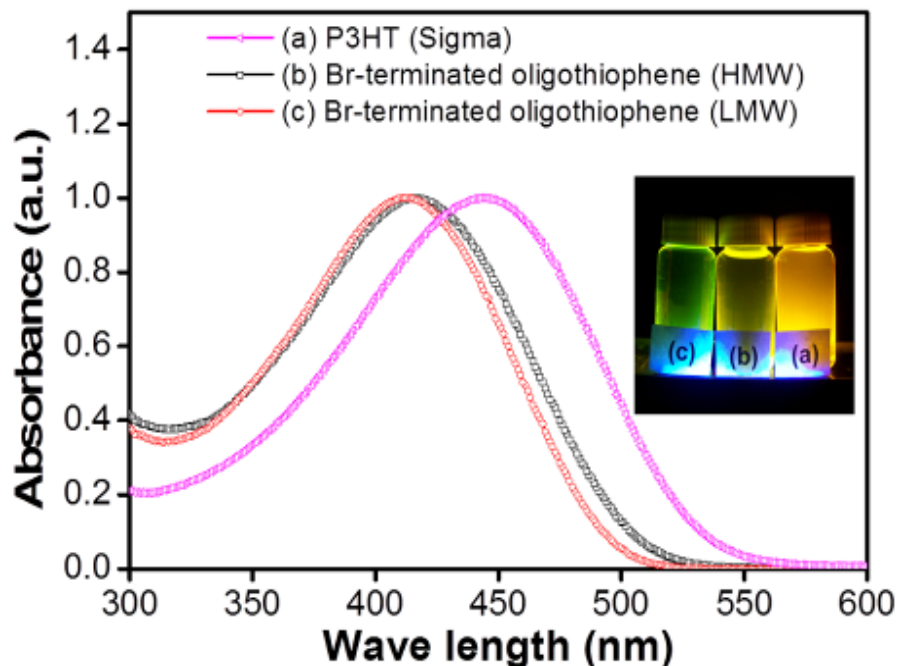


**Figure 8.9.** UVvis spectrophotometer spectra and a photoluminescence color picture of (a) P3HT (Sigma-Aldrich), (b) and (c)  $\alpha,\omega$ -dibromo-oligothiophenes (photoluminescence excited at 365nm).

They have shorter wave lengths of Abs<sub>max</sub> than that of P3HT and are longer than that of 2,6-dihexyl-sexithiophene, due to the conjugation length difference. These Abs<sub>max</sub> wave length values are shorter than those from the soluble UV-photo-polymerized oligothiophenes in Figure 8.2. It is possibly the result of the slight difference in the conjugation length but mainly due to the solvatochromic effect in different solvents. P3HT in CB generally shows more bathochromic absorption shift than in THF.

The photoluminescence results are matched well with the UVvis absorption results. A longer wave length of orange color photoluminescence comes from P3HT and yellow and green color photoluminescence are shown from the synthesized HMW and LMW  $\alpha,\omega$ -dibromo-oligothiophenes respectively. The optical band gaps of them in THF are 2.45 eV (HMW) and 2.51 eV (LMW) respectively (P3HT: 2.33 eV). Both HMW and LMW types have the low

crystallinity and looks like almost amorphous from the XRD results as shown in Figure 8.10 (a).

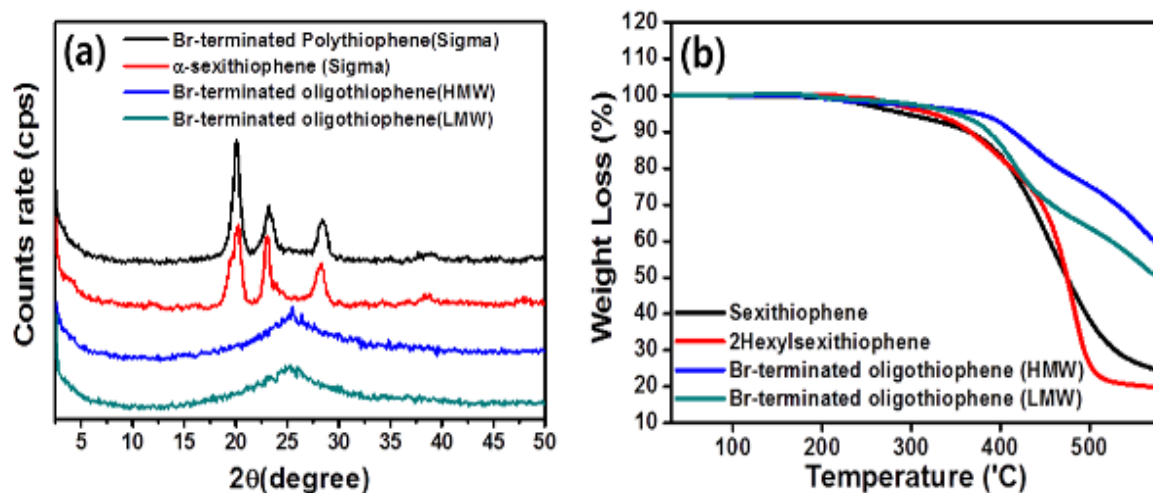


**Figure 8.10. X-ray diffraction (XRD) and thermogravimetric analysis (TGA) results of  $\alpha,\omega$ -dibromo-oligothiophenes.**

However, from DSC results, The HMW  $\alpha,\omega$ -dibromo-oligothiophenes show the melting point ( $m_p$ ) at 210°C, the crystallization temperature ( $T_c$ ) at 150°C and the glass transition temperature ( $T_g$ ) is around 80°C. Even with much shorter conjugation length and lower molecular weight than P3HT, they show similar thermal properties and this indicates that inherent polythiophenes or oligothiophenes free from alkyl side chains have better thermal stability than P3HT. However,  $\alpha,\omega$ -dibromo-oligothiophenes have lower  $T_m$  and  $T_c$  than those of  $\alpha$ -sexithiophene and 2-hexylsexithiophene which have the higher degree of crystallinity ( $T_m \sim 280^\circ\text{C}$  and  $T_c \sim 270^\circ\text{C}$ ). From TGA results as shown in Figure 8.10 (b) in  $\text{N}_2$  gas environment, it appear that the thermal stabilities of the synthesized  $\alpha,\omega$ -dibromo-oligothiophenes are interestingly better than P3HT,  $\alpha$ -sexithiophene and 2-hexyl sexithiophene.  $\alpha,\omega$ -dibromo-oligothiophenes mixed in DBT is placed under the UV light for 20minutes. The formed film was dissolved in CB and a bathochromic shift in the absorption spectrum results due to the increased conjugation length. Additionally, the orange-yellowish color of photoluminescence comes out of the reaction with DBT as shown in Figure 8.11.

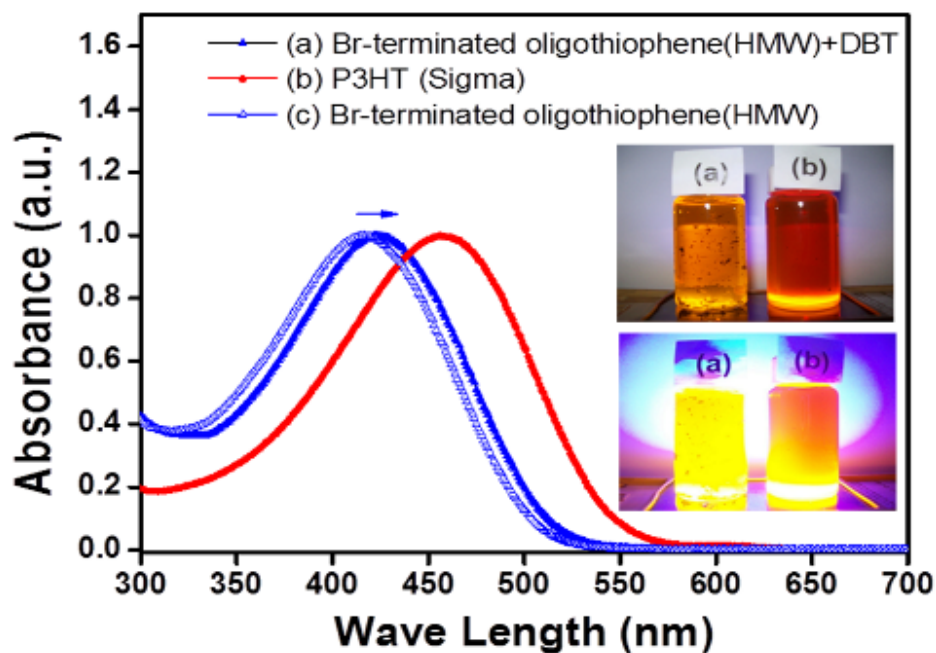


Figure 8.11. UVvis spectrophotometer spectra of (a) 20minutes UV exposed soluble portion of  $\alpha,\omega$ -dibromo-oligothiophenes/ DBTmixture, (b) P3HT (Sigma-Aldrich) and (c) pristine  $\alpha,\omega$ -dibromo-oligothiophene (HMW) (photoluminescence excited at 365nm).

It suggests that the solubility of  $\alpha,\omega$ -dibromo-oligothiophenes are very close to the critical solubility limit and slightly increased molecular weight of them results in the precipitation. The effect on the P3HT:PC<sub>61</sub>BM BHJ domain size and domain purity from the miscibility drop of  $\alpha,\omega$ -dibromo-oligothiophenes inside P3HT:PC<sub>61</sub>BM BHJ active were analyzed using a RSoXS as shown in Figure 8.12.

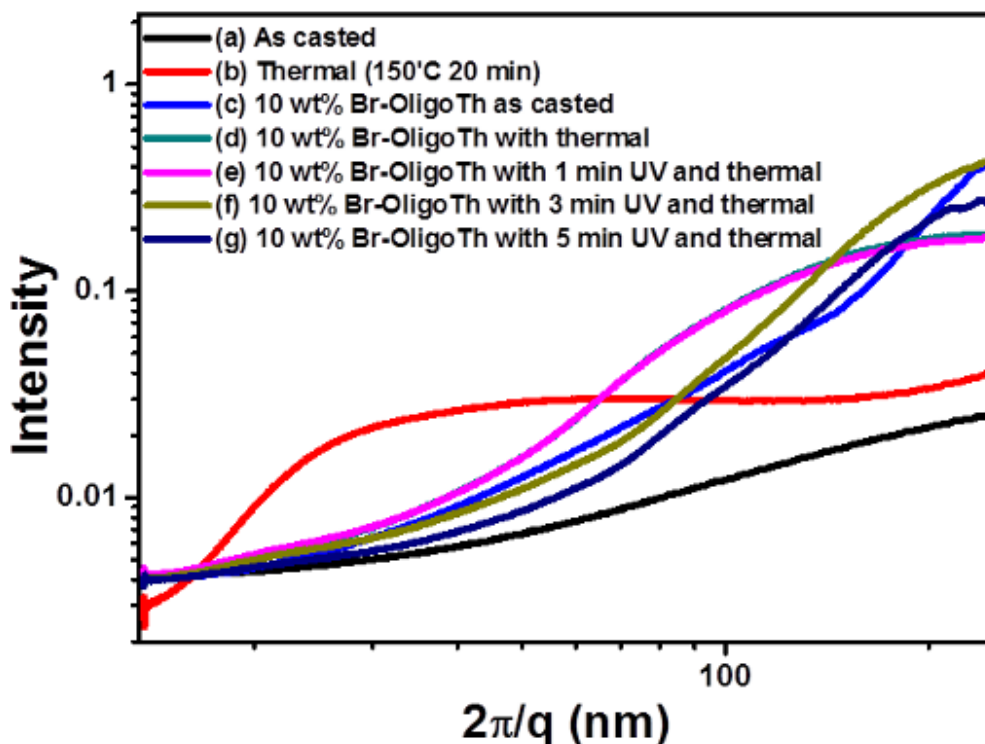


Figure 8.12. RSoXS analysis of P3HT:PC<sub>61</sub>BM BHJ active films with 10 wt% of  $\alpha,\omega$ -dibromo-oligothiophene: (a-b) conventional BHJ films w/wo post thermal annealing, (c-d) 10 wt%  $\alpha,\omega$ -dibromo-oligothiophene introduced BHJ films w/wo post thermal annealing and (e-g) *in situ* UV photo-polymerization of  $\alpha,\omega$ -dibromo-oligothiophene (10 wt%) in P3HT:PC<sub>61</sub>BM BHJ active films with various exposure times.

P3HT:PC<sub>61</sub>BM active films that contain 10 wt% of  $\alpha,\omega$ -dibromo-oligothiophene have much larger domain size around 35~50nm than the conventional P3HT:PC<sub>61</sub>BM BHJ polymer solar cell that have 15~20nm domain size. R-SoXS intensity from the P3HT:PC<sub>61</sub>BM BHJ active films that contain 10 wt% of  $\alpha,\omega$ -dibromo-oligothiophene is much stronger than that of post thermal annealing only. It appears that  $\alpha,\omega$ -dibromo-oligothiophene drives the macro-phase separation in the BHJ active layer due to the worse miscibility of it with P3HT and PC<sub>61</sub>BM components in BHJ active layer. It is very effective to carry out *in situ* UV photo-polymerization of DBT, which is a liquid phase reactive monomer that has the good miscibility with P3HT and PCBM, in P3HT: PC<sub>61</sub>BM BHJ active layer to have the smaller nano-phase separation and finer morphology.

## 8.4. Conclusions.

UV photo-polymerization of DBT was carried out and the reaction is verified using a FT-IR, an UVvis spectrophotometer and photoluminescence that is excited at 365nm. The UV photo-polymerized oligothiophene contains two portions: one is soluble low molecular weight and the other is insoluble high molecular weight oligothiophene. The insoluble portion is precipitated during the long time exposure to UV light. Based on this result, it confirms that a short time UV exposure 1~3 minutes during the *in situ* UV photo-polymerization of DBT inside a P3HT:PC<sub>61</sub>BM BHJ active layer cannot result in the insoluble oligothiophene that has high molecular weight. However, it convinces that *in situ* UV photo-polymerized soluble oligothiophene definitely derives the nano-scale phase separation inside a P3HT:PC<sub>61</sub>BM BHJ active layer to achieve fine morphology due to the miscibility drop of it through the *in situ* UV photo-polymerization of DBT.

A model, soluble Br-terminated  $\alpha,\omega$ -dibromo-oligothiophene was synthesized and its chemical properties were analyzed. From the TGA results, it is confirmed that  $\alpha,\omega$ -dibromo-oligothiophene has better thermal stability than those of insoluble  $\alpha$ -sexithiophene and P3HT, even though it has much small amount of crystalline phase compared with other commercially available thiophene-based materials.  $\alpha,\omega$ -dibromo-oligothiophene has good solubility in conventional solvents such as CB and can be spun cast on substrate as a yellowish colored film. From the MALDI TOF MS analysis Surprisingly, it contains a higher number of repeating units, more than 6 repeating units that is the repeating unit number of insoluble  $\alpha$ -sexithiophene. This relatively higher solubility even with the high number of repeating units comes from the low crystallinity. Further reaction of  $\alpha,\omega$ -dibromo-oligothiophene with DBT under UV light, there is a precipitation for a short time and the soluble portion showed a bathochromic shift in the UVvis absorption spectrum. It means that catalytically synthesized  $\alpha,\omega$ -dibromo-oligothiophene, a model Br-terminated oligothiophene is located near the solubility limit and the further increase of the molecular weight from the UV photo-polymerization with DBT decreases its solubility during the reaction and resulted in a precipitation due to the solubility drop above the solubility critical point. It is confirmed that the lower miscibility of  $\alpha,\omega$ -dibromo-oligothiophene with P3HT and PC<sub>61</sub>BM due to the

high molecular weight effects using R-SoXS analysis. Relatively higher intensity and larger domain size are monitored in the P3HT:PC<sub>61</sub>BM BHJ active layers that contain 10 wt%  $\alpha,\omega$ -dibromo-oligothiophene as an additive regardless of conventional post thermal annealing. In these films domain size decrease was not monitored even followed by a UV exposure with DBT, because  $\alpha,\omega$ -dibromo-oligothiophene itself already has poor miscibility with P3HT and PC<sub>61</sub>BM BHJ components.

## APPENDIX B

### 9. PHYSICS OF SOLAR CELLS

#### 9.1. Equation Derivation for Real Diode that Considers Series and Shunt Resistance

An equivalent circuit diagram (ECD) for ideal diode is shown in Figure 9.1.

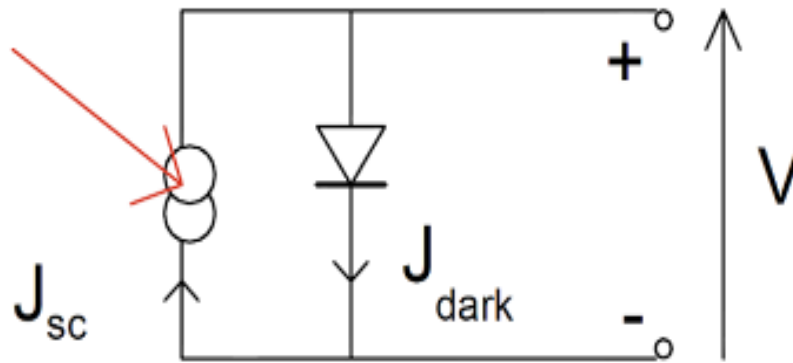


Figure 9.1. Equivalent circuit of an ideal solar cell (Figure are reproduced from [22]).

Solar cells are the conventional diode in the dark condition, and they allow much more current flow in the forward bias ( $V > 0$ ) than in the reverse bias ( $V < 0$ ). This kind of rectifying property is a characteristic of ideal diode properties. Using a simple ideal diode equation, called the Shockley equation, the  $J_{\text{dark}}(V)$  equation is normally formulated as shown in Equation (9-1):

$$J_{\text{dark}}(V) = J_o \left( e^{\frac{qV}{nk_B T}} - 1 \right) \quad (9-1)$$

In this equation,  $J_o$  is a constant,  $K_B$  is Boltzmann's constant,  $n$  is ideality factor and  $T$  is temperature in degrees Kelvin. Because  $R_s = 0\Omega$  and  $R_{sh} = \infty\Omega$  in an ideal diode, current through such an ideal solar cell is determined by current density only, and for an applied positive voltage, the current increases exponentially. Under illuminated conditions, photo-current density from the exposed light photons is generated, and the equation for net current density is modified as Equations (9-2) and (9-3).

The overall current voltage response of solar cells can be approximated as the sum of the

short-circuit photo-current and the dark current. This step is known as the superposition approximation. Although reverse current, which flows in response to voltage in an illuminated solar cell, is not formally equal to current that flows in dark current, the approximation is reasonable for many materials used in solar cells.

$$J(V) = J_{dark}(V) - J_{sc} \quad (9-2)$$

$$J(V) = J_o \left( e^{\frac{qV}{nk_B T}} - 1 \right) - J_{sc} \quad (9-3)$$

With isolated contact, the potential difference that originates from the difference in energy levels between the electron donors and electron acceptors reaches its maximum value, which is the open-circuit voltage ( $V_{oc}$ ). This voltage occurs when the dark current and short-circuit photo-current cancel each other out. The  $V_{oc}$  for an ideal diode is shown in Equation (9-4) when the current density = 0. The  $V_{oc}$  increases logarithmically with light intensity.

$$V_{oc} = \frac{nK_B T}{q} \ln\left(\frac{J_{sc}}{J_o} + 1\right) \quad (9-4)$$

The function of solar cells in the real world is slightly different than that of an ideal diode. The two inherent resistances,  $R_{sh}$  and  $R_s$ , are not considered in an ideal diode. Their effect on the final solar cells' performance is critical, and a more realistic model is needed to predict and to explain the real function and performance of solar cells.

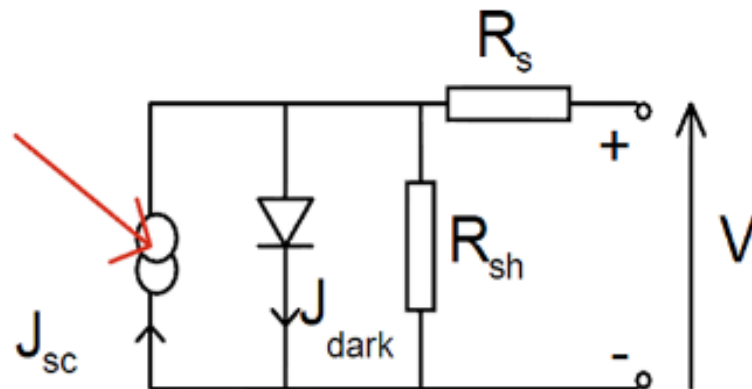


**Figure 9.2. Equivalent circuit, including series and shunt resistances (Figure are reproduced from [2222]).**

Series resistance depends mainly on the resistance of each of the solar cell materials and the surface contacts. High series resistance reduces the current flow under short-circuit conditions. Shunt resistance originates in current leakage through devices and results in

poorly rectifying solar cells. The series resistance and shunt resistance reduce the FF, as shown in Figure 9.2. A small series resistance and large shunt resistance are needed in order to have excellent working solar cells.

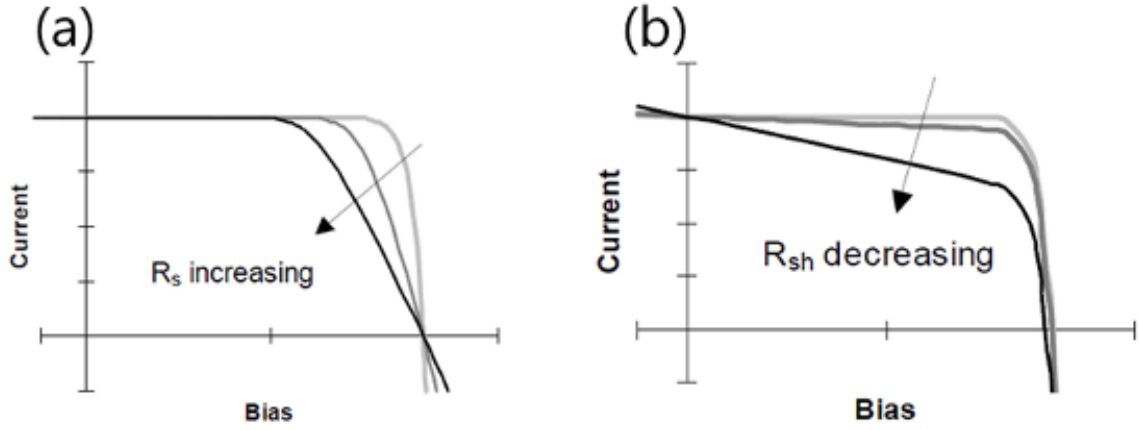


**Figure 9.3. Effect of (a) increasing series resistance and (b) decreasing shunt resistance on solar cell performance: In each case, the outer curve has  $R_s = 0\Omega$  and  $R_{sh} = \infty\Omega$ ; the effect of the resistances is to reduce the area of the maximum power compared to  $J_{sc} \times V_{oc}$  (Figure are reproduced from [22]).**

When parasitic series and shunt resistances are considered, as shown in Figure 8.14., Equation (9-4) should be modified to become Equation (9-5).

$$(J_{sc} - J_{dark} - J)R_{sh} = V + JR_s \quad (9-5)$$

This Equation (8-5) can be transformed into Equation (8-6).

$$J\left(\frac{R_s}{R_{sh}} + 1\right) = J_{sc} - J_{dark} - \frac{V}{R_{sh}} \quad (9-6)$$

Combined with Equation (8-1),

$$J_{dark}(V) = J_o \left( e^{\frac{qV}{nk_B T}} - 1 \right) \quad (9-1)$$

Equation (8-6) becomes Equation (8-7).

$$J = \left( J_{sc} - \frac{V}{R_{sh}} \right) \frac{R_{sh}}{R_{sh} + R_s} - J_o \frac{R_{sh}}{R_{sh} + R_s} \left( e^{\frac{V - JR_s}{nk_B T/q}} - 1 \right) \quad (9-7)$$

The final rearranged equation is Equation (8-8)

$$J = \frac{J_{sc} - \frac{V}{R_{sh}}}{1 + \frac{R_s}{R_{sh}}} - \frac{J_o}{1 + \frac{R_s}{R_{sh}}} \cdot \left( e^{\frac{V - JR_s}{nk_B T/q}} - 1 \right) \quad (9-8)$$

The open-circuit voltage ( $V_{oc}$ ) also should be modified in consideration of the shunt resistance effect, as shown in Equation (8-9).

$$V_{oc} = \frac{nK_B T}{q} \ln\left(\frac{J_{sc} - V_{oc} / R_{sh}}{J_o} + 1\right) \quad (9-9)$$